SAPIENZA
UNIVERSITÀ DI ROMA

**Sapienza University of Rome**

Department of Structural and Geotechnical Engineering

PhD in Structural Engineering

Thesis For The Degree Of Doctor Of Philosophy

# Experimental Investigations into Wave Propagation in Acoustic Metamaterials

PhD CANDIDATE
**Guruva Sawan Kumar**
ID number **1773514**

ADVISOR
**Prof. Walter Lacarbonara**

CO-ADVISORS
**Prof. Giuseppe Quaranta**
**Prof. Biagio Carboni**

Academic Year 2022-2025 (XXXVIII cycle)

*© 2025 Guruva Sawan Kumar. All rights reserved.*

**Abstract**

This study presents a comprehensive experimental and numerical investigation into the design, fabrication, and dynamic characterization of acoustic metamaterials. The metamaterial architectures investigated here incorporate embedded resonators arranged in periodic and quasi-periodic configurations to manipulate elastic wave propagation through local resonance effects. Samples are fabricated using stereolithography and fused deposition 3D printing, ensuring high geometric accuracy and repeatability, while their dynamic response is measured using 3D laser scanning vibrometry (Polytec PSV-500-3D), which provides full-field, non-contact measurements of velocity field.

The study focuses on honeycomb lattices with distributed resonators, analyzed under piezoelectric and electrodynamic excitations. Distinct vibration bandgaps are experimentally identified, with frequencies and bandwidths that show excellent agreement with theoretical predictions obtained through the Plane Wave Expansion (PWE) method and finite element simulations in COMSOL Multiphysics. The integration of multi-frequency resonators within the honeycomb structure broadens the attenuation range, while the spider-web configuration exhibits multiple low-frequency bandgaps resulting from coupling between radial and circumferential vibration modes.

Further investigations on 3D-printed spider-web resonator metamaterials reveal nonlinear behaviors and sensitivity to geometric imperfections. The baseline design of honeycombs with spider web-like resonators exhibits three distinct bandgaps and a hardening-type response under increasing excitation levels, whereas the imperfect variant shows detuned resonators and softening-type nonlinearity, leading to tunable bandgap behavior. Both designs display edge wave phenomena near the transition between acoustic and optical modes, confirmed through eigenvalue analyses.

Complementary studies extend the investigation to electrospun membrane-based metamaterials and aperiodic Penrose lattices, which reveal disorder-induced localization and hybrid bandgap mechanisms emerging from quasi-periodicity and multi-scale interference.

Overall, this work establishes a rigorous experimental framework for the study of wave propagation in periodic, nonlinear, and aperiodic resonant metamaterials. The findings demonstrate how geometry, nonlinearity, and structural imperfections jointly govern wave behavior, offering design principles for next-generation metamaterials in vibration suppression and noise control.

# Acknowledgments

First and foremost, I would like to express my deepest gratitude to my advisor, Prof. Walter Lacarbonara, for his unwavering guidance, patience, and encouragement throughout this journey. His steadfast support and insightful mentorship have been a constant source of strength and inspiration.

I am equally indebted to my co-advisors, Prof. Giuseppe Quaranta and Prof. Biagio Carboni, for their kindness, clarity, and invaluable feedback. Their thoughtful guidance, attention to detail, and willingness to address even my smallest doubts have profoundly shaped this work and my academic growth.

I wish to extend my heartfelt thanks to Prof. Giulia Lanzara and her team for their generous assistance and for cultivating a spirit of collaboration throughout this research

I would also like to extend my sincere thanks to Dr. Laura Di Gregorio and Dr. Mauro Murer for their continuous support, valuable suggestions, and for fostering a stimulating and collaborative research environment.

My heartfelt appreciation also goes to the laboratory staff, Giuliano Manganozzi and Stefano Putgioni, at the Department of Structural and Geotechnical Engineering, for providing not only the necessary technical resources but also a supportive atmosphere that greatly contributed to the success of this research.

To my colleagues and friends, your camaraderie made this journey truly memorable. A special mention goes to Dr. Stefano Catarci, Dr. Krishna Chytanya Chinnam and B. Sharath Chandra, whose constant encouragement, wisdom, and friendship both personal and professional were invaluable throughout this Ph.D. journey. I am also deeply thankful to G. Pranath Kumar, Dr. J. Vinay Yadav, and Harrish Joseph for their companionship and support. The shared struggles, discussions, and countless moments of laughter made the challenges along the way lighter and the accomplishments far more rewarding. I could not have asked for better companions.

Above all, none of this would have been possible without my parents, whose unconditional love, sacrifices, and unwavering belief in me have been my greatest motivation. Their encouragement carried me through the most difficult moments and inspired me to persevere. To my wonderful brothers, G. Charan Das and G. Arjun Dev, thank you for being my constant source of encouragement, for lifting me up when I stumbled, and for your endless support. Last but not least, I would like to acknowledge the support received

by the Air Force Office of Scientific Research (AFOSR) through Grants FA9550-14-1-0082 and FA8655-20-1-7025 and Rome Technopole covering some of the activities related to my thesis.

# Contents

**Acknowledgments** **1**

**1 Introduction** **16**
1.1 State of the art . . . 17
1.2 Achieved results . . . 20
1.2.1 Approach . . . 22
1.3 Outline of the thesis . . . 23

**2 Multiple bandgaps in locally resonant metamaterials** **26**
2.1 Additive manufacturing . . . 27
2.1.1 Stereolithography . . . 27
2.2 3D laser scanning vibrometry . . . 28
2.2.1 Polytec PSV-500-3D Scanning Vibrometer . . . 30
2.3 Cantilever with different tipmass . . . 31
2.3.1 Characterization with electrodynamic shaker . . . 32
2.3.2 Frequency response analysis . . . 36
2.3.3 Experimental response near the first bandgap . . . 37
2.3.4 Simulations vs. experiments . . . 41
2.3.5 Characterization under PZT excitation . . . 43
2.3.6 Characterization of LF in the absence of resonators . . . 43
2.4 Summary . . . 47

**3 Tunable bandgaps in locally resonant metamaterials** **49**
3.1 Fused deposition modeling . . . 50
3.2 Spider web-like resonators . . . 51
3.3 Test setup with PSV system . . . 53
3.3.1 Characterization of the SWR-I under PZT excitation . . . 53
3.3.2 Investigation around bandgaps . . . 57
3.3.3 Characterization of the SWR-II with PZT . . . 59
3.3.4 Observed edgewaves in SWR samples . . . 61
3.4 Bandgap via finite element model . . . 62

3.4.1 Unit cell geometry . . . 63
3.4.2 Modeling approach and physics selection . . . 64
3.4.3 Wave vector path and Bloch-Floquet boundary conditions . . . 64
3.4.4 Eigenfrequency analysis and mode characterization . . . 65
3.4.5 Experiments versus FEM results . . . 67
3.5 Frequency response curves . . . 69
3.6 Summary . . . 74

**4 Experimental results: Edgewave in Locally Resonant Metamaterial 75**
4.1 Edgewave in locally resonant . . . 75
4.1.1 Characterization of LR with PZT . . . 76
4.1.2 Numerical model for edgewave . . . 78
4.2 Summary . . . 79

**5 Experimental results: compositional disorder in periodic structures 81**
5.1 Test setup with PSV system . . . 82
5.1.1 Characterization of electrospun membrane with PZT . . . 82
5.1.2 Characterization of electrospun membrane with electrodynamic shaker 85
5.1.3 In-depth analysis of unitcells . . . 88
5.2 Summary . . . 90

**6 New directions: aperiodic metamaterials with resonators 92**
6.1 Penrose tiling by rhombi . . . 93
6.2 Penrose P3-pattern samples . . . 95
6.2.1 Characterization of P3-I with PZT . . . 96
6.2.2 Characterization of P3-II with PZT . . . 99
6.2.3 Characterization of P3-II with electrodynamic shaker . . . 100
6.3 Summary . . . 103

**7 Conclusions 104**

**A Modeling of Metamaterial with Local Resonator 107**
A.1 Metamaterial Modeling . . . 107
A.1.1 Resonators modeling . . . 111

**B Honeycomb Reduction to an Equivalent Orthotropic Plate 115**
B.1 Solution strategy for the mechanical system . . . 116

**C Operational Deflection Shape (ODS) Extraction Procedure 117**
C.1 Data requirements . . . 117
C.2 Time-domain ODS . . . 117
C.3 Frequency-domain ODS . . . 118

# List of Figures

2.1 Form 3+ 3D printer shown with a fabricated sample. . . . . 28
2.2 (a) Optical layout of a laser Doppler vibrometer [1]. (b) Polytec 3D Xtra 500 system for vibration measurement. . . . . 29
2.3 Snapshots of the 3D-printed samples mounted on the electrodynamic shaker, representing: (a) the low-frequency (LF) metamaterial sample, featuring cantilever resonators with a length of 10 mm and associated tip masses with dimensions of $6 \times 6 \times 5$ mm$^3$; (b) the medium-frequency (MF) sample, with 8 mm long cantilevers and tip masses of $2.5 \times 2.5 \times 3$ mm$^3$; and (c) the high-frequency (HF) metamaterial, utilizing 6 mm cantilevers with tip masses sized at $2 \times 2 \times 1$ mm$^3$ [2]. . . . . 31
2.4 A schematic representation of the experimental setup is shown, featuring the use of an electrodynamic shaker to excite the metamaterial sample and the integration of a Polytec PSV-500-3D Scanning Laser Vibrometer (PSV) system for dynamic response measurement. Using Polytec's software, a detailed scanning mesh was generated, enabling pointwise measurements across the sample. . . . . 32
2.5 Average Frequency Response Function (FRF) spectra with highlighted bandgap regions (shaded in grey): (a) low-stiffness sample, (b) medium-stiffness sample, and (c) high-stiffness sample. In the figure, GM denotes global mode. . . . . 33
2.6 Experimentally acquired operational deflection shapes (ODSs) of the low-stiffness metamaterial sample under chirp excitation from the electrodynamic shaker. The selected ODSs were acquired at the following frequencies: (a) 0.01718 kHz, (b) 0.0738125 kHz, (c) 0.145312 kHz, (d) 0.23597 kHz, (e) 0.4406 kHz, (f) 0.68437 kHz (bandgap), (g) 0.80156 kHz, (h) 0.95162 kHz, (i) 1.43437 kHz, (j) 1.58984 kHz, (k) 2.19921 kHz. . . . . 34

2.7 Experimentally acquired operational deflection shapes (ODSs) of the medium-stiffness metamaterial sample under chirp excitation from the electrodynamic shaker. The selected ODSs were acquired at the following frequencies: (a) 0.024 kHz, (b) 0.104 kHz, (c) 0.190 kHz, (d) 0.426 kHz, (e) 0.542 kHz, (f) 0.754 kHz (g) 0.960 kHz, (h) 1.112 kHz, (i) 1.69 kHz, (j) 1.882 kHz, (k) 2.14 kHz (bandgap), (l) 2.46 kHz, (m) 2.874 kHz, (n) 3.64 kHz, (o) 4.412 kHz, (p) 5.916 kHz. . . . . 35
2.8 Experimentally acquired operational deflection shapes (ODSs) of the high-stiffness metamaterial sample under chirp excitation from the electrodynamic shaker. The selected ODSs were acquired at the following frequencies: (a) 0.0225 kHz, (b) 0.1075 kHz, (c) 0.2075 kHz, (d) 0.4525 kHz, (e) 0.8025 kHz, (f) 1.01 kHz (g) 1.995 kHz, (h) 3.1025 kHz, (i) 3.825 kHz, (j) 4.2225 kHz, (k) 4.74 kHz (bandgap), (l) 5.37 kHz, (m) 6.435 kHz, (n) 7.7425 kHz. . . . . 36
2.9 Comparison between the experimentally observed bandgaps in the FRFs (mid column) and the theoretically predicted dispersions curves (right column) and sample are presented in left column: for (a) LF, (d) MF, and (g) HF samples. The blue and orange curves denote the experimental measurements of the cell vertex (yellow dot) and of the resonator tip mass (orange dot), respectively. The filled colored rectangles in the experimental FRFs indicate the theoretically predicted bandgpas. . . . . 38
2.10 Time histories and FFTs of the displacements of (a)-(b) the resonator tip mass and (c)-(d) of the hexagonal cell vertex (see Fig.2.4), when the LF sample was harmonically excited at 499 Hz (blue line), 600 Hz (red line), 797 Hz (black line), respectively. Near-zero response is observed for the excitation frequency of 600 Hz within the first bandgap. . . . . 39
2.11 Average FRFs of the MF sample where the blue line denotes the average FRF of the cells only, the magenta line indicates the average FRF of the resonators, and the green line the average FRF of the whole metamaterial sample. . . . . 39
2.12 FRFs and phases of the PSV scanned points on selected cell vertices and resonators when the sample is subject to a chirp input signal. The colored filled points indicate the acquired points and the curves with the same color indicate the corresponding acquired FRFs and phase outputs. The gray filled regions indicate the theoretically predicted first bandgap. . . . . 40

2.13 Time histories of the deflections of (a) resonator tip mass and (b) and honeycomb cell vertex (see Figure 12(c)), when the LF sample is excited by a harmonic base motion at 499 Hz (blue), 600 Hz (red), 797 Hz (black), respectively. The solid lines indicate the experimental results and the dotted lines denote the FEM predictions. . . . . 41
2.14 Mode shapes of the honeycomb metamaterial system with the embedded cantilever resonators and the associated frequencies. The modes in part (a) possess frequencies below the first bandgap, in part (b) within the bandgap, and in part (c) above the bandgap. . . . . 42
2.15 A schematic representation of the experimental setup is shown, featuring the use of an PZT disk to excite the metamaterial sample and the integration of a Polytec PSV-500-3D Scanning Laser Vibrometer (PSV) system for dynamic response measurement. . . . . 44
2.16 Average Frequency Response Function (FRF) spectra with highlighted bandgap regions (shaded in grey): (a) low-frequency (LF) sample with one missing resonator, (b) LF sample with four missing resonators, and (c) comparison of the average FRF spectra for samples with missing resonators. 44
2.17 Experimentally acquired operational deflection shapes (ODSs) of the LF with 1 resonator missing metamaterial sample under chirp excitation from the PZT actuation disk. The selected ODSs were acquired at the following frequencies: (a) 0.0975 kHz, (b) 0.180 kHz, (c) 0.2663 kHz, (d) 0.3288 kHz, (e) 0.465 kHz, (f) 0.5625 (first bandgap) kHz (g) 0.650 kHz, (h) 0.8613 kHz, (i) 0.9663 kHz, (j) 1.0936 kHz, (k) 1.2 kHz , (l) 1.4563 kHz, (m) 1.615 kHz, (n) 2.1638 kHz, (o) 2.450 kHz, (p) 2.830 kHz, (q) 3.015 kHz , (r) 3.790 kHz, (s) 4.0213 kHz, (t) 4.4088 kHz, (u) 4.850 kHz,(v) 5.5175 kHz (w) 6.0475 (second bandgap) kHz, (x) 6.6275 kHz and (y) 7.2475 kHz. . . 46
2.18 Experimentally acquired operational deflection shapes (ODSs) of the LF with 4 resonator missing metamaterial sample under chirp excitation from the PZT actuation disk. The selected ODSs were acquired at the following frequencies: (a) 0.1 kHz, (b) 0.175 kHz, (c) 0.275 kHz, (d) 0.375 kHz, (e) 0.5 kHz, (f) 0.55 (first bandgap) kHz (g) 0.7 kHz, (h) 5.2 kHz, (i) 5.725 (second bandgap) kHz, (j) 6 kHz, (k-l) 40.025 - 43.05 (third bandgap) kHz, (m) 46.85 kHz, (n-o) 53.5 - 57.3 (fourth bandgap) kHz, (p) 66.625 kHz (q) 68.725 (fifth bandgap) kHz and (r) 76.725 kHz. . . . . 47

3.1 Raiser 3D Pro3 Plus 3D printer shown with a fabricated sample. . . . . 51

3.2 (a) 3D geometric model of SWR-I resonator unit cell with parameters: m = 1, b = 0.5 mm, d = 0.5 mm, h = 3 mm, r = 3 mm, R = 6 mm, t = 1.5 mm, a = 9.34 mm, c = 3.04 mm, w = 2 mm, and L = 15.01 mm, the structure is 3D-printed and forms a 2D metamaterial arranged in an $N \times M$ size. (b) 3D geometric model of SWR-II resonator unit cell with parameters: m=2.5, b=1, d=0.5, h=3.5, r=3, R=8.08, t=2, a=12.7, c=4.23, w=2.88, L=19.63 (lengths expressed in mm), the structure is 3D-printed and forms a 2D metamaterial arranged in an $N \times M$ size. . . . . 52
3.3 (a) Snapshot of M1 sample with scan points highlighted in red color (b) average FRF spectrum highlighted with three bandgaps (grey). . . . . 54
3.4 Experimentally acquired ODSs excited by the chirp signal provided by the PZT cylindrical patch. The selected ODSs were acquired at the following frequencies: (a) 0.0390625 kHz, (b) 0.0734375 kHz, (c) 0.1328125 kHz, (d) 0.2171875 kHz, (e) 0.234375 kHz, (f) 0.2765625 kHz, (g) 0.3234375 kHz, (h) 0.3953125 kHz, (i) 0.43125 kHz, (j) 0.4765625 kHz, (k) 0.5625 kHz, (l) 0.59375 kHz, (m) 0.640625 kHz, (n) 0.7078125 kHz, (o) 0.7609375 kHz, (p) 0.8546875 kHz, (q) 0.89375 kHz, (r) 0.921875 kHz, (s) 0.9734375 kHz (1st bandgap), and (t) 1.0984375 kHz. . . . . 55
3.5 Experimentally acquired ODSs at the following frequencies: (a) 1.259375 kHz, (b) 1.3578125 kHz, (c) 1.4328125 kHz, (d) 1.578125 kHz, (e) 1.7296875 kHz, (f) 1.8609375 kHz, (g) 1.925 kHz, (h) 1.9953125 kHz (2nd bandgap), (i) 2.128125 kHz (j), 2.321875 kHz, (k) 2.4109375 kHz, (l) 2.5125 kHz, (m) 2.7046875 kHz, (n) 3.890625 kHz, (o) 4.0328125 kHz, (p) 4.1421875 kHz, (q) 4.4015625 kHz, (r) 4.653125 kHz (3rd bandgap), (s) 4.9234375 kHz, (t) 5.3734375 kHz, (u) 5.6625 kHz, (v) 7.6234375 kHz, (w) 7.6328125 kHz, and (x) 8.6328125 kHz. . . . . 56
3.6 Passage across three bandgaps. 1st bandgap at 0.9953 kHz, (c) optical mode at 1.2641 kHz. Second bandgap: (d) acoustic mode at 1.8625 kHz, (e) response in the 2nd bandgap at 1.9859 kHz,(f) optical mode at 2.3281 kHz. Third bandgap: (g) acoustic mode at 4.1016 kHz, (h) response in the 3rd bandgap at 4.6578 kHz, (i) optical mode at 4.9234 kHz. . . . . 58
3.7 FRFs of two arrays of resonators first array (1,2,3) shown in part a, second array (4,5,6) shown in part e - around the 1st bandgap (b,f,j), the 2nd bandgap (c,g,k), and the 3rd bandgap (d,h,l). . . . . 58
3.8 (a) Snapshot of the SWR-II sample with scan points highlighted in red, (b) close-up view highlighting the designed thickness non-uniformity and fabrication-induced deviations, (c) spatially averaged FRF over the range $[0, 4]$ kHz, and (d) zoom of the range $[0, 1]$ kHz. . . . . 60

3.9 Experimentally acquired ODSs at frequencies: (a) 0.0375 kHz, (b) 0.053 kHz, (c) 0.0703 kHz, (d) 0.1203 kHz, (e) 0.1266 kHz, (f) 0.2 kHz, (g) 0.2414 kHz, (h) 0.2969 kHz, (i) 0.325 kHz, (j) 0.3539 kHz, (k) 0.3859 kHz, (l) 0.4219 kHz, (m) 0.4625 kHz, (n) 0.493 kHz, (o) 0.505 kHz, (p) 0.5516 kHz, (q) 0.5805 kHz (1st bandgap), (r) 0.6203 kHz, and (s) 0.6555 kHz. . 61
3.10 Snapshots of edgewaves in SWR samples exhibiting edge-localized modes after the first bandgap: (a) SWR-1 sample, edgewaves observed in the frequency range of approximately 0.97–1.09 kHz; (b) SWR-2 sample, edgewaves observed in the frequency range of approximately 0.62–0.65 kHz. . 62
3.11 Detailed view of the unit-cell geometry with attached resonator for samples SWR-I and SWR-II. All geometric and material parameters of the unit cell and resonator are indicated in tab.3.3. . . . . 63
3.12 Eigenfrequencies and mode shapes obtained by COMSOL: (a) 1.0385 kHz, (b) 2.3578 kHz, (b1) 2.3579 kHz, (c) 5.4528 kHz, (c1) 5.4536 kHz, (d) 5.9655 kHz, (e) 6.1508 kHz, (f) 6.5067 kHz, (g) 6.8375 kHz, (h) 9.1182 kHz, (h1) 9.1189 kHz, (i) 9.3213 kHz (j) 9.324 kHz, (k) 10.166 kHz, (l) 10.591 kHz, and (l1) 10.591 kHz. The highlighted red box are belongs to complementary modes. . . . . 66
3.13 Eigenfrequencies and mode shapes obtained by COMSOL: (a) 0.49643 kHz, (b) 1.1867 kHz, (b1) 1.1868 kHz, (c) 2.5862 kHz, (c1) 2.5864 kHz, (d) 2.9663 kHz, (e) 3.016 kHz, (f) 3.1375 kHz, (g) 3.270 kHz, (h) 4.189 kHz, (h1) 4.1893 kHz, (i) 4.7501 kHz, (i1) 4.7503 kHz, (j) 6.4394 kHz, (j1) 6.440 kHz, (k) 6.9215 kHz, (l) 7.347 kHz, and (l1) 7.3471 kHz. The red boxes highlight companion modes. . . . . 66
3.14 Comparison of experimentally observed bandgaps and numerical predictions for (a) SWR-I and (d) SWR-II. The left column shows the physical samples, the middle column (b, e) presents the experimentally measured FRFs, and the right column (c, f) shows the FEM-predicted dispersion curves with associated eigenmodes. Red curves correspond to the experimental responses of the resonator (orange dot) and the structure. Black curves denote the FEM-predicted dispersion relations. Shaded regions indicate bandgaps: gray regions in the FRFs represent experimentally observed bandgaps, while colored regions (orange, green, gray) in the dispersion plots denote FEM-predicted bandgaps. . . . . 68
3.15 Schematic of the test setup used to obtain frequency response curves (FRCs) with laser sensors, where the spider-web resonator (SWR-II) metamaterial sample is clamped to the shaker expander. One laser is focused on the resonator (highlighted in green), while another laser is focused on the shaker head expander. . . . . 70

3.16 (a) FRF of the SWR-II sample with the large resonator (highlighted in green) obtained from the PSV system. (b) Resonator FRCs corresponding to the first acoustic mode under varying base excitation levels: 1g, 2g, 3g, 4g, 6g, 8g, 10g, 12g, 14g, and 16g. (c) Resonator FRCs within the first bandgap range under different base excitation amplitudes: 4g, 6g, 8g, 10g, 12g, 14g, 16g, 18g, 20g, and 22g. (d) Comparison of resonator response within the bandgap across excitation amplitudes, from the lowest (4g) to the highest (22g). . . . . 71
3.17 (a) FRF of the SWR-II unit cell sample, glued onto the shaker expander, with the large resonator highlighted in green. Data obtained from the PSV system. (b) FRCs of the first mode of the SWR-II resonator (highlighted in green) under excitation amplitudes of 5g, 6g, 8g, 10g, 12g, 14g, 16g, 18g, 20g, 22g, 24g, and 26g. . . . . 72
3.18 (a) Frequency response function of the SWR-II sample with the large resonator (highlighted in green), obtained from the PSV system. (b) Resonator frequency response curves (FRCs) of the SWR-II sample under varying base excitation levels: 0.5g, 0.75g, 1g, 2g, 3g, 4g, 5g, 6g, and 7g. (c) Frequency response function of the SWR-I sample with the large resonator (highlighted in green), obtained from the PSV system. (d) Resonator FRCs of the SWR-I sample under varying base excitation levels: 0.5g, 0.75g, 1g, 2g, 3g, 4g, 4g-b, 5g, 5g-b, 6g, 6g-b, 7g, and 7g-b. . . . . 73

4.1 (a) Snapshots of metamaterial sample patched with PZT (highlighted in white color) (b) detailed view of the corresponding unitcell. . . . . 76
4.2 (a) Snapshot of the sample with scan points highlighted in blue for the boundary unit cells and in red for the inner domain (b) spatially averaged frequency response function (FRF) of the sample (c) frequency range highlighting the edge-wave-affected region, where the blue curve corresponds to the boundary domain and the red curve corresponds to the inner domain. 76
4.3 Experimentally acquired ODSs and frequencies of the 3D printed of the sample excited by a PZT cylindrical patch. Snapshots of a few selected ODSs having frequencies: (a) 0.0266 kHz, (b) 0.05 kHz, (c) 0.081 kHz, (d) 0.1343 kHz, (e) 0.1953 kHz, (f) 0.2406 kHz, (g) 0.2593 kHz (h) 0.3396 kHz (i) 0.43906 kHz (j) 0.6848 kHz (k) 0.7234 kHz (l) 0.9047 kHz (m) 0.9406 kHz (n) 0.9719 kHz (o) 0.9984 kHz (p) 1.0203 kHz, (q) 1.1753 kHz (r) 1.1890 kHz (s) 1.2731 kHz (t) 1.9 kHz, (v) 2.12 kHz and (t) 2.4 kHz. Edge wave modes, highlighted in orange, are visible in the ODS plots from (l) to (p). . . . . 77

4.4 Experimentally acquired ODSs and frequencies of the 3D printed M3 sample excited by a PZT cylindrical patch. Snapshots edge wave region: (a) 0.9047 kHz, (b) 0.9406 kHz, (c) 0.9719 kHz, (d) 0.9984 kHz, (e) 1.0203 kHz. Numerically acquired eigen mode shapes (f) 0.91589 kHz, (g) 0.92328 kHz (h) 0.9551 kHz (i) 0.98198 kHz (j) 0.98198kHz (k) 1.0089 kHz (l) 1.0164 kHz (m) 1.0234 kHz. . . . . 78

5.1 unitcell to full scale sample . . . . . 82
5.2 Experimental ODSs of electrospun membrane unitcell with resonator in a frequency range restricted to [0.01 - 6] kHz. Experimental ODSs snapshots: (a) 0.890 kHz, (b) 1.55 kHz, (b1) 1.69 kHz, (c) 5.24 khz, (d)5.9 kHz and (d1)6 kHz. . . . . 83
5.3 Average FRF of the acquisition within the frequency range restricted to [0.05 - 1.2] kHz. The gray bands indicate the likely identified bandgaps at 0.32 kHz, 0.42 kHz, 0.65 kHz. . . . . 84
5.4 Experimental ODSs snapshots: (a) 0.078515 kHz, (b) 0.15078 kHz, (c) 0.16757 kHz, (d) 0.18203 kHz, (e) 0.20585 kHz, (f) 0.21718 kHz, (g) 0.25039 kHz, (h) 0.28632 kHz, (i) 0.31992 kHz, (j) 0.33906 kHz, (k) 0.34921 kHz, (l) 0.36445 kHz, (m) 0.38770 kHz, (n) 0.40351 kHz, (o) 0.41132 kHz, (p) 0.42851 kHz, (q) 0.45195 kHz, (r) 0.46718 kHz, (s) 0.49882 kHz, (t) 0.53242 kHz, (u) 0.56679 kHz, (v) 0.57695 kHz, (w) 0.58906 kHz, (x) 0.60156 kHz, (y) 0.61289 kHz, (z) 0.62812 kHz, (a1) 0.66484 kHz, (b1) 0.73007 kHz, (c1) 0.74570 kHz, (d1) 0.76171 kHz, (e1) 0.78867 kHz, (f1) 0.82539 kHz, (g1) 0.84140 kHz, (h1) 0.86328 kHz, (i1) 0.88828 kHz, (j1) 0.92187 kHz, (k1) 0.96757 kHz, (l1) 0.98828 kHz, (m1) 1.030859 kHz, (n1) 1.09375 kHz, (o1) 1.132815 kHz, (p1) 1.164843 kHz. Global modes are highlighted by the white bounding boxes, acoustic/optical modes by the red boxes, and the likely bandgap responses by the blue boxes. . . . . 84
5.5 (a) scan points assigned using PSV system on the sample (b) average FRF of the acquisition within the frequency range 2.5 kHz. The gray bands indicate the likely identified bandgaps at 0.51 kHz and 0.65 kHz. . . . . 86
5.6 Experimental ODSs: (a) 0.02109 kHz, (b) 0.03671 kHz, (c) 0.057812 kHz, (d) 0.07734 kHz, (e) 0.10781 kHz, (f) 0.12109 kHz, (g) 0.14375 kHz, (h) 0.16328 kHz, (i) 0.18671 kHz, (j) 0.23125 kHz, (k) 0.2414 kHz, (l) 0.28359 kHz, (m) 0.31484 kHz, (n) 0.34843 kHz, (o) 0.36953 kHz, (p) 0.37958 kHz, (q) 0.38984 kHz, (r) 0.42031 kHz, (s) 0.43515 kHz, (t) 0.44921 kHz, (u) 0.46484 kHz, (v) 0.50781 kHz, (w) 0.54921 kHz, (x) 0.56718 kHz. The modes are highlighted by the green bounding boxes, are similar mode shapes obtained with PZT actuation. . . . . 86

5.7 Experimental ODSs: (a) 0.58437 kHz, (b) 0.59765 kHz, (c) 0.62421 kHz, (d) 0.65546 kHz, (e) 0.67578 kHz, (f) 0.69609 kHz, (g) 0.71796 kHz, (h) 0.750 kHz, (i) 0.82421 kHz, (j) 0.8625 kHz, (k) 0.89453 kHz, (l) 0.91953 kHz, (m) 0.929687 kHz, (n) 0.99296 kHz, (o) 1.02343 kHz, (p) 1.04843 kHz, (q) 1.15234 kHz, (r) 1.26562 kHz, (s) 1.36562 kHz, (t) 1.41015 kHz, (u) 1.44687 kHz, (v) 1.51796 kHz, (w) 1.61015 kHz, (x) 1.66718 kHz, (y) 1.775 kHz, (z) 1.94140 kHz, (a1) 1.99921 kHz, (b1) 2.20625 kHz, (c1) 2.42968 kHz. . 87
5.8 (a) scan points assigned using Polytec PSV-500-3D scanning vibrometer system on the sample (b) average FRF of the acquisition within the frequency range 2.5 kHz. . . . . 88
5.9 Experimental ODSs: (a) 0.02109 kHz, (b) 0.057812 kHz, (c) 0.10781 kHz, (d) 0.128906 kHz, (e) 0.14609 kHz, (f) 0.17421 kHz, (g) 0.23203 kHz, (h) 0.24218 kHz, (i) 0.300 kHz, (j) 0.31562 kHz, (k) 0.32734 kHz, (l) 0.350 kHz, (m) 0.35464 kHz, (n) 0.38203 kHz, (o) 0.42031 kHz, (p) 0.43984 kHz, (q) 0.46640 kHz, (r) 0.50937 kHz, (s) 0.52265 kHz, (t) 0.55156 kHz, (u) 0.5875 kHz, (v) 0.59921 kHz, (w) 0.61796 kHz, (x) 0.628125 kHz, (Y) 0.66015 kHz, (Z) 0.67578 kHz. (a1) 0.68984 kHz, (b1) 0.69921 kHz, (c1) 0.720312 kHz, (d1) 0.74218 kHz, (e1) 0.75859 kHz, (f1) 0.80937 kHz, (g1) 0.82734 kHz, (h1) 0.84062 kHz, (i1) 0.86484 kHz, (j1) 0.886718 kHz, (k1) 0.90390 kHz, (l1) 0.97968 kHz and (m1) 0.99921 kHz. . . . . 90
5.10 Experimental ODSs: (a) 1.028125 kHz, (b) 1.05078 kHz, (c) 1.079687 kHz, (d) 1.1217968 kHz, (e) 1.132812 kHz, (f) 1.146093 kHz, (g) 1.158593 kHz, (h) 1.174218 kHz, (i) 1.217968 kHz, (j) 1.371825 kHz, (k) 1.414843 kHz, (l) 1.448437 kHz, (m) 1.515625 kHz, (n) 1.592968 kHz, (o) 1.621093 kHz, (p) 1.67578 kHz, (q) 1.871093 kHz, (r) 1.999218 kHz and (s) 2.223437 kHz. 91

6.1 Penrose prototiles $\varphi = \frac{1+\sqrt{5}}{2} \approx 1.618033988749895$. . . . . 93
6.2 (a) Rhombi with red and green arrows giving the matching rule. The half-rhombi of type A and B are also represented. (b) An example of iterative construction of a Penrose tiling by thick and thin rhombi. . . . . 94
6.3 Aperiodic Penrose P3 type geometry with square pattern: (a) Sample (P3-I) with resonators, where the five-fold symmetry is highlighted, and the corresponding resonators are shown in blue; (b) Sample (P3-II) with resonators incorporating tip masses, where the five-fold symmetry is highlighted, and the corresponding resonators are shown in green. . . . . 95
6.4 Average FRF of the acquisition within the frequency range [0.001 - 25] kHz highlighted pseudogap (grey), snapshot of sample. . . . . 96

6.5 Experimental ODSs: (a) 0.078125 kHz, (b) 0.09375 kHz, (c) 0.1328 kHz, (d) 0.22656 kHz, (e) 0.375 kHz, (f) 0.49218 kHz, (g) 0.59375 kHz, (h) 0.765625 kHz, (i) 1.046875 kHz, (j) 1.14843 kHz, (k) 1.296875 kHz, (l) 3.53125 kHz, (m) 4.84375 kHz, (n) 9.2890625 kHz, (o) 20.125 kHz, (p) 20.46875 kHz, (q) 21.35156 kHz and (r) 22.0390 kHz. Highlighted by the white bounding boxes likely to be a Pseudogap . . . . . 97
6.6 (A) Average FRF of the acquisition within the frequency range [15 - 50] kHz, snapshot of sample. Experimental ODS: (a) 19.5449 kHz, (b) 20.4433 kHz, (c) 21.9785 kHz, (d) 28.13671 kHz, (e) 43.41601 kHz, (f) 48.40234 kHz. Highlighted by the white bounding boxes likely to be a Pseudogap and Highlighted by the green bounding boxes likely to be a bandgaps . . 98
6.7 (A) Average FRF of the acquisition within the frequency range [0.001 - 1.25] kHz, snapshot of sample with scan points highlighted in green color. 99
6.8 Experimental ODSs: (a) 0.00391 kHz, (b) 0.00859 kHz, (c) 0.01758 kHz, (d) 0.04727 kHz, (e) 0.07109 kHz, (f) 0.1 kHz, (g) 0.37852 kHz, (h) 0.41484 kHz, (i) 0.43594 kHz, (j) 0.44844 kHz, (k) 0.46172 kHz, (l) 0.47891 kHz, (m) 0.51563 kHz, (n) 0.52891 kHz, (o) 0.53984 kHz, (p) 0.59727 kHz, (q) 0.59961 kHz, (r) 0.67148 kHz, (s) 0.72148 kHz, (t) 0.76328 kHz, (u) 0.91563 kHz, (v) 0.94297 kHz, (w) 0.96289 kHz, (x) 0.99883 kHz, (y) 1.01172 kHz, (z) 1.09453 kHz, (a1) 1.17305 kHz, (b1) 1.21875 kHz. Highlighted by the white bounding boxes likely to be a bandgap. . . . . 100
6.9 (A) Average FRF of the acquisition within the frequency range [0.001 - 1] kHz, snapshot of sample with scan points highlighted in green color. . . . 101
6.10 Experimental ODSs: (a) 0.00422 kHz, (b) 0.00875 kHz, (c) 0.02625 kHz, (d) 0.04891 kHz, (e) 0.05703 kHz, (f) 0.07219 kHz, (g) 0.10078 kHz, (h) 0.16734 kHz, (i) 0.22047 kHz, (j) 0.24313 kHz, (k) 0.25109 kHz, (l) 0.28063 kHz, (m) 0.28875 kHz, (n) 0.31234 kHz, (o) 0.32297 kHz, (p) 0.35391 kHz, (q) 0.36234 kHz, (r) 0.36875 kHz, (s) 0.37218 kHz, (t) 0.38297 kHz, (u) 0.42939 kHz, (v) 0.45563 kHz, (w) 0.45969 kHz, (x) 0.48269 kHz, (y) 0.48547 kHz, (z) 0.50922 kHz, (a1) 0.52359 kHz. . . . . 102
6.11 Experimental ODSs of new wave sequences: (a) 0.55016 kHz, (b) 0.55797 kHz, (c) 0.56594 kHz, (d) 0.56625 kHz, (e) 0.56875 kHz, (f) 0.58875 kHz, (g) 0.615 kHz, (h) 0.6225 kHz, (i) 0.630 kHz, (j) 0.64219 kHz, (k) 0.65266 kHz, (l) 0.66719 kHz, (m) 0.66844 kHz, (n) 0.69519 kHz, (o) 0.72156 kHz, (p) 0.73953 kHz, (q) 0.77031 kHz, (r) 0.79719 kHz. . . . . 102

A.1 Metamaterial cellular architectures: honeycomb structure hosting the intracellular resonators: (a) spider-web-inspired resonator with central mass and (d) cantilever resonator with tip mass. . . . . 108

A.2 Schematic view of the orthotropic plate models with the periodically distributed (left) spider-web resonators and (right) cantilever resonators. The hexagonal lattice vectors are denoted by ( $\mathbf{a}_1, \mathbf{a}_2$ ) and the fixed frame unit vectors by ( $\mathbf{e}_1, \mathbf{e}_2, \mathbf{e}_3$ ); (top) honeycomb cell geometry with wall height $h$, side length $l_h$, and thickness $t_h$. . . . . 108
A.3 The intracellular resonator architectures together with their mechanical models: (a) simplified spider web-like resonator and (b) cantilever with tip mass. The unit vectors ej are the local axes employed to describe the beam motion. . . . . 111
A.4 The lowest four mode shapes of the cantilever resonator. The nondimensional parameters and modal coefficients are provided in Tab. A.1. . . . . 112
A.5 The lowest four mode shapes of the spider-web resonator. The nondimensional parameters and modal coefficients are provided in Tab.A.2. . . . . 113
A.6 (a) Picture of the additively manufactured macrosample of the spider web-like resonator mounted onto an electrodynamic shaker. Snapshots of the PSV acquired (964 scan points) operational deflection shapes whose measured frequencies are: (b) 200 Hz, (c) 417 Hz, (d) 473 Hz, (e) 687 Hz, (f) 767 Hz. . . . . 114

# List of Tables

2.1 Frequencies and damping ratios of the mode shapes of the low, medium, and high frequency samples. . . . . 37

3.1 Resonance frequencies and associated damping ratios extracted from experimental modal analysis of the SWR-I metamaterial sample. . . . . 57
3.2 Resonance frequencies and associated damping ratios extracted from experimental modal analysis of the SWR-II metamaterial sample. . . . . 60
3.3 Geometrical dimensions of the unit cell samples . . . . . 64

4.1 Resonance frequencies and damping ratios extracted from experimental modal analysis of the finite honeycomb metamaterial sample used for the edge-wave study. . . . . 78

5.1 Electrospun membrane resonance frequencies associated with damping ratios up to 1.2 kHz. . . . . 85
5.2 Electrospun membrane resonance frequencies associated with damping ratios up to 2.5 kHz for chirp excitation with shaker. . . . . 88

A.1 Nondimensional parameters and modal coefficients for the cantilever resonators. Par stands for Parameter. . . . . 112
A.2 Nondimensional parameters and modal coefficients for the spider-web resonators. Par stands for Parameter. . . . . 113

# Chapter 1

# Introduction

Lightweight structural components used in aerospace, automotive, and precision mechanical systems must withstand dynamic loads while maintaining high stiffness and minimal mass. These same attributes, however, make them particularly susceptible to unwanted vibrations and noise transmission. Conventional vibration-control techniques, such as viscoelastic damping layers, tuned mass absorbers, and passive isolators are effective only within narrow frequency bands and typically require additional mass or complex feedback hardware [3, 4]. This trade-off between efficiency and practicality has created a critical need for new structural concepts that can confine mechanical energy and attenuate broadband, low-frequency vibrations using geometry rather than mass or active control [5, 6].

Metamaterials offer a powerful route toward this goal. They are engineered architectures whose extraordinary properties arise from their geometry rather than their base material composition [7, 8]. Properly designed, they can redirect, focus, or suppress mechanical and acoustic waves, functioning as wave-control strategies rather than passive material choices [9]. Elastic metamaterials, in particular, consist of periodic or quasi-periodic unit cells whose subwavelength dimensions endow them with effective dynamic properties such as density and stiffness not found in conventional solids [10, 11]. This enables phenomena such as negative effective parameters, bandgaps that block wave propagation, wave focusing, and even mechanical cloaking [12, 13]. As a result, metamaterials have emerged as promising candidates for lightweight vibration isolation, broadband noise suppression, and energy harvesting across scales ranging from microsystems to civil infrastructure [14, 15].

Despite these advances, most existing metamaterials remain limited by two key assumptions: linearity and perfect periodicity. Linear, periodic architectures can form well-defined bandgaps through Bragg scattering or local resonance (LR) effects, but their performance degrades under real-world conditions involving large amplitudes, manufacturing tolerances, or defects. Conventional periodic designs cannot adapt or maintain robustness when geometry or excitation conditions change. To overcome these constraints, this thesis deliberately introduces nonlinearity and aperiodicity as functional design features

rather than imperfections. Nonlinearity is exploited to generate amplitude-dependent bandgaps and localized oscillations that are unreachable in linear systems, while aperiodicity is employed to create edge-localized and defect-immune wave modes that mimic topological protection without the need for perfect periodic repetition. Through this combination, the present work establishes an experimental and theoretical framework for tunable, broadband, and robust vibration control in elastic metamaterials.

## 1.1 State of the art

Periodic structures such as phononic crystals and elastic metamaterials have attracted intense research interest because they can suppress or redirect wave propagation within specific frequency ranges called bandgaps [5, 3, 16]. Two main physical mechanisms create these stop bands. Bragg scattering results from destructive interference caused by periodic variations in geometry or material properties [17]. It requires the lattice spacing to be comparable to the target wavelength and thus primarily affects high frequencies. Local resonance (LR) arises when sub-wavelength resonators are coupled to a host structure [10, 18]. Interaction between the resonators' natural frequencies and the host's continuum modes opens stop bands at frequencies far below those predicted by Bragg theory [10]. The LR mechanism represents a key breakthrough for practical vibration control because it allows low-frequency attenuation without large mass or size increases [19, 3]. By embedding arrays of tuned resonators often simple masses on compliant supports one can achieve strong vibration suppression at frequencies up to two orders of magnitude lower than Bragg-based designs [20, 10, 5]. This capability has enabled applications in noise control, seismic shielding, and lightweight aerospace panels [6, 16, 21].

The seminal work of Liu et al. [10] established that subwavelength resonators embedded in an elastic matrix can induce locally resonant bandgaps far below the Bragg limit. This discovery initiated widespread research into lightweight, broadband, and tunable metamaterials. Yang et al. [20] and Airoldi and Ruzzene [19] subsequently extended LR principles to membrane-type and electromechanically coupled systems, showing that resonance wave interactions can be tuned via geometry or voltage. Hussein et al. [5] later unified these developments, clarifying how the coupling between local resonances and structural periodicity governs wave dispersion and attenuation. Within this framework, honeycomb and hexagonal lattices have become particularly attractive because of their high stiffness-to-weight ratio, geometric efficiency, and adaptability. Studies by Phani et al. [22] and Krushynska et al. [23] demonstrated that adding resonant inclusions into honeycomb frameworks produces Bragg-LR bandgaps, combining geometric scattering with subwavelength resonance. These architectures are lightweight, easily manufacturable, and ideal for broadband vibration suppression in real structures.

Building upon these foundational principles, researchers have extensively investigated

the engineering of targeted stop bands in locally resonant (LR) periodic structures, stimulating broad research on vibration and wave propagation control in two-dimensional systems [24, 25]. Recent studies have explored a wide range of modeling and design strategies, including finite element (FEM) analyses for complex geometries [26, 27], ad hoc analytical formulations for dispersion prediction [28, 29, 30], and simplified models for periodic systems to capture key dynamic features with reduced computational effort [31, 32]. A recent milestone was achieved by Lim et al. [33], who experimentally demonstrated a composite metamaterial featuring spherical and cylindrical steel masses embedded within a polymeric framework. This configuration, inspired by locally resonant sonic crystals, produced extremely broad low-frequency bandgaps with a bandwidth-to-midgap ratio exceeding 180%. Notably, the aperiodic arrangement of inclusions allowed the formation of bandgaps independent of strict structural periodicity, highlighting the effectiveness of locally resonant mechanisms in achieving broadband vibration isolation. The locally resonant (LR) mechanism enables design freedom unavailable to Bragg systems. By tuning resonator mass, stiffness, or coupling location, engineers can shift or widen bandgaps [34], tailor them to target frequencies, or even create multiple stop bands in a single lattice [5, 23]. When several resonators of different natural frequencies are embedded within one unit cell, multi-frequency bandgaps appear, offering broadband attenuation [35, 36]. Such adaptability makes LR metamaterials powerful tools for structural vibration control where space and weight constraints prohibit conventional absorbers [21].

While most early metamaterial models were linear, nonlinearity is now recognized as a deliberate and valuable design feature rather than a modeling complication. Nonlinear locally resonant metamaterials exploit amplitude-dependent stiffness, damping, or geometric effects to achieve behaviors unattainable in linear systems. These include amplitude-dependent bandgaps, where attenuation frequencies shift with vibration level; energy localization and transfer, where large oscillations concentrate energy in specific resonators or regions; and non-reciprocal wave propagation, where energy travels preferentially in one direction. Such phenomena arise from mechanisms like cubic stiffness, geometric nonlinearity in beams, or nonlinear coupling between host and resonators [37, 38, 39, 40, 41, 42, 43]. Researchers have also investigated the exploitation of nonlinear effects to achieve enhanced or unconventional wave behaviors such as amplitude-dependent bandgaps and non-reciprocal propagation [44, 45, 46, 47, 48], alongside comprehensive experimental investigations validating these phenomena in real structures [49, 50, 51]. Studies by Casalotti et al. [52] and Shen and Lacarbonara [53, 48] have shown that nonlinear multiresonator beams can produce multiple, tunable bandgaps that broaden as excitation amplitude increases. Fortunati et al. [54] demonstrated that adding nonlinear damping or viscoelastic effects leads to amplitude-dependent dissipation and energy localization. These behaviors are particularly relevant for real engineering applications mechanical filters that self-adjust to vibration level, passive isolators that harden

or soften under load, and broadband energy harvesters [52, 53, 48, 54, 49, 50, 51]. Nonlinearity thus becomes a functional mechanism for energy confinement and tunable vibration control.

Perfect periodicity, often assumed in theoretical models, is difficult to achieve in real structures. Small imperfections can disrupt Bragg scattering and reopen transmission paths [55, 56]. To overcome this limitation, researchers have explored topological and aperiodic metamaterials, which use symmetry breaking or intentional geometric detuning to create edge-localized modes that remain robust even in the presence of defects [57, 58]. Topological mechanical lattices draw analogies from condensed-matter physics such as the quantum Hall, spin Hall, and valley Hall effects to achieve defect immune energy transport [59, 60, 61, 62]. Among these, quantum-valley-Hall-type designs are especially feasible in elastic systems: by breaking spatial inversion symmetry through mass or stiffness contrast, one can generate interface modes that guide waves along boundaries while blocking bulk propagation [63, 64, 65]. These structures provide topological protection without requiring active control or perfect periodicity [66].

Similarly, aperiodic architectures exploit controlled disorder to localize energy. When translational symmetry is partially broken, wave modes hybridize and produce confined, defect-insensitive responses reminiscent of Anderson localization [55, 6]. Such aperiodic designs deliver robustness and tunability while relaxing manufacturing tolerances an important advantage for practical implementation. Disorder, whether random or structured, plays a dual role in metamaterials. Moderate disorder can enhance localization by breaking long-range coherence, leading to energy trapping in localized modes [56, 67]. However, excessive randomness may destroy the designed band structure entirely. Recent studies have explored this balance, showing that carefully introduced disorder can expand attenuation bandwidths and improve resilience to imperfections [68, 69]. For locally resonant systems, stochastic variations in resonator parameters shift hybridization frequencies, producing a continuum of mini-bandgaps that collectively yield broadband attenuation [70, 6]. Controlled disorder thus offers a new tuning dimension for robust vibration control.

A significant theoretical advance came from Murer et.al. [2], who extended locally resonant (LR) theory by replacing idealized lumped resonators with continuous, infinite-dimensional ones such as cantilever beams with tip masses and spider-web-like resonators with central masses. Each resonator acts as a continuous elastic beam whose bending motion is projected onto a few dominant modes, forming a multi-frequency resonator capable of producing several tunable bandgaps. Using the Plane Wave Expansion (PWE) method, the honeycomb host lattice was modeled as a homogenized orthotropic plate, and dispersion predictions were experimentally validated using high-resolution laser-scanning vibrometry. These tests confirmed multiple stop bands and revealed their strong sensitivity to resonator geometry and mass, laying the theoretical and experimental groundwork for the present study. A concise summary of this theoretical formulation is provided in

Appendix A for completeness.

## 1.2 Achieved results

This study used a combination of experimental and numerical methods to successfully capture and interpret complex wave propagation phenomena in acoustic metamaterials. Metamaterials with multiple or multi-frequency resonators have shown multi-bandgap and broadband attenuation behaviour. A multi-bandgap metamaterial with resonators tuned to different frequencies inside each honeycomb cell was reported by Murer et al. [2]. Each tuned resonator mode interacts with lattice waves to open a discrete stop band, resulting in robust multi-band performance, as demonstrated by analytical and experimental analyses. This study demonstrated how attenuation bandwidths can be increased without adding structural complexity through geometric and frequency tailoring.

Building on these advances, a subsequent study introduced a two-dimensional honeycomb metamaterial embedding intracellular multi-frequency resonators to realize broadband vibration attenuation via controlled resonance coupling. The embedded resonators were regarded as infinite-dimensional substructures, capturing their full dynamic influence despite their subwavelength scale. Two canonical configurations were investigated, cantilevers with tip masses and spider-web geometries with central masses. The spider-web design generated multiple low-frequency bandgaps, whereas the cantilever configuration yielded a narrower high-frequency gap, illustrating the tunability of bandgap formation through resonator topology. Experimental validation on 99-cell honeycomb lattices fabricated via high-resolution additive manufacturing confirmed the theoretical predictions. Frequency response measurements using 3D laser scanning vibrometry revealed multiple attenuation zones in excellent agreement with numerical models. Even in the presence of missing resonators, the fundamental bandgap formation mechanism remained robust, though affected in bandwidth and location by structural irregularities. Experimentally, broadband wave attenuation persisted up to 80 kHz, with minor bandgap narrowing attributed to damping (2.2-4.4%) and finite-size effects.

Expanding on these insights, attention was directed toward two-dimensional spider-web resonator (SWR) metamaterials, which embody the same fundamental resonance principles within architecturally complex geometries. Two variants were fabricated for comparative analysis: a pristine baseline configuration (SWR-I) and a geometrically imperfect counterpart (SWR-II). PSV vibrometer measurements revealed that SWR-I exhibited three distinct bandgaps, each verified through both Frequency Response Function (FRF) analysis and Operational deflection shapes (ODSs) visualization. The ODSs mappings captured the modal transitions from acoustic to optical regimes, demonstrating how vibrational energy progressively localizes and redistributes across the lattice as the excitation frequency increases. In contrast, SWR-II displayed only two bandgaps, with

the missing third attributed to detuned local resonators whose natural frequencies drifted out of synchronization due to fabrication induced imperfections. This desynchronization disrupted the collective resonant coupling required for the formation of the third bandgap. Finite element simulations showed strong agreement with experimental results for the first two bandgaps, while deviations observed in the third were primarily associated with the finite and suspended nature of the experimental lattices compared to ideal infinite models. Further analysis revealed the critical role of complementary modes nearly degenerate modal pairs arising from the geometric symmetry of the spider-web lattice, which can merge, split, or shift bandgaps depending on their phase coupling characteristics.

Nonlinear behaviors were also observed during testing. The SWR-II structure exhibited a softening-type response, particularly in the acoustic mode. In the first bandgap range, the bandgap increased with excitation amplitude, leading to its expansion under stronger excitation. Unit-cell experiments further confirmed this softening-type nonlinearity, which became increasingly pronounced with rising excitation amplitude. The nonlinear dynamics of the fourth global mode revealed a pronounced contrast between the two configurations: while the SWR-II resonator displayed softening-type nonlinearity, the SWR-I resonator demonstrated hardening-type behavior. Despite their similar design layouts, the scaled geometry of the SWR-II unit cell relative to that of the SWR-I produced distinctly different nonlinear responses, highlighting the strong sensitivity of nonlinear dynamic behavior to geometric scaling. These findings emphasize that imperfections, boundary conditions, complementary modes, and nonlinear effects act to determine the performance and robustness of spider-web resonator metamaterials. Nevertheless, further investigation is required to fully elucidate the complexity of their nonlinear responses and the mechanisms governing these behaviors.

In addition, both SWR-I and SWR-II samples exhibited edgewave behavior after the first bandgap, representing the transition from the bandgap to the optical mode. Based on these observations, another locally resonant metamaterial was found to exhibit edge-wave phenomena only within the 0.91-1.2 kHz frequency range. These edgewave, characteristic of metamaterial systems, displayed distinct mode patterns and propagation behaviors, differentiating them from the typical bandgap phenomena in locally resonant structures. Furthermore, the experimental results showed good agreement with simplified COMSOL eigenfrequency analyses, where the observed edge-wave modes closely matched the numerically predicted vibration modes.

The exploration subsequently extended to electrospun membrane metamaterials lightweight, flexible systems in which embedded resonators interact with thin-membrane dynamics. Excitation via PZT actuators and electrodynamic shakers, combined with full-field vibrometry, revealed pronounced compositional disorder in mass density, membrane stiffness, and resonator attachment, breaking the ideal periodicity of Bloch-type propagation. Under broadband excitation, the membranes exhibited strong spatial heterogene-

ity: regions near the excitation source displayed amplified out-of-phase vibrations, while others remained nearly quiescent. This interference driven confinement, along with the absence of a clear periodic bandgap and a transition to higher membrane modes above 1.1 kHz, provided compelling evidence of disorder-pinned localized modes consistent with Anderson localization, where wave energy becomes trapped by disorder and long-range transport is suppressed.

Introducing tip masses on the resonators yielded distinctive standing-wave patterns, while implementing a quasi-periodic Penrose P3 tiling introduced controlled spatial aperiodicity. This geometry fostered multiple scattering pathways and resonance hybridizations, producing unconventional dispersion and localization effects. Unlike strictly periodic metamaterials that rely on local resonances or Bragg scattering, the Penrose lattice achieved broadband attenuation through resonant hybridization and interference, demonstrating that aperiodicity can serve as a deliberate design strategy rather than a structural defect.

### 1.2.1 Approach

These results were achieved through a systematic experimental and computational approach designed to capture both linear and nonlinear dynamic responses of elastic metamaterials under various boundary conditions and excitation schemes. The study aimed to identify and interpret new wave phenomena not yet fully elaborated theoretically, while ensuring strong agreement between analytical predictions, numerical simulations, and experimental observations. The fundamental goal was to experimentally characterize periodic and aperiodic metamaterial structures incorporating local resonators, focusing on complex wave phenomena such as global modes, local resonances, acoustic and optical branches, and the formation of bandgaps as functions of excitation frequency. High-resolution laser scanning vibrometry was employed to visualize and quantify wave fields and mode shapes across the structures.

Building on this foundation, Mauro Murer et al. [2] extended the modeling framework by incorporating infinite-dimensional resonators within the PWE formulation. Their approach enabled the prediction of multiple tunable bandgaps resulting from multi-frequency resonators such as cantilevers with tip masses and spider-web configurations with central masses, providing a refined theoretical foundation for the present work.

Metamaterial samples were fabricated using additive manufacturing techniques including Fused Deposition Modeling (FDM) and Stereolithography (SLA). The Polytec Xtra 500-3D laser vibrometry system was employed to perform detailed dynamic experimental characterization of wave propagation. Experiments were conducted to capture and analyze complex wave sequences and investigate their dependence on lattice geometry, excitation frequency, and boundary conditions. These measurements provided insights into modal interactions, phase behavior, and propagation characteristics.

The study further aimed to experimentally identify and validate the existence of locally resonant bandgaps in periodic metamaterial structures with various resonator configurations. Emphasis was placed on generating and measuring low-frequency and multiple bandgaps and interpreting their relationship with lattice geometry and resonator parameters. Two-dimensional unit-cell geometries with resonators were designed and analyzed using COMSOL Multiphysics to compute dispersion curves, supporting experimental observations.

Amplitude-dependent nonlinear behaviors near bandgaps, such as frequency shifts, mode coupling, and the emergence of nonlinear effects were investigated to demonstrate bandgap tunability through geometric or dynamic modifications for adaptive wave control. Additional studies examined wave propagation in disordered or imperfectly periodic lattices, including cases with missing or perturbed resonators, to understand the influence of disorder on the dynamic response and to interpret wave behavior from experimental perspectives. Finally, the experimental framework was extended to aperiodic P3-type geometries incorporating local resonators, elucidating the influence of quasi-periodicity on wave propagation mechanisms and associated dynamic responses.

## 1.3 Outline of the thesis

Chapter 2 builds upon the theoretical results achieved by Mauro Murer et al. [2]. In their work, the honeycomb host lattice was represented as a homogenized orthotropic plate, whose validity was confirmed through two independent homogenization approaches. Expanding on this background, Chapter 2 focuses on the fabrication process and experimental characterization of acoustic metamaterial structures. The specimens were produced using high-precision Stereolithography (SLA) 3D printing to ensure geometric accuracy and material fidelity. Their dynamic response was evaluated using the Polytec PSV-500-3D laser-scanning vibrometer (PSV), a non-contact optical system that provides full-field vibration measurements. The chapter also introduces the operating principles of the PSV system and details the experimental procedures implemented to guarantee accurate data acquisition and repeatability. The experimental campaign investigated the wave-propagation characteristics of two-dimensional honeycomb metamaterials, selected for their intrinsic periodicity and excellent ability to sustain flexural and shear loads. To enhance tunability and dynamic performance, mass-loaded cantilever resonators with varying tip masses were integrated into the lattice. The propagation behavior of the structures was experimentally analyzed using the PSV system, which enabled visualization of wave fields and identification of distinct bandgaps. A comparative study on a non-resonant honeycomb lattice excited via piezoelectric transducers (PZT) was also conducted to distinguish bandgaps arising purely from geometric periodicity. Focused testing around the first bandgap region, performed using an electrodynamic shaker, demonstrated

a strong correlation between experimental observations and analytical predictions obtained through the Plane Wave Expansion (PWE) method. The chapter further explains how vibration data were processed to obtain operational deflection shapes (ODSs) and to extract key modal parameters-resonance frequencies, mode shapes, and damping ratios using an advanced modal analysis software (Polywave). Finally, numerical simulations were carried out in COMSOL Multiphysics, where a three-dimensional finite-element model of the honeycomb metamaterial comprising 534 elements and 2,616 degrees of freedom was developed to replicate the experimental setup under harmonic excitation. The simulation results exhibited excellent agreement with the experimental measurements, confirming the accuracy of the modeling approach and the physical fidelity of the fabricated prototypes.

Chapter 3 presents the experimental and numerical investigation of wave propagation in axially symmetric spider-web-like resonator samples fabricated via 3D printing. Each sample was suspended using nylon wires, and PZT actuators were bonded to the bottom surface with epoxy resin. Using the PSV system, the ODSs, symmetric and asymmetric modes, acoustic and optical modes, and bandgaps up to 10 kHz were captured. The specimens were excited with a chirp signal, and the velocity responses were acquired and processed through PSV system and PolyWave software. A detailed analysis of a representative unit cell revealed the transition from acoustic to optical modes through the bandgap region, while resonators in the left and middle rows were examined to study how excitation location affects bandgap behavior. Distinctive wave phenomena were observed at the transition between the first bandgap and optical modes, where edgewave behavior emerged in both SWR-I and SWR-II samples, motivating the fabrication of an additional specimen. Numerical validation performed in COMSOL Multiphysics using eigenfrequency analysis with periodic boundary conditions showed good agreement with experimental results for both SWR-I and SWR-II. The SWR-II sample further demonstrated nonlinear softening behavior, with the first bandgap between 0.58-0.68 kHz widening as excitation amplitude increased, confirming the tunable and nonlinear nature of locally resonant spider-web metamaterials.

Chapter 4 investigates edge-wave phenomena in a locally resonant metamaterial with a non-axially symmetric unit-cell geometry, motivated by the findings of Chapter 3. A newly designed specimen, consisting of a thin beam clamped to a hexagonal cell and coupled to a central resonator, intentionally breaks axial symmetry to suppress conventional bandgaps and promote boundary-localized dynamics. Experimental measurements obtained using scanning laser Doppler vibrometry reveal edge-localized modes in the 0.90-1.120 kHz frequency range. To support these observations, finite element eigenfrequency analyses are performed. The strong agreement between experimental and numerical results confirms that the observed localization originates from boundary-induced symmetry breaking in the finite structure.

Chapter 5 reports a collaborative study between Sapienza University of Rome and

Roma Tre University. The samples were fabricated in the Multifucntional Materials Lab of RomeTre by electrospinning membranes and integrating axially symmetric resonators produced via 3D printing. Their vibrational behavior was examined using the PSV system. Each specimen was suspended with nylon wires, and PZT actuators were attached to the underside with epoxy resin for excitation. The experiments aimed to identify ODSs, acoustic and optical modes, and bandgap formation up to 1.2 kHz. A second test series using an electrodynamic shaker extended the frequency range to 2.5 kHz. Excitation was applied through chirp signals, and out-of-plane velocities were measured with a PSV system. Data were processed with PolyWave and PSV software to extract modal parameters and to highlight the bandgap regions. A final experimental campaign on a 7-unit-cell membrane driven by an electrodynamic shaker revealed distinct vibration modes and disorder-induced effects, offering valuable insights into the dynamic behavior of flexible resonant metamaterials.

Chapter 6 focuses on the study of aperiodic metamaterials based on the Penrose P3 geometry, composed of large and small rhombi arranged in a non-repeating pattern that generates distinct geometrical configurations. Within this framework, the square pattern was examined, where cantilever-type resonators, both with and without tip masses, were integrated at points exhibiting five-fold symmetry. The designed samples were fabricated and experimentally analyzed using the PSV system. During testing, each specimen was suspended by nylon wires, and PZT actuators were attached to the bottom surface with epoxy resin for excitation. The main objective was to identify ODSs by exciting the structures with a chirp signal and recording the velocity response through the PSV system. Additionally, an electrodynamic shaker was employed to excite the aperiodic metamaterial, enabling visualization of wave sequences and revealing unique wave propagation phenomena associated with the Penrose-type geometry.

Chapter 7 presents the conclusions and final remarks

# Chapter 2

# Multiple bandgaps in locally resonant metamaterials

This chapter presents the first experimental validation of a two-dimensional (2D) elastic metamaterial designed on a honeycomb (hexagonal) geometry, selected for its intrinsic periodicity and high stiffness-to-weight ratio. The cellular framework incorporates periodic cantilever-type resonators equipped with additional lumped tip masses, enabling multi-mode vibration and tunable dynamic response. By adjusting the geometry and mass distribution of these resonators, distinct bandgaps can be induced over prescribed frequency ranges, leading to enhanced vibration attenuation.

The specimens were fabricated using additive manufacturing via stereolithography (SLA), ensuring high dimensional accuracy and faithful reproduction of the designed geometry and material properties. The experimental characterization was performed using non-contact three-dimensional laser scanning vibrometry (LSV), which enables full-field measurements of out-of-plane vibrations and provides direct visualization of wave propagation and bandgap formation. Controlled excitation of the samples was achieved using both an electrodynamic shaker and piezoelectric (PZT) actuators. The shaker-based experiments were used to characterize low-frequency bandgaps under controlled boundary conditions, whereas PZT excitation enabled the investigation of higher-frequency wave-propagation phenomena and higher-order resonator modes.

The experimental findings are compared with analytical predictions obtained using the Plane Wave Expansion (PWE) method and with finite element simulations conducted in COMSOL Multiphysics. Excellent agreement is observed between theoretical, numerical, and experimental results, validating the predicted multi-bandgap behavior of the proposed metamaterial architecture.

The chapter is organized as follows. Section 2.1 describes the additive manufacturing process. Section 2.2 introduces the experimental measurement methodology based on 3D laser scanning vibrometry. Section 2.3.1 presents the dynamic characterization of low-, medium-, and high-frequency metamaterial samples under electrodynamic shaker

excitation. Section 2.3.2 compares experimental bandgaps with theoretical dispersion predictions. Section 2.3.5 reports complementary high-frequency measurements using PZT excitation. Finally, Section 2.3.6 investigates the robustness of bandgap formation under broken periodicity using samples with missing resonators.

The theoretical modeling framework is adopted as a reference for the design of the resonant metamaterials investigated experimentally. In particular, the resonator geometries and design parameters are selected based on nondimensional parameters and modal coefficients derived from the analytical formulation. For the cantilever-type resonators, the relevant nondimensional parameters and modal coefficients are reported in Appendix A, where the complete theoretical model is documented for completeness and transparency.

## 2.1 Additive manufacturing

The concept of fabricating objects layer by layer has existed for several decades, initially implemented through techniques such as Rapid Manufacturing, Solid Freeform Fabrication, and Digital Direct Manufacturing [71, 72]. These methods have since been consolidated under the widely accepted term Additive Manufacturing (AM), which encompasses a range of technologies used to build components directly from digital models [73]. The process begins with the design of a unit cell or sample using Computer-Aided Design (CAD) software. The completed CAD model is then exported in the .AMF (Additive Manufacturing File) format (ISO/ASTM 52915:2020). This file is subsequently transferred to the 3D printer, where it is processed by slicing software and converted into .gcode format. The .gcode file contains the layer-by-layer instructions required for the printing process and is utilized by the RAISE3D Pro3 Plus machine to manufacture the sample.

### 2.1.1 Stereolithography

The Formlabs Form 3+ 3D printer operates using Low Force Stereolithography (LFS), a refined variation of traditional stereolithography (SLA) technology designed to produce high-precision parts with reduced mechanical stress during the printing process. At the core of its operation is a 405 nm laser, housed within a Light Processing Unit (LPU 2.0), which directs and focuses the laser beam using a combination of galvanometer mirrors and a parabolic mirror to ensure consistent accuracy across the entire build platform. The printing process involves selectively curing a liquid photopolymer resin contained within a transparent resin tank. The bottom of the tank is made from a flexible, transparent film, which allows for the gentle "peeling" of each cured layer from the tank surface. This significantly reduces the forces acting on the part during printing, enabling the creation of intricate details and fine surface finishes.

The printer constructs the object layer by layer. After each layer is cured by the laser,

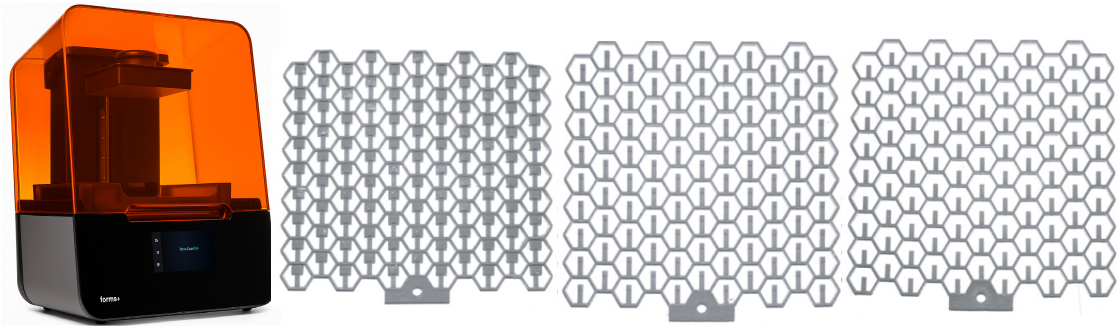

Figure 2.1: Form 3+ 3D printer shown with a fabricated sample.

the build platform lifts incrementally, allowing fresh resin to flow underneath before the next layer is exposed and cured. This process continues until the entire object is complete. Resin is automatically dispensed from cartridges to maintain the correct level in the tank throughout printing. Once printing is finished, the object is removed from the build platform, washed in isopropyl alcohol (IPA) to eliminate uncured resin, and then post-cured using UV light to solidify the material's mechanical and thermal properties. The combination of LFS technology, precision optics, and automated resin handling enables the Form 3+ to deliver high-quality prints with improved reliability, speed, and surface quality compared to earlier SLA systems.

## 2.2 3D laser scanning vibrometry

3D Laser Scanning Vibrometer (LSV) is a precision, non-contact measurement system designed to capture three-dimensional vibrations in mechanical structures with high fidelity and without physical interference [74]. It functions based on the optical Doppler effect, in which laser light scattered from a moving surface undergoes a frequency shift that is directly proportional to the instantaneous velocity of the vibrating object [75]. Although this frequency shift is exceedingly small typically on the order of less than $10^{-8}$ it can be measured with remarkable accuracy using interferometric techniques [76]. Within the vibrometer, the back-scattered laser signal is compared to a reference beam whose frequency has been shifted by a specific value through an acousto-optic modulator, in what is known as the heterodyne process [74] (heterodyne process, see Fig. 2.2). Only the velocity component aligned with the laser beam direction contributes to the Doppler frequency shift, enabling precise velocity and directional measurements.

In a heterodyne laser Doppler vibrometer, velocity is determined by comparing the back-scattered laser light with a frequency-shifted reference beam, achieved through an acousto-optic modulator (Bragg cell), enabling both high precision and directionality in motion detection [74]. The Doppler frequency shift $f_D$ follows the relation $f_D = \frac{2nv}{\lambda}$, where $v$ is the object's velocity, $n$ is the refractive index of the medium, and $\lambda$ is the laser wavelength [75]. Interferometric principles ensure high accuracy and make these sys-

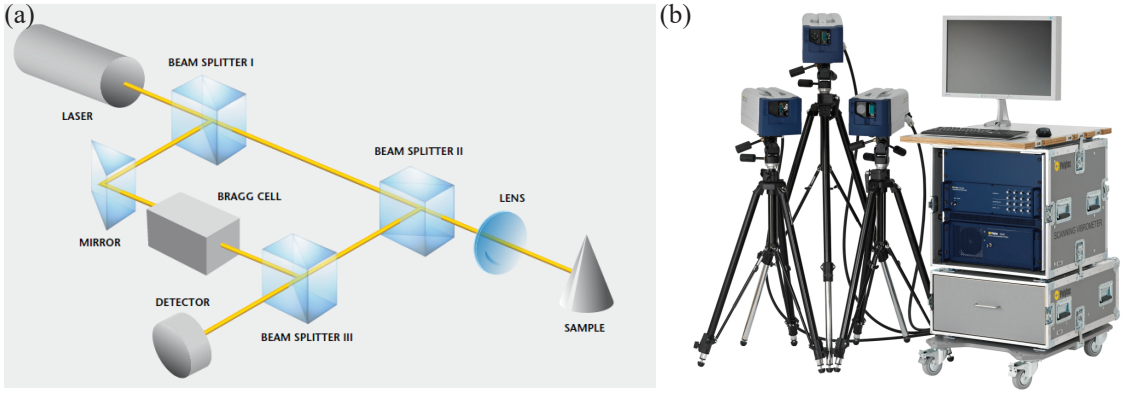


Figure 2.2: (a) Optical layout of a laser Doppler vibrometer [1]. (b) Polytec 3D Xtra 500 system for vibration measurement.

tems calibration-free, allowing their use in the primary calibration of accelerometers [76]. The photodetector captures the modulated return signal, which is demodulated using the ArcTan(I/Q) method to extract displacement, from which velocity and acceleration are derived [74]. Since demodulation occurs in the frequency domain, fluctuations in light intensity do not introduce noise, resulting in superior signal-to-noise ratio (SNR), analogous to the robustness of FM radio over AM [76]. Heterodyne systems outperform homodyne and self-mixing interferometers in terms of directionality and low-frequency noise performance [76]. Two major laser sources are used in vibrometry: helium-neon (HeNe, 633 nm) and infrared (IR, 1550 nm). HeNe-based systems offer low phase noise and high sensitivity on reflective and underwater surfaces, making them ideal for micro-scale applications. IR-based systems, while unsuitable for underwater use, excel in measuring low-reflectivity surfaces and at longer distances due to their higher power and lower shot noise [74]. Tri-axial (3D) vibrometers consist of three laser Doppler vibrometers oriented at different angles toward the same point, allowing for the extraction of $X$, $Y$, and $Z$ vibration components via coordinate transformation [77]. This method is commonly applied in the durability testing of PCB-mounted components and bonding wires. Full-field vibrometry measures vibration over a surface grid, either sequentially with beam steering mirrors or in parallel using sensor arrays. In scanning laser Doppler vibrometry (SLDV), a phase reference such as an excitation signal, voltage pulse, or trigger is required to correlate phase data across points and animate structural deflection modes. Geometry information can either be captured point by point or imported from pre existing models to ensure alignment with the test object's coordinate system. Maintaining a consistent spatial reference is critical for accurate data stitching when scanning from multiple perspectives [74].

In the following sections, the PSV-500-3D system is employed to acquire full-field frequency response functions (FRFs) and operational deflection shapes (ODSs), which are essential for identifying bandgaps and characterizing the transition between global, acoustic, and optical modes in the honeycomb metamaterial samples.

### 2.2.1 Polytec PSV-500-3D Scanning Vibrometer

The laser scanning vibrometry system procedure performed using the Polytec PSV-500-3D Scanning Vibrometer System and followed a systematic five-step process: (1) laser setup, (2) scan preparation, (3) acquisition parameter configuration, (4) measurement, and (5) post-processing of the acquired data. As illustrated in Fig. 2.4, the PSV-500-3D system includes three scanning heads arranged in an equilateral triangular configuration (highlighted in red bounded box) around the specimen to ensure optimal 3D surface coverage. The top scanning unit, positioned at the apex of the triangle, is a PSV-I-500 head equipped with a high-precision laser scanner, an HD video camera, and a PSV-G-500 geometry scanning module. This top head provides the highest-resolution video imaging and is primarily used to establish the reference geometry of the scanned object. The two lower scanning heads positioned at the left and right are both PSV-I-520 models and complement the system by capturing additional spatial and vibrational information. The scan preparation phase is a critical step in ensuring accurate geometric and vibrational mapping.

The 2D alignment process, which defines several alignment points on the object surface by focusing laser beams onto the video image, is the first step in the scan preparation process. This step ensures that each scanning head is correctly positioned relative to the measurement plane in the image frame and must be completed for all three scanning units. Following 2D alignment, the 3D coordinate system is established. The top scanning unit is used to define a reference frame by selecting three points: the origin, a point along one axis, and a point on the measurement plane. After that, a minimum of six non-coplanar 3D coordinate points must be defined. Alternatively, the system can perform automatic 3D alignment using an integrated alignment tool, which generates a complete coordinate system along with an arbitrary number ($n$) of 3D reference points distributed across the object's surface. The acquisition grid as shown in Fig. 2.4, is created by choosing scan points on the specimen surface after both alignment procedures are finished. A geometry scan is subsequently created using the top-mounted scanning head, which records the spatial coordinates of every point and reconstructs the specimen three-dimensional shape for vibration analysis. The acquisition settings were tuned to accurately record operational deflection forms, allowing the detection of global modes, acoustic/optical modes, and bandgaps within the desired frequency range. A broadband chirp signal was employed to excite the samples, while the vibrometer recorded spatially distributed velocity data across the surface.

Following 3D alignment, a secondary alignment in 2D is conducted. This step involves projecting the laser beams onto the object's surface as visualized by each scanning head's video camera. Users manually select various surface locations to generate 2D alignment points, which calibrate the laser's orientation relative to the measuring plane captured in the video feed. This 2D alignment must be performed individually for all three scanning

units to ensure full spatial registration. Once both 3D and 2D alignments are completed, scan points are defined across the surface of the metamaterial sample. As shown in Fig. 2.4, these include six points located at the vertices of each hexagonal cell (used as cell measurement points), and three additional points (highlighted in green bounded box) distributed along each cantilever resonator to capture its dynamic behavior. Finally, the geometry scan is executed, during which the system calculates the precise 3D coordinates of all defined scan points, thereby generating a complete spatial model of the test sample for dynamic analysis.

## 2.3 Cantilever with different tipmass

Fig. 2.3 presents a comparative visualization of the 3D-printed metamaterial samples designed for dynamic testing, specifically engineered to exhibit distinct frequency responses low frequency (LF), medium frequency (MF), and high frequency (HF). Each sample represents a variation of cantilever-based resonator architecture embedded within a honeycomb metamaterial framework. These structures were fabricated using a high-precision *Formlabs Stereolithography 3D Printer Form 3+*, which operates with a layer resolution of 25 microns and a laser spot size of approximately 85 microns.

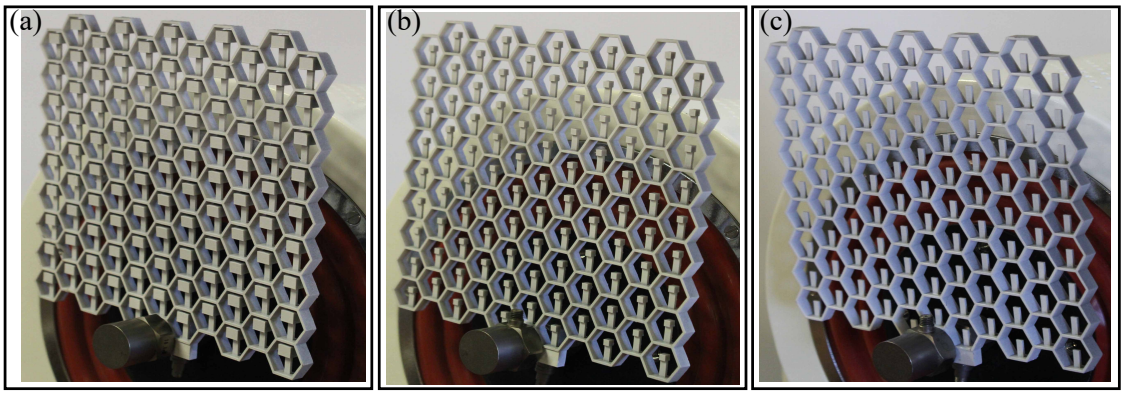


Figure 2.3: Snapshots of the 3D-printed samples mounted on the electrodynamic shaker, representing: (a) the low-frequency (LF) metamaterial sample, featuring cantilever resonators with a length of 10 mm and associated tip masses with dimensions of $6 \times 6 \times 5$ mm$^3$; (b) the medium-frequency (MF) sample, with 8 mm long cantilevers and tip masses of $2.5 \times 2.5 \times 3$ mm$^3$; and (c) the high-frequency (HF) metamaterial, utilizing 6 mm cantilevers with tip masses sized at $2 \times 2 \times 1$ mm$^3$ [2].

The overall dimensions of each printed sample are 140 $\times$ 134 $\times$ 5 mm $^3$, forming a planar structure composed of a repeating pattern of 11 $\times$ 9 hexagonal unit cells. Each cell features wall thicknesses of 1 mm, which contributes to both the structural rigidity and dynamic properties of the metamaterial. Integrated within every unit cell is a single cantilever beam resonator, rigidly clamped at the center of one of the cell's six edges. This arrangement is carefully designed such that the resulting honeycomb lattice vector maintains a constant length of 14 mm across the sample. This uniform geometric periodicity facilitates controlled wave propagation and localized resonant behavior. The base

material properties of the resin used in the 3D printing process are as follows: a density of 1,150 kg/m$^3$, a Young's modulus of 2.2 GPa, and a Poisson's ratio of 0.36.

### 2.3.1 Characterization with electrodynamic shaker

The PSV-500-3D laser scanning procedure consisted of five steps: laser setup, scan preparation, acquisition settings, measurement, and post-processing detailed explianied in the previous chapter 3. A schematic view of experimental test setup with PSV shown in Fig. 2.4. Although the operational deflection shape (ODSs) patterns[1] observed for the low-frequency (LF), medium-frequency (MF), and high-frequency (HF) samples exhibit similar qualitative features, they are reported separately to highlight the systematic upward shift of modal transitions and bandgap frequencies induced by increasing resonator stiffness and modifying the tip masses.

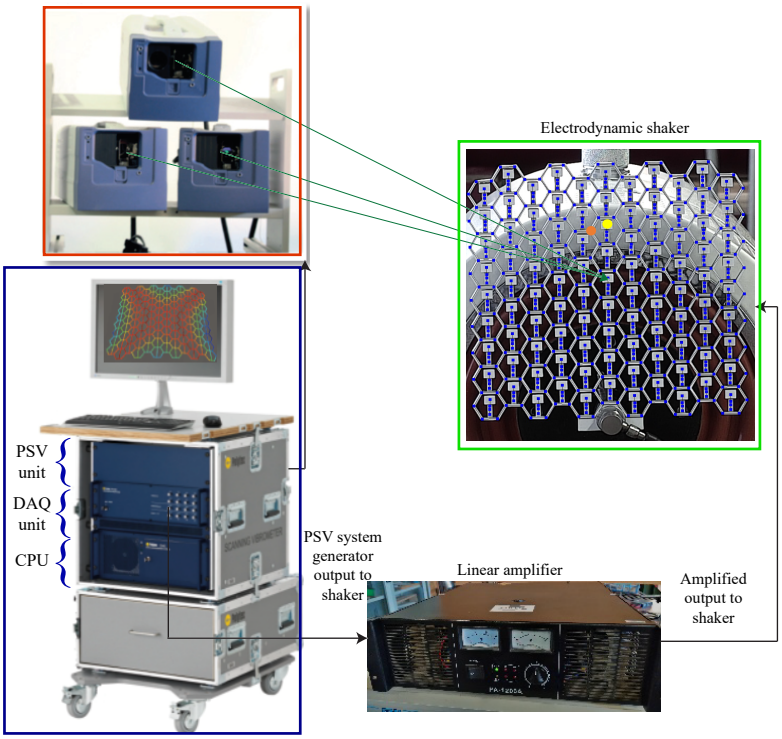


Figure 2.4: A schematic representation of the experimental setup is shown, featuring the use of an electrodynamic shaker to excite the metamaterial sample and the integration of a Polytec PSV-500-3D Scanning Laser Vibrometer (PSV) system for dynamic response measurement. Using Polytec's software, a detailed scanning mesh was generated, enabling pointwise measurements across the sample.

The metamaterial samples with low, medium, and high stiffness were excited using an electrodynamic shaker. The acquisition parameters were set as follows: number of complex averages = 3; bandwidth = 4 kHz, 6 kHz, and 8 kHz for the low, medium, and high stiffness samples, respectively; operating frequency ranges = 0.01–4 kHz, 0.01–6 kHz, and 0.01–8 kHz; number of scan points = 535; decoder velocity = 2.5 m/s; and input voltage

[1] In the colormaps used in this chapter, darker red shades represent negligible or near-zero displacement, whereas lighter shades indicate larger vibration amplitudes. The displacement field is normalized to highlight spatial variations in the operational deflection shapes (ODSs) Appendix C.

= 0.15 V. The experimental campaign consisted of two steps. First, a modal analysis was performed using chirp excitation to capture the evolution of global and local modes across the frequency spectrum. This allowed the unfolding of modal transitions and interactions specific to each stiffness configuration. Subsequently, a frequency response analysis was performed, as illustrated in Fig. 2.5, to identify and locate the bandgap regions can be observed from the experimentally obtained modal sequences and corresponding operational deflection shapes, the evolution of global and local modes differs across the stiffness configurations. The results for the low-stiffness sample are presented in Fig. 2.6, for the medium-stiffness sample in Fig. 2.7, and for the high-stiffness sample in Fig. 2.8.

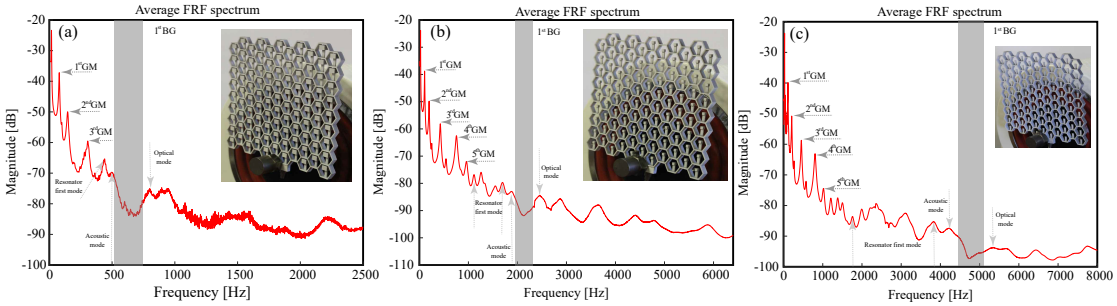


Figure 2.5: Average Frequency Response Function (FRF) spectra with highlighted bandgap regions (shaded in grey): (a) low-stiffness sample, (b) medium-stiffness sample, and (c) high-stiffness sample. In the figure, GM denotes global mode.

For the LF, the system exhibits global honeycomb modes in which the resonators are dragged rigidly with the overall motion of the structure. These global modes are illustrated in Fig. 2.6 (a–d). Around the fifth mode, at approximately 0.4406 kHz, the response of the local resonators begins to appear in phase with the global motion of the honeycomb, corresponding to the onset of the acoustic mode Fig. 2.6 (e). At 0.68437 kHz, a distinct feature is observed: the hexagonal cells of the honeycomb show nearly zero response, while the resonators near the excitation source undergo significant motion. This frequency region corresponds to the formation of the bandgap, highlighted by the white box in Fig. 2.6 (f). Beyond this range, the modes recover a global character, but with strong participation of the local resonators. Importantly, these resonators now vibrate out of phase with respect to the honeycomb cells, giving rise to the optical modes, as shown in Fig. 2.6 (g–h).

For the MF, the modal sequence and ODSs display a similar progression, though shifted to higher frequency ranges due to the increased stiffness of the resonators. At low frequencies, global honeycomb modes dominate, with the resonators moving rigidly in phase with the lattice as shown Fig. 2.7 (a–f). As the frequency increases, the coupling between the local resonators and the host lattice becomes evident. Around the mode at 0.935 kHz, the resonators begin to contribute significantly in phase with the honeycomb cells, corresponding to the acoustic mode as shown Fig. 2.7 (h-j). At approximately 2.14 kHz, the formation of the bandgap is clearly observed, where the honeycomb cells show minimal displacement while the resonators exhibit strong localized motion as shown

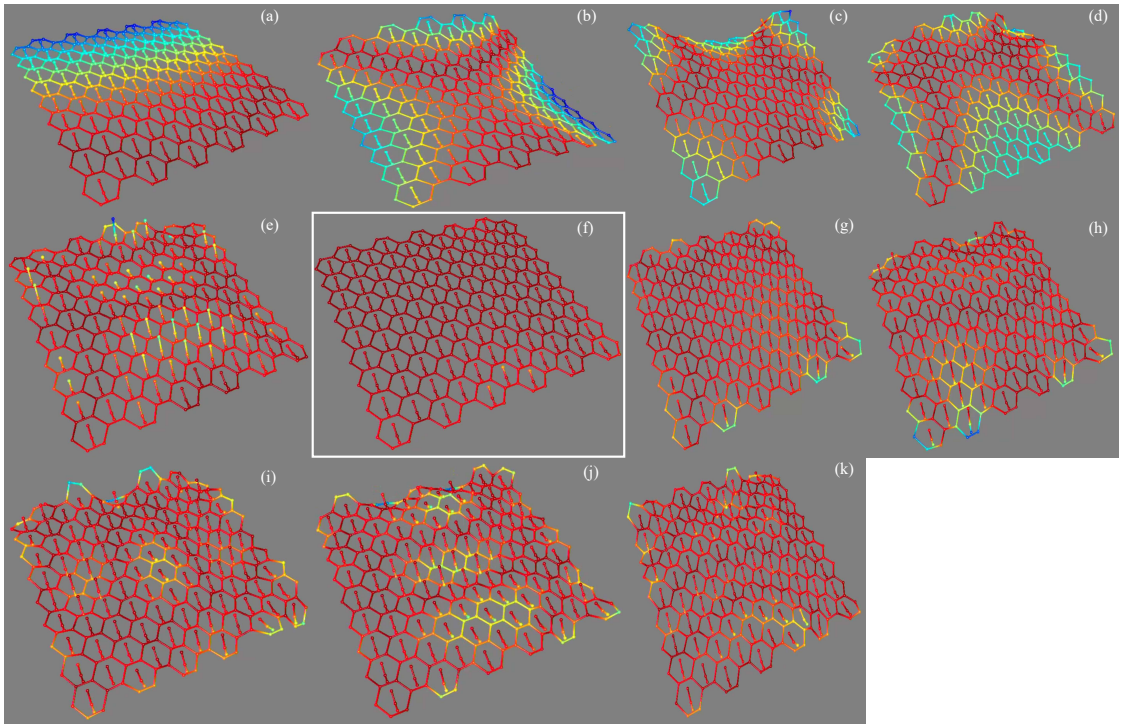


Figure 2.6: Experimentally acquired operational deflection shapes (ODSs) of the low-stiffness metamaterial sample under chirp excitation from the electrodynamic shaker. The selected ODSs were acquired at the following frequencies: (a) 0.01718 kHz, (b) 0.0738125 kHz, (c) 0.145312 kHz, (d) 0.23597 kHz, (e) 0.4406 kHz, (f) 0.68437 kHz (bandgap), (g) 0.80156 kHz, (h) 0.95162 kHz, (i) 1.43437 kHz, (j) 1.58984 kHz, (k) 2.19921 kHz.

Fig. 2.7 (k), highlighted by the white box. Beyond this point, the resonators vibrate increasingly out of phase with the host lattice, leading to the emergence of the optical modes, which are illustrated in Fig. 2.7 (l–n).

In the HF sample, the modal evolution follows the same qualitative trend but occurs at even higher frequencies, reflecting the larger restoring force of the resonators. Initially, global modes dominate, with resonators participating rigidly in the motion of the honeycomb lattice (see Fig. 2.8 (a–f)). As the excitation frequency approaches 3.1025 kHz, the local resonators start to move in phase with the global honeycomb motion, marking the onset of the acoustic mode (see Fig. 2.8 (h-j)). Around 4.74 kHz, the bandgap region becomes apparent, with suppressed motion in the hexagonal cells and pronounced resonator activity (see Fig. 2.8 (k)), highlighted. At higher frequencies, the modal behavior transitions into optical modes, where the resonators oscillate out of phase with the host lattice, as depicted in Fig. 2.8 (l–n).

An EMA analysis was first carried out making use of the PolyWave software which employs the method of the Complex Mode Indication Function (CMIF) applied to the operational deformed shapes of the tested samples. The CMIF, based on the singular value decomposition of the FRF matrix at each spectral line, provides modal parameters, such as damped natural frequencies, mode shapes, damping ratios, and modal participation vectors. EMA is a well-established technique for the estimation of the linear modal properties. The acquired frequencies and damping ratios of the low, medium and high

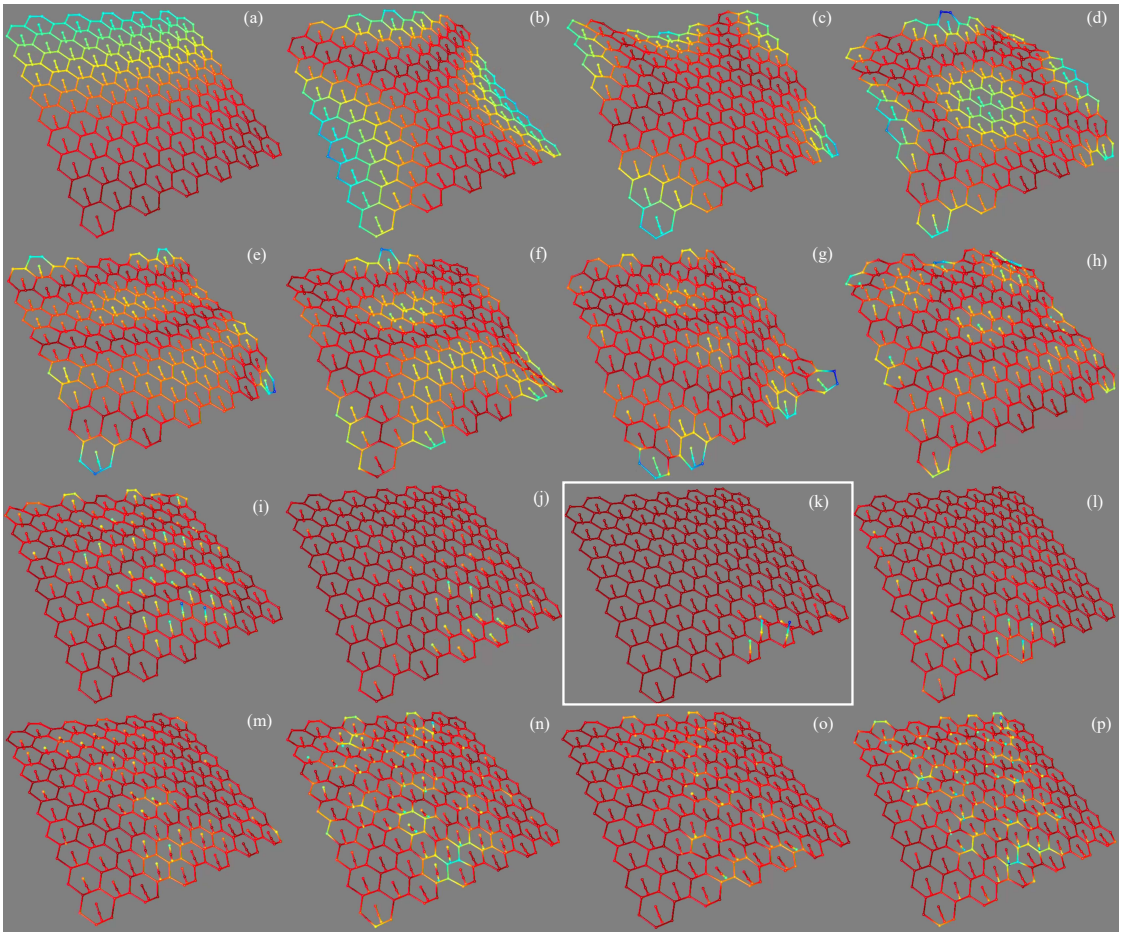


Figure 2.7: Experimentally acquired operational deflection shapes (ODSs) of the medium-stiffness metamaterial sample under chirp excitation from the electrodynamic shaker. The selected ODSs were acquired at the following frequencies: (a) 0.024 kHz, (b) 0.104 kHz, (c) 0.190 kHz, (d) 0.426 kHz, (e) 0.542 kHz, (f) 0.754 kHz (g) 0.960 kHz, (h) 1.112 kHz, (i) 1.69 kHz, (j) 1.882 kHz, (k) 2.14 kHz (bandgap), (l) 2.46 kHz, (m) 2.874 kHz, (n) 3.64 kHz, (o) 4.412 kHz, (p) 5.916 kHz.

frequency metamaterial samples are reported in Table 2.1.

Table 2.1 summarizes the experimentally identified modal characteristics of the structure across the low-, medium-, and high-frequency regimes. For each mode number, the table reports the natural frequency $f_n$ and the corresponding modal damping ratio $\zeta$, expressed as a percentage. This classification reflects the progressive activation of different resonator modes and wave-propagation mechanisms as the excitation frequency increases.

In the low-frequency regime, the identified modes occur below approximately 1.6 kHz and are characterized by relatively low damping ratios, particularly for higher mode numbers, indicating lightly damped structural responses dominated by long-wavelength behavior. The medium-frequency range extends roughly from 0.1 kHz to 5.9 kHz, where an increased density of modes is observed along with moderately higher damping levels, suggesting enhanced energy dissipation associated with resonator participation and internal interactions. In the high-frequency regime, modes extend up to approximately 7.7 kHz and generally exhibit higher damping ratios, consistent with the activation of higher-order

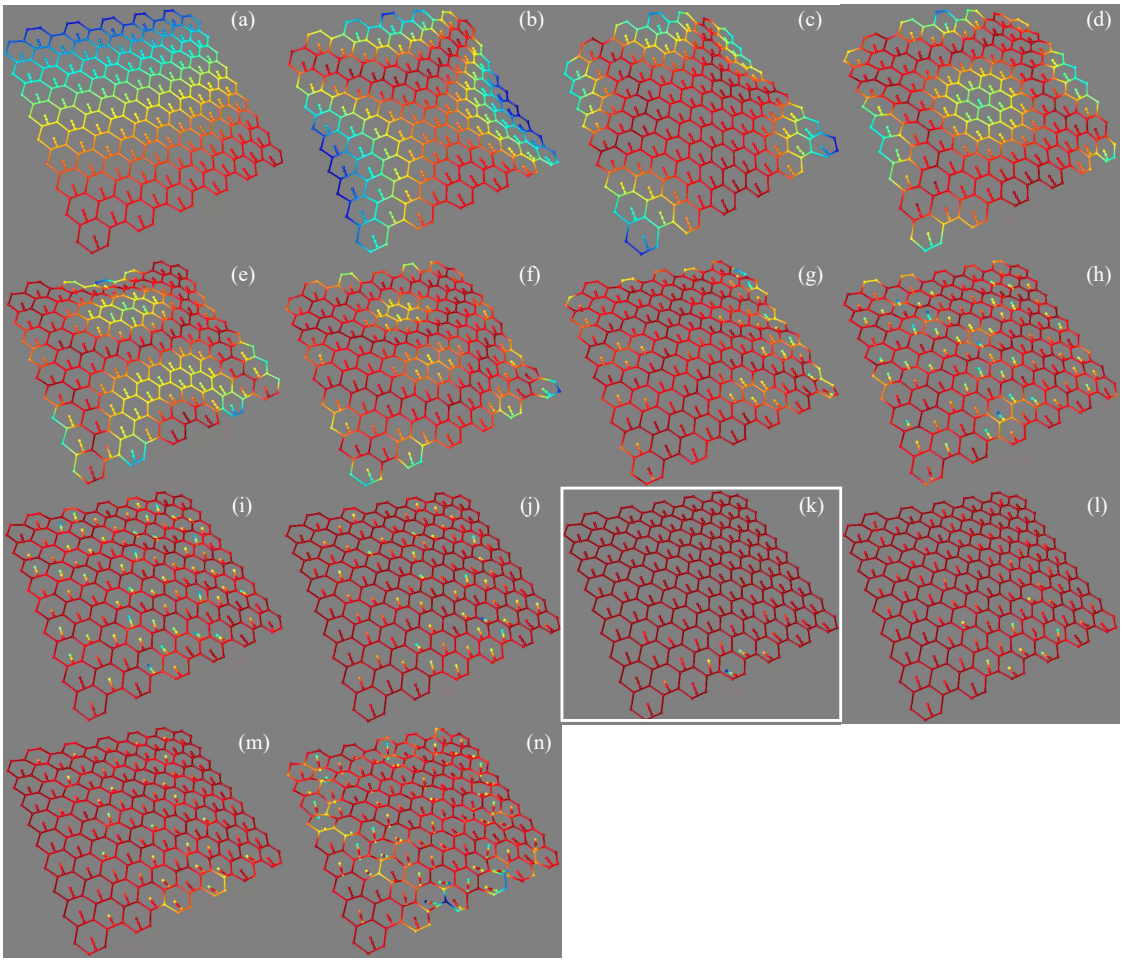


Figure 2.8: Experimentally acquired operational deflection shapes (ODSs) of the high-stiffness metamaterial sample under chirp excitation from the electrodynamic shaker. The selected ODSs were acquired at the following frequencies: (a) 0.0225 kHz, (b) 0.1075 kHz, (c) 0.2075 kHz, (d) 0.4525 kHz, (e) 0.8025 kHz, (f) 1.01 kHz (g) 1.995 kHz, (h) 3.1025 kHz, (i) 3.825 kHz, (j) 4.2225 kHz, (k) 4.74 kHz (bandgap), (l) 5.37 kHz, (m) 6.435 kHz, (n) 7.7425 kHz.

resonator modes and increased material and interfacial losses.

The systematic increase in natural frequency with mode number across all three frequency bands demonstrates the broadband dynamic behavior of the structure. Additionally, the variation in damping ratios across the different frequency regimes highlights the frequency-dependent nature of the energy dissipation mechanisms, which plays a critical role in bandgap formation and wave attenuation.

### 2.3.2 Frequency response analysis

The FRFs were acquired at two measurement points, as shown in Fig. 2.4, over a frequency range up to 6 kHz. One acquisition point was located at the vertex of a hexagonal cell (yellow), while the other corresponded to the tip mass of the in-cell resonator (orange). The experimentally measured FRFs of these points are presented in Fig. 2.9 (b), (e), and (h), where the blue and orange curves represent the responses of the cell vertex and resonator tip mass, respectively. The FRFs reveal that, within a specific frequency

Table 2.1: Frequencies and damping ratios of the mode shapes of the low, medium, and high frequency samples.

| Mode number | Low frequency | | Medium frequency | | High frequency | |
|---|---|---|---|---|---|---|
| | $f_n$ [Hz] | $\zeta$ [%] | $f_n$ [Hz] | $\zeta$ [%] | $f_n$ [Hz] | $\zeta$ [%] |
| 1 | 78.906 | 2.123 | 106 | 1.973787 | 112.5 | 2.580 |
| 2 | 146.094 | 2.681 | 198 | 1.732421 | 210 | 2.733 |
| 3 | 440.625 | 1.551 | 426 | 1.599213 | 802.5 | 2.419 |
| 4 | 503.906 | 4.562 | 756 | 1.5306 | 1380 | 2.609 |
| 5 | 600.000 | 1.717 | 962 | 1.7303 | 1502.5 | 2.815 |
| 6 | 800.781 | 2.638 | 1114 | 1.966 | 1995 | 2.894 |
| 7 | 895.313 | 0.138 | 1258 | 1.6850 | 2212.5 | 3.329 |
| 8 | 939.063 | 0.150 | 1696 | 2.004 | 2355 | 2.195 |
| 9 | 1081 | 0.044 | 2226 | 2.7416 | 3115 | 3.218 |
| 10 | 1138.3 | 0.045 | 2358 | 3.2469 | 3825 | 3.057 |
| 11 | 1205.5 | 0.0568 | 2874 | 2.7676 | 4235 | 3.617 |
| 12 | 1320.3 | 0.0294 | 3652 | 2.88 | 4937 | 3.657 |
| 13 | 1431.3 | 0.2518 | 4398 | 2.1538 | 5657 | 4.397 |
| 14 | 1537.5 | 0.028 | 4778 | 8.58 | 6425 | 3.328 |
| 15 | 1601 | 0.0250 | 5884 | 2.202 | 7732 | 2.501 |

range, the honeycomb response undergoes a sharp attenuation while only the cantilevers in the vicinity of the excitation source exhibit significant motion. This behavior is characteristic of the first bandgap. The experimentally estimated central frequencies of the first bandgap are approximately 600 Hz for the LF sample, 2.23 kHz for the MF sample, and 5.12 kHz for the HF sample.

A comparison between theoretical predictions and experimental measurements, focusing on the first bandgap, is shown in Fig. 2.9 (left panels). The dispersion curves predicted using the PWE method (Fig. 2.9 (c), (f), (i)) are displayed together with the frequency ranges of the first bandgap (shaded regions). For all three samples, the predicted bandgap positions and widths are in good agreement with the experimentally identified bandgaps, thereby validating the accuracy of the theoretical model.

The evolution of the metamaterial response within the first bandgap was further examined through an experimental time-domain analysis conducted on the LF sample. The specimen was subjected to sinusoidal excitation at three driving frequencies: 499 Hz, 600 Hz (the central bandgap frequency), and 797 Hz. Fig. 2.10 presents the corresponding time histories and FFT spectra of the resonator tip mass (top) and the hexagonal cell vertex (bottom). As expected, the response amplitudes of the honeycomb cell at 499 Hz and 797 Hz are an order of magnitude higher than the response amplitude at the central bandgap frequency, confirming the strong attenuation effect associated with the bandgap.

### 2.3.3 Experimental response near the first bandgap

The metamaterial response as the system approaches and traverses the first bandgap is a particularly intriguing phenomenon that warrants detailed investigation. To this end,

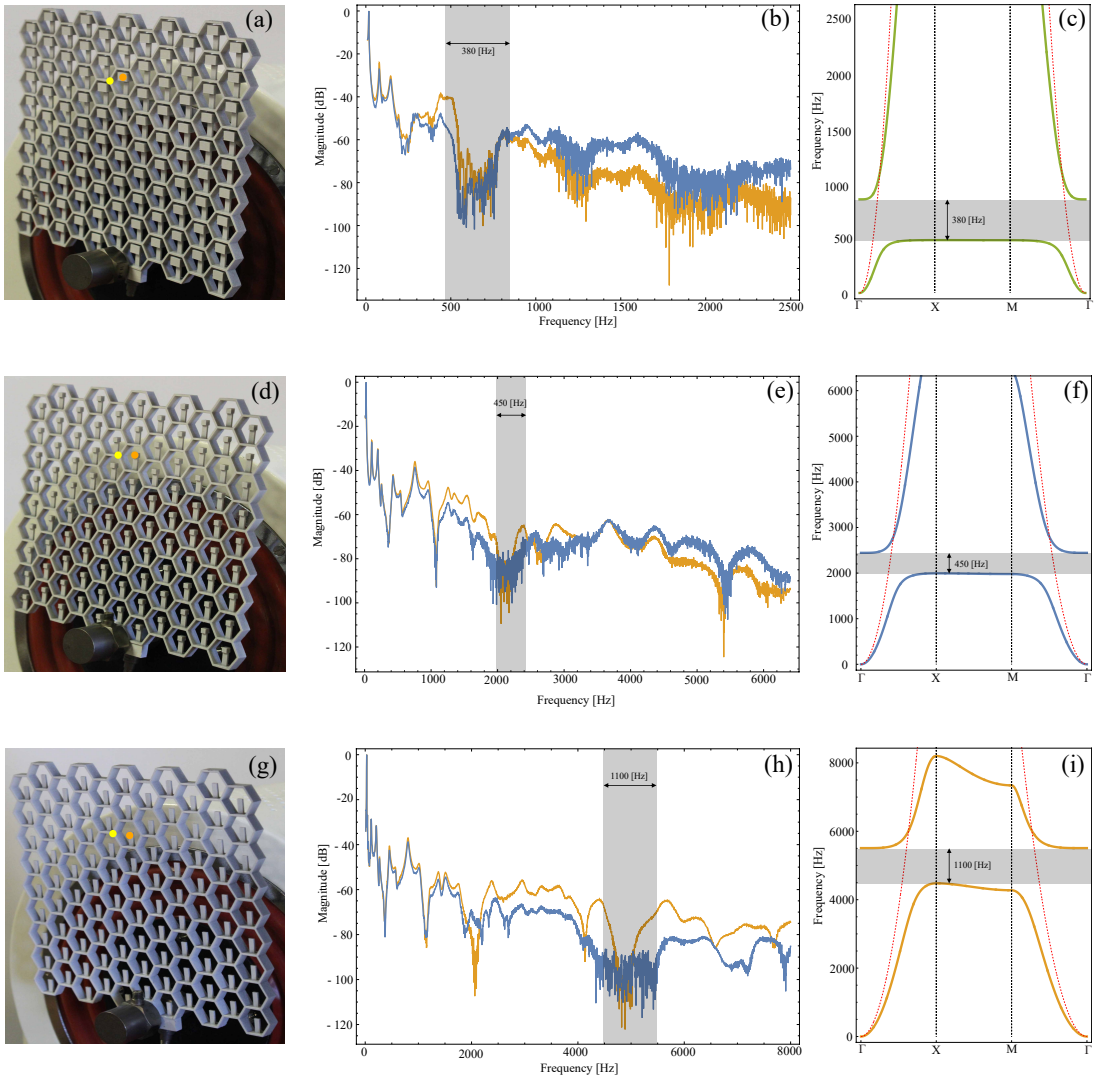


Figure 2.9: Comparison between the experimentally observed bandgaps in the FRFs (mid column) and the theoretically predicted dispersions curves (right column) and sample are presented in left column: for (a) LF, (d) MF, and (g) HF samples. The blue and orange curves denote the experimental measurements of the cell vertex (yellow dot) and of the resonator tip mass (orange dot), respectively. The filled colored rectangles in the experimental FRFs indicate the theoretically predicted bandgpas.

the FRFs and phase responses of the MF sample subjected to a chirp base acceleration were acquired in a narrow frequency window surrounding the first bandgap, in order to better capture the local and global response features. The PSV acquisition parameters were set as follows: complex averages = 5, bandwidth = 4 kHz, frequency resolution = 2.5 Hz, operating frequency range = [1.75 – 3] kHz, first cut-off frequency = 1.5 kHz, second cut-off frequency = 3.5 kHz, and decoder velocity = 2.5 m/s. A rectangular bandpass filter was applied during post-processing.

The average FRFs of the honeycomb cells (host lattice) and of the resonator ensemble are reported in Fig. 2.11. The bandgap, highlighted in gray, is centered at the frequency where the average FRF of the honeycomb points (blue curve) exhibits a distinct local minimum. It should be noted that the velocity response does not vanish completely

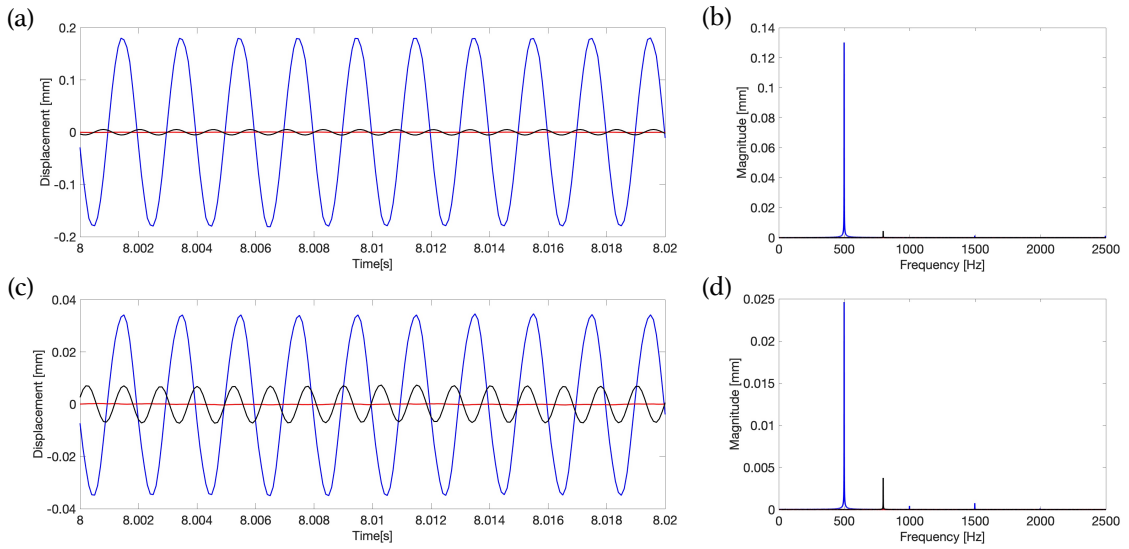


Figure 2.10: Time histories and FFTs of the displacements of (a)-(b) the resonator tip mass and (c)-(d) of the hexagonal cell vertex (see Fig.2.4), when the LF sample was harmonically excited at 499 Hz (blue line), 600 Hz (red line), 797 Hz (black line), respectively. Near-zero response is observed for the excitation frequency of 600 Hz within the first bandgap.

because the PSV measures the rigid-body velocity imposed by the shaker. Furthermore, the experimentally estimated bandgap bandwidth (2.20 - 2.45 kHz) is narrower than the theoretically predicted one (2.00 - 2.45 kHz) by approximately 200 Hz, corresponding to about 10% of the central bandgap frequency.

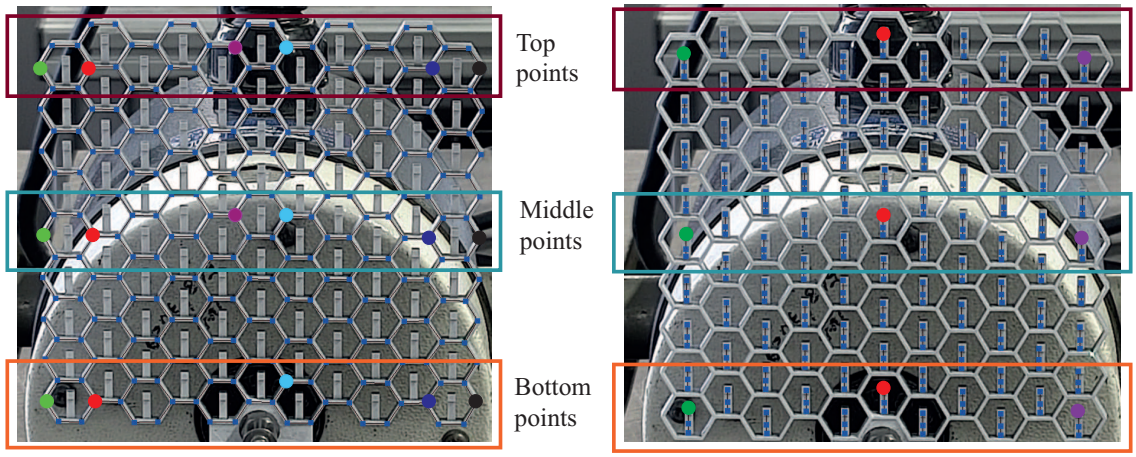


Figure 2.11: Average FRFs of the MF sample where the blue line denotes the average FRF of the cells only, the magenta line indicates the average FRF of the resonators, and the green line the average FRF of the whole metamaterial sample.

To further investigate the response of the metamaterial samples in the vicinity of the first bandgap, the FRFs and phases of different points belonging to the two subsystems, the honeycomb cells and the intracellular resonators were analyzed. Specifically, two points on lateral cells located on either side of the sample were selected, together with the midspan cell and the tip points of the cantilever resonators. The three selected cells (two lateral and one midspan) along three horizontal rows are indicated in Fig. 2.12: the top cells are bounded by a purple rectangle, the middle cells by a cyan rectangle, and the

bottom cells by an orange rectangle. The corresponding FRFs and phases of the selected control points are shown in Fig. 2.12, where the color of each curve matches the color scheme of the associated cell points (green, red, cyan, blue, magenta, and black for the hexagonal cell points). The same color coding is applied consistently for the top, middle, and bottom rows of cells.

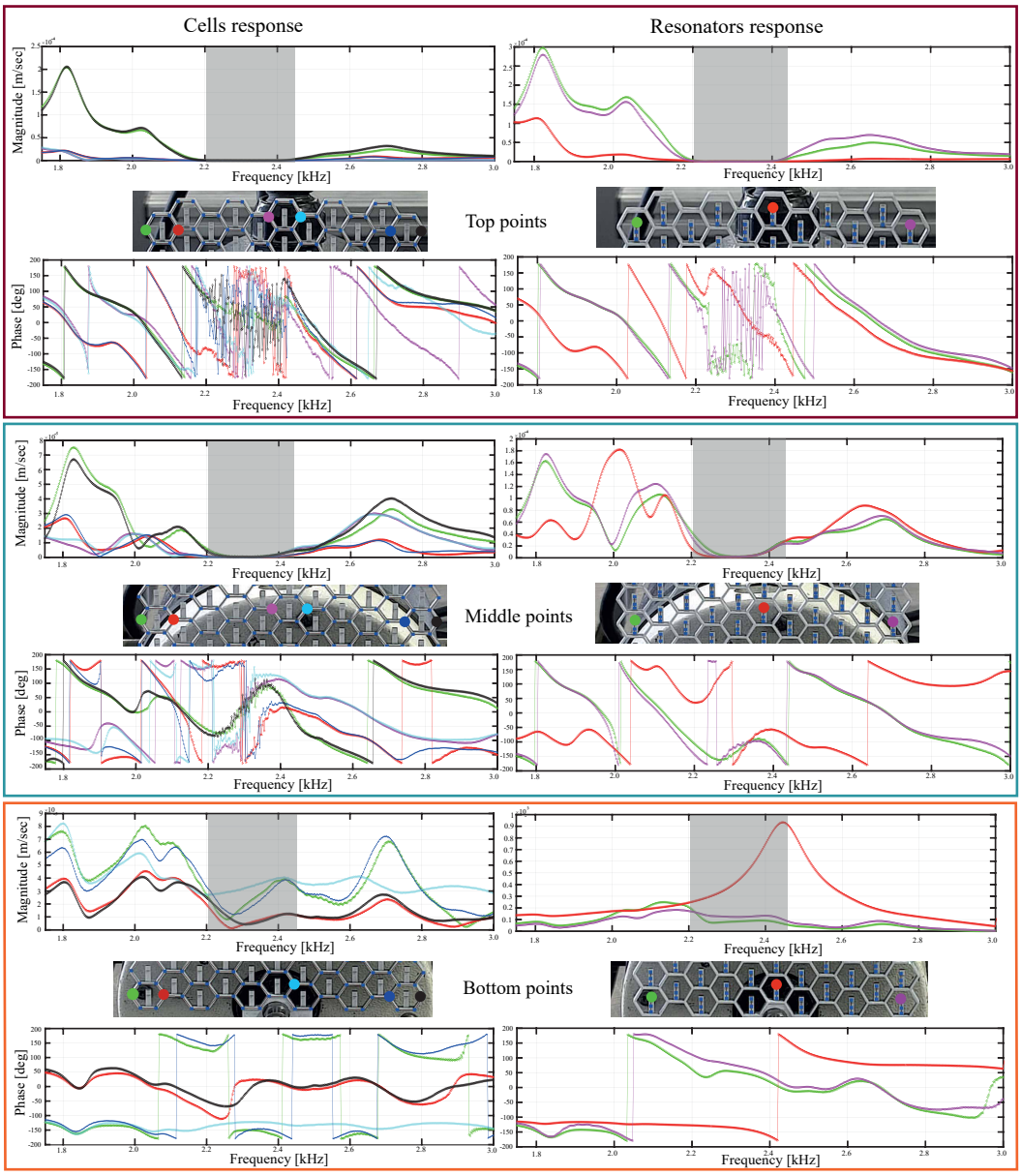


Figure 2.12: FRFs and phases of the PSV scanned points on selected cell vertices and resonators when the sample is subject to a chirp input signal. The colored filled points indicate the acquired points and the curves with the same color indicate the corresponding acquired FRFs and phase outputs. The gray filled regions indicate the theoretically predicted first bandgap.

The experimental results reveal that, as expected, the finite size of the investigated metamaterial samples and their prescribed boundary conditions lead to responses that differ from those of the ideally periodic, infinitely extended metamaterials typically studied

in wave propagation analyses. In particular, near the first bandgap, only the cells located away from the excitation source (applied at the central cell on the bottom boundary) exhibit clear stop-band behavior. By contrast, the cells in the vicinity of the excitation source (i.e., in the bottom region) do not display a distinct bandgap response. Furthermore, a notable number of phase shifts are observed in both the resonator and cell responses before, within, and after the bandgap. These phase variations are a direct manifestation of the local resonances of the cantilever resonators, which occur at slightly different frequencies across different clusters of resonators. This behavior arises from the fact that, depending on their position within the lattice, the resonators experience nonuniform local stiffness. For example, the bottom cells are strongly influenced by the higher stiffness of the solid cell clamped to the shaker head, whereas the more compliant cells located in the central and upper regions of the honeycomb sample behave consistently and clearly exhibit a bandgap between 2.20 and 2.4 kHz. This interpretation is further supported by the FEM simulations presented in the following section.

### 2.3.4 Simulations vs. experiments

A finite element (FE) analysis was performed in the vicinity of the first bandgap, where the metamaterial response undergoes significant changes. The honeycomb cellular structure was modeled in COMSOL Multiphysics as a network of 3D beam elements, including the cantilever resonators with tip masses. As a preliminary step, the 3D model of the honeycomb with resonators (534 elements, 2616 degrees of freedom) was validated. To reproduce the experimental testing conditions, a harmonic displacement was applied at the bottom central point of the model, with the driving frequency set equal to the experimental excitation and the amplitude slightly adjusted to match the measured displacements at the acquisition points shown in Fig. 2.6.

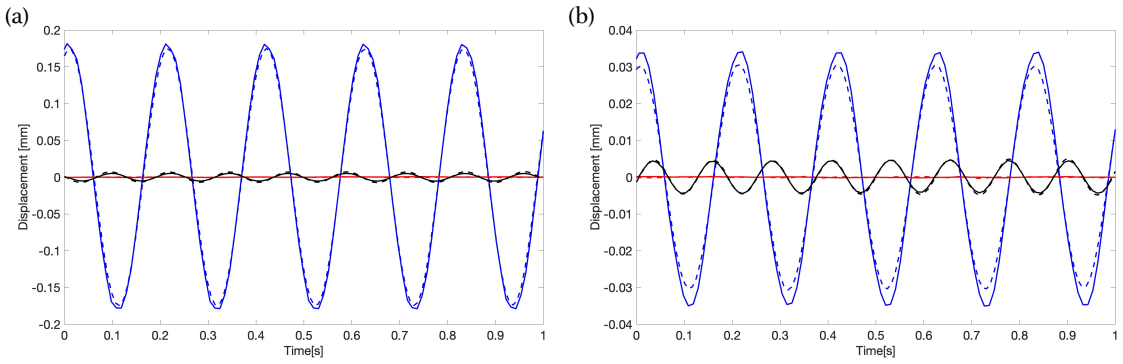


Figure 2.13: Time histories of the deflections of (a) resonator tip mass and (b) and honeycomb cell vertex (see Figure 12(c)), when the LF sample is excited by a harmonic base motion at 499 Hz (blue), 600 Hz (red), 797 Hz (black), respectively. The solid lines indicate the experimental results and the dotted lines denote the FEM predictions.

The simulated time histories of the cell vertex and resonator tip mass were then compared with the experimental measurements for the LF sample. For excitation frequencies

of 499 Hz (below the bandgap), 600 Hz (central bandgap frequency), and 797 Hz (above the bandgap), the numerical predictions showed very good agreement with the experimental results, as illustrated in Fig. 2.13. Notably, at the central bandgap frequency (red curves), both the experimental and simulated responses exhibit negligible motion, confirming the strong attenuation effect within the bandgap.

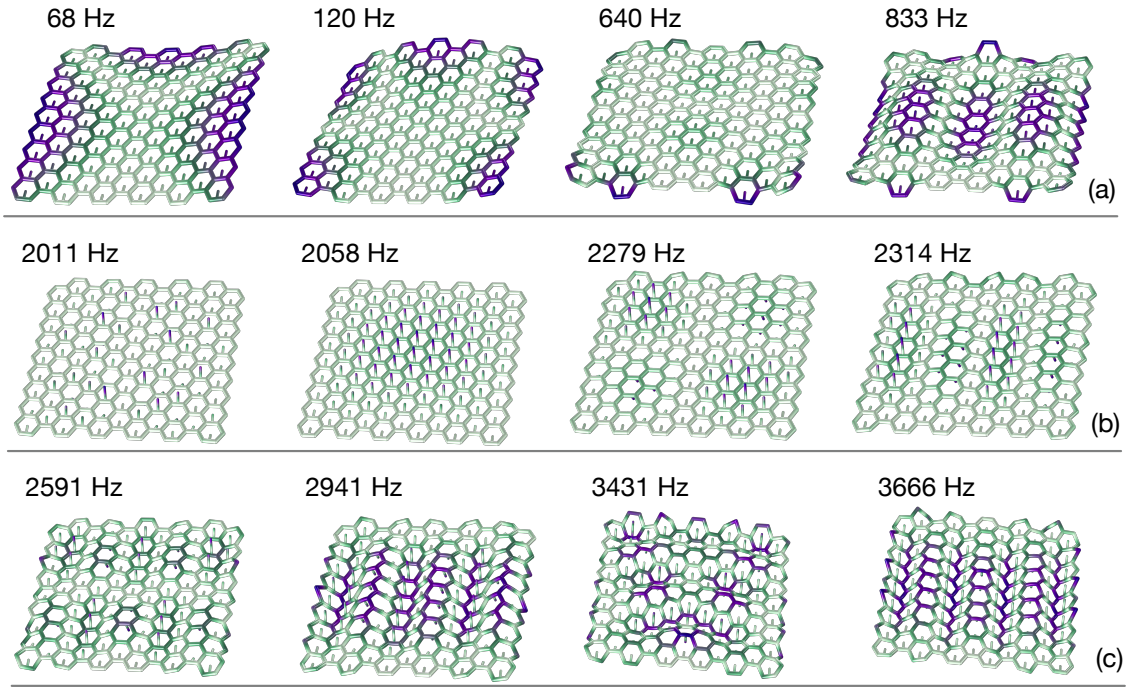


Figure 2.14: Mode shapes of the honeycomb metamaterial system with the embedded cantilever resonators and the associated frequencies. The modes in part (a) possess frequencies below the first bandgap, in part (b) within the bandgap, and in part (c) above the bandgap.

The sequence of mode shapes and associated frequencies was further investigated numerically to gain deeper insight into the metamaterial response as it transitions through the first bandgap. Fig. 2.14 illustrates representative mode shapes corresponding to frequencies below, within, and above the bandgap. Below the bandgap as shown Fig. 2.14 (a), the out-of-plane mode shapes are dominated by global honeycomb motion, since the embedded cantilevers are not yet excited in bending and therefore move in phase with the host lattice. When the system is excited near 2.0 kHz as shown in Fig. 2.14 (b), local modes of the cantilever resonators are activated. These modes involve clusters of resonators and appear in close succession within a narrow frequency interval inside the first bandgap. This behavior arises from the different boundary conditions imposed locally by the honeycomb structure, which provides nonuniform elastic stiffness across the panel: the central cells are stiffer than those at the sides. As a consequence, multiple local resonator modes are manifested within the (2.0-2.4) kHz range, overlapping with the expected acoustic response of the honeycomb, in which the cantilevers vibrate in their first bending mode in phase with the global motion of the structure. Beyond the bandgap frequency (Fig. 2.14 (c)), coupling between local and global modes becomes evident. In

this regime, the cantilever resonators oscillate in their first bending mode but out of phase with the global honeycomb motion, confirming the emergence of optical modes.

### 2.3.5 Characterization under PZT excitation

In the previous experimental setup, an electrodynamic shaker was used to excite the samples, which necessarily introduced boundary constraints through the mounting fixture. While the shaker provides a reliable means of exciting the honeycomb structures and accurately capturing their low-frequency dynamic response, its operational bandwidth is limited to approximately 8 kHz. This limitation restricts the investigation of higher-frequency wave-propagation phenomena and prevents the observation of additional bandgaps that occur beyond this range. To overcome these constraints, the subsequent experiments employ PZT excitation. PZT actuators are capable of driving the samples at frequencies exceeding 100 kHz, enabling the identification of multiple bandgaps and higher-order resonator modes that are inaccessible using shaker-based excitation.

In the current configuration, a piezoelectric (PZT) actuation disk is used as the excitation source. The sample is suspended using elastomer supports attached to a fixed stand, thereby minimizing boundary constraints and allowing a more representative dynamic response of the structure to be measured.

The experimental campaign employed a PSV system, a PZT actuator, and a linear amplifier (see Fig. 2.15). The PZT actuator operates on the principle of the piezoelectric effect, where mechanical energy is converted into electrical energy and vice versa. When mechanical stresses act on the piezoelectric body, the internal electrical dipoles are displaced, generating an electric field and a corresponding measurable voltage. This direct piezoelectric effect is often referred to as the sensor or generator effect. Conversely, the converse piezoelectric effect enables the PZT actuator to convert electrical input into mechanical motion, which is used here to excite the samples.

### 2.3.6 Characterization of LF in the absence of resonators

Based on observations from previous shaker-based experiments, the effect of broken periodicity on bandgap formation was further investigated. During the SLA fabrication process, support structures are required to manufacture the LF metamaterial samples. In the post-processing stage, while removing these supports, one and four cantilever resonators were inadvertently damaged, resulting in configurations with broken periodicity. Rather than discarding these samples, the resulting configurations motivated further investigation into how imperfections influence bandgap characteristics. To gain deeper insight into the associated wave-propagation behavior, additional experimental characterization was therefore conducted using PZT excitation, which enabled higher-frequency and spatially resolved measurements.

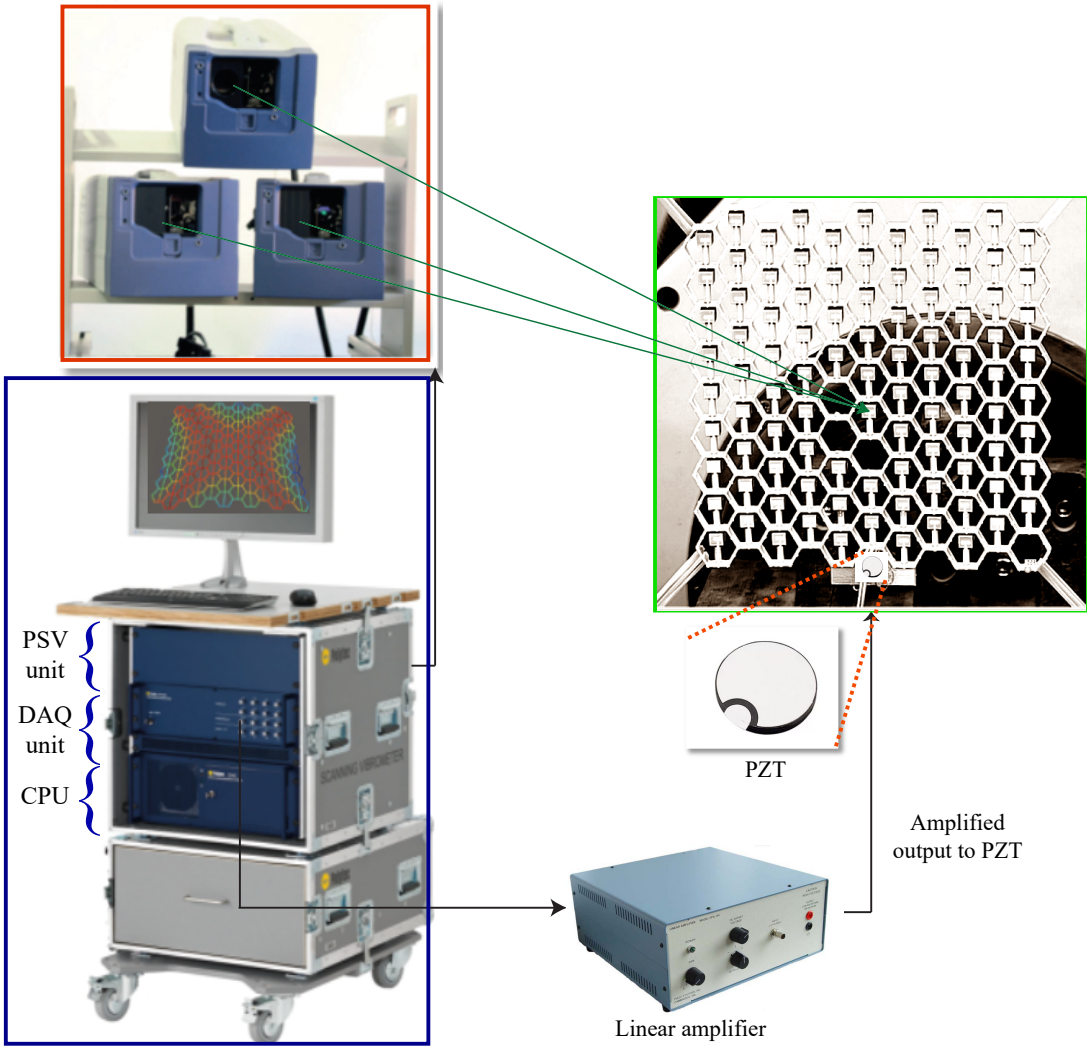


Figure 2.15: A schematic representation of the experimental setup is shown, featuring the use of an PZT disk to excite the metamaterial sample and the integration of a Polytec PSV-500-3D Scanning Laser Vibrometer (PSV) system for dynamic response measurement.

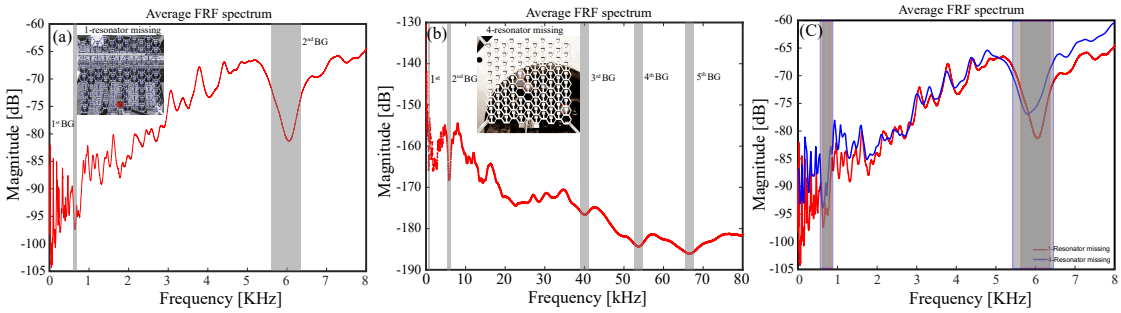


Figure 2.16: Average Frequency Response Function (FRF) spectra with highlighted bandgap regions (shaded in grey): (a) low-frequency (LF) sample with one missing resonator, (b) LF sample with four missing resonators, and (c) comparison of the average FRF spectra for samples with missing resonators.

To assess the robustness of the bandgap phenomenon, a low-frequency sample with one missing intra-cell resonator and another with four missing resonators were experimentally tested, as shown in Fig.2.15. In both configurations, the presence of multiple bandgaps

is clearly observed. The experimental results confirm not only the persistence of the low-frequency bandgaps but also the emergence of additional higher-frequency attenuation phenomena, as evidenced by the average FRF spectrum shown in Fig.2.16 and by the corresponding operational deflection shapes (ODSs) reported in Figs.2.17 and 2.18. The average FRF spectrum for the samples with one and four missing resonators are presented in Fig.2.16 (a), (b), where the detected bandgap regions are highlighted in grey. These results clearly demonstrate the persistence of attenuation zones despite the loss of strict periodicity. Although the precise locations and bandwidths of the bandgaps are affected by the introduced structural irregularities, the underlying bandgap formation mechanism remains robust.

To enable a direct comparison with the intact low-frequency (LF) sample, the first bandgap was quantified for all three configurations. Relative to the intact case, the configuration with one missing resonator exhibits a modest downward shift in the central bandgap frequency accompanied by a slight reduction in bandwidth. When four resonators are removed, the frequency shift becomes more pronounced; the bandgap width increases compared to the single–missing-resonator case, and additional higher-frequency bandgaps appear increasingly fragmented. Despite these quantitative changes, the attenuation level within the bandgaps remains comparable across all configurations, indicating that the fundamental bandgap formation mechanism is resilient to localized defects.

A selection of experimentally obtained ODSs for the sample with one missing resonator is shown in Fig.2.17. The lowest-frequency responses correspond to global honeycomb deformations, in which the resonators undergo nearly rigid-body motion. Fig.2.17(e) illustrates an ODS resembling an acoustic-type mode, while Fig.2.17(f) captures the first bandgap response, characterized by localized resonator motion and strongly suppressed lattice activity. At higher frequencies, Fig.2.17(g) depicts an optical-like ODS. Further along the spectrum, Fig.2.17(v) shows an acoustic-like response involving in-phase motion of the resonators vibrating in their second bending mode. This is followed by a second bandgap response (Fig.2.17(w)) and an optical-like ODS associated with out-of-phase resonator motion in the second bending mode (Fig.2.17(x)). Between these two bandgaps, a frequency range is observed in which the resonators are excited predominantly in their first torsional mode; however, this torsional response does not couple sufficiently with the lattice to open a distinct bandgap.

For the configuration with four missing resonators, up to five distinct bandgaps are experimentally identified within the investigated frequency range extending to 80 kHz (Fig.2.18). The first two bandgaps originate from the fundamental bending interaction between the resonators and the host lattice. At higher frequencies, additional bandgaps emerge due to higher-order resonator eigenmodes. Specifically, the second bending mode gives rise to a third bandgap, while the second torsional mode contributes to the formation of a fourth. A fifth bandgap is detected at even higher frequencies and is associated

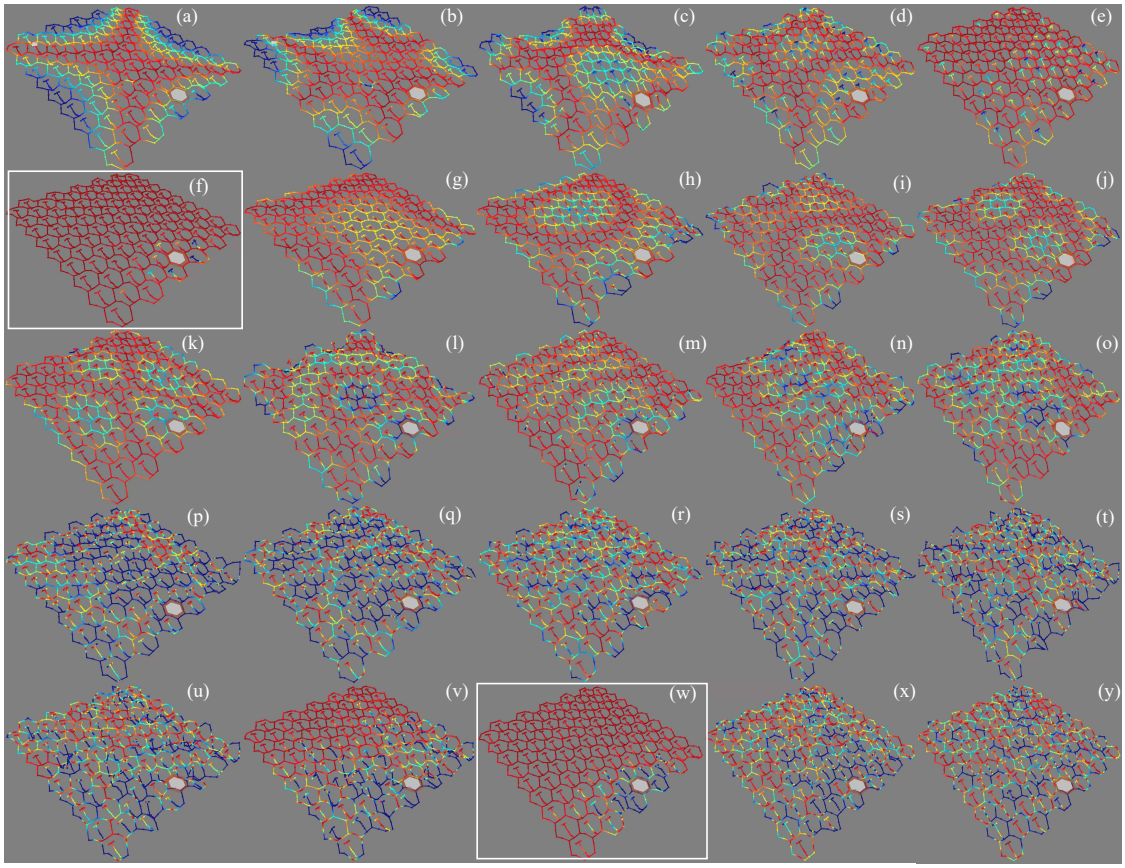


Figure 2.17: Experimentally acquired operational deflection shapes (ODSs) of the LF with 1 resonator missing metamaterial sample under chirp excitation from the PZT actuation disk. The selected ODSs were acquired at the following frequencies: (a) 0.0975 kHz, (b) 0.180 kHz, (c) 0.2663 kHz, (d) 0.3288 kHz, (e) 0.465 kHz, (f) 0.5625 (first bandgap) kHz (g) 0.650 kHz, (h) 0.8613 kHz, (i) 0.9663 kHz, (j) 1.0936 kHz, (k) 1.2 kHz , (l) 1.4563 kHz, (m) 1.615 kHz, (n) 2.1638 kHz, (o) 2.450 kHz, (p) 2.830 kHz, (q) 3.015 kHz , (r) 3.790 kHz, (s) 4.0213 kHz, (t) 4.4088 kHz, (u) 4.850 kHz,(v) 5.5175 kHz (w) 6.0475 (second bandgap) kHz, (x) 6.6275 kHz and (y) 7.2475 kHz.

with the coupling between complex higher-order resonator dynamics and the honeycomb lattice.

Overall, these experimental findings are consistent with prior studies demonstrating that multiple attenuation bands can arise from distinct resonator eigenmodes and their coupling with the host structure. In the present samples, higher-frequency bandgaps are linked to higher-order bending and torsional resonator dynamics, with their locations and bandwidths measurably influenced by the presence of missing resonators. Collectively, the results demonstrate multi-band attenuation and highlight the practical robustness of locally resonant bandgaps under localized defects. These observations are consistent with previous reports showing that bandgaps can persist and even broaden under structural disorder [78], that multi-bandgap responses can emerge from systems incorporating multiple resonators [2], and that tunable bandgaps can extend into high-frequency regimes approaching 80 kHz [79].

Chapter 3 extends the experimental investigation to spider-web-type resonators, following the same modeling, design, and validation framework.

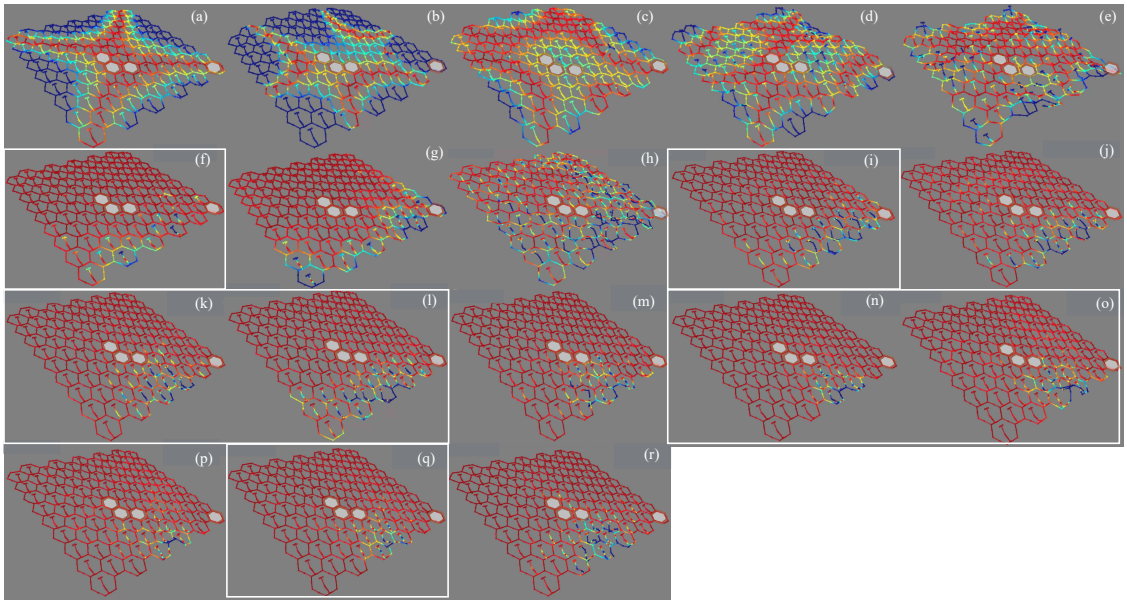


Figure 2.18: Experimentally acquired operational deflection shapes (ODSs) of the LF with 4 resonator missing metamaterial sample under chirp excitation from the PZT actuation disk. The selected ODSs were acquired at the following frequencies: (a) 0.1 kHz, (b) 0.175 kHz, (c) 0.275 kHz, (d) 0.375 kHz, (e) 0.5 kHz, (f) 0.55 (first bandgap) kHz (g) 0.7 kHz, (h) 5.2 kHz, (i) 5.725 (second bandgap) kHz, (j) 6 kHz, (k-l) 40.025 - 43.05 (third bandgap) kHz, (m) 46.85 kHz, (n-o) 53.5 - 57.3 (fourth bandgap) kHz, (p) 66.625 kHz (q) 68.725 (fifth bandgap) kHz and (r) 76.725 kHz.

## 2.4 Summary

This study investigated the linear bandgap behavior of 3D-printed low-frequency (LF), medium-frequency (MF), and high-frequency (HF) locally resonant metamaterials composed of cantilever-based resonators with varying tip masses. The samples were experimentally characterized using both electrodynamic shaker and piezoelectric (PZT) excitations. Under shaker excitation, a Polytec Scanning Vibrometer (PSV) system was employed to measure frequency response functions (FRFs) and operational deflection shapes (ODSs), revealing distinct bandgaps for all configurations, with ranges of approximately 0.48-0.86 kHz for LF, 2.0-2.45 kHz for MF, and 4.50- 5.60 kHz for HF samples. Complementary PZT-based experiments enabled higher-frequency wave-propagation measurements, particularly for the HF samples, and confirmed similar bandgap characteristics, with minor discrepancies attributed to differences in boundary conditions between the two excitation setups. Additional experiments on LF metamaterials with broken periodicity, achieved by removing one or four resonators, demonstrated that bandgap formation persists even in the absence of strict periodicity. Combined FRF and ODS analyses revealed modal transitions from acoustic to optical modes across the bandgaps, while local FRF measurements at different lattice locations provided further insight into the spatially varying dynamic response. Dispersion analyses based on the plane wave expansion (PWE) method demonstrated broad frequency tunability and confirmed the ability of cantilever-based resonator configurations to support multiple bandgaps. Strong agreement between numerical predictions and experimental observations was established through validation

on 99-cell samples excited using both PZT actuators and electrodynamic shakers. Due to finite sample size and damping effects, the experimentally measured bandgaps were slightly narrower than theoretical predictions, with damping ratios ranging from approximately 2.2% to 4.4%. Overall, the results confirm the robustness of multi-bandgap formation in locally resonant metamaterials and highlight their potential for broadband vibration attenuation and noise-control applications, providing a foundation for the nonlinear dynamic investigations presented in the subsequent chapter.

# Chapter 3

# Tunable bandgaps in locally resonant metamaterials

The theoretical modeling framework employed in this chapter is presented in Appendix A. While the underlying analytical formulation remains unchanged, the geometry of the spider-web-like resonator was adapted to accommodate fabrication constraints and to enable a systematic investigation of the effects of geometric variability on bandgap formation and nonlinear dynamic response.

This chapter presents an experimental and numerical study of axially symmetric spider web-like resonator (SWR) metamaterials fabricated using additive manufacturing. Two configurations are investigated. The first configuration, referred to as SWR-I, serves as a baseline design characterized by a nominally periodic geometry with uniform hexagonal host thickness and axially symmetric resonators. The second configuration, referred to as SWR-II, introduces a controlled geometric modification in which the hexagon thickness is intentionally made non-uniform at the CAD design stage, thereby imposing a spatial stiffness variation within the lattice. In addition to this intentional modification, the fabricated SWR-II specimen exhibits localized manufacturing-induced deviations, particularly near the specimen boundaries, which further perturb the nominal geometry.

The experimental campaign was conducted using a scanning laser Doppler vibrometry system (PSV). Each specimen was suspended using nylon wires to approximate free-free boundary conditions, and piezoelectric (PZT) actuators were bonded to the bottom surface using epoxy resin. Broadband chirp excitation was applied to capture full-field velocity responses over a frequency range extending up to 10 kHz. The primary objective of these measurements was to identify operational deflection shapes (ODSs), classify acoustic and optical mode families, and determine the associated locally resonant bandgaps. Particular attention was given to the transition across bandgap regions, from in-phase acoustic modes to attenuation-dominated behavior and subsequently to out-of-phase optical modes. Local frequency response measurements were performed on selected unit cells, primarily in the left and middle regions of the specimens, to minimize boundary

effects and to assess the influence of excitation location on bandgap characteristics.

Immediately beyond the first bandgap edge, distinctive wave phenomena were observed in both SWR configurations. These included edge-localized responses, which arise in finite specimens due to boundary-induced symmetry breaking and are not captured by idealized infinite periodic models. Edge waves were experimentally identified in the SWR-I sample within the frequency range of approximately 0.97-1.09 kHz and in the SWR-II sample between approximately 0.62-0.65 kHz, highlighting the role of finite-size and boundary effects in post-bandgap wave propagation.

To complement the experimental observations, both SWR-I and SWR-II unit-cell geometries were analyzed numerically using finite element eigenfrequency analysis under Bloch-Floquet periodic boundary conditions. Dispersion curves were extracted through parametric wave-vector sweeps to identify bandgaps predicted for idealized periodic structures. Comparisons between experimental results obtained from finite specimens and numerical predictions based on periodic unit cells provide insight into the influence of geometric variability, resonator detuning, and boundary conditions on bandgap robustness.

Finally, the nonlinear dynamic behavior of the SWR-II configuration was investigated through shaker-based frequency response measurements. Frequency response functions of selected resonators revealed a pronounced amplitude-dependent softening behavior, particularly in modes associated with the first bandgap. The first bandgap was identified experimentally in the frequency range of 0.58-0.68 kHz, and its apparent width was observed to increase with excitation amplitude. These results demonstrate that nonlinear effects can significantly influence the effective attenuation characteristics of locally resonant metamaterials, and that bandgap behavior in practical structures is governed by a coupled interplay between geometry, imperfections, boundary effects, and excitation amplitude.

## 3.1 Fused deposition modeling

Fused Deposition Modeling (FDM) is a prevalent additive manufacturing process in which a thermoplastic filament typically a polymer is heated to a semi-liquid state and extruded through a temperature-controlled nozzle across the print bed. The nozzle traces a predefined path to deposit the material layer by layer, with each layer solidifying as it cools. After completing one layer, the nozzle incrementally moves upward to begin the next, continuing this cycle until the full three-dimensional geometry is constructed (shown in Fig. 3.1). FDM offers several advantages that contribute to its widespread adoption in both academic and industrial settings. Notably, FDM is recognized for its cost-effectiveness, ease of operation, and the ability to process a wide range of thermoplastic materials [80]. These attributes make FDM particularly suitable for rapid prototyping, educational purposes, and low-volume manufacturing. The technology's simplicity and the availability of

consumer-grade printers have further facilitated its integration into various applications, including artistic and decorative design, as well as hobbyist projects [81].

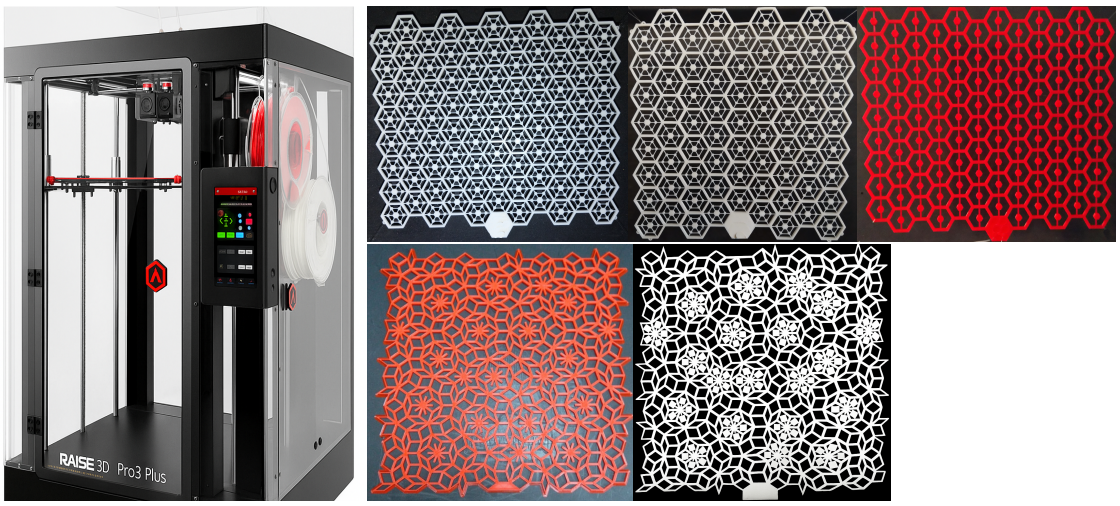


Figure 3.1: Raiser 3D Pro3 Plus 3D printer shown with a fabricated sample.

The layer-by-layer deposition process inherent to FDM can result in anisotropic mechanical properties, leading to reduced strength along the build direction. This anisotropy arises due to weaker interlayer bonding compared to the strength within individual layers [82]. Surface finish is another concern with FDM-printed parts, as the process often leaves visible layer lines and surface roughness. Achieving a smooth finish typically requires additional post-processing steps such as sanding or chemical smoothing, which can be time consuming and may not always yield the desired results [83].

## 3.2 Spider web-like resonators

The Fig. 3.2 presents, spider web resonator (SWR-1), spider web resonator (SWR-II) samples a comparative visualization of the 3D-printed metamaterial samples designed for dynamic testing, specifically engineered to exhibit multiple bandgaps in the lowest frequency range.

These structures were fabricated using a 3D-RASIER PRO Plus printer. The SWR-I, baseline structure, measuring $206 \times 237.87 \times 3\text{mm}^3$, consists of an $8 \times 11$ array of hexagonal cells. The SWR-II sample consisted of $8 \times 9$ hexagonal cells and measured $274 \times 260.96 \times 3.5\text{mm}^3$, slightly larger than the primary sample, which measured $206 \times 237.87 \times 3\text{mm}^3$. This uniform geometric periodicity facilitates controlled wave propagation and localized resonant behavior. The base material properties of the resin used in the 3D printing process are as follows: a density of 1,250 $\text{kg/m}^3$, a Young's modulus of 3.6 GPa, and a Poisson's ratio of 0.36.

**Definition of geometric imperfections** In this chapter, the term geometric imperfection is used in two distinct and well-defined senses, which are clearly distinguished

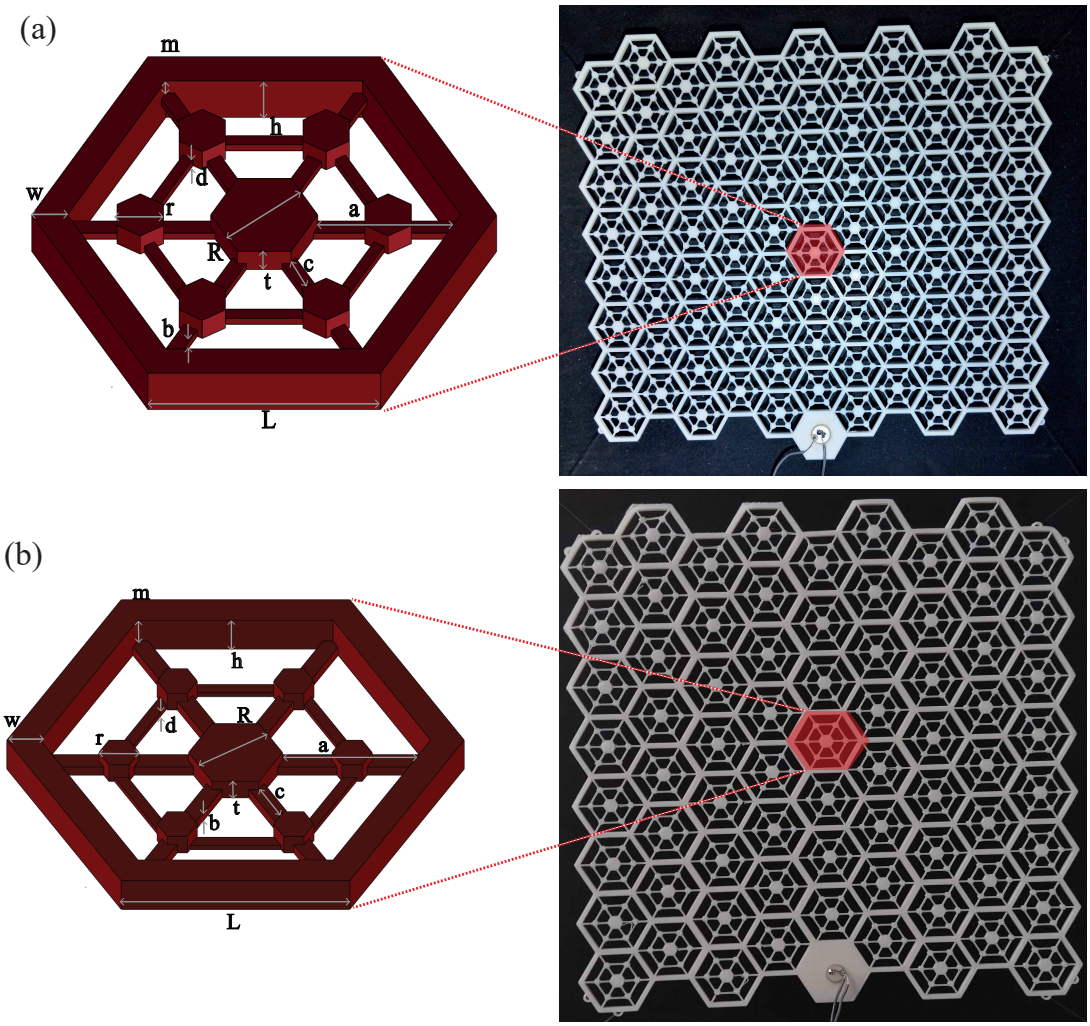


Figure 3.2: (a) 3D geometric model of SWR-I resonator unit cell with parameters: m = 1, b = 0.5 mm, d = 0.5 mm, h = 3 mm, r = 3 mm, R = 6 mm, t = 1.5 mm, a = 9.34 mm, c = 3.04 mm, w = 2 mm, and L = 15.01 mm, the structure is 3D-printed and forms a 2D metamaterial arranged in an $N \times M$ size. (b) 3D geometric model of SWR-II resonator unit cell with parameters: m=2.5, b=1, d=0.5, h=3.5, r=3, R=8.08, t=2, a=12.7, c=4.23, w=2.88, L=19.63 (lengths expressed in mm), the structure is 3D-printed and forms a 2D metamaterial arranged in an $N \times M$ size.

throughout the analysis.

1. **Designed (intentional) geometric imperfection:** In the SWR-II specimen, the hexagonal host structure was intentionally designed with non-uniform thickness in the CAD model. This deliberate geometric modification introduces a controlled spatial variation in stiffness within the unit cell, thereby breaking the ideal periodicity of the baseline SWR-I design.

2. **Fabrication-induced (unintentional) geometric imperfection:** In addition to the intentional CAD-defined thickness variation, the fabricated SWR-II sample exhibited manufacturing-related deviations from the nominal geometry. These imperfections were most pronounced to the specimen and are attributed to limitations of the fabrication process. Such deviations introduce additional variability in the

local resonator geometry.

The designed geometric imperfection is therefore a controlled feature introduced at the design stage, whereas the fabrication-induced imperfection is an uncontrolled deviation arising during manufacturing. Both effects contribute to local resonator detuning, which can weaken resonance synchronization across the lattice and influence the formation, width, and robustness of the observed bandgaps.

## 3.3 Test setup with PSV system

The experimental campaign was conducted using a scanning laser scanning vibrometry (PSV) system, a piezoelectric (PZT) actuator, and a linear power amplifier. The PZT actuator was used to excite the specimens by converting the applied electrical signal into mechanical vibrations, while the linear amplifier ensured proportional amplification of the input signal.

The PSV system was employed to measure the out-of-plane velocity response of the specimens based on laser Doppler vibrometry. The experimental setup and measurement principle are identical to those described in Chapter 2 and are therefore not repeated here. The PSV measurement procedure followed the same workflow, consisting of laser setup, scan preparation, acquisition parameter definition, measurement, and post-processing.

### 3.3.1 Characterization of the SWR-I under PZT excitation

The baseline spider web resonator (SWR-I) specimen was fully fabricated via additive manufacturing to ensure geometric repeatability of the resonator elements, as shown in Fig. 3.3(a). The specimen measures $206 \times 237.87 \times 3$ mm$^3$ and consists of an $8 \times 11$ array of hexagonal unit cells. Each unit cell hosts a central resonator mass and six secondary masses, connected to the hexagonal frame by slender ligaments, forming an axially symmetric spider web–like configuration.

Full-field velocity responses were measured using the PSV system at selected points located at the six vertices of each hexagonal cell, on each secondary resonator mass, and on the central resonator mass, as indicated in Fig. 3.3(a). The measurements were performed using a broadband chirp excitation over the frequency range 0.01–10 kHz, with three complex averages, a bandwidth of 10 kHz, and a total of 830 scan points. The excitation voltage was set to 180 V, and the decoder velocity was 2.5 m/s.

Post-processing of the measured velocity field yielded a comprehensive set of ODSs together with the corresponding spatially averaged frequency response function. The averaged FRF, shown in Fig. 3.3(b), reveals three distinct bandgaps within the investigated frequency range. These bandgaps were identified from the experimental data as continuous frequency intervals in which the response amplitude drops significantly relative to the adjacent passbands, indicating strong attenuation of wave propagation through the

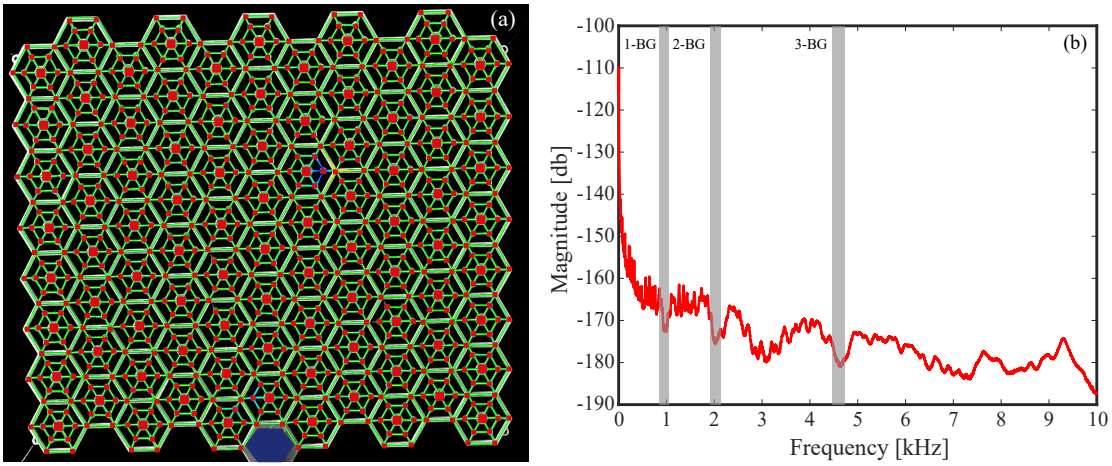


Figure 3.3: (a) Snapshot of M1 sample with scan points highlighted in red color (b) average FRF spectrum highlighted with three bandgaps (grey).

lattice. This identification was corroborated by the associated ODSs, which exhibit suppressed vibration levels within the bandgaps and characteristic modal transitions across their boundaries. Representative ODSs associated with the bandgaps and the surrounding passbands are presented in Figs. 3.4 and 3.5.

At low frequencies, the response is dominated by global honeycomb-type deformations, in which the resonators follow the motion of the host structure (Fig. 3.4(a,b)). With increasing frequency, symmetric local resonator modes emerge (Fig. 3.4(c–p)). Immediately below the first bandgap, acoustic wave modes are observed, characterized by in-phase motion of the hexagonal cells and resonators (Fig. 3.4(q,r)). Within the first bandgap, the response is strongly attenuated (Fig. 3.4(s)), while above the bandgap optical wave modes appear, exhibiting out-of-phase motion between the resonators and the host structure (Fig. 3.4(t)).

To consistently determine the bandgap boundaries, a response amplitude threshold was applied to resonators located away from the excitation source and specimen boundaries. The threshold level was chosen to be sufficiently above the measurement noise floor while remaining insensitive to localized response variations caused by boundary effects or resonator-to-resonator variability. The same threshold criterion was applied uniformly across all measurements to ensure consistent bandgap identification.

Under increasing excitation amplitude, changes in the apparent bandgap width were observed. These changes are interpreted as amplitude-dependent modifications of the effective attenuation behavior arising from nonlinear dynamic effects in the finite structure, rather than as a direct shift of the linear Bloch band structure. Consequently, the observed bandgap widening reflects nonlinear modulation of wave transmission properties, rather than closed-loop or externally controlled tunability.

A similar sequence of acoustic, bandgap, and optical modes is observed around the second and third bandgaps, as illustrated in Fig. 3.5. These observations confirm the

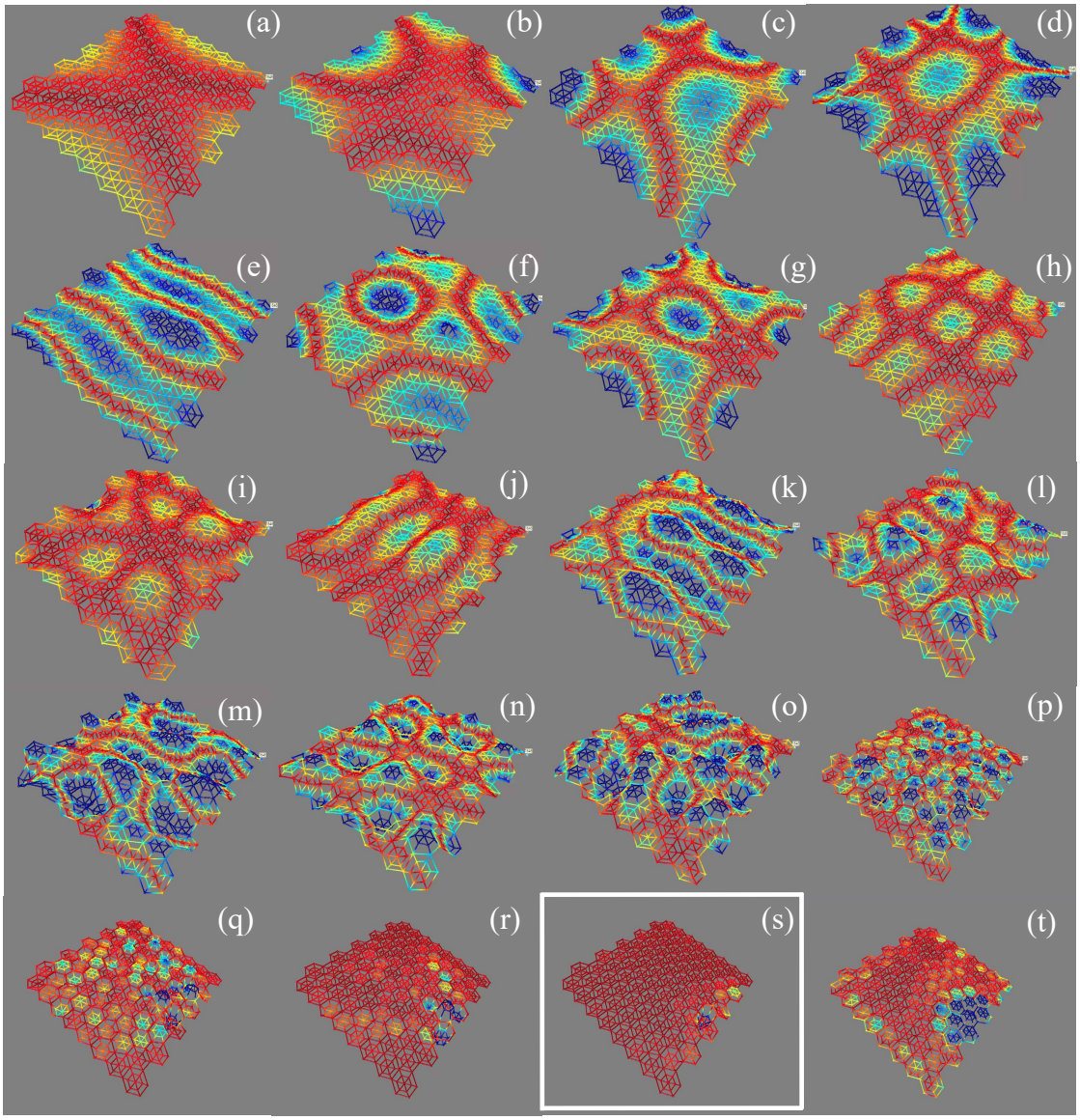


Figure 3.4: Experimentally acquired ODSs excited by the chirp signal provided by the PZT cylindrical patch. The selected ODSs were acquired at the following frequencies: (a) 0.0390625 kHz, (b) 0.0734375 kHz, (c) 0.1328125 kHz, (d) 0.2171875 kHz, (e) 0.234375 kHz, (f) 0.2765625 kHz, (g) 0.3234375 kHz, (h) 0.3953125 kHz, (i) 0.43125 kHz, (j) 0.4765625 kHz, (k) 0.5625 kHz, (l) 0.59375 kHz, (m) 0.640625 kHz, (n) 0.7078125 kHz, (o) 0.7609375 kHz, (p) 0.8546875 kHz, (q) 0.89375 kHz, (r) 0.921875 kHz, (s) 0.9734375 kHz (1st bandgap), and (t) 1.0984375 kHz.

presence of multiple locally resonant bandgaps arising from the interaction between the host lattice and the spider-web-like resonators.

Tab.3.1 summarizes the resonance frequencies and associated damping ratios extracted from experimental modal analysis of the SWR-I sample. The identified modal spectrum is dense, spanning a wide frequency range with closely spaced modes, which is characteristic of locally resonant metamaterials. The damping ratios exhibit significant variability, ranging from approximately 0.3% to over 11%, reflecting the coexistence of global lattice modes and highly dissipative local resonator modes.

Notably, clusters of modes are observed in the vicinity of the experimentally identi-

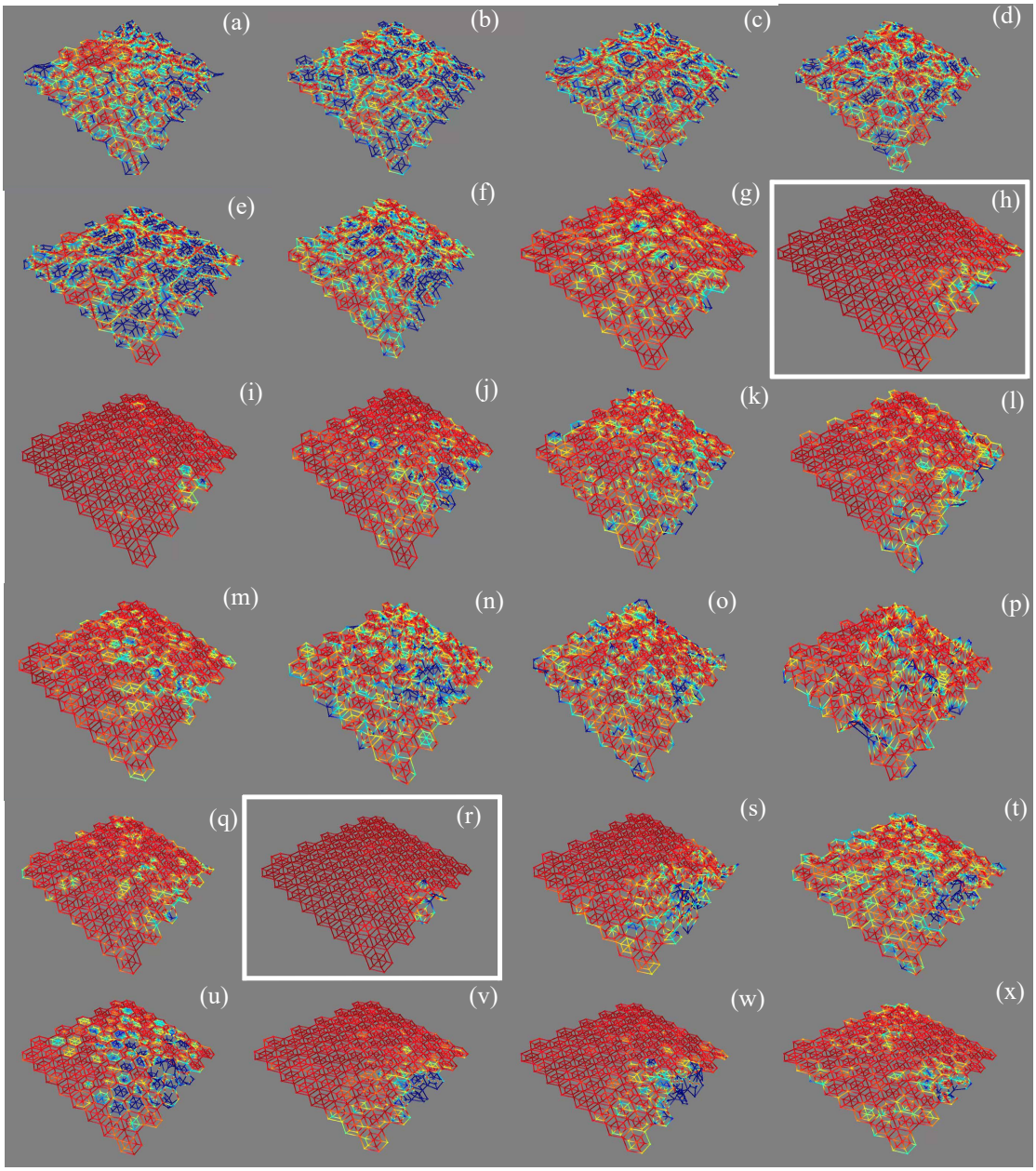


Figure 3.5: Experimentally acquired ODSs at the following frequencies: (a) 1.259375 kHz, (b) 1.3578125 kHz, (c) 1.4328125 kHz, (d) 1.578125 kHz, (e) 1.7296875 kHz, (f) 1.8609375 kHz, (g) 1.925 kHz, (h) 1.9953125 kHz (2nd bandgap), (i) 2.128125 kHz (j), 2.321875 kHz, (k) 2.4109375 kHz, (l) 2.5125 kHz, (m) 2.7046875 kHz, (n) 3.890625 kHz, (o) 4.0328125 kHz, (p) 4.1421875 kHz, (q) 4.4015625 kHz, (r) 4.653125 kHz (3rd bandgap), (s) 4.9234375 kHz, (t) 5.3734375 kHz, (u) 5.6625 kHz, (v) 7.6234375 kHz, (w) 7.6328125 kHz, and (x) 8.6328125 kHz.

fied bandgaps, indicating strong modal interactions near the acoustic–optical transition regions. These results provide quantitative support for the bandgap identification based on frequency response functions and operational deflection shapes, and highlight the influence of finite-size effects and modal coupling on the experimentally observed dynamic response.

Table 3.1: Resonance frequencies and associated damping ratios extracted from experimental modal analysis of the SWR-I metamaterial sample.

| Mode number | Frequency [Hz] | Damping ratio [%] | Mode number | Frequency [Hz] | Damping ratio [%] |
|---|---|---|---|---|---|
| 1 | 39.1 | 11.4853 | 19 | 2518.8 | 0.8144 |
| 2 | 73.4 | 3.2284 | 20 | 2703.09 | 1.1514 |
| 3 | 132.8 | 1.3980 | 21 | 3190.59 | 0.8096 |
| 4 | 218.8 | 0.7071 | 22 | 3471.9 | 0.9248 |
| 5 | 276.6 | 1.3281 | 23 | 3706.3 | 0.9563 |
| 6 | 325 | 0.7192 | 24 | 3895.3 | 1.2281 |
| 7 | 398.39 | 0.316 | 25 | 4039.09 | 0.9490 |
| 8 | 414.1 | 3.9185 | 26 | 4170.3 | 2.7970 |
| 9 | 484.3 | 1.0305 | 27 | 4412.5 | 1.1507 |
| 10 | 564.1 | 0.6278 | 28 | 4923.36 | 2.3518 |
| 11 | 640.6 | 0.5474 | 29 | 5670.32 | 2.1909 |
| 12 | 854.7 | 0.7153 | 30 | 5789.14 | 2.6185 |
| 13 | 1096.9 | 0.6064 | 31 | 5981.32 | 7.4791 |
| 14 | 1357.8 | 0.5648 | 32 | 6623.36 | 0.8599 |
| 15 | 1731.3 | 0.6137 | 33 | 7642.18 | 0.9821 |
| 16 | 1860.9 | 0.6132 | 34 | 7937.5 | 1.0946 |
| 17 | 2334.4 | 3.4889 | 35 | 8620.23 | 0.8876 |
| 18 | 2412.5 | 3.7467 | 36 | 8976.4 | 3.3979 |
| 37 | 9312.5 | 0.8154 | | | |

### 3.3.2 Investigation around bandgaps

An in-depth experimental analysis was conducted within a narrow frequency range around the bandgaps to closely observe the transition across each bandgap. To comprehensively characterize this transition and confirm the consistent pattern of acoustic wave modes preceding and optical wave modes following, we closely observed the local response of selected cells. In this analysis, a snapshot of the ODSs was superimposed onto the undeformed configuration, and the motion of each node was indicated by arrows. Each arrow had a bullet on the starting undeformed node, and its end coincided with the deformed node. Seven cells, positioned far from the excitation source, were chosen for examination. Near the first bandgap, the acoustic mode at 0.8547 kHz (Fig. 3.6 (a)) exhibited resonators excited in the first spider web axi-symmetric mode, with cells moving in phase. The ODSs of the first bandgap, possibly a topologically protected mode, was captured at 0.9953 kHz (Fig. 3.6 (b)). Beyond the bandgap, the optical mode at 1.2641 kHz featured out-of-phase motion components of the resonators with respect to the cells. The second bandgap, generated by the second spider web mode, displayed an acoustic mode at 1.8625 kHz (Fig. 3.6 (d)), where resonators were excited in the first skew-symmetric mode, resulting in rotational motion of the central mass. The ODSs of the second bandgap at 1.9859 kHz is shown in Fig. 3.6 (e). Subsequently, the optical mode at 2.3281 kHz is observed in Fig. 3.6 (f). The third bandgap, created by the second skew-symmetric resonator mode, featured an acoustic mode at 4.1016 kHz (Fig. 3.6 (g)), characterized by in-phase movement of the cell nodes and resonator nodes. The ODSs of the third bandgap

at 4.6578 kHz is shown in Fig. 3.6 (h), followed by the optical mode at 4.9234 kHz in Fig. 3.6 (i).

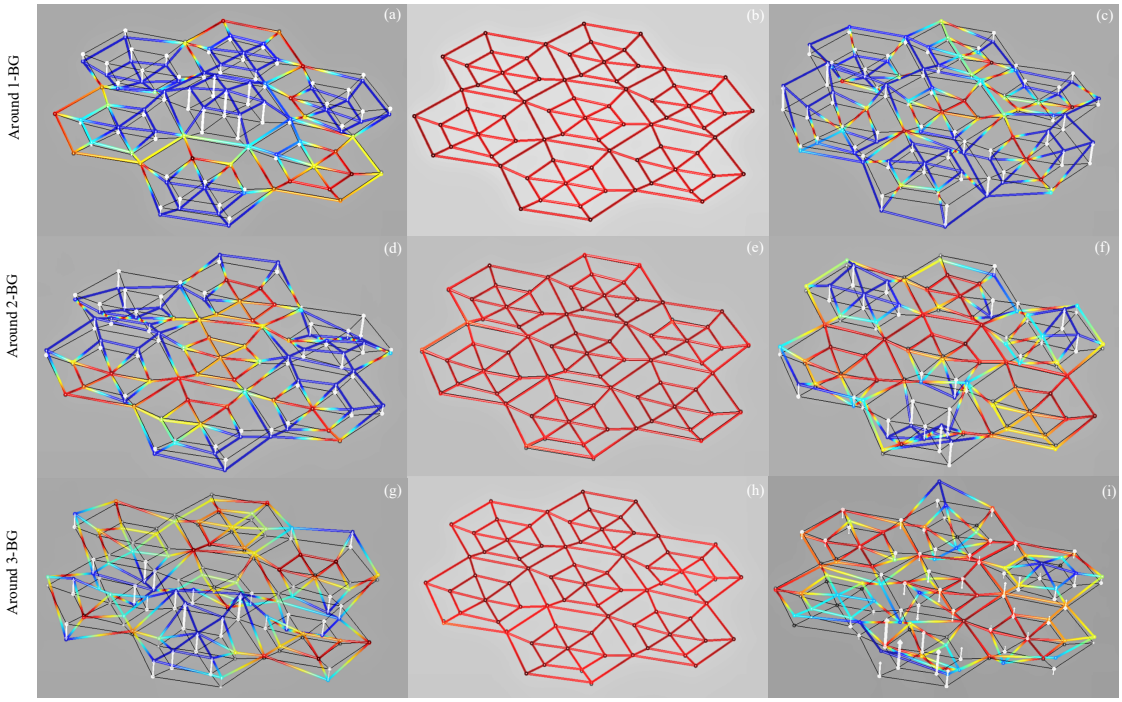


Figure 3.6: Passage across three bandgaps. 1st bandgap at 0.9953 kHz, (c) optical mode at 1.2641 kHz. Second bandgap: (d) acoustic mode at 1.8625 kHz, (e) response in the 2nd bandgap at 1.9859 kHz,(f) optical mode at 2.3281 kHz. Third bandgap: (g) acoustic mode at 4.1016 kHz, (h) response in the 3rd bandgap at 4.6578 kHz, (i) optical mode at 4.9234 kHz.

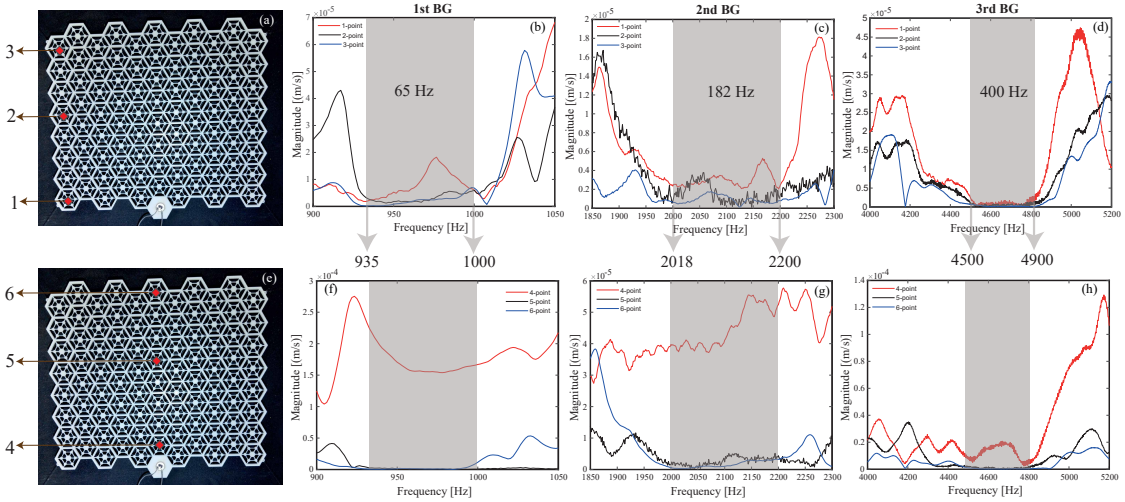


Figure 3.7: FRFs of two arrays of resonators first array (1,2,3) shown in part a, second array (4,5,6) shown in part e - around the 1st bandgap (b,f,j), the 2nd bandgap (c,g,k), and the 3rd bandgap (d,h,l).

We also devised an experimental procedure to better identify the bandgap central frequency and width. Selected 2 arrays of 3 resonators (left and middle) as shown in Fig. 3.7 (a) and Fig. 3.7 (e). Obtained the FRFs of each resonator when the sample was subject to the chirp excitation with frequency spanning the range of each of the three

bandgaps, namely, [0.93 -0.95] kHz, [1.95 - 2.05 ] kHz, [4.5 - 4.75] kHz, for the first, the second and the third bandgap, respectively. The FRFs of each resonator central mass labelled 1, 2, 3 in Fig. 3.7 (a) when the frequency spans the range around the first, the second and the third bandgaps are shown in Fig. 3.7 (b),Fig. 3.7 (c), and Fig. 3.7 (d), respectively. The FRFs of each resonator central mass labelled 4, 5, 6 in Fig. 3.7 (e) when the frequency spans the range around the first, the second and the third bandgaps are shown in Fig. Fig. 3.7 (f), Fig. 3.7 (g), and Fig. 3.7 (h), respectively. By setting a threshold response amplitude for the cells away from the bottom boundary cells close to the excitation source, the frequency bandwidth for the bandgaps could be identified and is highlighted by the gray bands.

### 3.3.3 Characterization of the SWR-II with PZT

The SWR-II specimen was fabricated using an FDM 3D printer. In this configuration, the hexagon thickness was intentionally designed to be non-uniform in the CAD model (Fig.3.2(b)) in order to introduce a controlled spatial stiffness variation. In addition, the printed specimen exhibited localized fabrication-induced defects, most notably near the top row (Fig.3.2(a)), which further increased geometric variability. The specimen measures $274 \times 260.96 \times 3.5$ mm$^3$ and consists of an $8 \times 9$ array of hexagonal unit cells. Each axially symmetric unit cell hosts a central mass and six secondary masses connected to the hexagon vertices through slender compliant ligaments (Fig. 3.2(b)). Full-field PSV measurements were performed using a total of 730 scan points distributed at the hexagon vertices and on the central and secondary resonator masses (Fig. 3.8(a)). The acquisition parameters were set to three complex averages, 10 kHz bandwidth, a frequency range of 0.01-4 kHz, decoder velocity of 2.5 m/s, and an excitation voltage of approximately 180 V.

Post-processing of the measured velocity field yielded the operational deflection shapes (ODSs) and the spatially averaged frequency response function (FRF), shown in Fig. 3.8(c). Two bandgaps were identified and are highlighted by the grey shaded regions. A zoomed view of the low-frequency range (Fig. 3.8(d)) shows a clear bandgap between approximately 0.550- 0.600 kHz. A representative set of experimentally acquired ODSs is presented in Fig. 3.9. At low frequencies, the response is dominated by global honeycomb-type modes in which the resonators follow the host motion (Fig. 3.9(a-i)). With increasing frequency, in-phase acoustic modes are observed (Fig. 3.9(k-p)), followed by a strongly attenuated response within the first bandgap (Fig. 3.9(q)). Above the bandgap, optical modes emerge in which the resonators oscillate out of phase with the hosting lattice (Fig. 3.9(r-s)).

Tab.3.2 reports the resonance frequencies and damping ratios extracted from experimental modal analysis of the SWR-II sample. Compared to the baseline SWR-I configuration, the modal spectrum of SWR-II exhibits increased irregularity in frequency spacing

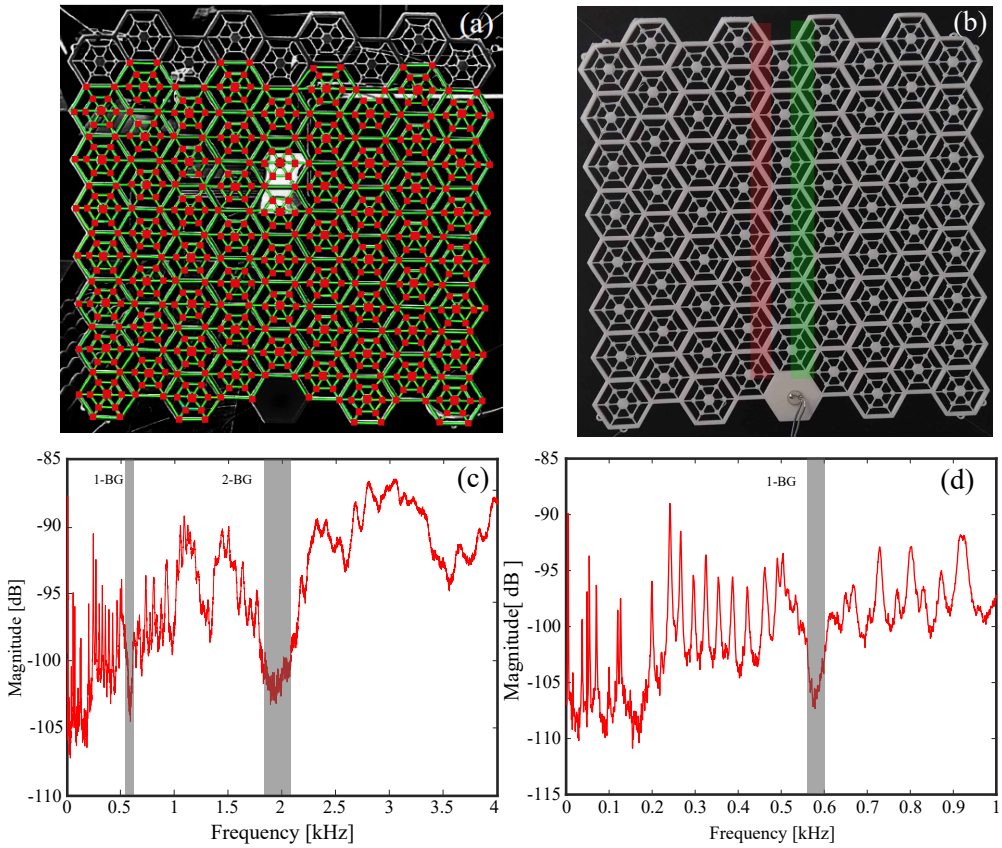


Figure 3.8: (a) Snapshot of the SWR-II sample with scan points highlighted in red, (b) close-up view highlighting the designed thickness non-uniformity and fabrication-induced deviations, (c) spatially averaged FRF over the range $[0, 4]$ kHz, and (d) zoom of the range $[0, 1]$ kHz.

Table 3.2: Resonance frequencies and associated damping ratios extracted from experimental modal analysis of the SWR-II metamaterial sample.

| Mode number | Frequency [Hz] | Damping ratio [%] | Mode number | Frequency [Hz] | Damping ratio [%] |
|---|---|---|---|---|---|
| 1 | 37.5 | 1.583 | 18 | 729.39 | 0.556 |
| 2 | 53.79 | 0.504 | 19 | 800 | 0.708 |
| 3 | 70 | 0.827 | 20 | 872.5 | 0.601 |
| 4 | 126.9 | 0.550 | 21 | 916.89 | 1.053 |
| 5 | 199.4 | 0.510 | 22 | 1019.4 | 0.657 |
| 6 | 241.3 | 0.485 | 23 | 1050 | 0.629 |
| 7 | 266.3 | 0.459 | 24 | 1085 | 0.664 |
| 8 | 269.89 | 0.641 | 25 | 1117.5 | 1.765 |
| 9 | 325 | 0.488 | 26 | 1140.59 | 1.839 |
| 10 | 386.89 | 0.553 | 27 | 1176.3 | 5.397 |
| 11 | 421.3 | 0.503 | 28 | 1300.5 | 1.218 |
| 12 | 461.3 | 0.564 | 29 | 1433.8 | 1.506 |
| 13 | 503.8 | 0.535 | 30 | 1496.3 | 0.609 |
| 14 | 533.1 | 5.435 | 31 | 1626.9 | 0.605 |
| 15 | 559.3 | 1.510 | 32 | 1695 | 0.831 |
| 16 | 617.5 | 2.091 | 33 | 1760 | 0.633 |
| 17 | 668.1 | 0.851 | | | |

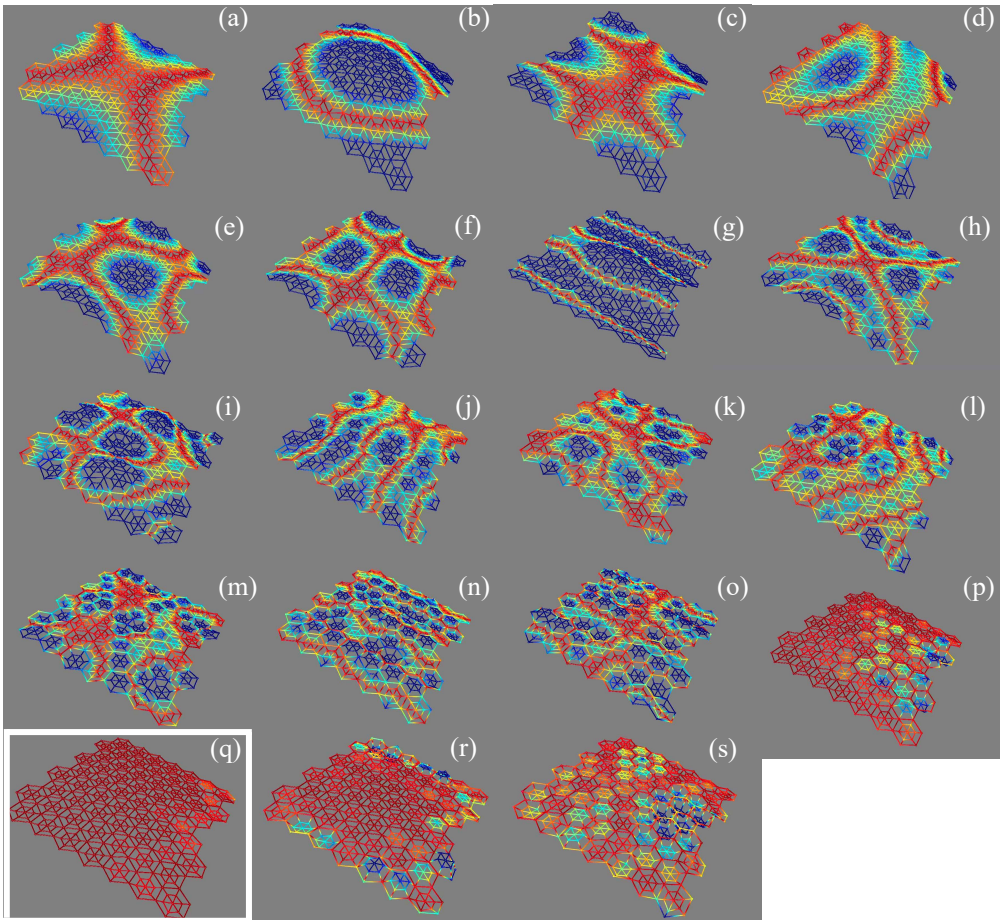


Figure 3.9: Experimentally acquired ODSs at frequencies: (a) 0.0375 kHz, (b) 0.053 kHz, (c) 0.0703 kHz, (d) 0.1203 kHz, (e) 0.1266 kHz, (f) 0.2 kHz, (g) 0.2414 kHz, (h) 0.2969 kHz, (i) 0.325 kHz, (j) 0.3539 kHz, (k) 0.3859 kHz, (l) 0.4219 kHz, (m) 0.4625 kHz, (n) 0.493 kHz, (o) 0.505 kHz, (p) 0.5516 kHz, (q) 0.5805 kHz (1st bandgap), (r) 0.6203 kHz, and (s) 0.6555 kHz.

and a broader dispersion of damping ratios. These features are indicative of unit-to-unit variability and resonator detuning arising from the intentionally introduced geometric non-uniformity combined with fabrication-induced imperfections.

In particular, the absence of clear modal clustering at higher frequencies is consistent with the experimentally observed suppression of the third bandgap, as detuned resonators hinder the synchronized local resonance mechanisms required for well-defined acoustic-optical mode separation. The elevated damping observed in several modes further suggests enhanced energy dissipation associated with imperfect resonator coupling and local structural defects. Overall, the EMA results provide quantitative support for the reduced number of experimentally observed bandgaps in the SWR-II configuration.

### 3.3.4 Observed edgewaves in SWR samples

Edge-guided wave phenomena were experimentally observed in both the SWR-I and SWR-II samples, as illustrated in Fig. 3.10. In the SWR-I sample, edge waves appeared in the frequency range of approximately 0.97-1.09 kHz, i.e., immediately above the first

bandgap. Similarly, in the SWR-II sample, edge-localized responses were identified in the frequency range of approximately 0.62-0.65 kHz, also just beyond the first bandgap. As the excitation frequency exceeds the upper edge of the first bandgap, optical branches emerge and wave propagation in the bulk is strongly modified. At this transition, the finite boundaries of the specimen break the translational symmetry assumed in Bloch-wave theory, enabling vibrational energy to become preferentially localized along the specimen edges rather than being uniformly distributed throughout the lattice. Consequently, edge-guided modes are observed only above the first bandgap, whereas below it acoustic modes dominate and propagate freely through the bulk of the structure [84, 85, 86, 5].

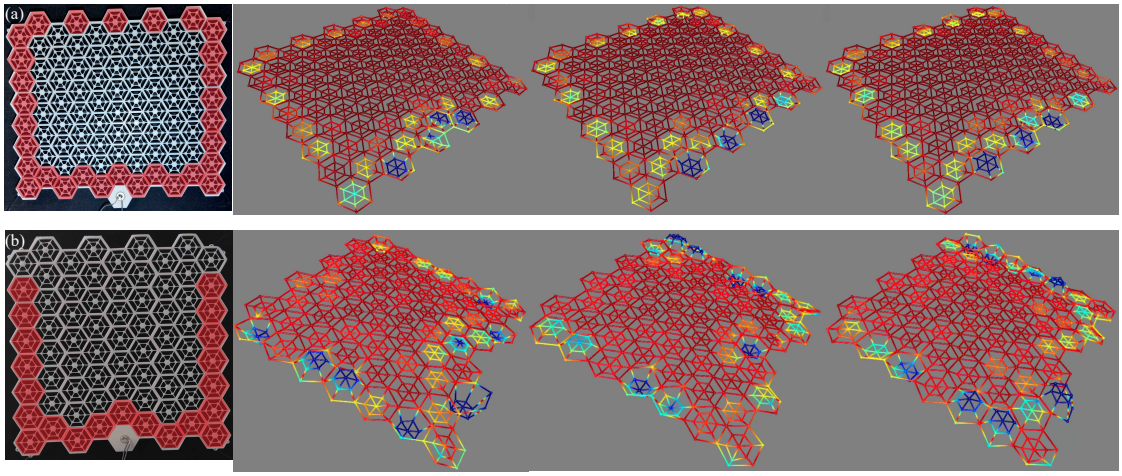


Figure 3.10: Snapshots of edgewaves in SWR samples exhibiting edge-localized modes after the first bandgap: (a) SWR-1 sample, edgewaves observed in the frequency range of approximately 0.97–1.09 kHz; (b) SWR-2 sample, edgewaves observed in the frequency range of approximately 0.62–0.65 kHz.

For the SWR-I sample, the observed edge waves exhibit stronger spatial confinement along the boundaries, whereas in the SWR-II sample they display a broader spatial distribution. This difference reflects variations in unit-cell geometry, stiffness non-uniformity, and resonator arrangement between the two configurations. The occurrence of edge-localized modes in this frequency regime is consistent with prior studies on elastic and acoustic metamaterials, which have shown that boundary-induced symmetry breaking in finite samples supports edge-guided wave propagation near bandgap transitions [87, 85, 86]

## 3.4 Bandgap via finite element model

The numerical investigation of elastic wave propagation and bandgap formation in the SWR-I, SWR-II unit cells using FEM. The simulations were performed in COMSOL Multiphysics using the Solid Mechanics Module and its Shell Interface. The objective of this analysis is to predict the frequency bandgaps that is, frequency ranges in which elastic waves cannot propagate through the structure. These bandgaps occur due to destructive interference and local resonance effects arising from the periodic arrangement of resonators in the metamaterial. To determine the presence of bandgaps, Bloch Flo-

quet periodic boundary conditions are applied to the unit cell geometry, enabling the calculation of eigenfrequencies for different wave vectors along the boundary of the irreducible Brillouin zone (IBZ). The resulting dispersion diagram (frequency versus wave vector) is then analyzed to identify frequency ranges where no propagating modes exist i.e., bandgaps.

The following sections describe the modeling approach, geometry, material parameters, simulation configuration, and interpretation of the obtained dispersion results.

### 3.4.1 Unit cell geometry

The SWR-I unit cell shown in Fig.3.11 consists of a hexagonal host matrix with lattice constant $LC = 26\,\text{mm}$. A primary resonator responsible for inducing local resonance band gaps is centered in the cell; its characteristic length is $R_{\text{res}} = 6\,\text{mm}$, and it is connected to the matrix by six slender ligaments of width 1 mm. Surrounding the primary resonator are six secondary (small) resonators of length $r_{\text{res}} = 3\,\text{mm}$, positioned at a radial offset $a = 3.04\,\text{mm}$ from the primary resonator. The secondary resonators are connected by slender hexagonal ligaments, as depicted in Fig. 3.11 (UC: SWR-I). All geometric parameters for SWR-I are listed in Tab.3.3. The host thickness is $th1 = 3\,\text{mm}$; the primary and secondary resonators have thickness $th2 = 1.5\,\text{mm}$; and the slender beams have thickness $th3 = 0.5\,\text{mm}$.

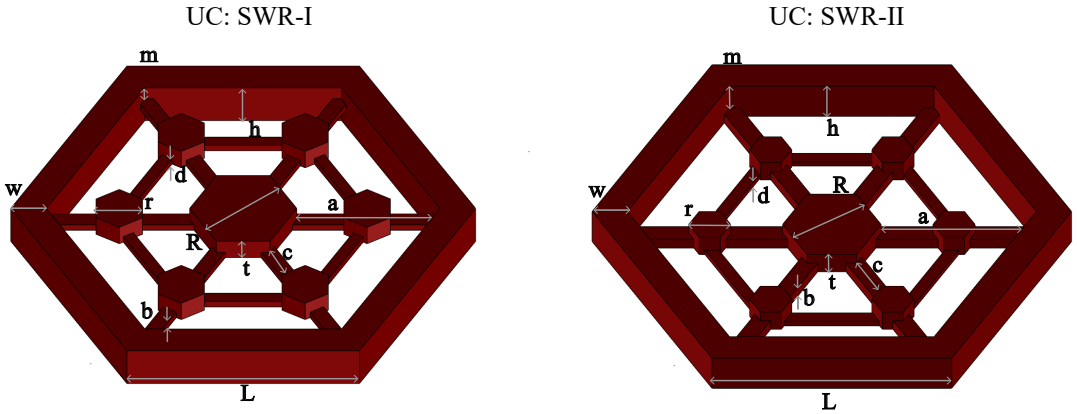


Figure 3.11: Detailed view of the unit-cell geometry with attached resonator for samples SWR-I and SWR-II. All geometric and material parameters of the unit cell and resonator are indicated in tab.3.3.

The SWR-II unit cell shown in Fig.3.11 comprises a hexagonal host matrix with lattice constant $LC = 34\,\text{mm}$. A primary resonator is centered in the cell with length $R_{\text{res}} = 7\,\text{mm}$ and is connected to the matrix through six slender ligaments of width 1 mm. Six secondary resonators of length $r_{\text{res}} = 3\,\text{mm}$ are placed at a distance $a = 4.23\,\text{mm}$ from the primary resonator and are connected by hexagonal slender ligaments, as shown in Fig.3.11 (UC: SWR-II). All geometric parameters for SWR-II are reported in Tab.3.3. The host thickness is $th1 = 3.5\,\text{mm}$; the primary and secondary resonators have thickness $th2 = 2\,\text{mm}$; and the slender beams have thickness $th3 = 0.5\,\text{mm}$.

Table 3.3: Geometrical dimensions of the unit cell samples

| Sample | $m$ [mm] | $b$ [mm] | $d$ [mm] | $h$ [mm] | $r$ [mm] | $R$ [mm] | $t$ [mm] | $a$ [mm] | $c$ [mm] | $W$ [mm] | $L$ [mm] | LC [mm] |
|---|---|---|---|---|---|---|---|---|---|---|---|---|
| SWR-I | 1.0 | 0.5 | 0.5 | 3.0 | 3.0 | 6.0 | 1.5 | 9.34 | 3.04 | 2.0 | 15.01 | 26 |
| SWR-II | 2.5 | 1.0 | 0.5 | 3.5 | 3.0 | 7.0 | 2.0 | 12.70 | 4.23 | 2.5 | 19.63 | 34 |

**Material Properties** Each unit cell was modeled as a single periodic domain, with Bloch–Floquet boundary conditions applied to opposite sides to represent an infinite array. The material used was polylactic acid (PLA) with the following properties:

$$\rho = 1240 \text{ kg/m}^3, \quad E = 2.685 \text{ GPa}, \quad \nu = 0.36.$$

### 3.4.2 Modeling approach and physics selection

The governing physics of this COMSOL-driven FEM analysis is the structural mechanics of plate-like structures, where the low-frequency dynamic response is dominated by flexural (out-of-plane) bending waves. Accordingly, COMSOL's Shell Interface was employed instead of a full three-dimensional solid mechanics formulation. This choice is justified because the shell approach (i) accurately captures the bending and transverse-shear kinematics that govern the behavior of plate-like media, and (ii) reduces the computational domain by one spatial dimension, resulting in significant efficiency gains [88].

**Reasons for using the shell model**

1. **Computational Efficiency:** The shell formulation reduces the problem dimensionality, substantially lowering the number of degrees of freedom while maintaining accurate representation of the physical response.

2. **Physical Fidelity for Thin Plates:** Shell theories, such as Kirchhoff–Love (for thin plates) and Reissner–Mindlin (for moderately thick plates), inherently capture bending and transverse shear deformation, making them particularly suitable for modeling low-frequency flexural waves and local resonance phenomena.

Distinct thickness values were assigned to the hosting plate, resonators, and connecting ligaments to represent the multi-layered structure accurately. A free triangular mesh was applied to the two-dimensional geometry, with local mesh refinement around the resonators and slender connections to ensure accurate resolution of stress concentrations and deformation gradients.

### 3.4.3 Wave vector path and Bloch-Floquet boundary conditions

The simulation core is an eigenfrequency analysis coupled with a parametric sweep. Periodic boundary conditions, as required by Bloch's theorem, were enforced via COMSOL's

Floquet Periodicity feature [89], which imposes

$$\mathbf{u}(\mathbf{r}+\mathbf{R}) = \mathbf{u}(\mathbf{r})\, e^{i\,\mathbf{k}\cdot\mathbf{R}},$$

where $\mathbf{R}$ is a lattice translation vector and $\mathbf{k}$ is the Bloch wave vector.

The wave vector $\mathbf{k} = (k_x, k_y)$ was swept along the high-symmetry path of the first irreducuble Brillouin zone (IBZ):

$$\Gamma(0,0) \;\rightarrow\; K\big(\tfrac{4\pi}{3a},\,0\big) \;\rightarrow\; M\Big(\tfrac{\pi}{a},\,\tfrac{\pi}{\sqrt{3}\,a}\Big) \;\rightarrow\; \Gamma(0,0).$$

**Components of the wave vector k:**
Along the IBZ path $\Gamma \rightarrow K \rightarrow M \rightarrow \Gamma$, the components can be parameterized by a dimensionless variable $k \in [0,3]$ as

$$k_x(k) = \begin{cases} \dfrac{4\pi}{3a}\,k, & 0 \le k \le 1, \quad \Gamma \leftrightarrow K, \\ \dfrac{4\pi}{3a} - \dfrac{\pi}{3a}\,(k-1), & 1 < k \le 2, \quad K \leftrightarrow M, \\ \dfrac{\pi}{a} - \dfrac{\pi}{a}\,(k-2), & 2 < k \le 3, \quad M \leftrightarrow \Gamma, \end{cases}$$

$$k_y(k) = \begin{cases} 0, & 0 \le k \le 1, \quad \Gamma \leftrightarrow K, \\ \dfrac{\pi}{\sqrt{3}\,a}\,(k-1), & 1 < k \le 2, \quad K \leftrightarrow M, \\ \dfrac{\pi}{\sqrt{3}\,a}\,\big(1-(k-2)\big), & 2 < k \le 3, \quad M \leftrightarrow \Gamma. \end{cases}$$

$$k_i(0) = k_i(3), \qquad i \in \{x, y\}.$$

The dimensionless path parameter $k \in [0,3]$ with an increment of $\Delta k = 0.01$ was used. For each wave vector, the eigenfrequency solver extracted the first 30 eigenmodes to capture the relevant low-frequency behavior and identify potential bandgaps.

### 3.4.4 Eigenfrequency analysis and mode characterization

The eigenfrequency solver was configured to extract the first 30 modes at each $\mathbf{k}$-point, ensuring coverage of the low-frequency bands of interest and clear identification of possible bandgaps. Let the displacement field of the plate mid-surface be $\mathbf{u} = (u, v, w)^{\mathsf{T}}$, where $w$ is the transverse (out-of-plane) component. To quantify the bending (flexural) character of a computed Bloch mode, we monitor the following polarization indicator, defined over the unit cell mid-surface $\Omega$:

$$\eta_w \;=\; \frac{\texttt{intop1}\big(w^2\big)}{\texttt{intop1}(u^2+v^2+w^2)} \;\in\; [0,1], \tag{3.1}$$

where `intop1` denotes a COMSOL domain-integration operator restricted to $\Omega$. Values $\eta_w \approx 1$ indicate flexural (bending-dominated) modes, while $\eta_w \approx 0$ indicate predominantly in–plane (longitudinal/shear) modes.

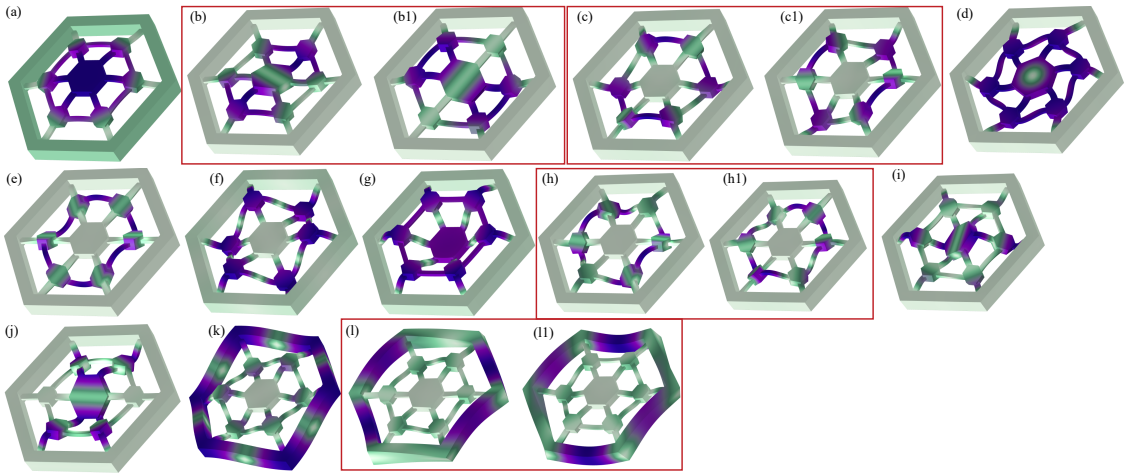


Figure 3.12: Eigenfrequencies and mode shapes obtained by COMSOL: (a) 1.0385 kHz, (b) 2.3578 kHz, (b1) 2.3579 kHz, (c) 5.4528 kHz, (c1) 5.4536 kHz, (d) 5.9655 kHz, (e) 6.1508 kHz, (f) 6.5067 kHz, (g) 6.8375 kHz, (h) 9.1182 kHz, (h1) 9.1189 kHz, (i) 9.3213 kHz (j) 9.324 kHz, (k) 10.166 kHz, (l) 10.591 kHz, and (l1) 10.591 kHz. The highlighted red box are belongs to complementary modes.

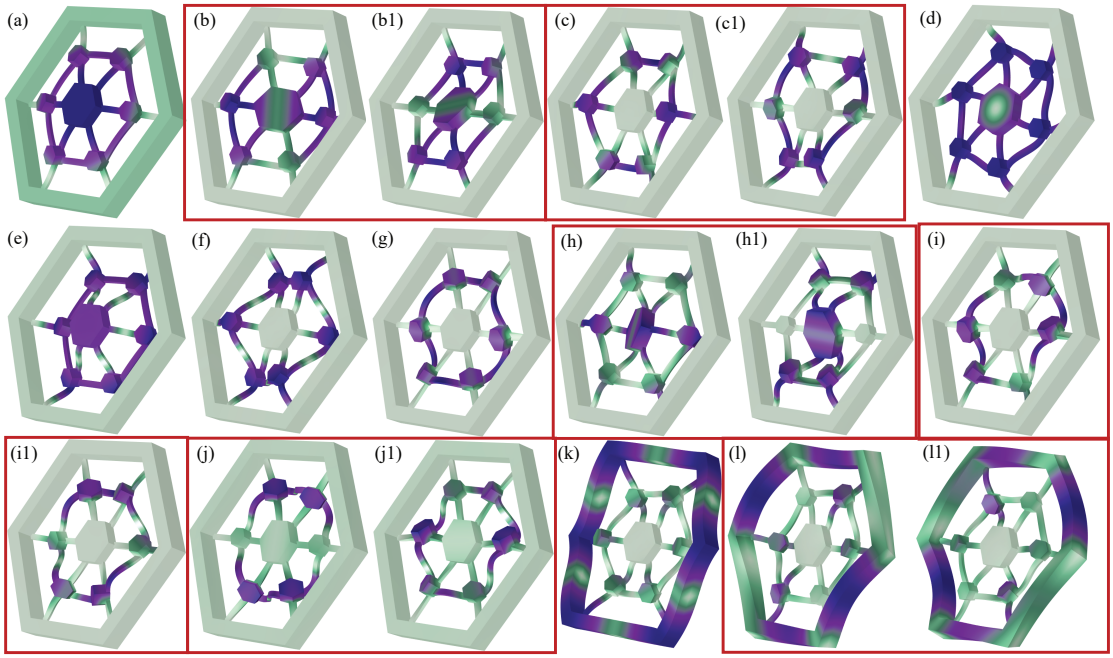


Figure 3.13: Eigenfrequencies and mode shapes obtained by COMSOL: (a) 0.49643 kHz, (b) 1.1867 kHz, (b1) 1.1868 kHz, (c) 2.5862 kHz, (c1) 2.5864 kHz, (d) 2.9663 kHz, (e) 3.016 kHz, (f) 3.1375 kHz, (g) 3.270 kHz, (h) 4.189 kHz, (h1) 4.1893 kHz, (i) 4.7501 kHz, (i1) 4.7503 kHz, (j) 6.4394 kHz, (j1) 6.440 kHz, (k) 6.9215 kHz, (l) 7.347 kHz, and (l1) 7.3471 kHz. The red boxes highlight companion modes.

Both SWR-I and SWR-II unit cells with embedded resonators were designed in COMSOL, the first 30 eigenmodes were then evaluated. The eigenfrequencies obtained by COMSOL for both samples are presented in Fig. 3.12 and Fig. 3.13. For the SWR-I sample, the first 16 eigenmode shapes and their corresponding eigenfrequencies are pre-

sented in Fig. 3.12. The first bending mode occurs at 1.0385 kHz. The second bending mode is axisymmetric, exhibiting companion mode shapes as shown in Fig. 3.12 (b, b1), with closely spaced frequencies of 2.3578 kHz and 2.3579 kHz, differing by only 0.1 Hz for numerical approximaton reasons. This degeneracy is characteristic of axi-symmetric structures, where companion axi-symmetric modes emerge in pairs with identical frequencies [5, 90]. Similarly, the third axi-symmetric mode, with companion mode shapes illustrated in Fig. 3.12 (c, c1), occurs at 5.4528 kHz and 5.4536 kHz, with a frequency separation of 0.8 Hz. The fourth mode is a flexural–rotational mode at 5.9655 kHz (Fig. 3.12 (d)), while the fifth mode is axi-symmetric at 6.1508 kHz (Fig. 3.12 (e)). The sixth and seventh modes are bending modes with frequencies of 6.5067 kHz and 6.6375 kHz (Fig. 3.12 (f,g)). The third pair of axi-symmetric modes appears at 9.1182 kHz and 9.1189 kHz (Fig. 3.12 (h,h1)). At higher frequencies, additional axi-symmetric rotational and complementary mode shapes are observed, as shown in Fig. 3.12 (i-l,l1).

For the SWR-II sample, the first 16 mode shapes and their corresponding eigenfrequencies are presented in Fig. 3.13. The first bending mode occurs at 0.4964 kHz. The second bending mode is axi-symmetric, with companion mode shapes illustrated in Fig. 3.13 (b, b1), occurring at 1.1867 kHz and 1.1868 kHz, differing by only 0.1 Hz. Again, this degeneracy arises from structural symmetry and is consistent with axi-symmetric paired modes [5, 90]. The third axi-symmetric mode, with companion modes shown in Fig. 3.13 (c, c1), occurs at 2.5862 kHz and 2.5864 kHz, with a separation of 0.2 Hz. The fourth mode is a flexural-rotational mode at 2.9663 kHz (Fig. 3.13 (d)). The fifth, sixth, and seventh modes are bending modes at 3.016 kHz, 3.1375 kHz, and 3.270 kHz (Fig. 3.13 (e-g)). The eighth mode is axi-symmetric at 4.189 kHz and 4.1893 kHz (Fig. 3.13 (h,h1)). As the frequency increases, further sets of companion axi-symmetric modes are observed, as illustrated in Fig. 3.13 (i-j1).

The occurrence of repeated axi-symmetric modes with very small frequency separations highlights the rotational symmetry of the resonator and indicates that these modes contribute significantly to the formation of bandgaps through mode coupling [5, 91, 16, 92]. The identification of bending, axisymmetric, and flexural–rotational modes is therefore essential in understanding the dynamic response and bandgap characteristics of both SWR-I and SWR-II unit cells.

### 3.4.5 Experiments versus FEM results

After performing a parametric sweep along the wave vector $\vec{k} = (k_x, k_y)$ using Eq. (5.1), FEM dispersion curves for the SWR-I and SWR-II samples were obtained, as shown in Fig. 3.14 (c, f), together with their associated mode shapes. The corresponding experimentally observed bandgaps are presented in Fig. 3.14 (b, e).

For the SWR-I sample, three bandgaps were identified from the FEM dispersion curves. The first bandgap, highlighted in orange in Fig. 3.14 (c), is associated with

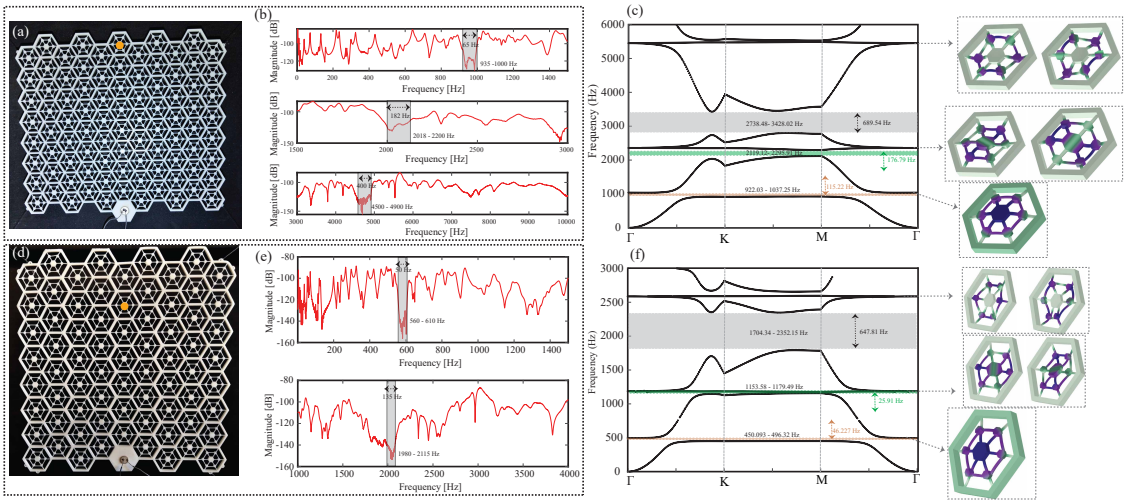


Figure 3.14: Comparison of experimentally observed bandgaps and numerical predictions for (a) SWR-I and (d) SWR-II. The left column shows the physical samples, the middle column (b, e) presents the experimentally measured FRFs, and the right column (c, f) shows the FEM-predicted dispersion curves with associated eigenmodes. Red curves correspond to the experimental responses of the resonator (orange dot) and the structure. Black curves denote the FEM-predicted dispersion relations. Shaded regions indicate bandgaps: gray regions in the FRFs represent experimentally observed bandgaps, while colored regions (orange, green, gray) in the dispersion plots denote FEM-predicted bandgaps.

optical modes above the gap. The FEM-predicted frequency range is 0.922-1.037 kHz, while the experimentally measured range is 0.935-1.000 kHz (Fig. 3.14 (b), top row). The second bandgap, highlighted in green, is also associated with axi-symmetric optical modes with companion modes (Fig. 3.14 (c)). The FEM-predicted frequency range is 2.119-2.296 kHz, whereas the experimental range is 2.018-2.200 kHz (Fig. 3.14 (b), middle row), yielding a reduced width of about 62 Hz. Companion modes, which often occur in degenerate pairs due to structural symmetry [5, 90], play a crucial role here: depending on their coupling, they can shrink the bandgap width, shift it, or in some cases cause the coalescence of multiple smaller gaps into a wider one [34]. The third bandgap, highlighted in gray, is formed between two axi-symmetric companion modes (Fig. 3.14 (c)). The FEM analysis predicts this gap in the range 2.738-3.428 kHz. However, the experimental data show a third bandgap at a much higher frequency range of 4.5-4.9 kHz (Fig. 3.14 (b), bottom row). Thus, the third bandgap does not align well with the FEM model.

For the SWR-II sample, three bandgaps were identified. The first bandgap, highlighted in orange in Fig. 3.14(f), is associated with the first mode bandgap, with a FEM-predicted range of 0.450–0.496 kHz. The second bandgap, highlighted in green, corresponds to axi-symmetric modes with companion shapes (Fig. 3.14(f)), and has a FEM-predicted range of 1.154–1.179 kHz. Companion modes are particularly important here, as their interaction can split or transition bandgaps [34]. The third bandgap, highlighted in gray, is formed between two axi-symmetric companion modes, with a FEM-predicted range of 1.704–2.352 kHz.

Experimentally, the first bandgap of the SWR-II sample was measured in the range

0.56-0.61 kHz (Fig. 3.14 (b), top row), showing good agreement with the FEM results. The second experimental bandgap was observed in the range 1.98-2.115 kHz (Fig. 3.14 (b), middle row), which does not match the FEM prediction but overlaps partially with the FEM third bandgap. This mismatch can be attributed to fabrication-induced imperfections in the finite sample (an $8 \times 9$ array of unit cells) suspended using nylon wire rope. Such irregularities detuned several resonators, mainly affecting skew-symmetric modes [91, 16]. By disrupting the synchronization of local resonances, these imperfections altered the bandgap range and likely prevented the formation of multiple well-defined bandgaps.

Overall, the first two bandgaps show acceptable agreement between FEM predictions and experimental results, whereas the third bandgap exhibits significant deviation. This discrepancy is primarily attributed to boundary effects: in the experiments, the SWR-I and SWR-II samples (finite arrays suspended using nylon wire rope) experienced finite-size and boundary compliance, while the FEM model was based on an idealized unit cell with periodic boundary conditions [92].

## 3.5 Frequency response curves

To investigate the dynamic behavior of the locally resonant system, a transverse harmonic base excitation was applied. The excitation frequency was swept both upward and downward in discrete steps around the resonance of the spider-web unit-cell resonator. At each frequency step, the steady-state response was recorded, and the peak displacement amplitude was extracted to construct frequency response curves (FRCs), relating oscillation amplitude to excitation frequency. One accelerometer was used for control, while two laser displacement sensors were employed: one to measure the resonator displacement amplitude and the other to measure the shaker displacement amplitude. This configuration enabled the relative displacement amplitude to be determined for the construction of the FRCs. Multiple frequency sweeps were performed at increasing acceleration levels, with the excitation amplitude held constant across all frequencies within each sweep.

Excitation was provided by a MADE 500 shaker (Fig. 3.15), capable of generating accelerations up to $30\,g$ and frequencies up to 6 kHz. The shaker was controlled using LMS software (Siemens), and its input was monitored by a PCB piezoelectric accelerometer with a measurement range up to $50\,g$. Resonator displacement was measured using a Micro-Epsilon optoNCDT 1220 laser sensor, featuring a 10 $\mu$m measurement range and approximately 0.01% repeatability. A second laser sensor was mounted on the shaker head expander to record the input excitation displacement. Both displacement and acceleration signals were recorded simultaneously using LabVIEW software. A schematic of the experimental setup is shown in Fig. 3.15.

Based on the bandgaps identified using the PSV system, the specimen was mounted on the shaker expander, and a representative unit cell with its resonator was selected for

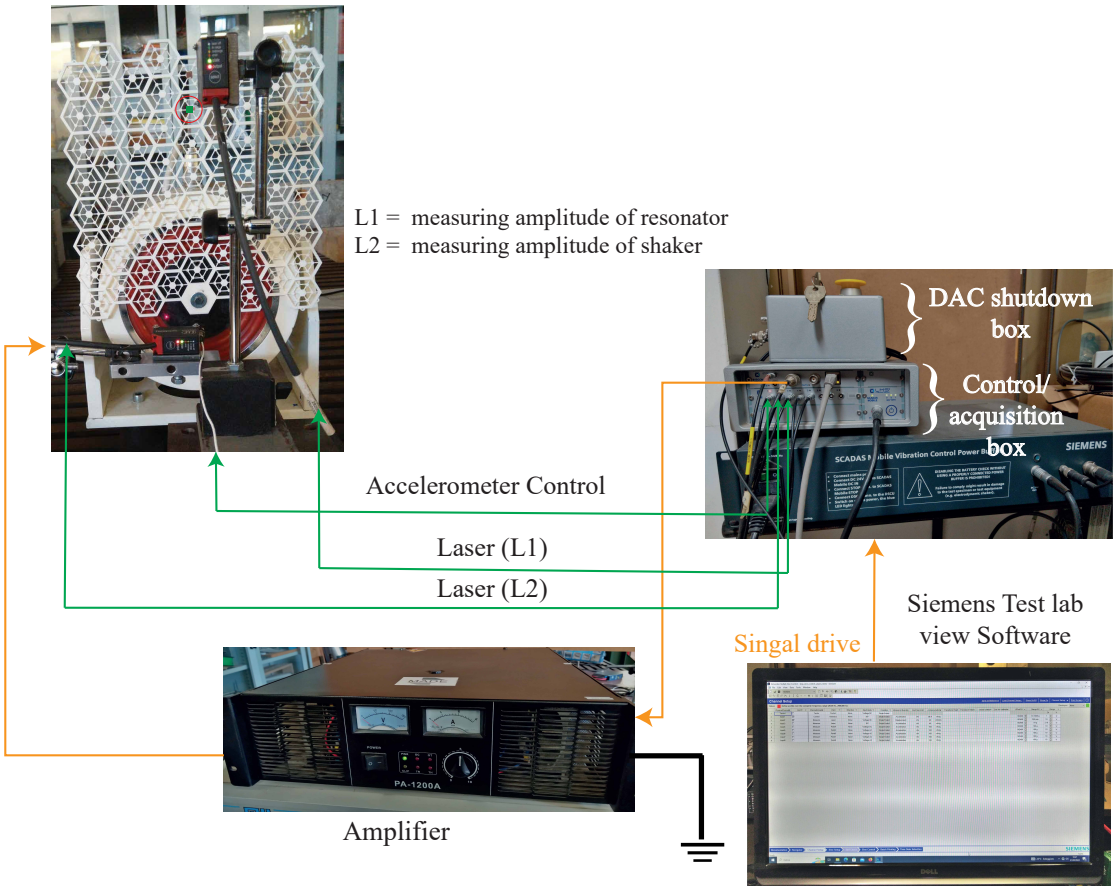


Figure 3.15: Schematic of the test setup used to obtain frequency response curves (FRCs) with laser sensors, where the spider-web resonator (SWR-II) metamaterial sample is clamped to the shaker expander. One laser is focused on the resonator (highlighted in green), while another laser is focused on the shaker head expander.

FRC measurements, as shown in Fig. 3.16. The PSV system was first used to acquire the FRF spectrum (Fig. 3.16(a)) to accurately locate the bandgap range. The SWR-II sample was then selected for FRC measurements in order to capture the nonlinear response of the resonator around the bandgap under increasing excitation amplitudes.

From the FRF spectrum, attention was focused on the acoustic mode within the bandgap region of the resonator (highlighted in green). This acoustic mode was identified in the frequency range 0.545-0.575 kHz, as shown in Fig. 3.16(b). At low excitation levels ($1g$-$2g$), the response was essentially linear. However, as the excitation amplitude increased ($3g$, $4g$, $6g$, $8g$, $10g$, $12g$, $14g$, and $16g$), the resonance frequency progressively shifted toward lower values. This leftward shift indicates a clear softening behavior of the acoustic mode with increasing excitation amplitude. Such nonlinear softening is commonly associated with local resonator dynamics and has been reported in similar metamaterial systems [93, 94, 95].

The identified bandgap range was 0.58-0.68 kHz. Following a similar experimental procedure, the excitation amplitude was varied from $4g$ to $22g$ in increments of $2g$ (Fig. 3.16(c)). It was observed that the bandgap width increased with excitation amplitude, indicating a nonlinear response. This widening was accompanied by a pronounced

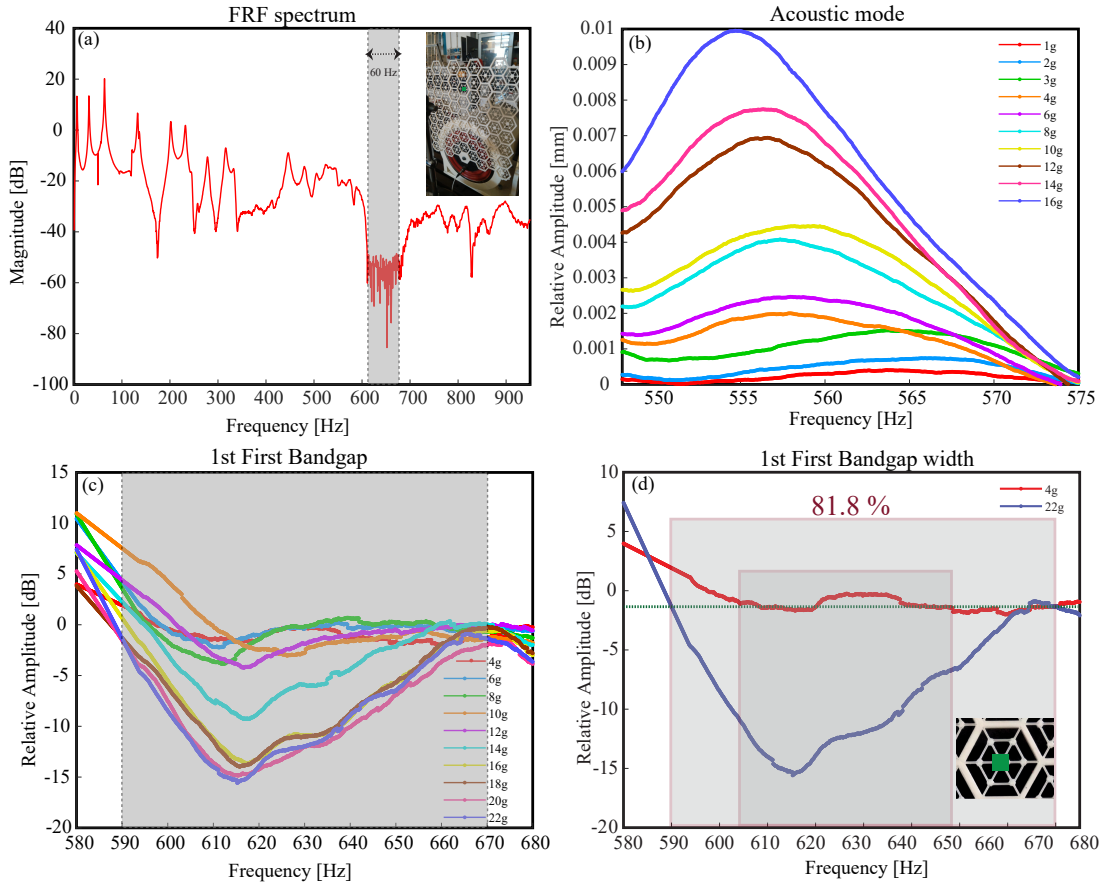


Figure 3.16: (a) FRF of the SWR-II sample with the large resonator (highlighted in green) obtained from the PSV system. (b) Resonator FRCs corresponding to the first acoustic mode under varying base excitation levels: 1g, 2g, 3g, 4g, 6g, 8g, 10g, 12g, 14g, and 16g. (c) Resonator FRCs within the first bandgap range under different base excitation amplitudes: 4g, 6g, 8g, 10g, 12g, 14g, 16g, 18g, 20g, and 22g. (d) Comparison of resonator response within the bandgap across excitation amplitudes, from the lowest (4g) to the highest (22g).

hardening effect, characteristic of geometric nonlinearity [96], and is consistent with theoretical studies on nonlinear locally resonant metamaterials reported by Lacarbonara and co-workers [93, 96, 97]. Within the bandgap region, the width increased progressively with excitation amplitude, reaching an expansion of approximately 81.8%, as shown in Fig. 3.16(d). These results demonstrate that nonlinear effects can be exploited to achieve amplitude-dependent modulation of bandgap characteristics. Such behavior has implications for adaptive wave-control and vibration-isolation applications, as nonlinear metamaterials allow bandgap properties to vary with excitation level, unlike linear metamaterials where bandgaps are fixed by geometry and material properties [98, 99, 100, 101].

To further investigate the nonlinear behavior of the resonator, a single unit cell was fabricated with dedicated supports to allow mounting on the shaker expander, as shown in Fig. 3.17(a). The unit cell was first characterized using the PSV system to obtain the FRF spectrum of the central resonator (highlighted in green). The FRF spectrum, shown in Fig. 3.17(a), indicates that the first linear resonance frequency occurs at 1.30938 kHz. FRCs were subsequently measured in the vicinity of this frequency, as

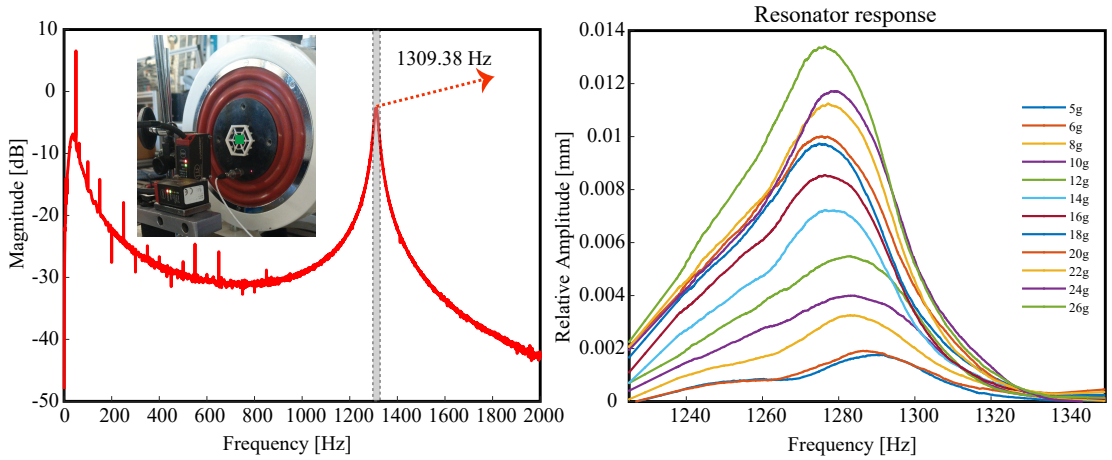


Figure 3.17: (a) FRF of the SWR-II unit cell sample, glued onto the shaker expander, with the large resonator highlighted in green. Data obtained from the PSV system. (b) FRCs of the first mode of the SWR-II resonator (highlighted in green) under excitation amplitudes of 5g, 6g, 8g, 10g, 12g, 14g, 16g, 18g, 20g, 22g, 24g, and 26g.

shown in Fig. 3.17(b).

In this configuration, the excitation amplitude was increased from $5g$ to $26g$ in increments of $2g$. Frequency sweeps performed at $5g$, $6g$, $8g$, $10g$, $12g$, $14g$, $16g$, $18g$, $20g$, $22g$, $24g$, and $26g$ revealed a distinct softening-type nonlinear response over the frequency range 1.225-1.350 kHz. Up to $16g$, the softening effect was clearly pronounced; beyond this level, the nonlinear response became more stable and was accompanied by a further increase in oscillation amplitude. This behavior is consistent with amplitude-dependent dynamics reported for nonlinear locally resonant metamaterials and is typically associated with Duffing-type nonlinearities arising from negative cubic stiffness terms [102].

To further examine nonlinear effects at the structural level, FRC measurements were extended to both the SWR-II and SWR-I samples, focusing on their global mode shapes. Snapshots of the specimens with the monitored resonators highlighted are shown in Fig. 3.18(a,c). FRF spectra were obtained for both samples, and the fourth global mode was selected for detailed investigation. Attempts to measure FRCs for the first three global modes were unsuccessful, as displacement amplitudes exceeding approximately 1.4 mm caused contact between the specimen and the shaker expander. Consequently, the analysis focused on the fourth global mode, with resonance frequencies of 0.132875 kHz for the SWR-II sample and 0.131875 kHz for the SWR-I sample. Well-defined FRCs were obtained around these frequencies.

For the SWR-II sample, FRCs were measured over the frequency range 0.129-0.135 kHz. At low excitation levels ($0.5g$ and $0.75g$), the response remained linear. As the excitation amplitude increased from $1g$ to $7g$ in increments of $1g$, the global mode exhibited a clear softening behavior, manifested by a leftward bending of the resonance peak. This behavior is characteristic of Duffing-type nonlinearities associated with negative cubic stiffness [102].

In contrast, for the SWR-I sample, FRCs were measured over the frequency range

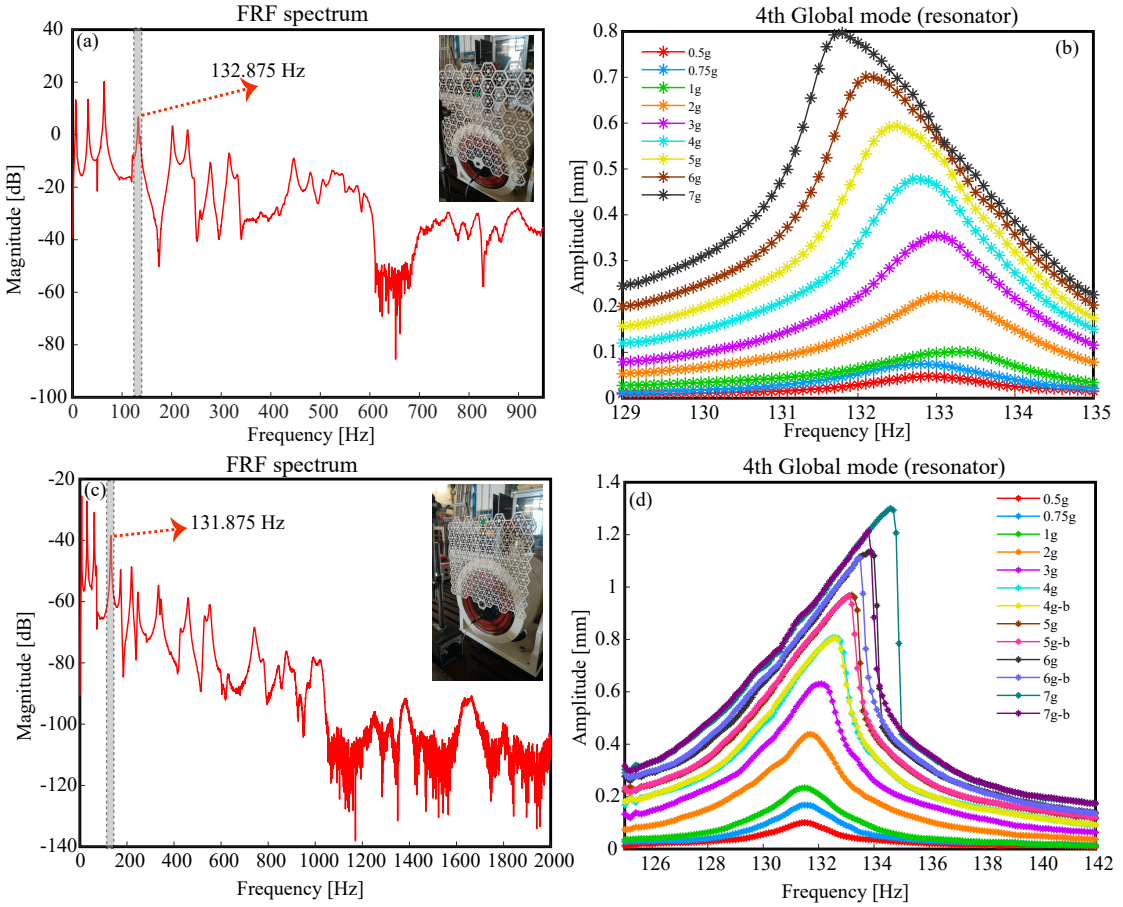


Figure 3.18: (a) Frequency response function of the SWR-II sample with the large resonator (highlighted in green), obtained from the PSV system. (b) Resonator frequency response curves (FRCs) of the SWR-II sample under varying base excitation levels: 0.5g, 0.75g, 1g, 2g, 3g, 4g, 5g, 6g, and 7g. (c) Frequency response function of the SWR-I sample with the large resonator (highlighted in green), obtained from the PSV system. (d) Resonator FRCs of the SWR-I sample under varying base excitation levels: 0.5g, 0.75g, 1g, 2g, 3g, 4g, 4g-b, 5g, 5g-b, 6g, 6g-b, 7g, and 7g-b.

0.124-0.142 kHz. The response remained linear at low excitation levels ($0.5g$, $0.75g$, and $1g$). As the excitation amplitude increased from $2g$ to $7g$ in increments of $1g$, the global mode response exhibited a pronounced hardening behavior attributed to geometric nonlinearities. During forward sweeps at $4g$ and $7g$, transitions from high-amplitude resonant states to low-amplitude non-resonant states were observed, indicating bistability. To capture additional stable response branches, backward sweeps ($4g$-b to $7g$-b) were also conducted. This behavior is consistent with the nonlinear response of cantilever-like structures composed of linear elastic materials, where geometric nonlinearities dominate [96].

Overall, the nonlinear dynamics of the fourth global mode reveal a clear contrast between the two configurations: the SWR-II sample exhibits softening-type nonlinearity, whereas the SWR-I sample displays hardening-type nonlinearity. Despite their similar design concepts, geometric scaling differences between the SWR-II and SWR-I unit cells lead to markedly different nonlinear responses, highlighting the strong sensitivity of non-

linear dynamic behavior to geometric parameters.

## 3.6 Summary

The dynamic responses of two additively manufactured spider web resonator (SWR) metamaterial configurations were investigated in this chapter. Two designs were considered: a baseline configuration (SWR-I) with nominally uniform geometry, and a modified configuration (SWR-II) incorporating intentional geometric non-uniformity together with additional fabrication-induced deviations.

Experimental investigations using scanning laser vibrometry revealed that the baseline SWR-I configuration exhibits three distinct locally resonant bandgaps within the investigated frequency range. These bandgaps were consistently identified through averaged FRF analysis and visualizations of ODSs, which highlighted the characteristic transitions from in-phase acoustic modes to attenuation-dominated regions and subsequently to out-of-phase optical modes. Local FRF measurements performed at different lattice locations further confirmed the robustness and spatial coherence of these bandgaps.

In contrast, the SWR-II configuration exhibited only two clearly defined bandgaps. This reduction is attributed to the combined effects of the intentionally introduced geometric non-uniformity and additional fabrication-induced imperfections, which led to detuning of individual resonators and disrupted the synchronization required for the formation of multiple well-separated bandgaps. For the first two bandgaps, comparisons with finite element dispersion predictions showed reasonable agreement. Discrepancies observed at higher frequencies are primarily attributed to finite-size and boundary effects, as the numerical models assume idealized periodic unit cells, whereas the experimental specimens consist of finite arrays suspended under free-free conditions. The dynamic response was further influenced by complementary mode pairs arising from structural symmetry, which can narrow, shift, or merge bandgaps depending on their coupling characteristics [34].

Nonlinear dynamic behavior was also observed under increasing excitation amplitudes. In the SWR-I configuration, higher excitation levels activated geometric hardening effects, whereas the SWR-II configuration exhibited a pronounced softening-type nonlinear response, particularly in modes associated with the first bandgap. This softening behavior was corroborated through single unit-cell measurements and became more prominent with increasing excitation amplitude. Overall, the results demonstrate that bandgap behavior in spider web resonator metamaterials is governed by a coupled interplay between geometry, imperfections, boundary conditions, modal interactions, and nonlinear dynamics. While the present study provides experimental evidence of these effects, further investigation is required to fully characterize their relative contributions and to establish predictive design guidelines for nonlinear and imperfect locally resonant metamaterials.

# Chapter 4

# Experimental results: Edgewave in Locally Resonant Metamaterial

This chapter investigates edge-wave phenomena in a locally resonant metamaterial with a non-axially symmetric unit-cell geometry. Motivated by the observations reported in the previous Chapter 3, a new specimen was designed and fabricated in which the unit cell consists of a thin beam clamped to two sides of a hexagonal cell and coupled to a central resonator. This intentional departure from axial symmetry suppresses conventional locally resonant bandgaps and promotes boundary-localized dynamic behavior. Experimental investigations were conducted using scanning laser Doppler vibrometry to capture the operational deflection shapes of the structure under piezoelectric excitation. The measurements revealed the presence of edge-localized vibrational modes in the frequency range of approximately 0.90-1.120 kHz, characterized by energy confinement along the specimen boundaries rather than propagation through the bulk. To support the experimental findings and enable direct comparison, a finite element eigenfrequency analysis was performed using COMSOL Multiphysics. The numerical results show strong agreement with the experimentally observed edge-wave modes, confirming that the observed localization arises from boundary-induced symmetry breaking in the finite metamaterial structure.

## 4.1 Edgewave in locally resonant

The honeycomb sample unit cell, as depicted in Figure 4.1 (b), was crafted using 3D printing. This specific sample, featuring a 9x12 array of hexagonal cells showcased in Figure 4.1 (a), boasts a design that deviates from axial symmetry. Its dimensions measure $221.51 \times 249.13 \times 1.5$ mm$^3$. Defining the geometric properties of this honeycomb structure are several crucial parameters: $m = 1$ mm, $b = 0.5$ mm, $h = 1.5$ mm, $R = 6$ mm, $t = 3$ mm, $a = 7$ mm, $w = 3$ mm, and $L = 15.01$ mm. Unlike a conventional axially symmetric design, the sample central mass is supported by a single wire, introducing a departure

from symmetry.

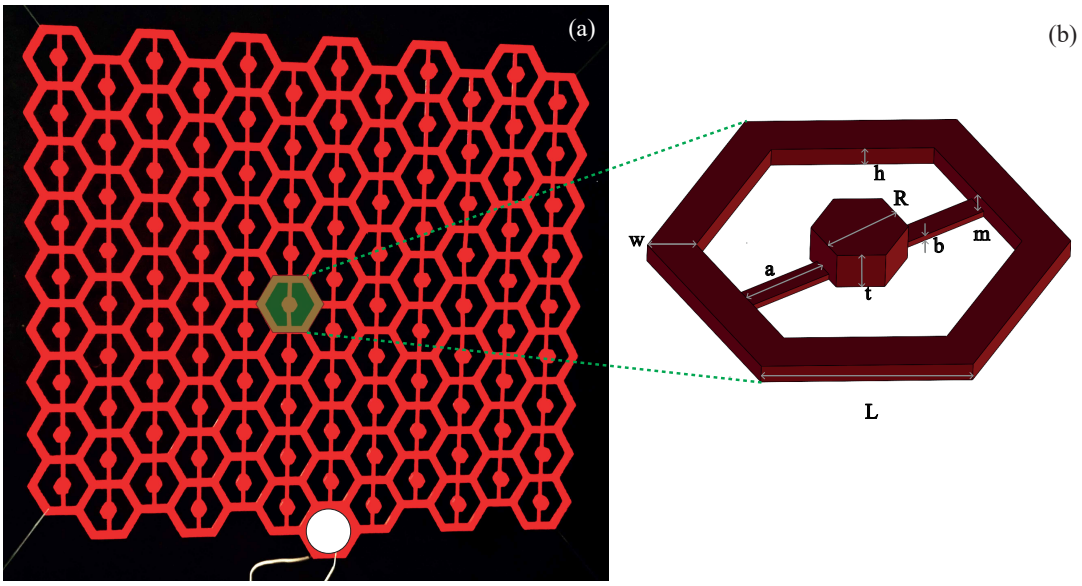


Figure 4.1: (a) Snapshots of metamaterial sample patched with PZT (highlighted in white color) (b) detailed view of the corresponding unitcell.

### 4.1.1 Characterization of LR with PZT

For the experimental campaign, employed a PSV system together with a PZT actuator and a linear amplifier. The scan grid diagram is shown in Figure 4.2(a). The parameters for acquiring the PSV data were set as follows: a total of three complex averages, a bandwidth of 4 kHz, an operating frequency range of 0.01-4 kHz, 792 scan points, a decoder velocity of 2.5 m/s, and an actuation voltage of 180 V.The frequencies and damping ratios obtained from the Polytec modal analysis software, Polywave, are documented in Tab.4.1. An intriguing phenomenon known as the edge wave has been observed in this particular sample, as highlighted in Figure 4.2 (d).

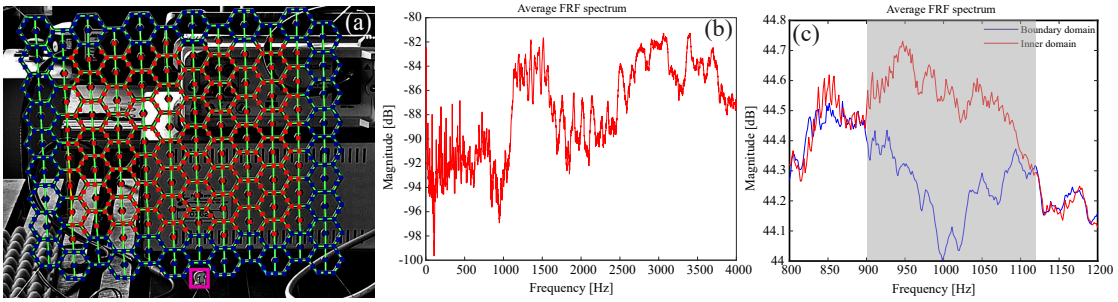


Figure 4.2: (a) Snapshot of the sample with scan points highlighted in blue for the boundary unit cells and in red for the inner domain (b) spatially averaged frequency response function (FRF) of the sample (c) frequency range highlighting the edge-wave-affected region, where the blue curve corresponds to the boundary domain and the red curve corresponds to the inner domain.

The results obtained from the PSV analysis are presented in the FRF plots. As shown in Fig.4.2(c), no clear bandgap is observed. However, an intriguing feature emerges in

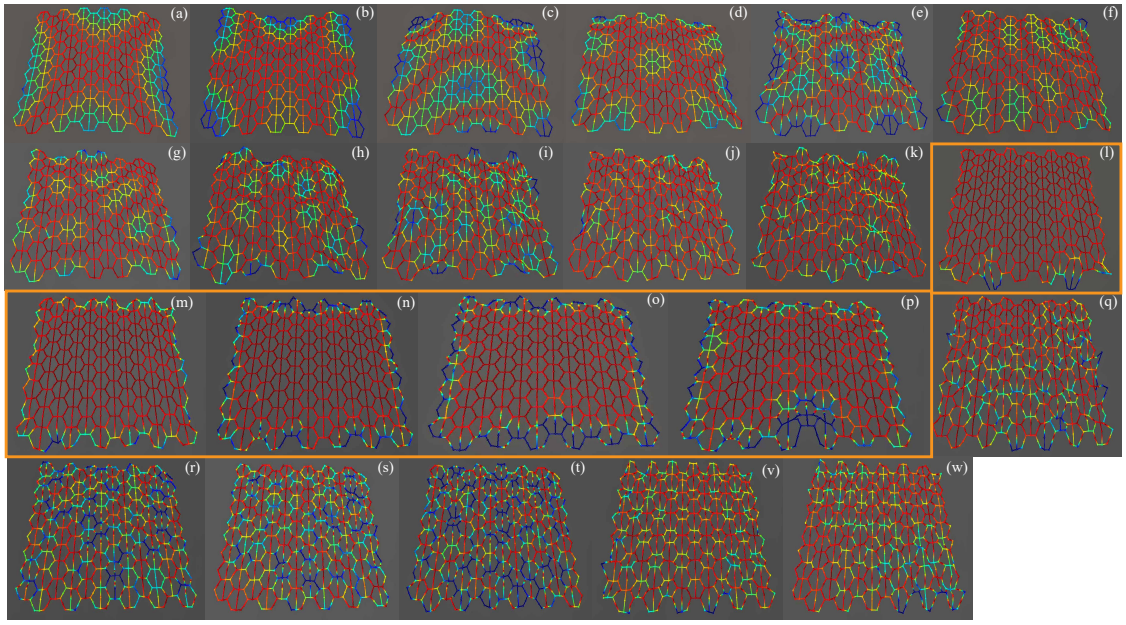


Figure 4.3: Experimentally acquired ODSs and frequencies of the 3D printed of the sample excited by a PZT cylindrical patch. Snapshots of a few selected ODSs having frequencies: (a) 0.0266 kHz, (b) 0.05 kHz, (c) 0.081 kHz, (d) 0.1343 kHz, (e) 0.1953 kHz, (f) 0.2406 kHz, (g) 0.2593 kHz (h) 0.3396 kHz (i) 0.43906 kHz (j) 0.6848 kHz (k) 0.7234 kHz (l) 0.9047 kHz (m) 0.9406 kHz (n) 0.9719 kHz (o) 0.9984 kHz (p) 1.0203 kHz, (q) 1.1753 kHz (r) 1.1890 kHz (s) 1.2731 kHz (t) 1.9 kHz, (v) 2.12 kHz and (t) 2.4 kHz. Edge wave modes, highlighted in orange, are visible in the ODS plots from (l) to (p).

the FRF illustrated in Fig.4.2(d): within a distinct frequency range, the response of the inner cells decreases while the kinetic energy remains confined to the boundary cells. This observation strongly suggests the presence of edgewaves, indicating that wave energy propagates preferentially along the boundaries of the metamaterial. Such interactions between waves and boundaries give rise to localized edge modes, a phenomenon commonly referred to as mode localization. To further illustrate this, Fig.4.3 presents a selection of experimentally acquired ODSs. The lowest mode shapes, shown in Fig.4.3(a)–(c), correspond to global honeycomb modes in which the resonators undergo rigid displacement. In contrast, Fig.4.3(l)–(o) clearly demonstrate the occurrence of edgewaves.

Tab.4.1 reports the resonance frequencies and damping ratios extracted from the experimental modal analysis. The results show a dense cluster of modes in the vicinity of the experimentally observed edge-wave region. In particular, modes 14-16 occur at approximately 0.97-1.02 kHz, which overlaps the frequency interval where boundary-localized responses were detected in the FRF and confirmed by the ODSs. This concentration of nearby modes is consistent with the emergence of boundary-dominated dynamics in finite metamaterial specimens. Moreover, the measured damping ratios exhibit noticeable variability across modes, indicating non-uniform dissipation and coupling conditions between the boundary and the interior domains. In this chapter, the EMA results are therefore used primarily to support frequency localization of the edge wave regime and to complement the spatial evidence provided by the ODSs.

Table 4.1: Resonance frequencies and damping ratios extracted from experimental modal analysis of the finite honeycomb metamaterial sample used for the edge-wave study.

| Mode number | Frequency [Hz] | Damping ratio [%] | Mode number | Frequency [Hz] | Damping ratio [%] |
|---|---|---|---|---|---|
| 1 | 26.6 | 2.377 | 14 | 971.8 | 3.915 |
| 2 | 50 | 1.24 | 15 | 998.3 | 2.005 |
| 3 | 81.29 | 0.742 | 16 | 1021.9 | 0.469 |
| 4 | 132.8 | 1.187 | 17 | 1192.2 | 0.826 |
| 5 | 195.3 | 0.430 | 18 | 1282.8 | 0.928 |
| 6 | 260.89 | 0.462 | 19 | 1353.09 | 0.533 |
| 7 | 340.6 | 0.404 | 20 | 1462.5 | 1.164 |
| 8 | 439.1 | 0.558 | 21 | 1512.5 | 0.915 |
| 9 | 479.6 | 2.051 | 22 | 1756.3 | 0.812 |
| 10 | 567.2 | 1.740 | 23 | 1906.3 | 0.517 |
| 11 | 687.5 | 1.047 | 24 | 1906.3 | 0.517 |
| 12 | 723.3 | 0.509 | 25 | 1906.3 | 0.517 |
| 13 | 812.5 | 1.581 | | | |

### 4.1.2 Numerical model for edgewave

A finite element analysis (FEA) was carried out to investigate the possibility of unfolding edge or boundary wave mode shapes. The analysis was performed in COMSOL Multiphysics, using PLA material properties with a mass density of 1,240 kg/m$^3$, a Young's modulus of 2.685 GPa, and a Poisson's ratio of 0.36. A mesh consisting of tetrahedral elements was generated to discretize the geometry. The numerically obtained mode shapes were then compared with the experimentally acquired ODS, as shown in Fig. 4.4. In this figure, the top row corresponds to the experimentally measured mode shapes, while the bottom row presents the numerically simulated mode shapes obtained from COMSOL.

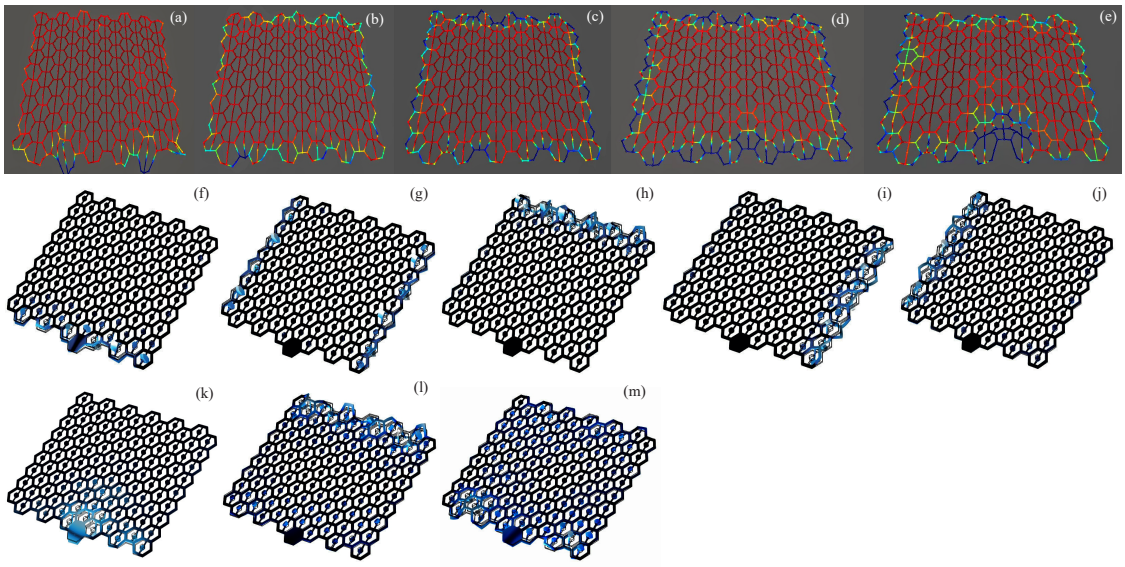


Figure 4.4: Experimentally acquired ODSs and frequencies of the 3D printed M3 sample excited by a PZT cylindrical patch. Snapshots edge wave region: (a) 0.9047 kHz, (b) 0.9406 kHz, (c) 0.9719 kHz, (d) 0.9984 kHz, (e) 1.0203 kHz. Numerically acquired eigen mode shapes (f) 0.91589 kHz, (g) 0.92328 kHz (h) 0.9551 kHz (i) 0.98198 kHz (j) 0.98198kHz (k) 1.0089 kHz (l) 1.0164 kHz (m) 1.0234 kHz.

The comparison between the numerical and experimental mode shapes revealed strong agreement within the edge-wave frequency range of 0.90-1.02 kHz. In this interval, both the simulated and experimentally measured ODSs exhibited similar boundary-localized characteristics, confirming that the FE model successfully reproduces the edge-guided behavior observed in the physical specimen. This close correspondence indicates that the numerical analysis not only captures the global dynamics of the metamaterial but also accurately reflects the subtle localization effects associated with edgewaves. Overall, the FE analysis provides reliable insights, and the observed agreement between simulation and experiment validates the modeling approach for investigating edge-mode phenomena in non-axially symmetric metamaterials. The edge wave can be interpreted as a localized vibrational mode, confined along the boundaries of the structure in contrast to bulk modes that distribute energy throughout the interior. This boundary localization is a defining feature of metamaterial dynamics and has been widely reported in prior studies, where edge-localized vibrational modes arise near bandgap transitions due to boundary induced symmetry breaking [87, 85, 84, 5].

The emergence of edgewaves and the associated edgewave effect plays a pivotal role in shaping the dynamic response and overall functionality of metamaterial structures. A comprehensive understanding of these phenomena is essential for the design and optimization of metamaterials in applications such as wave manipulation, energy harvesting, and vibration control. Recent studies have demonstrated that exploiting the localized resonances and scattering mechanisms inherent to edgewaves enables the development of novel strategies for tailoring wave propagation and achieving enhanced performance in engineered systems [103, 104, 85, 105]. By leveraging these mechanisms, researchers are opening new pathways for the realization of robust and versatile metamaterial based devices.

## 4.2 Summary

This chapter examined edge-wave phenomena in a locally resonant metamaterial featuring a non-axially symmetric unit-cell design. Unlike the locally resonator configurations discussed in Chapters 2 and 3, this metamaterial did not exhibit locally resonant bandgaps within the investigated frequency range. Instead, the dynamic response was dominated by edge-localized modes occurring between approximately 0.91-1.20 kHz.

Experimental measurements based on frequency response functions and operational deflection shapes demonstrated that vibrational energy became confined to the boundaries of the structure, while the response of the interior cells was strongly attenuated. These edge-wave modes exhibited distinct spatial patterns that differ fundamentally from the bandgap-related phenomena observed in the axially symmetric SWR samples discussed previously. Finite element eigenfrequency analyses performed using COMSOL Multi-

physics showed good agreement with the experimentally observed edge-wave modes, confirming that the measured boundary localization originates from the underlying structural asymmetry and finite-size effects. The results are consistent with previous studies reporting that edge-localized modes arise in metamaterial systems due to boundary-induced symmetry breaking near bandgap transitions [87, 85, 84, 5].

Overall, this chapter highlights that locally resonant metamaterials can exhibit fundamentally different wave phenomena depending on unit-cell symmetry and boundary conditions. While axially symmetric spider-web resonator lattices support locally resonant bandgaps, non-axially symmetric configurations may instead favor edge-wave localization, offering alternative mechanisms for wave confinement and boundary-guided energy transport.

# Chapter 5

# Experimental results: compositional disorder in periodic structures

This chapter presents the results of a collaborative study between Sapienza University of Rome and Roma Tre University. The electrospun membrane metamaterial specimens were fabricated at Roma Tre University under the supervision of Prof. Giulia Lanzara, Director of the Multifunctional Materials Laboratory, while the experimental dynamic characterization was conducted at Sapienza University of Rome. The samples were manufactured by electrospinning polymer fibers to form compliant membranes and by 3D printing axially symmetric hexagonal resonators subsequently attached to the membranes. Although the architecture is nominally periodic, unavoidable variations introduced during the electrospinning and assembly processes resulted in unit-to-unit differences in membrane density, stiffness, and resonator attachment, giving rise to compositional disorder. This chapter focuses on experimentally characterizing the dynamic consequences of such disorder on wave propagation and modal behavior.

In the first phase, the fabricated specimens were investigated using a Polytec scanning laser vibrometer (PSV) system. Each sample was suspended using two nylon wires to approximate free-free boundary conditions, and ceramic PZT actuators were bonded to the underside using epoxy resin. Broadband chirp excitations were applied, and out-of-plane velocity responses were measured to identify operational deflection shapes (ODSs), symmetric and antisymmetric (acoustic and optical) modes, and potential bandgap features over a frequency range up to 1.2 kHz. In a second phase, an electrodynamic shaker was employed to extend the investigation to a broader frequency range up to 2.5 kHz and to provide global excitation of the specimens. The measured responses were processed using PolyWave for experimental modal analysis and PSV post-processing tools to extract resonance frequencies, damping ratios, and mode shapes. In the final phase, a detailed

experimental campaign was conducted on a reduced configuration consisting of seven unit cells driven by the shaker, enabling an in-depth investigation of unit-to-unit variability, mode localization, and disorder-induced effects.

## 5.1 Test setup with PSV system

To do the experimental campaign employed PSV system, a PZT actuator and a linear amplifier. The piezoelectric change mechanical energy from electrical energy and vice versa. The mechanical stresses that come from an external force acting on the piezoelectric body cause the electrical dipoles to move. This causes an electric field to be created, and the resulting electric voltage follows suit. Also known as the sensor or generator effect, this direct piezoelectric phenomenon. In general, the linear amplifiers used to amplify the input signal at a fixed ratio and output it (that is which implies the input and output level are proportional).

### 5.1.1 Characterization of electrospun membrane with PZT

After the 3D and 2D alignments, the measurement/scan points were selected. Finally, the geometry scan was carried out to acquire the 3D shape of the sample calculating the 3D coordinates of the scan points. The acquisition parameters properly selected to capture the global, symmetric, a symmetric, acoustic, optical modes around the bandgaps. The velocity data acquired by the PSV system were post-processed employing the Polytec modal analysis software (*PolyWave*) and by the post-processing software (*PSV*).

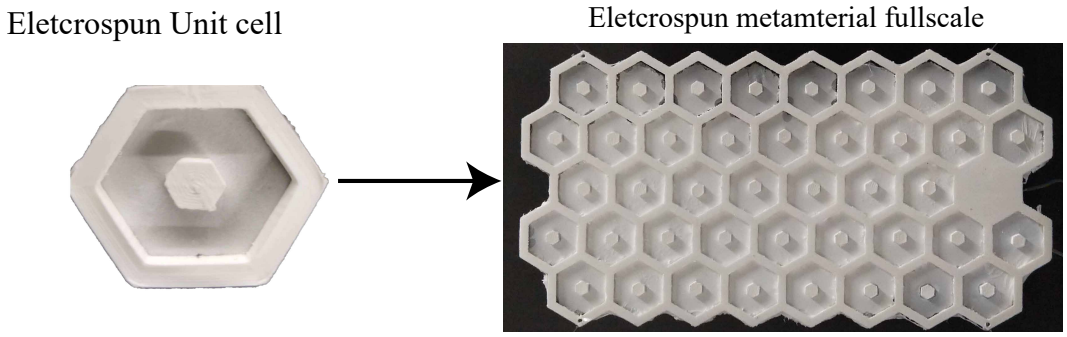


Figure 5.1: unitcell to full scale sample

Initially, the experimental campaign began on a single unit cell of the electrospun membrane with an attached resonator (Fig. 5.1). The primary objective was to identify the first five bending modes. We successfully captured the first four (Fig. 5.2). Notably, the second and fourth bending modes exhibit axisymmetric shapes with complementary (near-degenerate) counterparts. The measured modal frequencies are: first bending mode at 0.89 kHz; second axisymmetric/complementary pair at 1.55 kHz and 1.69 kHz; third

bending mode at 5.24 kHz; and fourth bending mode with its complementary pair at 5.90 kHz and 6 kHz

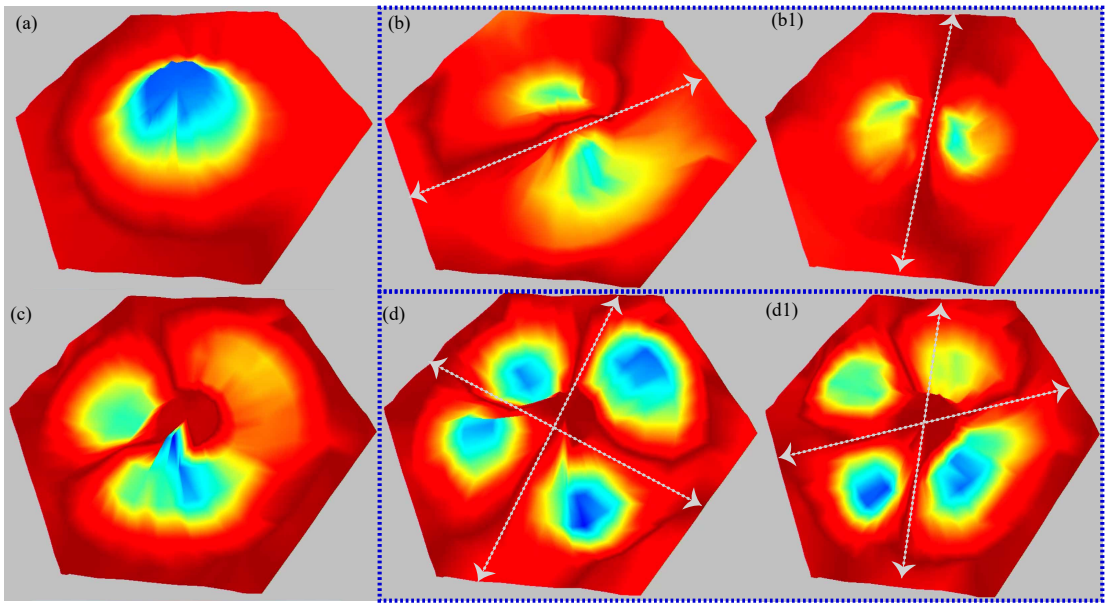


Figure 5.2: Experimental ODSs of electrospun membrane unitcell with resonator in a frequency range restricted to [0.01 - 6] kHz. Experimental ODSs snapshots: (a) 0.890 kHz, (b) 1.55 kHz, (b1) 1.69 kHz, (c) 5.24 khz, (d)5.9 kHz and (d1)6 kHz.

The electrospun samples were subjected to vibration testing using the following acquisition parameters: three complex averages, a bandwidth of 2.4 kHz, operating frequencies ranging from 0.01 kHz to 1.2 kHz, 1,893 scan points, a decoder velocity of 2.5 m/s, and an excitation voltage of 9 V amplified by a 20 times linear gain. Following the tests, frequency response analysis was performed to investigate the presence of bandgaps. Using the PSV system, the scan-point mesh shown in Fig. 5.3 (a) and (b) provided valuable insight into the measured responses. Within the frequency range of 0.05 kHz-1.2 kHz, with a frequency resolution of 0.39 Hz, multiple global modes and a dense sequence of local and coupled local/global modes were identified.

These modes primarily involved the activation of first membrane vibration modes across different clusters of resonators. Initially, resonators excited in the first membrane mode were situated at sample edges, followed by the activation of local resonances in groups of resonators within the inner/central region. Alongside global modes, featuring motion of cells without resonant resonators, local modes were predominantly characterized by resonant membrane motion. Notably, certain global/local modes, highlighted by red boxes, showcased groups of membranes resonating either in-phase or out-of-phase with global cell motion, identified as special acoustic (in-phase) or optical modes (out-of-phase). Responses indicative of bandgaps were observed within the frequency range between these acoustic/optical modes, likely attributed to non-uniform stretching of membranes, resulting in frequency detunings between resonators. These detunings obstructed the formation

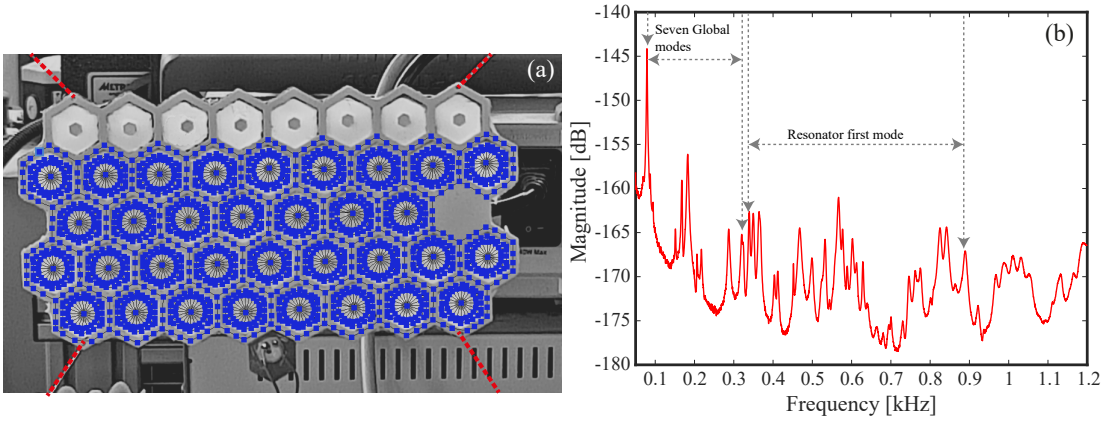


Figure 5.3: Average FRF of the acquisition within the frequency range restricted to [0.05 - 1.2] kHz. The gray bands indicate the likely identified bandgaps at 0.32 kHz, 0.42 kHz, 0.65 kHz.

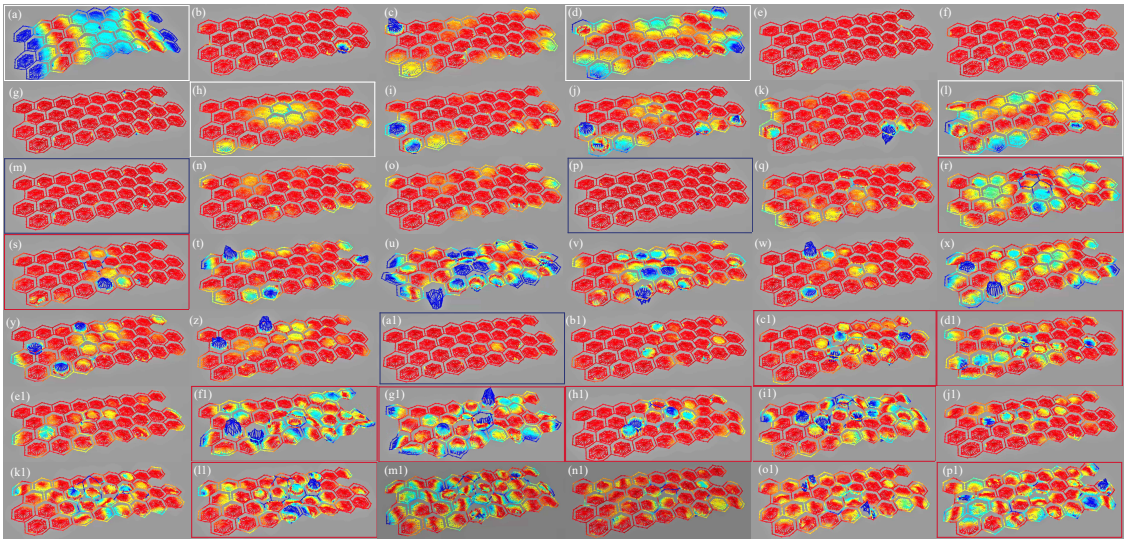

Figure 5.4: Experimental ODSs snapshots: (a) 0.078515 kHz, (b) 0.15078 kHz, (c) 0.16757 kHz, (d) 0.18203 kHz, (e) 0.20585 kHz, (f) 0.21718 kHz, (g) 0.25039 kHz, (h) 0.28632 kHz, (i) 0.31992 kHz, (j) 0.33906 kHz, (k) 0.34921 kHz, (l) 0.36445 kHz, (m) 0.38770 kHz, (n) 0.40351 kHz, (o) 0.41132 kHz, (p) 0.42851 kHz, (q) 0.45195 kHz, (r) 0.46718 kHz, (s) 0.49882 kHz, (t) 0.53242 kHz, (u) 0.56679 kHz, (v) 0.57695 kHz, (w) 0.58906 kHz, (x) 0.60156 kHz, (y) 0.61289 kHz, (z) 0.62812 kHz, (a1) 0.66484 kHz, (b1) 0.73007 kHz, (c1) 0.74570 kHz, (d1) 0.76171 kHz, (e1) 0.78867 kHz, (f1) 0.82539 kHz, (g1) 0.84140 kHz, (h1) 0.86328 kHz, (i1) 0.88828 kHz, (j1) 0.92187 kHz, (k1) 0.96757 kHz, (l1) 0.98828 kHz, (m1) 1.030859 kHz, (n1) 1.09375 kHz, (o1) 1.132815 kHz, (p1) 1.164843 kHz. Global modes are highlighted by the white bounding boxes, acoustic/optical modes by the red boxes, and the likely bandgap responses by the blue boxes.

of comprehensive acoustic and optical modes, typically involving synchronized motions of all resonators concerning honeycomb cells.

Tab.5.1. summarizes the experimentally extracted modal frequencies and damping ratios of the electrospun membrane metamaterial up to 1.2 kHz. The results reveal a dense and irregular modal spectrum, with non-uniform frequency spacing and significant variability in damping ratios across modes. Such frequency spread and modal clustering are indicative of resonator-to-resonator detuning and compositional disorder arising from fabrication-induced variations in membrane stiffness, mass density, and attachment conditions.

The measured damping ratios span approximately 0.38% to 1.99%, while adjacent

Table 5.1: Electrospun membrane resonance frequencies associated with damping ratios up to 1.2 kHz.

| Mode number | Frequency [Hz] | Damping ratio [%] | Mode number | Frequency [Hz] | Damping ratio [%] |
|---|---|---|---|---|---|
| 1 | 78.79 | 0.80598 | 11 | 701.29 | 1.33459 |
| 2 | 168.09 | 0.43541 | 12 | 761.89 | 0.84215 |
| 3 | 182.5 | 1.27915 | 13 | 775.6 | 0.47388 |
| 4 | 348.8 | 0.51284 | 14 | 825.6 | 0.50341 |
| 5 | 466.3 | 1.25660 | 15 | 888.1 | 0.45610 |
| 6 | 497.5 | 0.78071 | 16 | 983.1 | 1.96758 |
| 7 | 530 | 0.49827 | 17 | 1008.1 | 1.98957 |
| 8 | 565 | 0.44661 | 18 | 1133.09 | 0.66031 |
| 9 | 601.29 | 1.36778 | 19 | 1185.59 | 1.01259 |
| 10 | 628.79 | 0.37615 | | | |

resonance frequencies are unevenly spaced, confirming substantial unit-to-unit variability rather than ideal periodic behavior. The experimentally observed spatial localization of vibration energy in the ODSs is consistent with the dense and irregular modal spectrum revealed by the experimental modal analysis, as disorder-induced mode splitting and frequency detuning favor localized rather than extended Bloch modes.

During testing, observed that material properties varied from one unit cell to the next. We nevertheless proceeded to assess the robustness of band formation and to identify which forms of disorder invalidate the periodic (Bloch-wave) assumptions [5, 106, 6]. Although the architecture is nominally periodic, variability in the electrospun membrane density, membrane stiffness, resonator position, and bonding/attachment conditions introduced compositional disorder i.e., random variations in intrinsic properties (density, elastic modulus, Poisson's ratio) that govern elastic-wave propagation [5, 6, 107]. Such disorder modifies local mass spring parameters without changing the lattice geometry and can smear or suppress Bragg/locally resonant bandgaps and even drive Anderson localization [108, 109, 110, 111, 112].

### 5.1.2 Characterization of electrospun membrane with electrodynamic shaker

The experimental setup employed a PSV system in conjunction with an electrodynamic shaker (MADE 500) for vibration testing and modal analysis. The shaker, capable of generating vibrations up to 30 g and 6 kHz, was operated under precise control to ensure accurate testing parameters and a stable, cohesive testing environment. The velocity data acquired by the *Polytec Scanning Vibrometer PSV-500-3D* were post-processed employing the Polytec modal analysis software (*PolyWave*) and by the post-processing software (*PSV*).

The samples were subjected to vibration testing with specific acquisition parameters: complex averages set to 3, a bandwidth of 5 kHz, operating frequencies ranging from 0.01

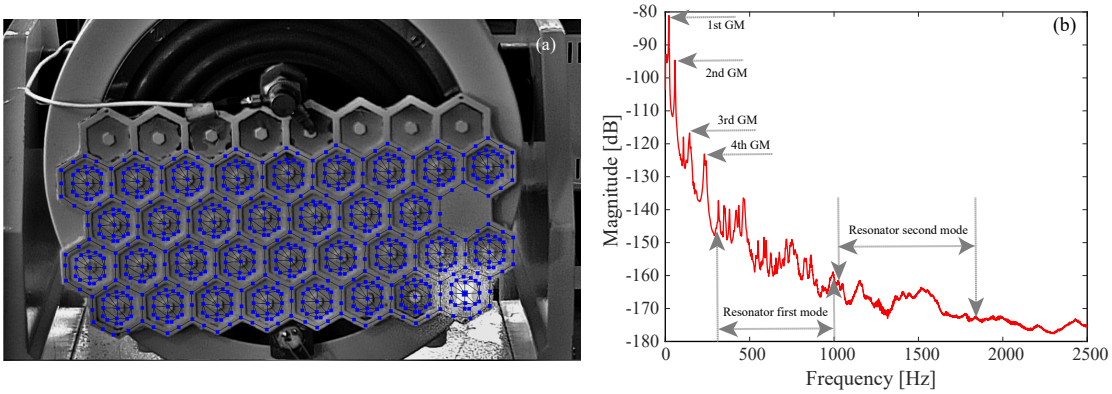


Figure 5.5: (a) scan points assigned using PSV system on the sample (b) average FRF of the acquisition within the frequency range 2.5 kHz. The gray bands indicate the likely identified bandgaps at 0.51 kHz and 0.65 kHz.

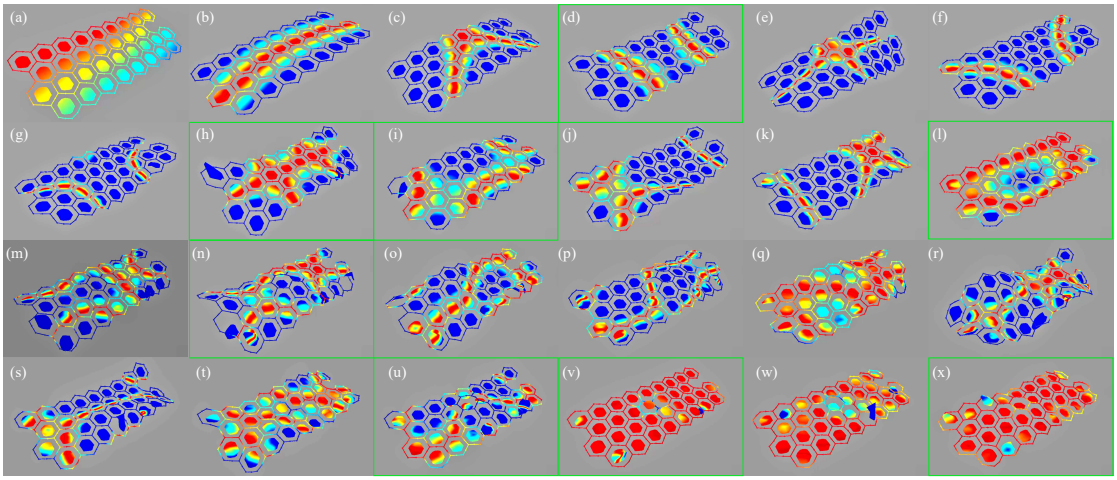


Figure 5.6: Experimental ODSs: (a) 0.02109 kHz, (b) 0.03671 kHz, (c) 0.057812 kHz, (d) 0.07734 kHz, (e) 0.10781 kHz, (f) 0.12109 kHz, (g) 0.14375 kHz, (h) 0.16328 kHz, (i) 0.18671 kHz, (j) 0.23125 kHz, (k) 0.2414 kHz, (l) 0.28359 kHz, (m) 0.31484 kHz, (n) 0.34843 kHz, (o) 0.36953 kHz, (p) 0.37958 kHz, (q) 0.38984 kHz, (r) 0.42031 kHz, (s) 0.43515 kHz, (t) 0.44921 kHz, (u) 0.46484 kHz, (v) 0.50781 kHz, (w) 0.54921 kHz, (x) 0.56718 kHz. The modes are highlighted by the green bounding boxes, are similar mode shapes obtained with PZT actuation.

to 2.5 kHz, 779 scan points, a decoder velocity of 2.5 m/sec, and a voltage of 0.1 V. First, the modal analysis of each metamaterial sample aimed at determining the global/ local mode shapes and frequencies was carried out by exciting the samples via a chirp signal. Subsequently, a frequency response analysis was carried out to explore the bandgaps. The response of the sample was further explored using shaker as shown in Fig. 5.6, Fig. 5.7.

Within the frequency range of 0.05 to 2.5 kHz, various global modes and a dense sequence of local and combined local/global modes were identified. The captured mode-shapes shown in Figure 5.6 (a) and (b) are attributed to cantilever boundary conditions, characterized by skew-symmetric modeshapes. Figures 5.6 (c) to (g) illustrate unique global modeshapes. Beyond 0.160 kHz, the sample exhibits a series of local modes and combinations of local/global vibration modes. The primary modes observed involve the activation of two membrane vibration modes across different clusters of resonators. Initially, the resonators excited in the first membrane mode are situated at the sample edges. This is followed by the activation of local resonances within groups of resonators located

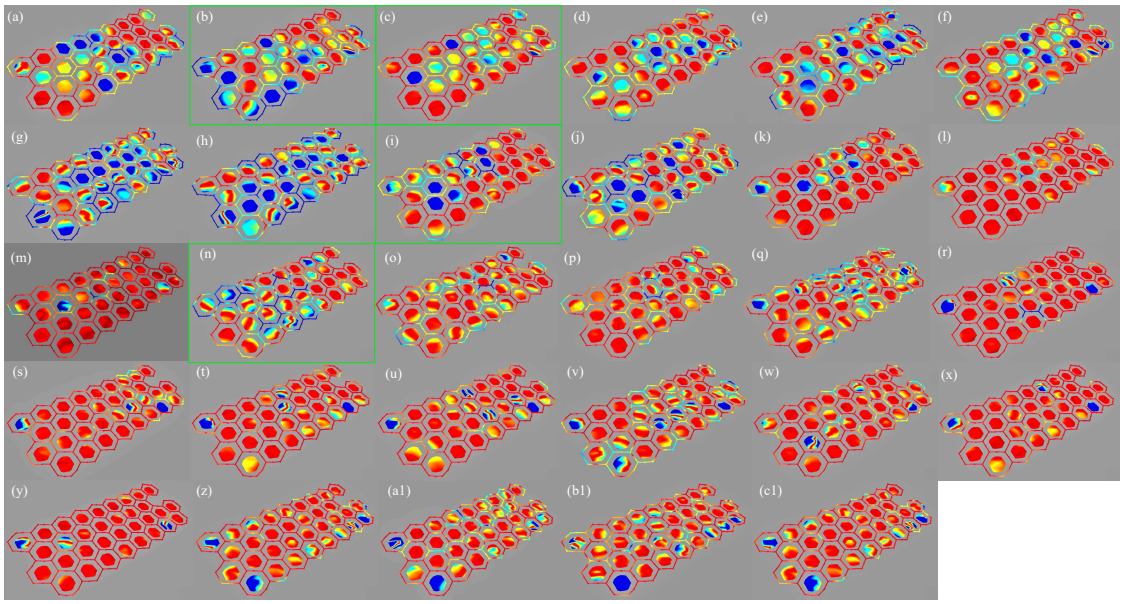


Figure 5.7: Experimental ODSs: (a) 0.58437 kHz, (b) 0.59765 kHz, (c) 0.62421 kHz, (d) 0.65546 kHz, (e) 0.67578 kHz, (f) 0.69609 kHz, (g) 0.71796 kHz, (h) 0.750 kHz, (i) 0.82421 kHz, (j) 0.8625 kHz, (k) 0.89453 kHz, (l) 0.91953 kHz, (m) 0.929687 kHz, (n) 0.99296 kHz, (o) 1.02343 kHz, (p) 1.04843 kHz, (q) 1.15234 kHz, (r) 1.26562 kHz, (s) 1.36562 kHz, (t) 1.41015 kHz, (u) 1.44687 kHz, (v) 1.51796 kHz, (w) 1.61015 kHz, (x) 1.66718 kHz, (y) 1.775 kHz, (z) 1.94140 kHz, (a1) 1.99921 kHz, (b1) 2.20625 kHz, (c1) 2.42968 kHz.

in the inner or central region of the sample. In terms of mode behavior, global modes are characterized by the movement of cells without resonant resonators, while local modes predominantly involve resonant membrane motion. Notably, certain combined global/local modes showcase groups of membranes resonating either in-phase or out-of-phase with the global cell motion. These are identified as special acoustic modes (in-phase) or optical modes (out-of-phase). Responses indicative of bandgaps were observed within the frequency range between these acoustic and optical modes. These bandgaps are likely due to non-uniform stretching of the membranes, resulting in frequency detunings between resonators. These detunings obstruct the formation of comprehensive acoustic and optical modes, which typically involve synchronized motion of all resonators within the honeycomb cells.

Tab.5.2 reports the experimentally identified resonance frequencies and damping ratios obtained under broadband chirp excitation using an electrodynamic shaker, extending the investigated frequency range up to 2.5 kHz. The resulting modal spectrum is dense and highly irregular, with non-uniform frequency spacing and pronounced variability in damping ratios across modes. This behavior confirms that the observed resonator detuning and modal crowding are intrinsic features of the electrospun membrane metamaterial and are not specific to the PZT-based excitation employed in earlier measurements.

The measured damping ratios span more than two orders of magnitude, from approximately 0.04% to over 8%, indicating strong spatial variability in energy dissipation and local resonator–membrane coupling. The dense modal spectrum and large damping variability revealed by the shaker-based experimental modal analysis provide a quantitative

Table 5.2: Electrospun membrane resonance frequencies associated with damping ratios up to 2.5 kHz for chirp excitation with shaker.

| Mode number | Frequency [Hz] | Damping ratio [%] | Mode number | Frequency [Hz] | Damping ratio [%] |
|---|---|---|---|---|---|
| 1 | 21.1 | 2.02832 | 14 | 1161.7 | 0.41298 |
| 2 | 57.79 | 1.34003 | 15 | 1264.09 | 0.036334 |
| 3 | 143.8 | 1.39912 | 16 | 1369.5 | 8.31932 |
| 4 | 232 | 0.82969 | 17 | 1411.7 | 6.42079 |
| 5 | 314.8 | 0.40844 | 18 | 1451.59 | 5.03784 |
| 6 | 435.19 | 0.36496 | 19 | 1528.5 | 1.61891 |
| 7 | 463.3 | 1.06267 | 20 | 1580.5 | 3.78225 |
| 8 | 549.2 | 0.29002 | 21 | 1776.59 | 0.47090 |
| 9 | 584.39 | 0.19980 | 22 | 1939.09 | 0.40266 |
| 10 | 715.6 | 0.46891 | 23 | 1975.8 | 0.046450 |
| 11 | 750.79 | 0.59012 | 24 | 2061.69 | 0.98071 |
| 12 | 863.29 | 0.12748 | 25 | 2203.09 | 0.97944 |
| 13 | 995.29 | 0.59186 | 26 | 2432 | 1.02454 |

basis for the strong spatial localization observed in the ODSs, as disorder-induced mode splitting suppresses extended Bloch-type wave propagation in favor of localized resonant responses.

While the present analysis focuses on modal identification under nominally linear excitation conditions, the wide spread in damping ratios and resonance frequencies suggests that amplitude-dependent effects, similar to those discussed in Chapter 3, may further influence the effective detuning of resonators at higher excitation levels.

### 5.1.3 In-depth analysis of unitcells

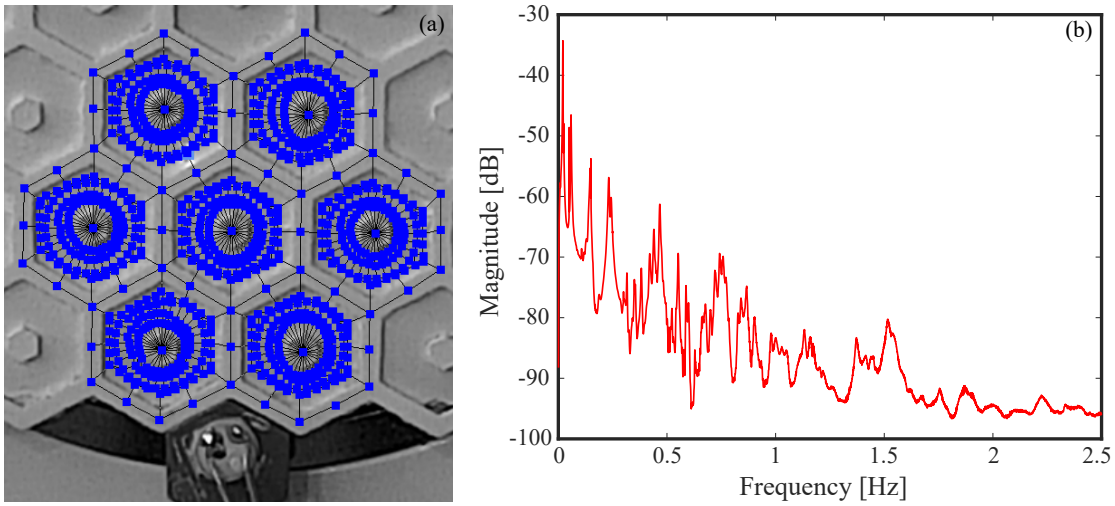


Figure 5.8: (a) scan points assigned using Polytec PSV-500-3D scanning vibrometer system on the sample (b) average FRF of the acquisition within the frequency range 2.5 kHz.

An in-depth experimental analysis was conducted on seven unit cells, positioned close to the excitation source, to observe the vibration mode shapes of the membranes within

a frequency range of 0.01 to 2.5 kHz. The unitcell labeled as U1, U2, U3, U4, U5, U6 and U7 as shown in Fig. 5.9 (a). Snapshots of the ODSs were recorded, as shown in Fig. 5.9 and 5.10. The U1 unit cell exhibited its first vibration or local mode shape at a frequency of 0.42031 kHz, continuing up to 0.43984 kHz (Fig. 5.9 (o) to (p)). Similarly, the U2 cell displayed its first mode shape starting at 0.50937 kHz and extending up to 0.55156 kHz (Fig. 5.9 (u) to (v)). Unit cells U7, U2, and U3 also exhibited their first mode shapes. Detailed observations of the first vibration mode shapes include unit cells U7 and U4 in Fig. 5.9 (x), unit cells U3, U4, U5, U6, and U7 in Fig. 5.9 (y), unit cells U2, U3, U5, U6 and U7 in Fig. 5.9 (z). Further, unit cells U1, U3, U4, U5, and U6 are shown in Fig. 5.9 (a1), U3, U4, U5, U6, and U7 in Fig. 5.9 (b1), and all unit cells in Fig. 5.9 (c1) and (e1). Fig. 5.9 (d1) specifically highlights unit cells U4, U5, and U7. Interestingly, in Fig 5.9 (g1) to (k1), the U1 unit cell exhibited its second vibration mode shape, while the other unit cells continued to exhibit their first mode shapes. In Fig. 5.9 (l1), U1 exhibited a second membrane vibration mode-II, while the other unit cells remained in their first mode shapes.

Interestingly, as shown in Figs. 5.10 (a)-(b), the neighboring unit cells (U2, U3, U5, U6, U7) begin to exhibit the second membrane mode. Beyond 1.1 kHz, all unit cells display the second membrane mode shapes (Types I and II). This analysis reveals distinct vibration characteristics for each unit cell relative to the excitation location, delineates the frequency ranges associated with specific mode shapes, and provides insight into their dynamic behavior. The identification of both first and second mode shapes particularly for U1-highlights the complex interactions within the membrane structure under varying frequencies.

Following rigorous experiments, using both PZT excitation and an electrodynamic shaker together with an in-depth unit cell analysis, we identified *compositional disorder* arising from unit-to-unit variations in resonant properties (e.g., mass density, membrane stiffness, resonator placement/attachment) [5, 6, 106]. When an incident wave enters this disordered metamaterial, it encounters these variations at each cell and is scattered with amplitude and phase set by the mismatch between the cell's resonance and the driving frequency [6, 113]. The multiply scattered fields then interfere: constructive interference yields an amplified response and strong, out-of-phase motion of nearby resonators (energy concentration), whereas destructive interference suppresses motion and leaves other resonators relatively quiescent [114, 111, 110]. This spatially heterogeneous amplitude–phase field is the hallmark of Anderson localization [114, 111]. Disorder induced scattering generates localized modes that trap energy within finite regions of the structure; the associated localization length, which sets the spatial extent of these modes typically decreases as disorder increases, leading to tighter confinement [114, 115]. The observed pattern of few resonators oscillating out of phase while others remain still, thus reflects the spatial footprint of localized modes and signals the breakdown of Bloch-wave propa-

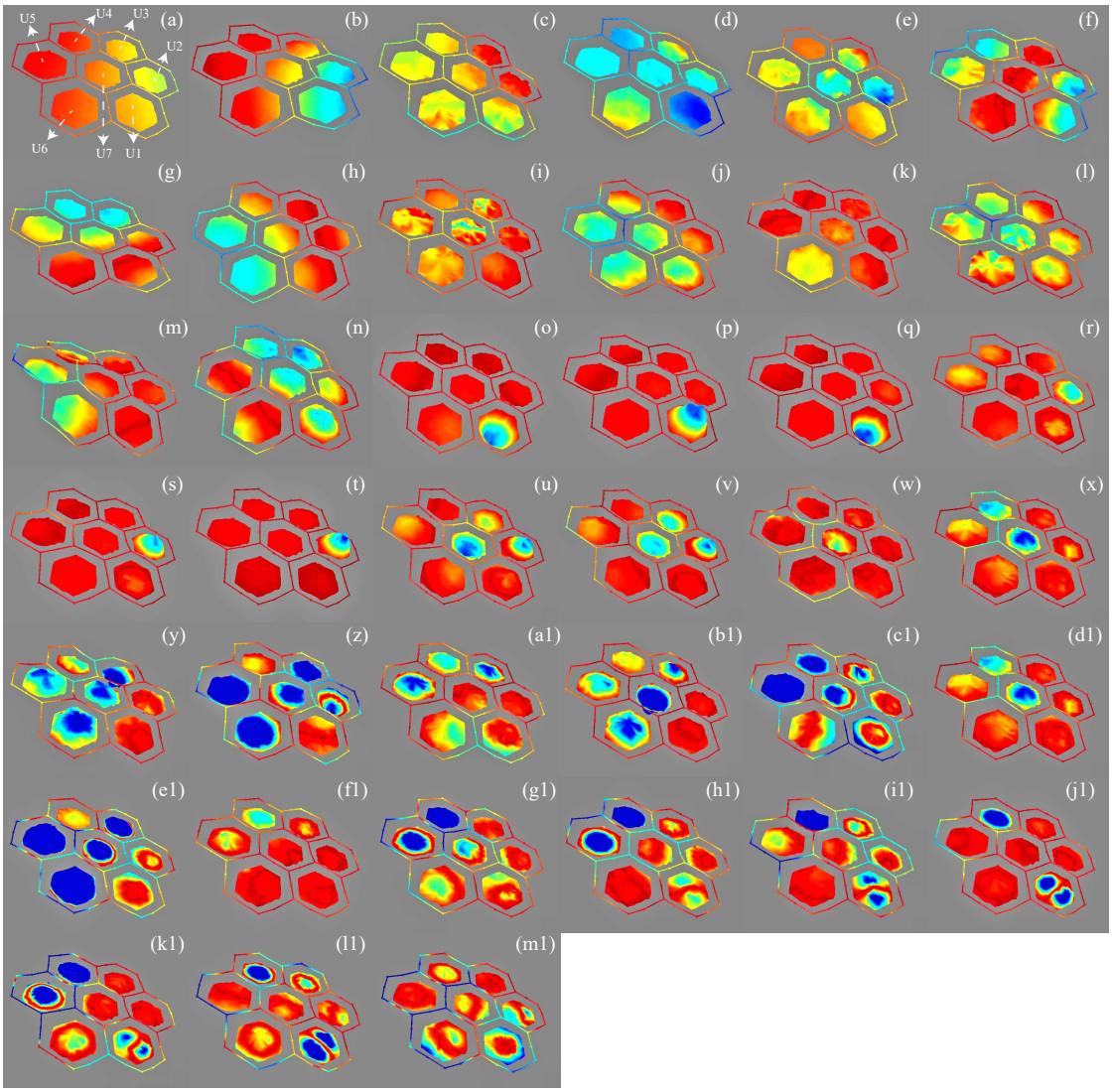


Figure 5.9: Experimental ODSs: (a) 0.02109 kHz, (b) 0.057812 kHz, (c) 0.10781 kHz, (d) 0.128906 kHz, (e) 0.14609 kHz, (f) 0.17421 kHz, (g) 0.23203 kHz, (h) 0.24218 kHz, (i) 0.300 kHz, (j) 0.31562 kHz, (k) 0.32734 kHz, (l) 0.350 kHz, (m) 0.35464 kHz, (n) 0.38203 kHz, (o) 0.42031 kHz, (p) 0.43984 kHz, (q) 0.46640 kHz, (r) 0.50937 kHz, (s) 0.52265 kHz, (t) 0.55156 kHz, (u) 0.5875 kHz, (v) 0.59921 kHz, (w) 0.61796 kHz, (x) 0.628125 kHz, (Y) 0.66015 kHz, (Z) 0.67578 kHz. (a1) 0.68984 kHz, (b1) 0.69921 kHz, (c1) 0.720312 kHz, (d1) 0.74218 kHz, (e1) 0.75859 kHz, (f1) 0.80937 kHz, (g1) 0.82734 kHz, (h1) 0.84062 kHz, (i1) 0.86484 kHz, (j1) 0.886718 kHz, (k1) 0.90390 kHz, (l1) 0.97968 kHz and (m1) 0.99921 kHz.

gation in favor of disorder-driven interference [5, 106]. These observations are consistent with subwavelength Anderson localization in a resonant array [113].

The localization of vibration energy was therefore assessed qualitatively through the spatial extent of the active unit cells observed in the ODSs, providing an experimental proxy for the localization length without requiring direct statistical averaging.

## 5.2 Summary

We experimentally investigated an electrospun membrane metamaterial with attached resonators using both PZT excitation and an electrodynamic shaker, with full-field measure-

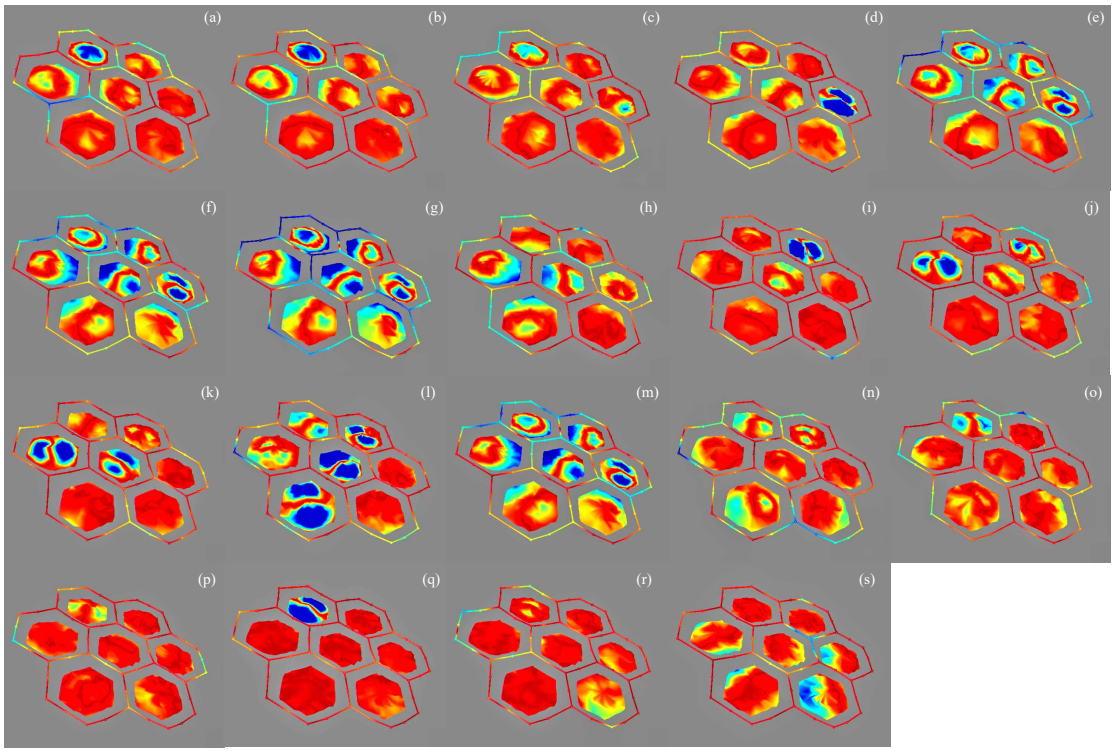


Figure 5.10: Experimental ODSs: (a) 1.028125 kHz, (b) 1.05078 kHz, (c) 1.079687 kHz, (d) 1.1217968 kHz, (e) 1.132812 kHz, (f) 1.146093 kHz, (g) 1.158593 kHz, (h) 1.174218 kHz, (i) 1.217968 kHz, (j) 1.371825 kHz, (k) 1.414843 kHz, (l) 1.448437 kHz, (m) 1.515625 kHz, (n) 1.592968 kHz, (o) 1.621093 kHz, (p) 1.67578 kHz, (q) 1.871093 kHz, (r) 1.999218 kHz and (s) 2.223437 kHz.

ments from a PSV system. we identified manufacturing-induced compositional disorder, arising from unit-to-unit variability in mass density, membrane stiffness, and resonator placement/attachment, which disrupts periodic (Bloch) transport. Under broadband frequency sweeps, we observed pronounced spatial heterogeneity: near the excitation, certain cells exhibited amplified, out-of-phase motion while others remained comparatively quiescent. This interference-driven confinement, together with the absence of a clean periodic bandgap and the transition of all cells to second membrane modes above 1.1 kHz, indicates the formation of disorder pinned, localized modes. The results are consistent with Anderson localization characterized by a disorder-dependent reduction of localization length and align with the subwavelength, resonator-hybridization picture reported in the literature [113].

Although the present experiments were conducted primarily within a nominally linear excitation regime, amplitude-dependent nonlinear effects may also contribute to the observed detuning behavior. As demonstrated in Chapter 3 for spider-web resonator metamaterials, nonlinear dynamics can induce effective resonance shifts under increased excitation levels. Given the high compliance of electrospun membranes, such nonlinearities could further enhance or mask disorder-induced frequency variability at higher excitation amplitudes. While nonlinear effects were not explicitly isolated in this study, their potential influence should be considered in future investigations.

# Chapter 6

# New directions: aperiodic metamaterials with resonators

A tiling of the plane, also known as tessellation, refers to the division of the Euclidean plane into regions without gaps or overlaps using one or more geometric shapes, called tiles. Each tile is either an exact copy or a transformed version (e.g., rotated, reflected, or translated) of a base shape. Tiling has fascinated mathematicians, scientists, and artists for centuries, as it blends geometric precision with aesthetic appeal. In the 17th century, Johannes Kepler investigated geometric configurations that use regular polygons to tile the plane without gaps or overlaps. These patterns, known as Kepler tilings, include arrangements of regular polygons such as triangles, squares, and hexagons in repetitive patterns [116, 117].

This contribution provided an essential framework for understanding symmetry and tiling, inspiring future explorations into more complex and aperiodic patterns. Aperiodic structures are not invariant under any spatial translation. Centuries later, in 1974, the challenge of aperiodic tilings captured the attention of Roger Penrose, a distinguished British physicist and mathematician [118, 119]. The symmetry observed in aperiodic Penrose tilings is closely related to the structure of quasicrystals, which exhibit similar patterns in physical materials [120, 121]. Indeed, quite surprisingly, in 2011, the Nobel Prize in Chemistry was awarded to Dan Shechtman for his discovery of quasicrystals [122, 121]. Shechtman discovered ordered but aperiodic crystalline structures, which revolutionized the understanding of matter and crystallography.

Unlike periodic structures, which exhibit predictable band structures and wave behaviors, aperiodic geometries such as Penrose tilings introduce unique scattering, localization, and transmission characteristics. These can lead to novel bandgap formations and, at least in principle, reduced sensitivity to resonance phenomena [123]. Such configurations also provide insights into quasicrystal mechanics, helping to explain how order without periodicity influences material properties in nature, with important implications for the design of advanced phononic and mechanical metamaterials [124].

In this chapter, the initial focus is on the aperiodic geometry of the Penrose P3 type, which consists of small and large rhombi arranged in a specific pattern. Resonators such as cantilevers and cantilevers with tip masses were introduced at locations where fivefold symmetry occurred within the arrangement. The designed samples were subsequently fabricated and analyzed using a PSV system. For the experimental study, each sample was suspended using nylon wires, while PZT actuators were securely attached to the bottom surface with epoxy resin. The primary objective of the experiments was to capture the ODSs. This was achieved by exciting the specimens with a chirp signal and recording the velocity response using the PSV system. Additionally, an electrodynamic shaker was employed to excite the aperiodic metamaterial in order to capture wave sequences, thereby revealing interesting propagation phenomena associated with this type of geometry.

## 6.1 Penrose tiling by rhombi

Following [125] for $0 < \alpha < 90$, we denote by $R_{\alpha^\circ}$ the planar rhombus with an acute angle of $\alpha$ degrees. In 1974, Penrose introduced two rhombic prototiles: a thick rhombus $R_{72^\circ}$ with angles of $72^\circ$ and $108^\circ$, and a thin rhombus $R_{36^\circ}$ with angles $36^\circ$ and $144^\circ$, see Fig. 6.1.

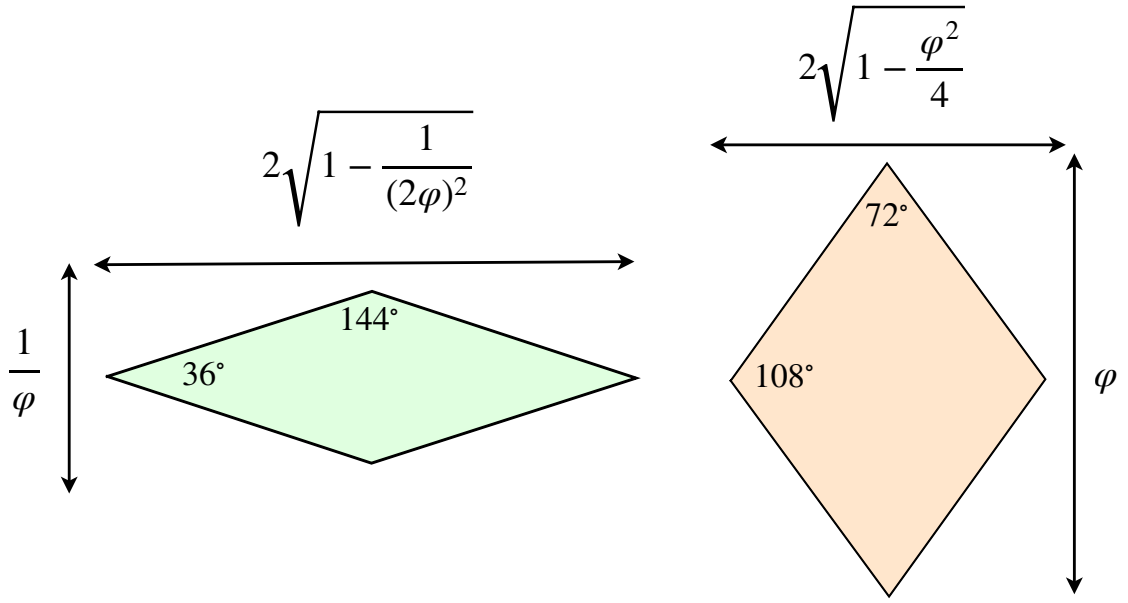


Figure 6.1: Penrose prototiles $\varphi = \frac{1+\sqrt{5}}{2} \approx 1.618033988749895$.

Note that the angles of the Penrose rhombi are multiples of $\pi/5 = 36^\circ$ :

$$\frac{2}{5}\pi = 72^\circ, \quad \frac{3}{5}\pi = 108^\circ, \quad \frac{4}{5}\pi = 144^\circ.$$

The matching rule is shown in Fig. 6.2. The sides of the Penrose rhombi are marked with red and green arrows. The tiles are designed to be arranged in such a way that the

color and direction of the arrows align between adjacent tiles.

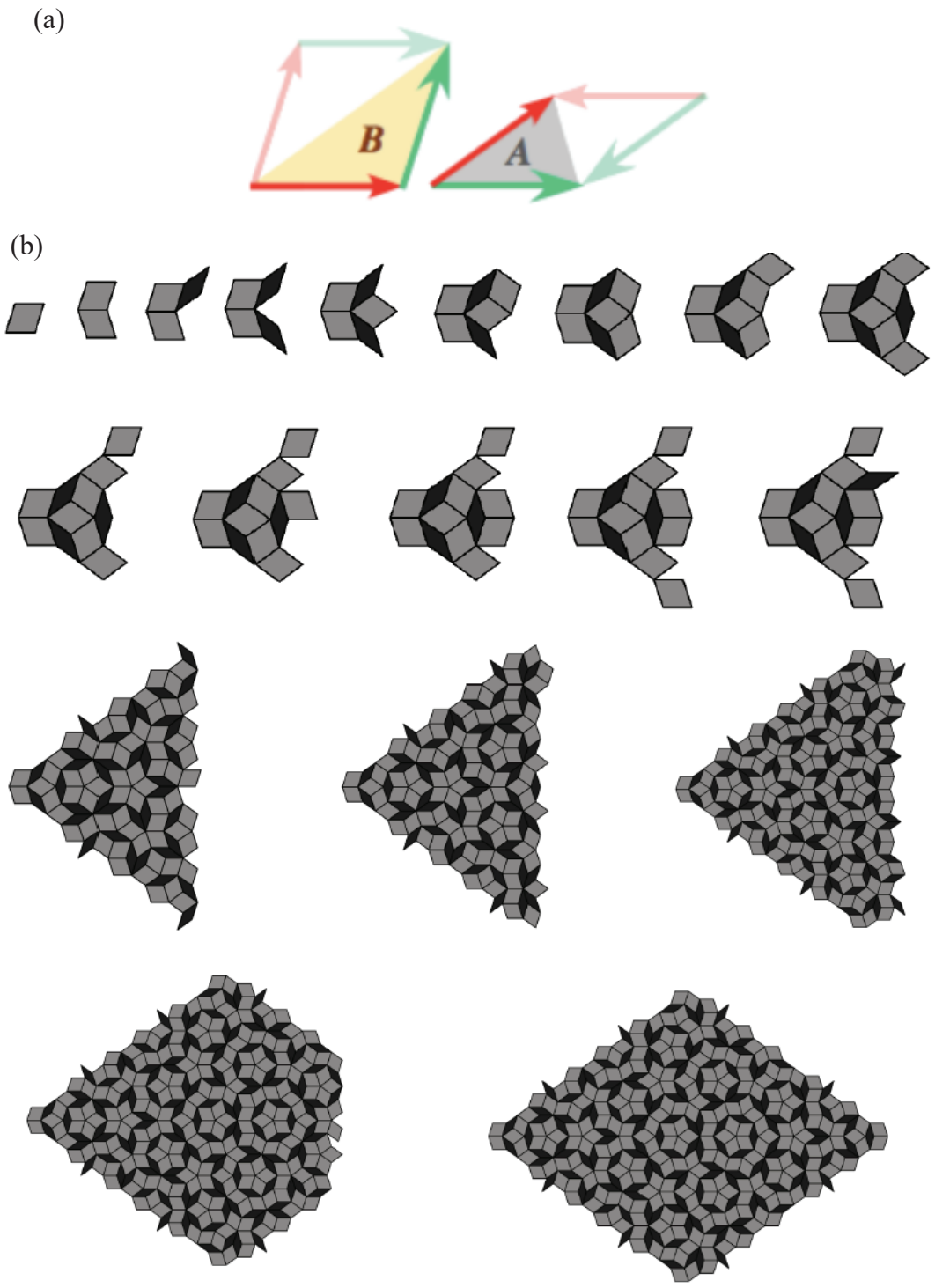


Figure 6.2: (a) Rhombi with red and green arrows giving the matching rule. The half-rhombi of type A and B are also represented. (b) An example of iterative construction of a Penrose tiling by thick and thin rhombi.

## 6.2 Penrose P3-pattern samples

The Penrose P3 pattern sample (P3-I), shown in Fig. 6.3 (a), provides an effective framework for designing metamaterials optimized for elastic wave propagation. Its unique aperiodic architecture allows precise control over wave behavior. The Penrose metamaterial is composed of thick and thin rhombuses, each measuring 12 mm in length, 0.75 mm in thickness, and 5 mm in height. These rhombuses are systematically arranged within a finite square domain, producing a non-repetitive yet organized configuration. The intrinsic fivefold symmetry of the pattern gives rise to a central pentagonal region that accommodates a resonator. This resonator is designed as a cantilever with dimensions of 6.79 mm in length, 1.76 mm in width, and 5 mm in height.

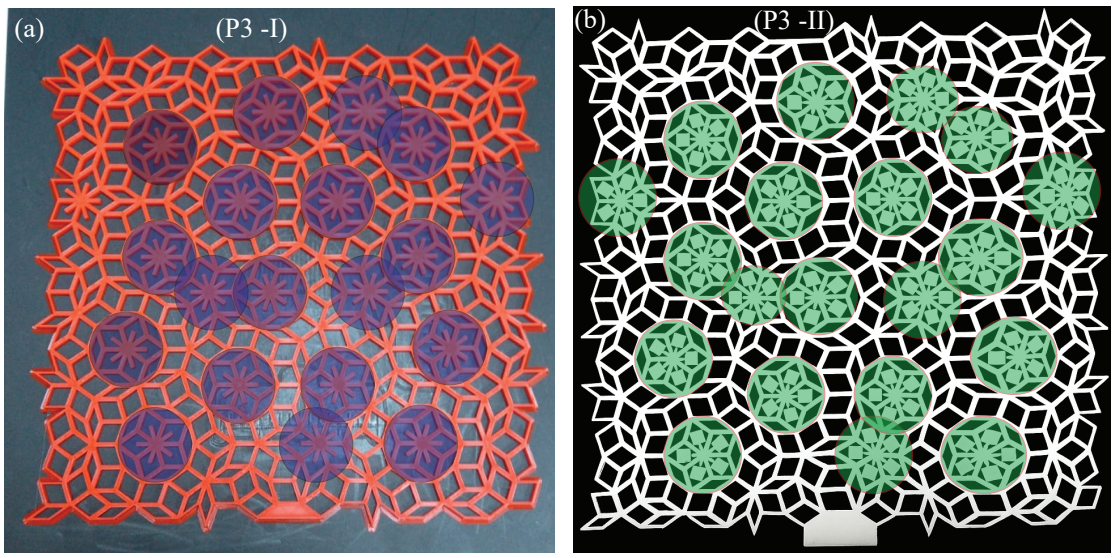


Figure 6.3: Aperiodic Penrose P3 type geometry with square pattern: (a) Sample (P3-I) with resonators, where the five-fold symmetry is highlighted, and the corresponding resonators are shown in blue; (b) Sample (P3-II) with resonators incorporating tip masses, where the five-fold symmetry is highlighted, and the corresponding resonators are shown in green.

The Penrose P3 pattern sample (P3-II), shown in Fig. 6.4 (b), serves as the foundation for the metamaterial design, comprising an arrangement of thick and thin rhombuses. Each rhombus measures 12 mm in length, 0.75 mm in thickness, and 2.5 mm in height. These elements are systematically organized within a finite square domain, creating a structured yet non-repetitive configuration that retains the characteristic properties of aperiodic tiling. The inherent fivefold symmetry of the Penrose P3 pattern gives rise to pentagonal regions, within which resonators are embedded. Each resonator consists of a cantilever with an attached tip mass, designed to induce localized resonant modes. The cantilever measures 4.0688 mm in length, 1 mm in width, and 1 mm in height, while the tip mass measures 6.5 mm in length, 6 mm in width, and 2.5 mm in height.

### Test setup with PSV system

The PSV system's laser scanning procedure provides a highly precise, non-contact method for measuring and analyzing the dynamic behavior of complex structures. The measurement process comprises five primary steps: laser setup, scan preparation, acquisition parameter configuration, data measurement, and post-processing, all of which were described in detail in Chapter 2.

For excitation, a PZT disk actuator was used as the input source. Both Penrose samples (P3-I and P3-II) were suspended using nylon wire ropes attached to a fixed frame, thereby minimizing boundary constraints. This suspension configuration allowed the samples to vibrate freely, ensuring that the measured responses accurately represented their intrinsic dynamic behavior.

## 6.2.1 Characterization of P3-I with PZT

The experimental parameters were configured as follows: three complex averages, a bandwidth of 25 kHz, an operating frequency range from 0.01-25 kHz, a total of 856 scan points, a decoder velocity of 1250 mm/s, and an excitation voltage of 120 V.

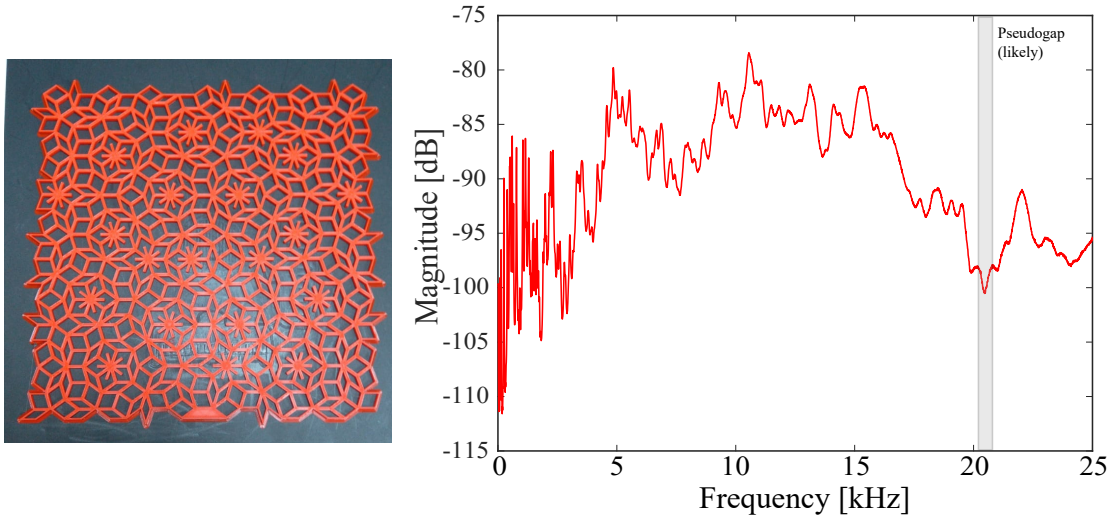


Figure 6.4: Average FRF of the acquisition within the frequency range [0.001 - 25] kHz highlighted pseudogap (grey), snapshot of sample.

The average FRF, presented in Fig. 6.4, reveals the emergence of a pseudogap within the frequency range of approximately 20.125 kHz to 20.46875 kHz. This observed pseudogap corresponds to a region of significantly reduced wave transmission. Moreover, the presence of this pseudogap is corroborated by the ODSs analysis, where it is distinctly highlighted within the white box, indicating a frequency region in which wave propagation is notably altered.

A subset of selected ODSs is presented in Fig. 6.5. The initial mode shapes, shown in Fig. 6.5 (a–e), correspond to global vibration modes in which the resonators move coherently with the overall structure. Symmetric mode shapes are observed in Fig. 6.5 (f–i),

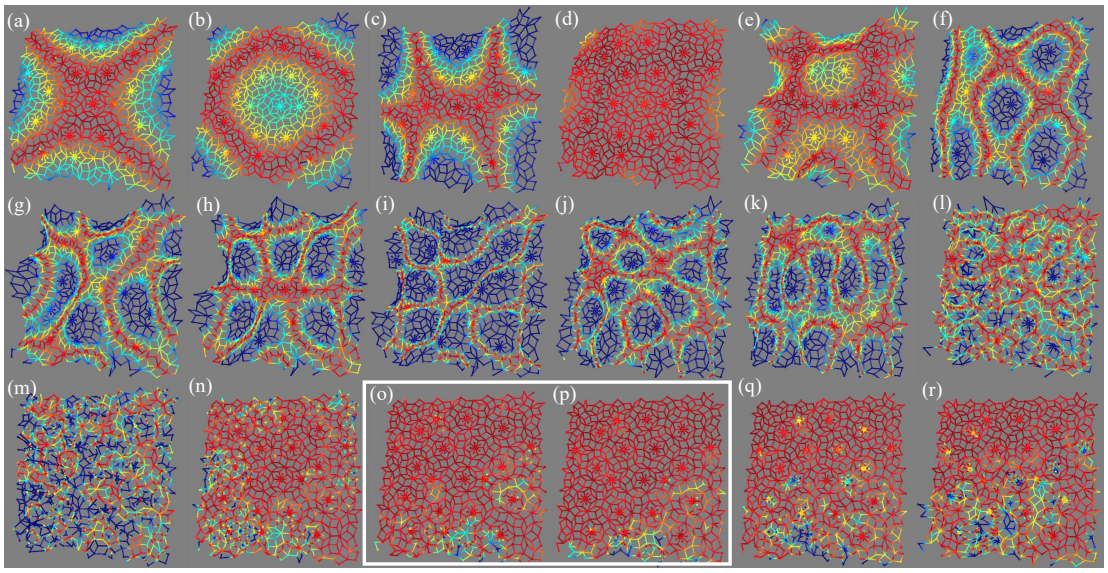


Figure 6.5: Experimental ODSs: (a) 0.078125 kHz, (b) 0.09375 kHz, (c) 0.1328 kHz, (d) 0.22656 kHz, (e) 0.375 kHz, (f) 0.49218 kHz, (g) 0.59375 kHz, (h) 0.765625 kHz, (i) 1.046875 kHz, (j) 1.14843 kHz, (k) 1.296875 kHz, (l) 3.53125 kHz, (m) 4.84375 kHz, (n) 9.2890625 kHz, (o) 20.125 kHz, (p) 20.46875 kHz, (q) 21.35156 kHz and (r) 22.0390 kHz. Highlighted by the white bounding boxes likely to be a Pseudogap

whereas Fig. 6.5 (j–m) illustrates distinct resonance patterns arising from the interaction of the incident elastic waves with the fivefold symmetric arrangement of resonators, a characteristic feature of Penrose-type quasi-periodic structures [126]. Figure 6.5 (n) depicts localized scattering behavior occurring just before the pseudobandgap region, highlighted by the white bounded box. Following the pseudobandgap, as shown in Fig. 6.5 (o–p), another unique scattering phenomenon emerges, signifying a transition from extended to localized modes across the pseudobandgap, which is a hallmark of wave localization in quasi-periodic metamaterials [127, 128, 129]. These observations further confirm that the Penrose-inspired aperiodic design effectively modifies wave transport characteristics through multi-scale scattering and hybridized resonance effects [130, 131].

The experimental parameters were systematically configured to ensure accurate characterization of the elastic wave propagation behavior. These parameters included three complex averages to improve signal fidelity, a bandwidth of 50 kHz, and an operating frequency range spanning from 15 kHz to 50 kHz. A total of 856 scan points were defined to achieve high-resolution spatial mapping, while a decoder velocity of 1250 mm/s ensured consistent scanning conditions. The excitation was applied using a 120 V driving voltage, providing sufficient energy to excite both global and localized modes within the sample. The results obtained from the PSV analysis, illustrated in the average FRF in Fig. 6.6, reveal the formation of multiple stop-band features consistent with bandgap and pseudobandgap phenomena. Two prominent suppressed transmission intervals were identified: the first centered near 28.137 kHz and the second near 43.416 kHz. These spectral gaps correspond to frequency ranges where wave propagation is strongly attenuated is a sig-

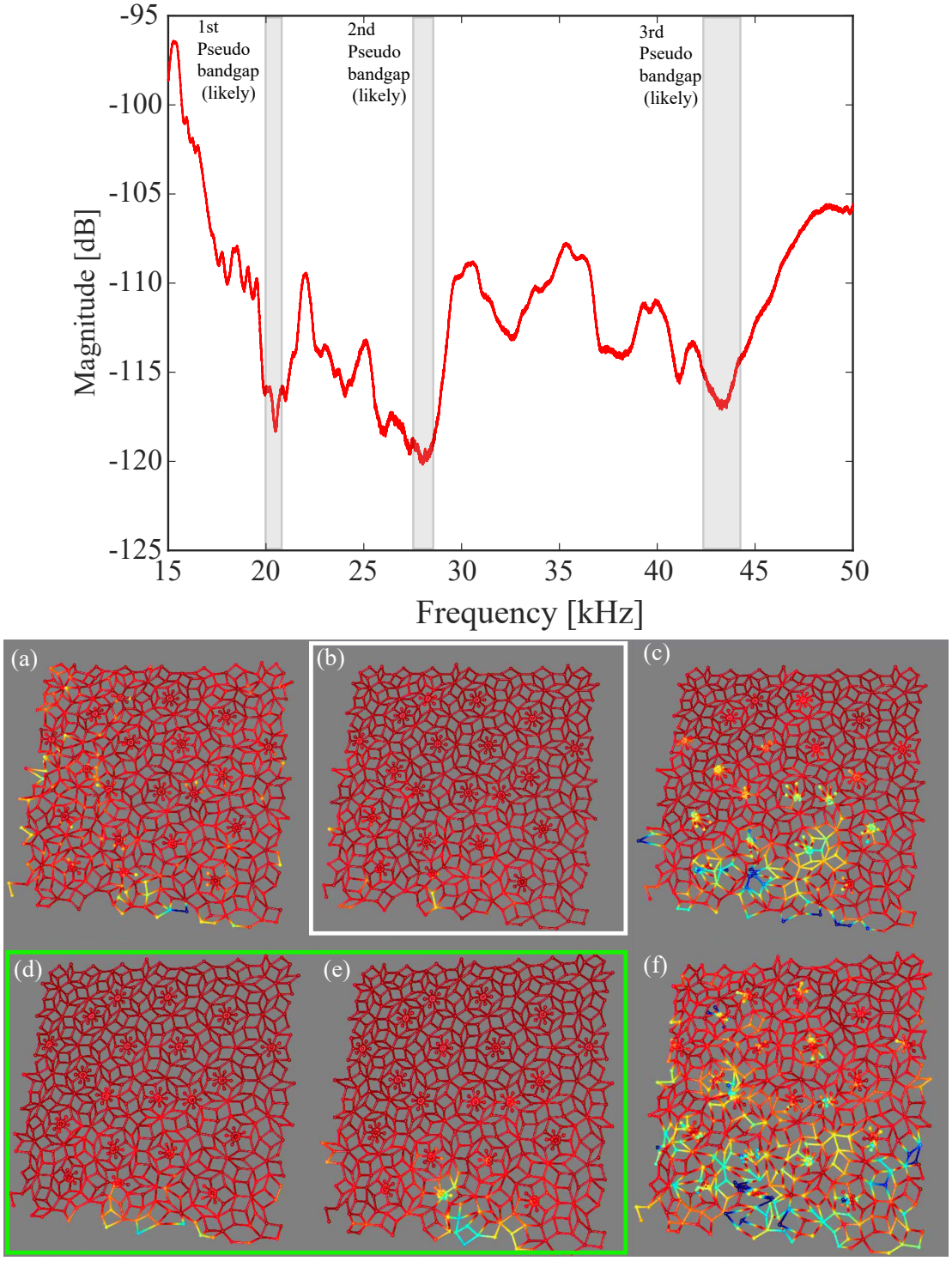


Figure 6.6: (A) Average FRF of the acquisition within the frequency range [15 - 50] kHz, snapshot of sample. Experimental ODS: (a) 19.5449 kHz, (b) 20.4433 kHz, (c) 21.9785 kHz, (d) 28.13671 kHz, (e) 43.41601 kHz, (f) 48.40234 kHz. Highlighted by the white bounding boxes likely to be a Pseudogap and Highlighted by the green bounding boxes likely to be a bandgaps

nature of engineered metamaterial behavior via local resonances and multiple scattering [131, 130]. The corresponding ODSs analysis (Fig. 6.6) highlights regions of diminished motion (green box), confirming that within these bandgap frequencies, vibrational energy

becomes localized or suppressed completely, preventing transmission. These observations align with prior experimental demonstrations of quasi-periodic metastructures, in which modulated resonator arrays produced nontrivial spectral gaps and edge-localized states [132], and quasicrystalline lattices exhibited complex wave beaming and scattering phenomena unique to aperiodic order [133].

### 6.2.2 Characterization of P3-II with PZT

The experimental parameters were systematically configured to ensure precise characterization of the elastic wave behavior. The setup employed three complex averages to enhance signal fidelity, a bandwidth of 1.25 kHz, and an operating frequency range spanning from 0.001 kHz to 1.25 kHz. A total of 951 scan points were defined to achieve high-resolution spatial mapping, while a decoder velocity of 1250 mm/s maintained consistent scanning conditions. An excitation voltage of 120 V was applied to drive the actuation source and effectively excite the structural modes of interest.

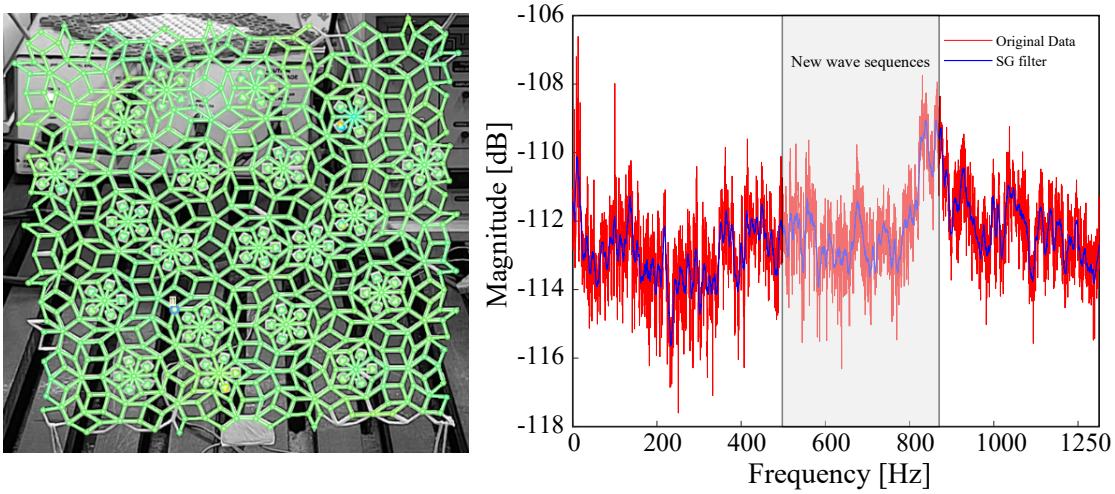


Figure 6.7: (A) Average FRF of the acquisition within the frequency range [0.001 - 1.25] kHz, snapshot of sample with scan points highlighted in green color.

The results obtained from the PSV analysis, as shown in the average FRF in Fig. 6.7, indicate the emergence of a potential bandgap at the lower end of the frequency spectrum, specifically within the range of 0.07109 kHz to 0.1 kHz.

The experimental ODSs revealed the emergence of new wave sequences within the frequency range of 0.44844 kHz to 0.81563 kHz. In this work, the term new wave sequences denotes distinct and repeatable spatial vibration patterns identified through systematic visual inspection of the measured ODSs, which differ from the global and symmetric modes observed at lower frequencies. Within this frequency range, the resonators display irregular oscillatory motion, characterized by nonuniform phase relationships and amplitude distributions, resulting from their interaction with the incoming waves. These sequences are identified through systematic visual inspection of the measured ODSs, fo-

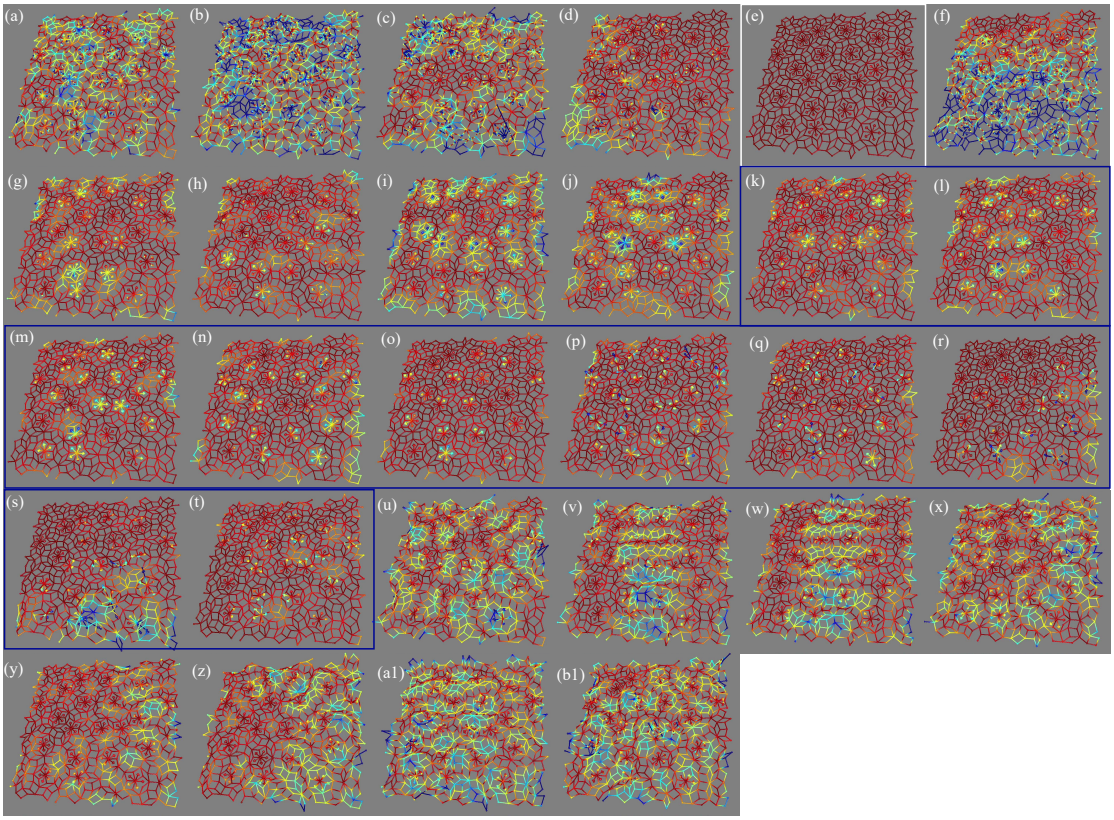


Figure 6.8: Experimental ODSs: (a) 0.00391 kHz, (b) 0.00859 kHz, (c) 0.01758 kHz, (d) 0.04727 kHz, (e) 0.07109 kHz, (f) 0.1 kHz, (g) 0.37852 kHz, (h) 0.41484 kHz, (i) 0.43594 kHz, (j) 0.44844 kHz, (k) 0.46172 kHz, (l) 0.47891 kHz, (m) 0.51563 kHz, (n) 0.52891 kHz, (o) 0.53984 kHz, (p) 0.59727 kHz, (q) 0.59961 kHz, (r) 0.67148 kHz, (s) 0.72148 kHz, (t) 0.76328 kHz, (u) 0.91563 kHz, (v) 0.94297 kHz, (w) 0.96289 kHz, (x) 0.99883 kHz, (y) 1.01172 kHz, (z) 1.09453 kHz, (a1) 1.17305 kHz, (b1) 1.21875 kHz. Highlighted by the white bounding boxes likely to be a bandgap.

cusing on changes in spatial phase, amplitude distribution, and the selective activation of resonators embedded along the fivefold symmetric axes of the Penrose P3 pattern. Such behavior is attributed to the interaction between incident elastic waves and the quasi-periodic stiffness distribution of the aperiodic lattice [126, 127, 130].

### 6.2.3 Characterization of P3-II with electrodynamic shaker

The experimental parameters were systematically configured to ensure precise characterization of wave behavior. These parameters included three complex averages = 3, a bandwidth of 1.25 kHz, and an operating frequency range spanning from 0.001 kHz to 1 kHz. Additionally, a total of 948 scan points were utilized for high-resolution spatial mapping. A decoder velocity of 2.5 m/s was maintained to ensure consistent scanning conditions, while an applied voltage of 0.1 V was supplied to the electrodynamic shaker.

From the averaged Frequency Response Function (FRF), the system initially exhibits global vibrational modes up to approximately 0.38297 kHz. Beyond this frequency, a transition occurs where both local and global modes coexist, extending up to 0.52359 kHz. Furthermore, a distinct region associated with new wave sequences is identified

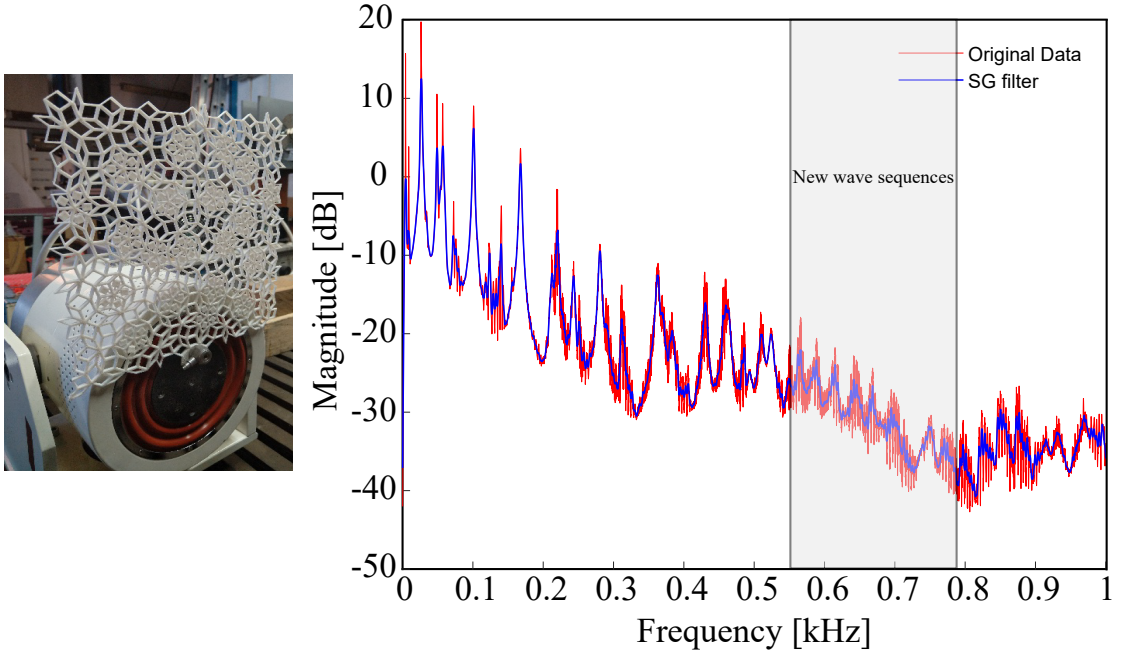


Figure 6.9: (A) Average FRF of the acquisition within the frequency range [0.001 - 1] kHz, snapshot of sample with scan points highlighted in green color.

within the gray-shaded bandgap in the FRF spectrum, as shown in Figure 6.9.

A subset of selected ODSs is presented in Fig. 6.10. The initial mode shapes, shown in Fig. 6.10(a–b), correspond to low-frequency global translational modes of the structure. The subsequent modes, displayed in Fig. 6.10 (c–h), represent global vibration modes in which the resonators move rigidly and coherently with the overall framework. Both symmetric and asymmetric mode shapes are observed in Fig. 6.10 (i–q), while Fig. 6.10 (r–a1) illustrates distinct localized resonance patterns that emerge from the interaction between the incident elastic waves and the fivefold symmetric arrangement of the resonators. Such phenomena are characteristic of Penrose-type quasi-periodic architectures, where the inherent aperiodic order gives rise to complex mode coupling and unique vibrational behaviors [126].

The new wave sequences observed within the frequency range of 0.55-0.79 kHz exhibit highly distinctive dynamic characteristics, as illustrated in Fig. 6.11 (a–r). Interestingly, within this range, only the resonators positioned along the fivefold symmetric axes display pronounced oscillatory motion. As the excitation frequency varies, these resonators respond in a highly frequency-sensitive manner, where even slight frequency shifts lead to substantial changes in the overall wave pattern across the aperiodic structure. Notably, certain wave sequence patterns emerge at closely spaced frequencies yet produce markedly different spatial responses. This phenomenon underscores the sensitivity and robustness of the aperiodic Penrose geometry, in which the inherent stiffness irregularity and quasi-periodic ordering contribute to the formation of these distinctive wave behaviors, rendering the structure highly responsive to dynamic excitation.

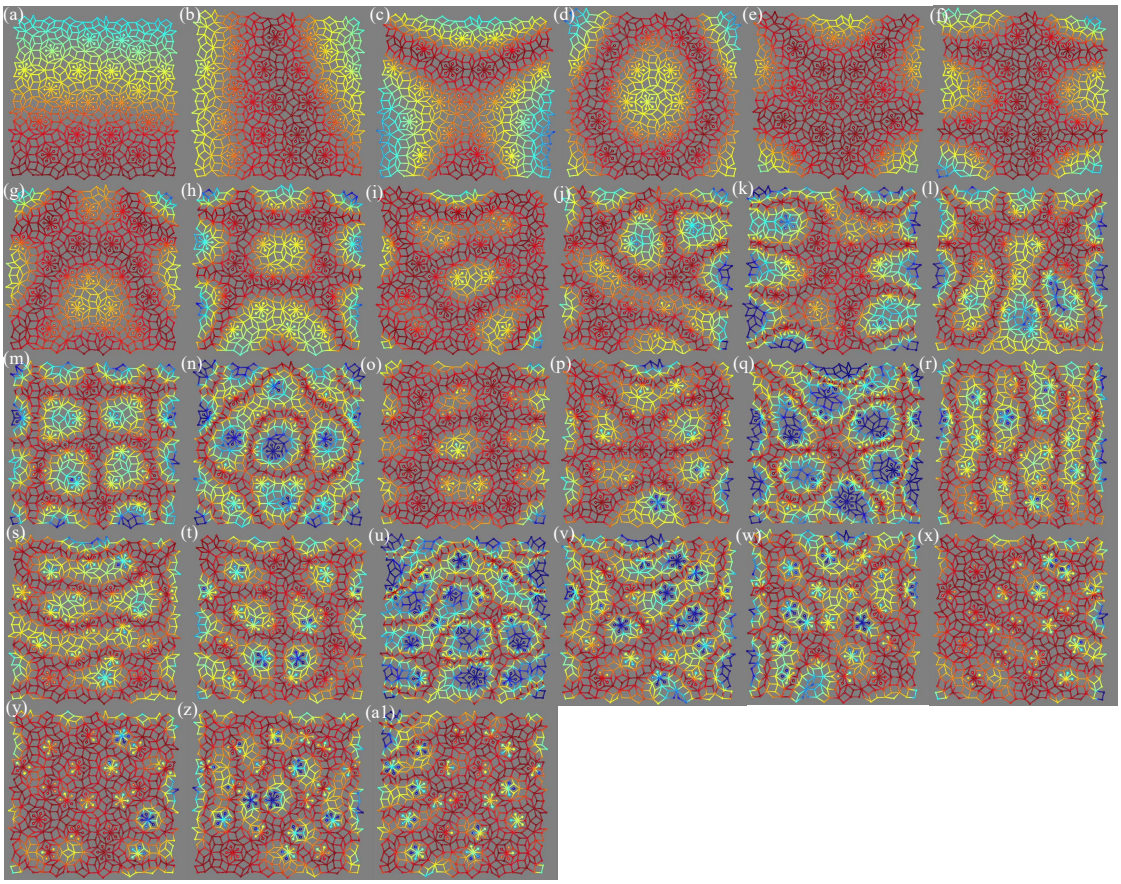


Figure 6.10: Experimental ODSs: (a) 0.00422 kHz, (b) 0.00875 kHz, (c) 0.02625 kHz, (d) 0.04891 kHz, (e) 0.05703 kHz, (f) 0.07219 kHz, (g) 0.10078 kHz, (h) 0.16734 kHz, (i) 0.22047 kHz, (j) 0.24313 kHz, (k) 0.25109 kHz, (l) 0.28063 kHz, (m) 0.28875 kHz, (n) 0.31234 kHz, (o) 0.32297 kHz, (p) 0.35391 kHz, (q) 0.36234 kHz, (r) 0.36875 kHz, (s) 0.37218 kHz, (t) 0.38297 kHz, (u) 0.42939 kHz, (v) 0.45563 kHz, (w) 0.45969 kHz, (x) 0.48269 kHz, (y) 0.48547 kHz, (z) 0.50922 kHz, (a1) 0.52359 kHz.

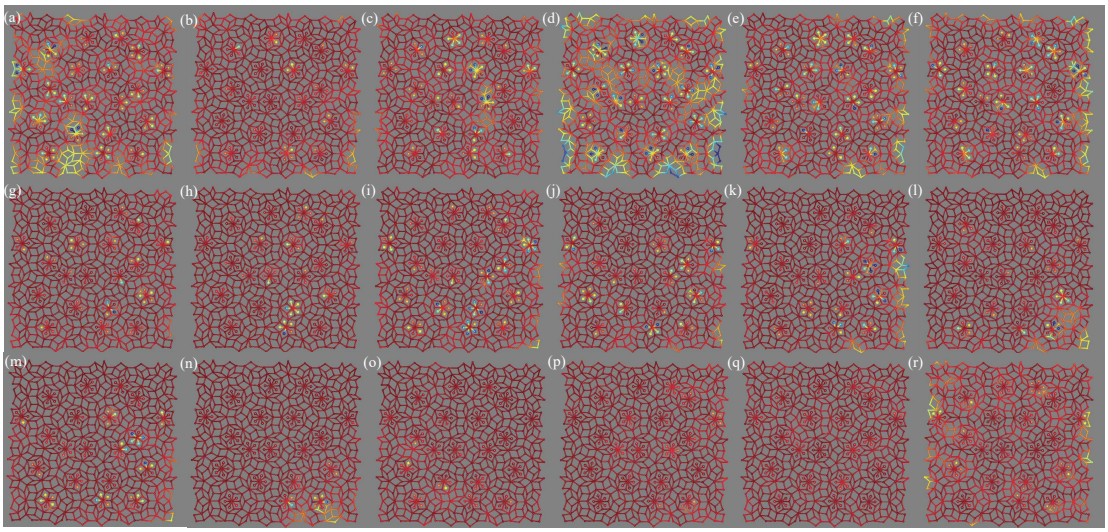


Figure 6.11: Experimental ODSs of new wave sequences: (a) 0.55016 kHz, (b) 0.55797 kHz, (c) 0.56594 kHz, (d) 0.56625 kHz, (e) 0.56875 kHz, (f) 0.58875 kHz, (g) 0.615 kHz, (h) 0.6225 kHz, (i) 0.630 kHz, (j) 0.64219 kHz, (k) 0.65266 kHz, (l) 0.66719 kHz, (m) 0.66844 kHz, (n) 0.69519 kHz, (o) 0.72156 kHz, (p) 0.73953 kHz, (q) 0.77031 kHz, (r) 0.79719 kHz.

## 6.3 Summary

Remarkably, the aperiodic system was capable of exhibiting both pseudobandgaps and pronounced bandgaps, even when implemented with relatively simple cantilever-type resonators. This observation highlights the inherent versatility of quasi-periodic configurations for controlling elastic wave propagation without requiring complex resonant geometries. The introduction of a tip mass significantly modified the system dynamics, leading to the emergence of new wave sequences in addition to localized resonant modes at specific frequencies. As expected, the added mass reduced the resonant frequency of the cantilevers, thereby enhancing local resonance effects and promoting stronger attenuation in the vicinity of these frequencies. The aperiodic tiling realized through the Penrose P3 pattern plays a central role in this behavior. Its spatial heterogeneity and fivefold rotational symmetry introduce translational irregularity, resulting in non-equivalent scattering centers distributed throughout the structure. These scattering centers promote multiple interference mechanisms through the interaction of locally resonant modes, driven by the aperiodic geometry. Compared with conventional periodic metamaterials, the Penrose P3 configuration enables bandgap formation through a combination of multi-scale scattering, resonator coupling, and wave localization induced by interference. Consequently, the system operates through a hybrid mechanism in which structural aperiodicity and resonator dynamics jointly govern wave suppression and localization, offering enhanced and tunable control of elastic wave transport relative to traditional periodic lattices [126, 127, 130, 132, 133].

# Chapter 7

# Conclusions

This dissertation investigated the dynamic behavior of acoustic metamaterial architectures aimed at low-frequency and broadband vibration mitigation, with a particular focus on locally resonant two-dimensional honeycomb lattices and their aperiodic counterparts. The central contribution of this work lies in the systematic experimental and numerical investigation of embedded resonators-orders of magnitude smaller than the host lattice-that act as continuous substructures capable of generating multiple low-frequency attenuation bands. Through coordinated experimental measurements and finite element modeling, this thesis establishes a consistent framework for characterizing multi-bandgap behavior in finite, non-ideal metamaterial systems.

Two resonator architectures were examined in detail: cantilever beams with tip masses and spider-web–like resonators with central masses. The spider-web configuration proved especially effective due to its high modal density in the low-frequency regime, enabling the formation of multiple locally resonant bandgaps below 10 kHz, a frequency range of direct relevance for engineering vibration and noise control. Parametric dispersion analyses demonstrated that bandgap positions and widths can be shifted through geometric and material variations, primarily by altering resonator stiffness, while preserving the underlying multi-bandgap structure. Experimental investigations on large-scale prototypes, characterized using three-dimensional laser scanning vibrometry under electrodynamic shaker and PZT excitation, confirmed the predicted bandgaps with good agreement. Although finite-size effects and structural damping resulted in modest reductions in bandgap width, the experimentally observed modal transitions and attenuation levels remained consistent with numerical predictions.

Across all periodic configurations, a recurring modal sequence was identified: global honeycomb-type deformations dominate at low frequencies, followed by acoustic modes immediately below the first bandgap and optical modes above it. These transitions were robust under moderate parameter variations and limited structural disorder, such as missing or detuned resonators, highlighting the intrinsic resilience of locally resonant bandgap mechanisms compared to Bragg-based scattering in conventional phononic crystals.

The nonlinear dynamic response of spider-web resonator metamaterials was further examined under increasing excitation amplitude. The baseline configuration exhibited hardening-type behavior in higher global modes, attributed to geometric nonlinearities. In contrast, an intentionally non-uniform and fabrication-imperfect variant displayed pronounced softening behavior in both local and global modes, particularly within the acoustic branch. This softening response was associated with effective mass changes induced by large-amplitude resonator motion and resulted in an apparent widening of the first attenuation band. These observations are interpreted as excitation-dependent modifications of wave attenuation in finite structures, rather than as shifts of the underlying linear Bloch band structure. Unit-cell measurements corroborated these findings, revealing amplitude-dependent frequency shifts consistent with Duffing-type oscillator behavior.

Beyond periodic lattices, wave confinement was explored in electrospun membrane metamaterials incorporating attached resonators and exhibiting manufacturing-induced compositional disorder. Variations in membrane stiffness, mass density, and resonator attachment disrupted periodic wave transport and led to spatially localized vibrational modes. The observed confinement is consistent with disorder-induced multiple scattering and Anderson-type localization, wherein energy becomes trapped in spatially confined regions without reliance on physical boundaries or topological protection. These results demonstrate that disorder, when properly characterized, can promote robust localization phenomena distinct from periodic bandgap formation.

Finally, aperiodic metamaterials based on Penrose quasilattice tilings were investigated to assess wave propagation in the absence of translational symmetry. In these systems, attenuation bands and localized responses emerged from a combination of local resonance, multi-scale interference, and geometric aperiodicity. The introduction of tip masses enhanced low-frequency resonances and promoted hybridized localization mechanisms driven by the intrinsic geometric diversity of the quasilattice. Unlike periodic lattices, where bandgaps arise from synchronized resonator behavior, the Penrose-based structures exhibited unconventional modal sequences governed by local environments rather than Bloch-wave ordering.

Taken together, the results of this thesis demonstrate that nonlinearity, geometric variability, and disorder are not merely imperfections to be avoided, but influential factors that can be leveraged to tailor wave attenuation and localization in realistic metamaterial systems. The findings show that multiple low-frequency attenuation mechanisms-locally resonant bandgaps, nonlinear amplitude-dependent modulation, disorder-induced localization, and aperiodic interference-can coexist and complement one another in finite structures.

Future research may focus on extending these concepts to three-dimensional architectures, systematically controlling disorder statistics, and exploring hybrid numerical-experimental optimization strategies. While the present work demonstrates passive excitation-

dependent modulation, the integration of active elements and feedback-based control strategies remains an open direction for future investigation. Overall, this dissertation provides experimental evidence and physical insight into wave propagation in non-ideal metamaterials and contributes to the development of robust, lightweight structures for vibration-sensitive engineering applications operating under realistic conditions.

# Appendix A

# Modeling of Metamaterial with Local Resonator

## A.1 Metamaterial Modeling

The mechanical modeling of the honeycomb metamaterial and the Plane Wave Expansion (PWE) method employed to predict its bandgap behavior and perform the sensitivity analyses summarized here are the result of the work of my co-authors in the paper M. Murer, S. K. Guruva, G. Formica, and W. Lacarbonara, "A multi-bandgap metamaterial with multi-frequency resonators," Journal of Composite Materials, vol. 57, pp. 783–804, Feb. 2023. In the present work, the modeling and computational results from that study are reported to provide the theoretical and numerical framework within which I have conducted the experimental campaigns aimed at validating and refining the proposed modeling approach. The honeycomb framework is modeled using a homogenization approach that simplifies the nonuniform cellular geometry into an equivalent homogeneous orthotropic plate. This plate incorporates a periodic distribution of resonators arranged according to the hexagonal lattice of the honeycomb cells. In this chapter, an extension of the locally resonant (LR) mechanism is introduced by embedding infinite-dimensional resonators within a honeycomb-inspired cellular framework (Fig. A.1). The resonators, modeled as beams undergoing flexural motion, emulate either spider-web configurations with a central mass or cantilever beams with a tip mass. Spider webs, renowned for their lightweight structure, high strength, and remarkable resilience due to their high degree of connectivity have inspired numerous engineering designs [134, 135]. These resonators are further reduced into multi-frequency systems by projecting their bending motions onto their respective modal bases. As a result, multiple bandgaps arise, exhibiting strong sensitivity to the parameters of the intracellular resonators.

This formulation is consistent with previous analytical studies on two-dimensional (2D) cellular structures, which have been investigated through homogenized, equivalent continuum plate-like models. In the equivalent plate model for honeycomb-shaped 2D

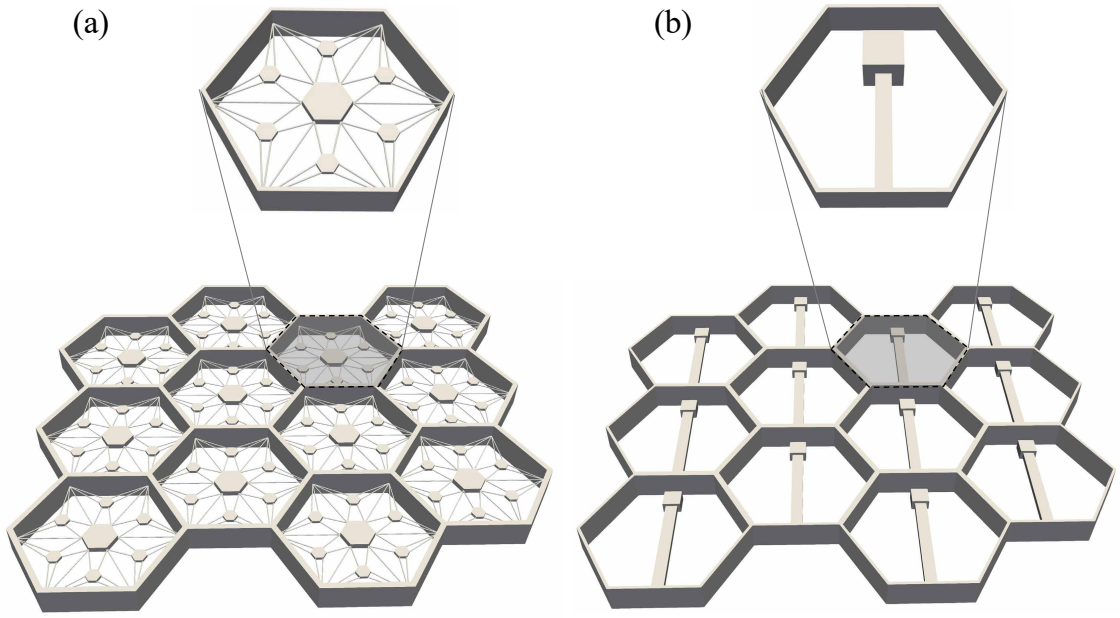


Figure A.1: Metamaterial cellular architectures: honeycomb structure hosting the intracellular resonators: (a) spider-web-inspired resonator with central mass and (d) cantilever resonator with tip mass.

cellular structures proposed by Gibson and Ashby [136], the honeycomb cells are represented as beam network systems. Subsequent improvements and generalizations of this model accounted for the influence of stresses in the cell vertices [137, 138].

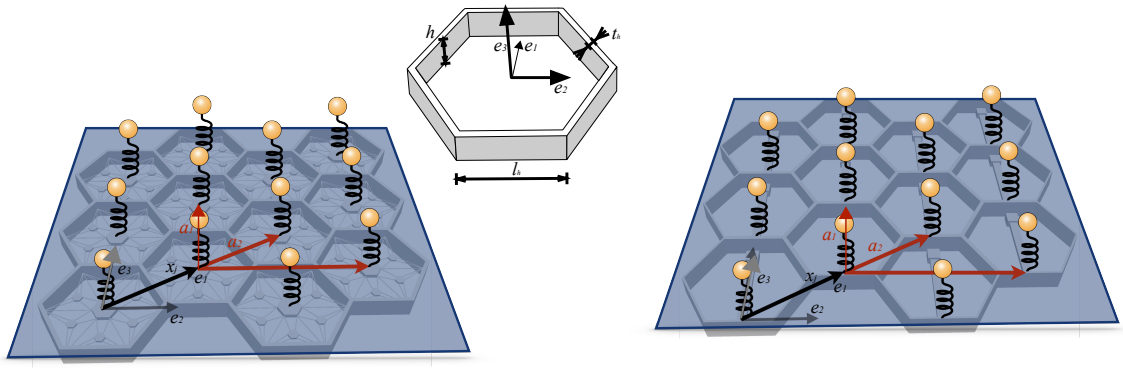

Figure A.2: Schematic view of the orthotropic plate models with the periodically distributed (left) spider-web resonators and (right) cantilever resonators. The hexagonal lattice vectors are denoted by ( $\mathbf{a}_1, \mathbf{a}_2$ ) and the fixed frame unit vectors by ( $\mathbf{e}_1, \mathbf{e}_2, \mathbf{e}_3$ ); (top) honeycomb cell geometry with wall height $h$, side length $l_h$, and thickness $t_h$.

Fig. A.2 illustrates the two reference configurations of the infinitely long equivalent orthotropic plates, whose mid-surfaces lie in the $\mathbf{e}_1$–$\mathbf{e}_2$ plane. The locations of the equivalent resonators (left) spider-web and (right) cantilever types, are determined by the lattice vectors $\mathbf{a}_1 = a\mathbf{e}_1$ and $\mathbf{a}_2 = a/2\left(\mathbf{e}_1 + \sqrt{3}\mathbf{e}_2\right)$, where $a$ denotes the lattice parameter (see Figure 2). Each multi-degree-of-freedom (multi-DOF) resonator, simplified here as a mass–spring system, results from the modal reduction process in which the motion of the infinite-dimensional, spatially continuous resonators (i.e., spider webs with a central

mass and cantilevers with a tip mass) is projected onto the modal basis of the system, retaining an arbitrary number of modes.The modal reduction of the partial differential equations governing the motion of the spatially continuous resonators is carried out via the Galerkin method, yielding the modal masses and stiffnesses associated with each bending mode (see, e.g., [139, 140]). The $j$-th resonator is located at the lattice point $\mathbf{x}_j = m\mathbf{a}_1 + n\mathbf{a}_2$, where $m$ and $n$ are integers.

The equivalent orthotropic plate model derived from the homogenization of the honeycomb structure [136, 137] is characterized by the equivalent elastic moduli $\left(E^\star_\star, G^\star_{\star\beta}, v^\star_{\star\beta}\right)$ $(\star, \beta = 1, 2, 3)$ and the equivalent mass density $\rho^\star$ (see Appendix B). The thin-plate theory [139] is adopted to describe the dynamics of the honeycomb structure with attached resonators. The resulting equations of motion governing the orthotropic plate resonator coupled system are then established as follows:

$$\begin{aligned}\rho^\star h\,\frac{\partial^2 w(\mathbf{x},t)}{\partial t^2} + D^\star_{11}\,\frac{\partial^4 w(\mathbf{x},t)}{\partial x_1^4} + \left(2D^\star_{12} + 4D^\star_{66}\right)\frac{\partial^4 w(\mathbf{x},t)}{\partial x_1^2 \partial x_2^2} + D^\star_{22}\,\frac{\partial^4 w(\mathbf{x},t)}{\partial x_2^4} \\ = \sum_{i,j} k_{ij}\left[z_{ij}(t) - w(\mathbf{x}_j,t)\right]\delta(\mathbf{x}-\mathbf{x}_j)\,,\end{aligned} \tag{A.1}$$

$$m_{ij}\,\frac{\mathrm{d}^2 z_{ij}(t)}{\mathrm{d}t^2} + k_{ij}\left[z_{ij}(t) - w(\mathbf{x}_j,t)\right] = 0 \tag{A.2}$$

where $\mathbf{x} = x_1\mathbf{e}_1 + x_2\mathbf{e}_2$ is the position vector of a plate mid-surface point; $t$ is time; $w(\mathbf{x},t)$ is the plate deflection at $\mathbf{x}$; $z_{ij}(t)$ is the generalized displacement of the $i$-th mode of the $j$-th resonator located at $\mathbf{x}_j$; $h$ is the plate thickness (Fig. A.2); $D^\star_{rs}$ are the bending stiffnesses; $k_{ij}$ and $m_{ij}$ are the modal stiffness and mass of the $i$-th mode of the $j$-th resonator; and $\delta(\mathbf{x}-\mathbf{x}_j)$ is the 2D Dirac delta.

In order to recast the problem in nondimensional form, the following variables and parameters are introduced:

$$\begin{aligned}&\tilde{x}_1 = \frac{x_1}{a}, \quad \tilde{x}_2 = \frac{x_2}{a}, \quad \tilde{t} = \omega_0 t, \quad \tilde{w} = \frac{w}{a}, \quad \tilde{w}_{ij} = \frac{w_j}{a}, \\ &\tilde{\mathbf{x}} = \frac{\mathbf{x}}{a}, \quad \tilde{\mathbf{x}}_j = \frac{\mathbf{x}_j}{a}, \quad \tilde{D}_{12} = \frac{D^\star_{12}}{D^\star_{11}}, \quad \tilde{D}_{22} = \frac{D^\star_{22}}{D^\star_{11}}, \quad \tilde{D}_{66} = \frac{D^\star_{66}}{D^\star_{11}}\end{aligned} \tag{A.3}$$

where $a = |\mathbf{a}_1|$ is the length of the basis vector $\mathbf{a}_1$ of the direct lattice, $S = |\mathbf{a}_1 \times \mathbf{a}_2|$ is the area of the unit cell associated with the periodic lattice, and $\omega_0 = \sqrt{D^\star_{11}/\left(\rho^\star h a^4\right)}$ is the characteristic frequency.

The rescaling set forth by (2.3) in the equations of motion given by (2.1) yields the following nondimensional form:

$$\frac{\partial^2\tilde{w}(\tilde{\mathbf{x}},\tilde{t})}{\partial\hat{t}^2}+\frac{\partial^4\tilde{w}(\tilde{\mathbf{x}},\tilde{t})}{\partial\tilde{x}_1^4}+\left(2\tilde{D}_{12}+4\tilde{D}_{66}\right)\frac{\partial^4\tilde{w}(\tilde{\mathbf{x}},\tilde{t})}{\partial\tilde{x}_1^2\partial\tilde{x}_2^2}+\tilde{D}_{22}\frac{\partial^4\tilde{w}(\tilde{\mathbf{x}},\tilde{t})}{\partial\tilde{x}_2^4} = \sum_{i,j} S\left\{\tilde{k}_{ij}\left[\tilde{z}_{ij}(\tilde{t})-\tilde{w}\left(\tilde{\mathbf{x}}_j,\tilde{t}\right)\right]\delta\left(\tilde{\mathbf{x}}-\tilde{\mathbf{x}}_j\right)\right\}, \tag{A.4}$$

$$\tilde{m}_{ij}\frac{d^2\tilde{z}_{ij}(\tilde{t})}{d\tilde{t}^2}+\tilde{k}_{ig}\left[\tilde{z}_{ij}(\tilde{t})-\tilde{w}\left(\tilde{\mathbf{x}}_j,\tilde{t}\right)\right]=0 \tag{A.5}$$

where $\tilde{m}_{ij}=m_{ij}/\left(\rho^\star hS\right)$ is the ratio between the $ith$ modal mass of the $jth$ resonator and the unit cell mass and $\tilde{k}_{ij}=\left(k_{ij}S/D_{11}^\star\right)a^4/S^2$ is the nondimensional modal resonator stiffness.

According to the PWE method, [141, 142, 143] the solutions of equations (2.4) and (2.5) are first sought as harmonic solutions; that is, $\tilde{w}(\tilde{\mathbf{x}},\tilde{t})=\bar{w}(\tilde{\mathbf{x}})e^{-i\bar{\omega}\bar{t}}$ and $\tilde{z}_{ij}(t)=\bar{z}_{ij}e^{-i\bar{\omega}\bar{t}}$. Moreover, due to the space periodicity of the resonators lattice, according to the Floquet-Bloch theorem, the plate and resonators displacements are quasi-periodic functions (in space) expressed in a Fourier series of the reciprocal-lattice vector $\tilde{\mathbf{G}}_{mn}=a\left(m\mathbf{b}_1+n\mathbf{b}_2\right)$ in which the basis vectors of the reciprocal lattice are given by $\mathbf{b}_1=2\pi/a\left(\mathbf{e}_1-1/\sqrt{3}\mathbf{e}_2\right)$ and $\mathbf{b}_2=4\pi/(a\sqrt{3})\mathbf{e}_2$ and satisfy the condition $\mathbf{a}_i\cdot\mathbf{b}_j=2\pi\delta_{ij}$. The components of $\tilde{\mathbf{G}}_{mn}$ along the basis vectors will be denoted, henceforth, by $\tilde{G}_{mn}^{(1)}$ and $\tilde{G}_{mn}^{(2)}$, respectively. The solutions are thus expressed as

$$\begin{aligned}\bar{w}(\tilde{\mathbf{x}}) &= e^{-i\tilde{\mathbf{k}}\tilde{\mathbf{x}}}\sum_{m,n}\bar{W}_{mn}e^{-j\tilde{G}_{mn}\tilde{\mathbf{x}}},\\ \left(\bar{w}\left(\tilde{\mathbf{x}}_j\right),z_{ij}\left(\tilde{\mathbf{x}}_j\right)\right) &= \left(\bar{w}(\mathbf{0}),z_{j0}\right)e^{-j\tilde{\mathbf{k}}\tilde{\mathbf{x}}_j}.\end{aligned} \tag{A.6}$$

where the space modulation is ruled by the nondimensional Bloch wave vector $\overline{\mathbf{k}}=a\mathbf{k}$; $\bar{w}(\mathbf{0})$ and $\bar{z}_{i0}$ denote the plate and resonator displacements at the origin, respectively. By making use of the following key formula:

$$\sum_{i,j}e^{-i\mathbf{k}\tilde{\mathbf{x}}_j}\delta\left(\tilde{\mathbf{x}}-\tilde{\mathbf{x}}_j\right)=e^{-i\mathbf{k}\tilde{\mathbf{x}}^2}\sum_{i,j}\delta\left(\tilde{\mathbf{x}}-\tilde{\mathbf{x}}_j\right) \quad =\left(e^{-i\mathbf{k}\tilde{\mathbf{x}}}\right)\frac{1}{S}\sum_{m,n}e^{-j\tilde{\mathbf{G}}\tilde{\mathbf{x}}} \tag{A.7}$$

and substituting (2.6) into (2.4) and (2.5) yields the following reduced equations governing the harmonic components $\bar{W}_{mn}$ and the amplitudes $\bar{z}_{i0}$ of the resonators motion at the origin:

$$\begin{aligned}&-\tilde{\omega}^2\bar{W}_{mn}+\left[\left(\tilde{k}_1+\tilde{G}_{mn}^{(1)}\right)^4+\left(2\tilde{D}_{12}+4\tilde{D}_{66}\right)\left(\tilde{k}_1+\tilde{G}_{mn}^{(1)}\right)^2\left(\tilde{k}_2+\tilde{G}_{mn}^{(2)}\right)^2\right.\\ &\left.+\tilde{D}_{22}\left(\tilde{k}_2+\tilde{G}_{mn}^{(2)}\right)^4\right]\bar{W}_{mn}=\tilde{k}_{ij}\left[\bar{z}_{i0}-\sum_{m,n}\bar{W}_{mn}\right],\end{aligned} \tag{A.8}$$

$$-\tilde{m}_{ij}\tilde{\omega}^2\bar{z}_0 + \tilde{k}_{ij}\left[\bar{z}_{i0} - \sum_{m,n}\bar{W}_{mn}\right] = 0\,. \tag{A.9}$$

The computational strategy to find the solutions of equations (2.8) and (2.9) is discussed in Appendix B.1.

### A.1.1 Resonators modeling

The spatially continuous resonators can be represented by an equivalent set of discrete mass-spring systems, allowing their ability to induce multiple band gaps to be effectively analyzed. The two resonator architectures under investigation, along with their corresponding simplified mechanical models, are illustrated in Fig. A.3.

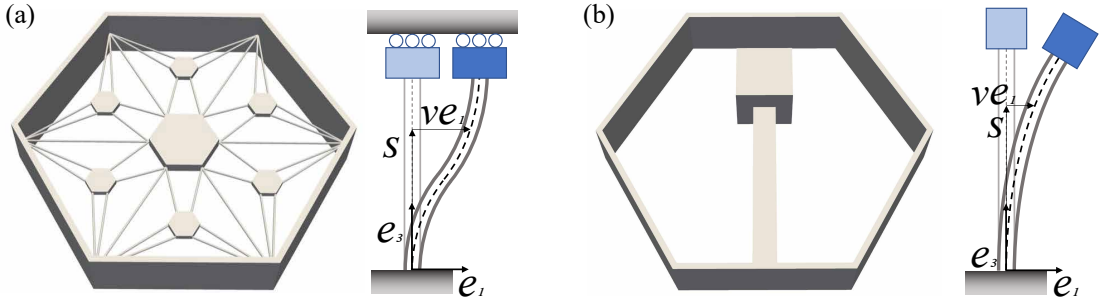


Figure A.3: The intracellular resonator architectures together with their mechanical models: (a) simplified spider web-like resonator and (b) cantilever with tip mass. The unit vectors ej are the local axes employed to describe the beam motion.

For both resonator configurations, the adopted mechanical model consists of an equivalent beam subjected to appropriate boundary conditions and equipped with lumped masses. In the case of the spider-web-like resonator, the equivalent beam represents one of the six primary radial beams, clamped to the hexagonal wall at one end and connected to a sliding clamp with a lumped mass corresponding to one-sixth of the central resonator mass at the other. For the cantilever-type resonator architecture, the equivalent beam is modeled as a cantilever with a tip mass undergoing planar bending motion (see Fig. A.3). The $j$-th resonator modal mass $m_{ij}$ and stiffness $k_{ij}$ associated with the $i$-th mode can be obtained via a Galerkin based modal reduction of the governing PDE. For the sake of generality, the Euler-Bernoulli beam model is considered accounting also for the presence of prestress $N_j$ so that the equation of motion for the $j$-th resonator can be written as

$$\rho_j A_j \partial_{tt} v_j + EI_j \partial_{ssss} v_j + N_j \partial_{ss} v_j = 0 \tag{A.10}$$

where $v_j$ is the beam bending displacement, $\rho_j$ is the beam density, $A_j$ is the area of the beam cross section, and $EI_j$ is the bending stiffness. Equation (2.10) is supplemented by the boundary conditions associated with each of the two designs. Upon rescaling the lengths by $a$ so that the nondimensional span is $l_j = l_j/a$, the nondimensional ar-

clength is $\tilde{s} = s/a$, the nondimensional modal mass $\tilde{m}_{ij} = m_{ij}/(\rho^\star hS)$ and stiffness $\dot{k}_{ij} = k_{ij}a^4/(D_{11}^\star S)$ become:

$$\begin{aligned}\tilde{m}_{ij} &= \mu_{lj} + \phi_{ij}(\tilde{l}_j)\mu_{Mj}\phi_{ij}(\tilde{l}_j) \\ \tilde{k}_{ij} &= -\tilde{N}_j \int_0^{\tilde{l}} \phi'_{ij}(\tilde{s})\phi'_{ij}(\tilde{s})\tilde{d}s + \tilde{E}I_j \int_0^{\tilde{l}} \phi''_{ij}(\tilde{s})\phi''_{ij}(\tilde{s})\tilde{d}s, \quad i = 1, \ldots, n_r\end{aligned} \tag{A.11}$$

where $n_r$ denotes the number of retained modes, $\phi_y(s)$ is the *ith* eigenfunction, and $M_j$ is the tip mass. The following nondimensional quantities are introduced to obtain the nondimensional modal mass $\tilde{m}_{ij}$ and stiffness $\tilde{k}_{ij}$:

$$\tilde{E}I_j = \frac{EI_j a}{D_{11}^\star S'},\ \mu_{lb} = \frac{\rho A_j a}{\rho^\star hS'},\ \mu_{Mj} = \frac{M_j}{\rho^\star hS},\ \tilde{N}_j = \frac{N_j a^3}{D_{11}^\star S} \tag{A.12}$$

Note that the classical normalization condition was enforced on the mode shapes: $\int_0^{\tilde{l}} \phi_{ij}(\tilde{s})\phi_{ij}(\tilde{s})d\tilde{s} = 1$.

**Cantilever with varying tip-mass resonator**

Figure A.4 illustrates the lowest four mode shapes of the cantilever resonator, while the corresponding nondimensional parameters and modal coefficients are summarized in Table A.1. The resonators were tuned such that, once embedded in the host structure, the resulting metamaterials exhibited low-, medium-, and high-frequency band gaps.

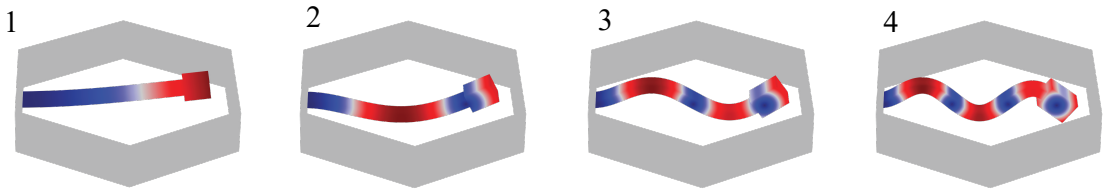


Figure A.4: The lowest four mode shapes of the cantilever resonator. The nondimensional parameters and modal coefficients are provided in Tab. A.1.

Table A.1: Nondimensional parameters and modal coefficients for the cantilever resonators. Par stands for Parameter.

| **Par** | **LF** | **MF** | **HF** |
|---|---|---|---|
| $I$ | 0.78 | 0.57 | 0.42 |
| $\tilde{h}_b$ | 0.07 | 0.07 | 0.07 |
| $\widehat{E}I$ | 0.0413 | 0.0413 | 0.0413 |
| $\mu_b$ | 0.288 | 0.288 | 0.288 |
| $\mu_M$ | 0.742 | 0.0773 | 0.016 |
| $\tilde{m}_{ij}$ | 4.26, 0.30, 0.29, 0.28 | 0.85, 0.33, 0.31, 0.30 | 0.44, 0.35, 0.32, 0.31 |
| $k_{ij}$ | 1.4, 27.7, 278.2, 1196 | 4.8, 130.5, 1111, 4532 | 15.2, 531.7, 4105, 15836 |
| $f_i$ | 0.56, 9.63, 30.86, 64.19 | 2.38, 19.70, 60.13, 123.24 | 5.84, 38.94, 112.77, 226.09 |

The resonators were tuned such that, once embedded in the host structure, the resulting metamaterials exhibited low, medium, and high-frequency band gaps. Using the

selected parameters, the lowest four nondimensional frequencies $\tilde{f}_i$ corresponding to the low-frequency, medium-frequency, and high-frequency designs for the cantilever configuration are reported in Tab. A.1. The corresponding mode shapes of the two resonator architectures, along with the parameters used for the computations, are illustrated in Fig. A.4. Further details of the experimental results are provided in Chapter 2.

**Spider-web-resonator**

Similarly, using the selected parameters, the lowest four nondimensional frequencies $\tilde{f}_i$ corresponding to the low-frequency, medium-frequency, and high-frequency designs for the spider-web resonators are reported in Tab. A.2. The resulting mode shapes of the two resonator architectures, along with the parameters used for the computations, are illustrated in Fig. A.2.

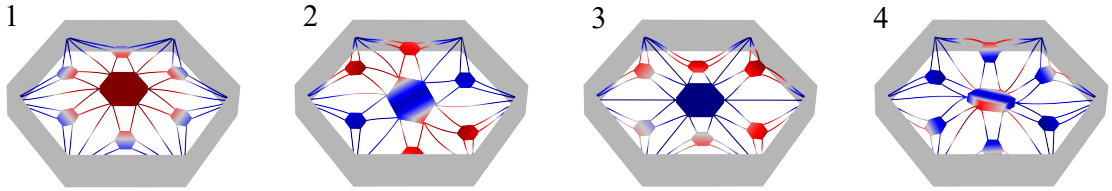


Figure A.5: The lowest four mode shapes of the spider-web resonator. The nondimensional parameters and modal coefficients are provided in Tab.A.2.

Table A.2: Nondimensional parameters and modal coefficients for the spider-web resonators. Par stands for Parameter.

| **Par** | **LF** | **MF** | **HF** |
|---|---|---|---|
| $\tilde{h}_b$ | 0.009 | 0.018 | 0.026 |
| $EI$ | 0.00016 | 0.0013 | 0.0043 |
| $\mu_b$ | 0.072 | 0.144 | 0.216 |
| $\mu_M$ | 1.34 | 0.685 | 0.289 |
| $\tilde{m}_{ij}$ | 7.26, 0.073, 0.072, 0.071 | 3.82, 0.146, 0.145, 0.144 | 1.75, 0.23, 0.22, 0.21 |
| $k_{ij}$ | 0.083, 1.31, 9.93, 38.12 | 0.66, 10.79, 80.27, 306.5 | 2.20, 39.40, 279.60, 1051.70 |
| $f_i$ | 0.10, 4.25, 11.72, 22.97 | 0.41, 8.57, 23.50, 46.01 | 1.12, 13.12, 35.54, 69.29 |

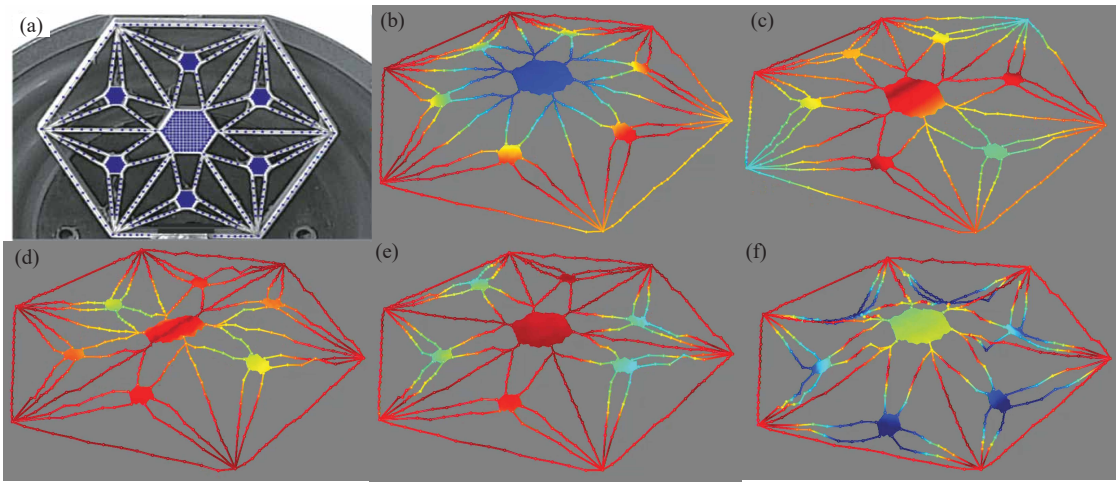


Figure A.6: (a) Picture of the additively manufactured macrosample of the spider web-like resonator mounted onto an electrodynamic shaker. Snapshots of the PSV acquired (964 scan points) operational deflection shapes whose measured frequencies are: (b) 200 Hz, (c) 417 Hz, (d) 473 Hz, (e) 687 Hz, (f) 767 Hz.

The mode shapes were obtained by manipulating symbolic expressions and numerically solving the corresponding eigenvalue problems using Wolfram Mathematica. An experimental validation of the spider-web resonators modal response was also carried out, and the main results, in terms of operational deformed shapes, are shown in Fig. A.6. The detailed experimental results are presented in Chapter 3.

# Appendix B

# Honeycomb Reduction to an Equivalent Orthotropic Plate

The elastic constants of the equivalent elastic continuum, obtained from the homogenization proposed in Gibson and Ashby [136] for a 3D regular honeycomb lattice, are: $E^\star_\star, G^\star_{\star\beta}$, $v^\star_{\star\beta}$, for $(\star,\beta) = 1,2,3$, (i.e., equivalent Young's moduli, equivalent shear moduli, and equivalent Poisson's ratios, respectively). By considering regular hexagons (with the same length $l_h$ for each side and $\theta = \pi/6$ ), such constants, for the in-plane moduli, turn out to be:

$$E^\star_1 = E^\star_2 = 2.3\,(t_h/l_h)\,E, \quad G^\star_{12} = 0.57\,(t_h/l_h)^3\,E$$
$$v^\star_{12} = v^\star_{21} = \frac{1+(1.4+1.5v)\,(t_h/l_h)^2}{1+(5.4+1.5v)\,(t_h/l_h)^2}$$

while, for the out-of-plane moduli, the formulas read:

$$\frac{E^\star_3}{E} = \left[\frac{1+2}{2(1+\sin\theta)\cos\theta}\right]\frac{t_h}{l_h}, \quad \frac{G^\star_{13}}{G} = \frac{G^\star_{23}}{G} = 0.577\left(\frac{t_h}{l_h}\right)$$
$$v^\star_{13} = \frac{E^\star_1}{E^\star_3}v \approx 0, \quad v^\star_{23} = \frac{E^\star_2}{E^\star_3}v \approx 0, \quad v^\star_{31} = v^\star_{32} = v.$$

The parameters ( $h, t_h, l_h, \theta$ ) describe the cell geometry as shown in Figure 2. Finally, the mass density ratio is given by:

$$\frac{\rho^\star}{\rho} = \left[\frac{1+2}{2(1+\sin\theta)\cos\theta}\right]\frac{t_h}{l_h}$$

which gets simplified into $\rho^\star/\rho = \frac{2}{\sqrt{3}}t_h/l_h$ for regular hexagons. The above formulas lead to $E^*_3/E = \rho^*/\rho \approx t_h/l_h$. The bending stiffness coefficients of the (thin) orthotropic plate can be therefore obtained according to Lacarbonara [139] as functions of the equivalent elastic coefficients: $D^\star_{rs} = h^3/12 L^\star_{rs}\left(E^\star_i, v^\star_{ij}, G^\star_{ij}\right)$, where the coefficients $L^\star_{rs}$ are expressed in terms of the angle $\phi$ between the orthotropy axis and $\mathbf{e}_1$. That is, $L^\star_{11} = \bar{C}_1 + \bar{C}_2\cos 2\phi + \bar{C}_3\cos 4\phi$, $L^\star_{12} = \bar{C}_4 - \bar{C}_3\cos 4\phi$, $L^\star_{22} = \bar{C}_1 - \bar{C}_2\cos 2\phi + \bar{C}_3\cos 4\phi$, $L^\star_{66} =$

$\bar{C}_5 - \bar{C}_3 \cos 4\phi$, in which, upon setting $\bar{v}^\star = (1 - v_{12}^\star v_{21}^\star)$, $\bar{C}_2 = \frac{1}{2\bar{v}^*}\left(E_1^\star - E_2^\star\right), \bar{C}_1 = \frac{1}{8\bar{v}^*}\left[(3 + 2v_{21}^\star) E_1^\star + 3E_2^\star + 4v^\star G_{12}^\star\right]$, $\bar{C}_3 = \frac{1}{8\bar{v}^\star}\left[(1 - 2v_{21}^\star) E_1^\star + E_2^\star - 4v^\star G_{12}^\star\right]$, $\bar{C}_4 = \frac{1}{8\bar{v}^\star}\left[(1 + 6v_{21}^\star) E_1^\star + E_2^\star - 4v^\star G_{12}^\star\right], \bar{C}_5 = \frac{1}{8\bar{v}^\star}\left[(1 - 2v_{21}^\star) E_1^\star + E_2^\star + 4v^\star G_{12}^\star\right]$.

## B.1 Solution strategy for the mechanical system

The solution of equations (2.8) and (2.9) is obtained by truncating the series $\bar{W}_{mn}$ to a finite number of plane waves. Since the resonator lattice periodicity is defined by the integers $(m, n) \in [-M, \ldots, M]$, the number of waves in the two plane directions is $N \times N$ where $N = 2M + 1$. Thus $\bar{W}_{mn}$ can be collected in the column vector $\overline{\mathbf{w}}$ of size $N \times N$, which has the same size of the reciprocal lattice vector $\left(G_p^{(1)}, G_p^{(2)}\right)$ for $p = 1, \ldots, N \times N$. Consequently, expressing equations (8) and (9) in the standard eigenvalue problem form yields

$$\left( \begin{bmatrix} \mathbf{K}_W + \tilde{k}_{ij}\left[\mathbf{u}\mathbf{u}^\top\right] & -\tilde{k}_{ij}\mathbf{u} \\ -\tilde{k}_{ij}\mathbf{u}^\top & \tilde{k}_{ij} \end{bmatrix} - \tilde{\omega}^2 \begin{bmatrix} \mathbf{I} & 0 \\ 0 & \tilde{m}_{ij} \end{bmatrix} \right) \begin{Bmatrix} \overline{\mathbf{w}} \\ \bar{z}_{i0} \end{Bmatrix} = \begin{Bmatrix} 0 \\ 0 \end{Bmatrix}$$

where $\tilde{\omega}$ are the eigenvalues and $\mathbf{v} = \left(\overline{\mathbf{w}}, \bar{z}_{i0}\right)^\top$ denotes the eigenvectors; $\mathbf{K}_W = \operatorname{diag}\left[\kappa_1, \ldots, \kappa_{N\times N}\right]$ is the diagonal matrix collecting the $p$ th stiffness contribution:

$$\begin{aligned} \kappa_p = &\left(\tilde{k}_1 + G_p^{(1)}\right)^4 + \left(2\tilde{D}_{12} + 4\tilde{D}_{66}\right)\left(\tilde{k}_1 + G_p^{(1)}\right)^2\left(\tilde{k}_2 + G_p^{(2)}\right)^2 \\ &+ \tilde{D}_{22}\left(\tilde{k}_2 + G_p^{(2)}\right)^4 \end{aligned}$$

Moreover, $\mathbf{u}$ is the $N \times N$-dimensional vector made of 1 and $\mathbf{I}$ is the identity matrix of size $N \times N$. Note that the matrix-valued equation has to be consistently augmented when the number of retained modes of the resonator becomes greater than one (e.g., $\bar{z}_{i0}$ is substituted by a vector of length equal to the number of retained modes).

# Appendix C

# Operational Deflection Shape (ODS) Extraction Procedure

This appendix describes the procedure adopted to extract the operational deflection shapes (ODSs) from the laser scanning vibrometry measurements. ODS analysis provides a visualization of the vibration field of a structure under operating or externally applied excitation conditions and does not require the measurement of the input force, unlike classical experimental modal analysis. The ODS post-processing was carried out using the Polytec *PolyWave* software package, following the methodology described in the official user documentation provided by Polytec GmbH [144].

## C.1 Data requirements

The extraction of ODSs requires two main inputs such as

• Vibration response data measured at multiple spatial locations on the structure and

• A geometric model defining the spatial coordinates of the measurement points. Depending on the available data type, PolyWave allows ODS visualization in the time domain (Time ODS) or in the frequency domain (Frequency ODS) [144].

## C.2 Time-domain ODS

For Time ODS analysis, the measured signals consist of time-domain vibration responses acquired at each scan point. PolyWave computes a time–frequency representation of the response data and allows the user to select a specific time interval for visualization. The operational deflection shape is obtained by mapping the instantaneous vibration amplitudes at each scan point onto the geometric model over the selected time window. Color contours represent the vibration amplitude distribution across the structure. When necessary, interpolation is applied to geometry nodes without direct measurement data to enhance visualization quality [144].

## C.3 Frequency-domain ODS

In Frequency ODS analysis, the deformation pattern is visualized at a selected frequency. PolyWave constructs frequency-domain response functions from the measured time signals or directly uses frequency-domain data when available. Resonance-related peaks are identified in an indicator function, and the selected frequency is used to generate the ODS animation. The resulting deflection shape represents the spatial distribution of the vibration response amplitude at the chosen frequency, visualized on the geometric model using color contours [144].

Operational deflection shapes represent the measured response of the structure under specific excitation and boundary conditions. As such, ODSs generally correspond to a superposition of multiple modal contributions and should be interpreted as operational response patterns rather than pure eigenmodes, unless the response is dominated by a single mode within a narrow frequency band [144].

# Bibliography


[1] "Structural health monitoring using lamb wave testing," Application Note OM_AN_VIB_G_020, Polytec GmbH, 2020. Accessed: 2025-04-19.

[2] M. Murer, S. K. Guruva, G. Formica, and W. Lacarbonara, "A multi-bandgap metamaterial with multi-frequency resonators," *Journal of Composite Materials*, vol. 57, pp. 783–804, Feb. 2023.

[3] M. Ruzzene and A. Baz, "Control of wave propagation in periodic composite rods using shape memory inserts," *Journal of Vibration and Acoustics*, vol. 125, no. 3, pp. 330–337, 2003.

[4] J. P. Den Hartog, *Mechanical Vibrations*. McGraw-Hill, 1956.

[5] M. I. Hussein, M. J. Leamy, and M. Ruzzene, "Dynamics of phononic materials and structures: Historical origins, recent progress, and future outlook," *Applied Mechanics Reviews*, vol. 66, no. 4, p. 040802, 2014.

[6] G. Ma and P. Sheng, "Acoustic metamaterials: From local resonances to broad horizons," *Science Advances*, vol. 2, no. 2, p. e1501595, 2016.

[7] S. A. Cummer, J. Christensen, and A. Alù, "Controlling sound with acoustic metamaterials," *Nature Reviews Materials*, vol. 1, no. 3, p. 16001, 2016.

[8] G. Failla *et al.*, "Current developments in elastic and acoustic metamaterials," *Frontiers in Materials*, vol. 11, p. 11391293, 2024.

[9] A. Srivastava, "Elastic metamaterials and dynamic homogenization: a review," *International Journal of Smart and Nano Materials*, vol. 6, no. 1, p. 41–60, 2015.

[10] Z. Liu, X. Zhang, Y. Mao, Y. Y. Zhu, Z. Yang, C. T. Chan, and P. Sheng, "Locally resonant sonic materials," *Science*, vol. 289, no. 5485, pp. 1734–1736, 2000.

[11] D. Torrent, Y. Pennec, and B. Djafari-Rouhani, "Effective medium theory for elastic metamaterials in thin elastic plates," *arXiv preprint*, 2014.

[12] Y. Wu, Y. Lai, and Z.-Q. Zhang, "Elastic metamaterials with simultaneously negative effective shear modulus and mass density," *Physical Review Letters*, vol. 107, no. 10, p. 105506, 2011.

[13] J. H. Oh, Y. E. Kwon, H. J. Lee, and Y. Y. Kim, "Elastic metamaterials for independent realization of negativity in density and stiffness," *Scientific Reports*, vol. 6, p. 23630, 2016.

[14] F. Cottone, H. Vocca, and L. Gammaitoni, "Nonlinear energy harvesting," *Phys. Rev. Lett.*, vol. 102, no. 8, p. 080601, 2009.

[15] G. Trainiti and M. Ruzzene, "Non-reciprocal elastic wave propagation in spatiotemporal periodic structures," *New Journal of Physics*, vol. 21, no. 1, p. 013001, 2019.

[16] M. Ruzzene, "Vibration and sound radiation of sandwich beams with honeycomb truss core," *Journal of Vibration and Acoustics*, vol. 125, no. 3, pp. 301–312, 2003.

[17] M. S. Kushwaha, P. Halevi, L. Dobrzynski, and B. Djafari-Rouhani, "Acoustic band structure of periodic elastic composites," *Physical Review Letters*, vol. 71, no. 13, pp. 2022–2025, 1993.

[18] N. Fang, D. Xi, J. Xu, M. Ambati, W. Srituravanich, C. Sun, and X. Zhang, "Ultrasonic metamaterials with negative modulus," *Nature Materials*, vol. 5, no. 6, pp. 452–456, 2006.

[19] L. Airoldi and M. Ruzzene, "Design of tunable acoustic metamaterials through periodic arrays of resonant shunted piezos," *New Journal of Physics*, vol. 13, p. 113010, 2011.

[20] Z. Yang, J. Mei, M. Yang, N. H. Chan, and P. Sheng, "Membrane-type acoustic metamaterial with negative dynamic mass," *Physical Review Letters*, vol. 101, no. 20, p. 204301, 2008.

[21] H. Ding, N. Huang, C. Xu, Y. Xu, Z. Cao, C. Zeng, and L. Tong, "A locally resonant metamaterial and its application in vibration isolation: Experimental and numerical investigations," *Earthquake Engineering & Structural Dynamics*, vol. 53, no. 13, pp. 4099–4113, 2024.

[22] A. S. Phani, J. Woodhouse, and N. A. Fleck, "Wave propagation in two-dimensional periodic lattices," *Journal of the Acoustical Society of America*, vol. 119, no. 4, pp. 1995–2005, 2006.

[23] A. O. Krushynska, V. G. Kouznetsova, and M. G. D. Geers, "Towards optimal design of locally resonant acoustic metamaterials," *Journal of the Mechanics and Physics of Solids*, vol. 71, pp. 179–196, 2014.

[24] L. Liu, A. Sridhar, M. Geers, *et al.*, "Computational homogenization of locally resonant acoustic metamaterial panels towards enriched continuum beam/shell structures," *Comput. Methods Appl. Mech. Eng.*, vol. 387, p. 114161, 2021.

[25] L. Fan, Y. He, X. Chen, *et al.*, "A frequency response function-based optimization for metamaterial beams considering both location and mass distributions of local resonators," *J. Appl. Phys.*, vol. 130, no. 11, p. 115101, 2021.

[26] J. Jung, S. Goo, and S. Wang, "Investigation of flexural wave band gaps in a locally resonant metamaterial with plate-like resonators," *Wave Motion*, vol. 93, p. 102492, 2020.

[27] C. Lim, J. T. Li, Z. Zhao, *et al.*, "Lightweight architected lattice phononic crystals with broadband and multiband vibration mitigation characteristics," *Extreme Mech. Lett.*, vol. 41, p. 100994, 2020.

[28] R. Chaunsali, C. W. Chen, and J. Yang, "Subwavelength and directional control of flexural waves in zone-folding induced topological plates," *Phys. Rev. B*, vol. 97, no. 5, p. 054307, 2018.

[29] E. M. Jr, S. Rodrigues, C. A. Jr, *et al.*, "Plane wave expansion and extended plane wave expansion formulations for mindlin-reissner elastic metamaterial thick plates," *J. Math. Anal. Appl.*, vol. 505, no. 2, p. 125503, 2022.

[30] W. Guo, Z. Yang, Q. Feng, *et al.*, "A new method for band gap analysis of periodic structures using virtual spring model and energy functional variational principle," *Mech. Syst. Signal Process.*, vol. 168, p. 108634, 2022.

[31] A. Bacigalupo and L. Gambarotta, "Simplified modelling of chiral lattice materials with local resonators," *Int. J. Solids Struct.*, vol. 83, pp. 126–141, 2016.

[32] C. Comi and L. Driemeier, "Wave propagation in cellular locally resonant metamaterials," *Lat. Am. J. Solids Struct.*, vol. 15, 2018.

[33] C. Lim, Z. Yaw, Z. Chen, *et al.*, "Periodic and aperiodic 3d composite metastructures with ultrawide bandgap for vibration and noise control," *Compos. Struct.*, vol. 287, p. 115324, 2022.

[34] A. Stein, M. Nouh, and T. Singh, "Widening, transition and coalescence of local resonance band gaps in multi-resonator acoustic metamaterials: From unit cells to finite chains," *Journal of Sound and Vibration*, vol. 419, pp. 324–343, 2018.

[35] Q. Qin and M. P. Sheng, "Analyses of multi-bandgap property of a locally resonant plate composed of periodic resonant subsystems," *Int. J. Mod. Phys. B*, vol. 32, no. 24, p. 1850269, 2018.

[36] E. M. Jr and J. D. Santos, "Flexural wave band gaps in elastic metamaterial thin plate," in *Proceedings of the IX Mechanical Engineering Brazilian Congress*, (Fortaleza, Brazil), pp. 1–10, 2016.

[37] A. F. Vakakis and M. E. King, "Nonlinear wave transmission in a monocoupled elastic periodic system," *J. Acoust. Soc. Am.*, vol. 98, no. 3, pp. 1534–1546, 1995.

[38] G. Chakraborty and A. K. Mallik, "Dynamics of a weakly non-linear periodic chain," *Int. J. Non-Linear Mech.*, vol. 36, no. 2, pp. 375–389, 2001.

[39] R. K. Narisetti, M. J. Leamy, and M. Ruzzene, "Study of wave propagation in strongly nonlinear periodic lattices using a harmonic balance approach," *Wave Motion*, vol. 49, no. 2, pp. 394–410, 2012.

[40] A. Banerjee, R. Das, and E. P. Calius, "Waves in structured mediums or metamaterials: A review," *Arch. Comput. Methods Eng.*, vol. 26, no. 4, pp. 1029–1058, 2019.

[41] A. Fortunati, A. Bacigalupo, M. Lepidi, A. Arena, and W. Lacarbonara, "Nonlinear wave propagation in locally dissipative metamaterials via hamiltonian perturbation approach," *Nonlinear Dynamics*, vol. 108, pp. 765–787, Feb. 2022.

[42] P. G. Kevrekidis, "Non-linear waves in lattices: past, present, future," *IMA Journal of Applied Mathematics*, vol. 76, no. 3, pp. 389–423, 2011.

[43] C. Chong, M. A. Porter, P. G. Kevrekidis, and C. Daraio, "Nonlinear coherent structures in granular crystals," *Journal of Physics: Condensed Matter*, vol. 29, p. 413003, 2017.

[44] M. Bukhari and O. Barry, "Spectro-spatial analyses of a nonlinear metamaterial with multiple nonlinear local resonators," *Nonlinear Dyn.*, vol. 99, no. 2, pp. 1539–1560, 2020.

[45] E. Basta, M. Ghommem, and S. Emam, "Vibration suppression of nonlinear rotating metamaterial beams," *Nonlinear Dyn.*, vol. 101, no. 1, pp. 311–332, 2020.

[46] L. Fang, A. Darabi, A. Mojahed, *et al.*, "Broadband non-reciprocity with robust signal integrity in a triangle-shaped nonlinear 1d metamaterial," *Nonlinear Dyn.*, vol. 100, no. 1, pp. 1–13, 2020.

[47] Y. Xia, M. Ruzzene, and A. Erturk, "Bistable attachments for wideband nonlinear vibration attenuation in a metamaterial beam," *Nonlinear Dyn.*, vol. 102, no. 3, pp. 1285–1296, 2020.

[48] Y. Shen and W. Lacarbonara, "Nonlinear dispersion properties of metamaterial beams hosting nonlinear resonators and stop band optimization," *Mech. Syst. Signal Process.*, vol. 187, p. 109920, 2023.

[49] K. H. Matlack, A. Bauhofer, S. Krödel, *et al.*, "Composite 3d-printed metastructures for low-frequency and broadband vibration absorption," *Proc. Natl. Acad. Sci. U.S.A.*, vol. 113, no. 30, pp. 8386–8390, 2016.

[50] E. M. Jr, E. Nobrega, S. Rodrigues, *et al.*, "Wave attenuation in elastic metamaterial thick plates: analytical, numerical and experimental investigations," *Int. J. Solids Struct.*, vol. 204, pp. 138–152, 2020.

[51] Q. Wang, J. Li, Y. Zhang, *et al.*, "Bandgap properties in metamaterial sandwich plate with periodically embedded plate-type resonators," *Mech. Syst. Signal Process.*, vol. 151, p. 107375, 2021.

[52] A. Casalotti, S. El-Borgi, and W. Lacarbonara, "Metamaterial beam with embedded nonlinear vibration absorbers," *Int. J. Nonlinear Mech.*, vol. 98, pp. 32–42, 2018.

[53] Y. Shen and W. Lacarbonara, "Dispersion properties of nonlinear metamaterial beams hosting nonlinear resonators," in *Proceedings of the ASME 2022 International Design Engineering Technical Conferences & Computers and Information in Engineering Conference (IDETC/CIE 2022)*, (St. Louis, MI), August 14–17 2022.

[54] A. Fortunati, A. Bacigalupo, M. Lepidi, A. Arena, and W. Lacarbonara, "Nonlinear wave propagation in locally dissipative metamaterials via hamiltonian perturbation approach," *Nonlinear Dynamics*, vol. 108, no. 2, pp. 765–787, 2022.

[55] Y. Pennec, J. O. Vasseur, B. Djafari-Rouhani, L. Dobrzyński, and P. A. Deymier, "Two-dimensional phononic crystals: Examples and applications," *Surface Science Reports*, vol. 65, no. 8, pp. 229–291, 2009.

[56] P. Sheng, *Introduction to Wave Scattering, Localization and Mesoscopic Phenomena*. Springer, 2nd ed., 2006.

[57] S. D. Huber, "Topological mechanics," *Nature Physics*, vol. 12, no. 7, pp. 621–623, 2016.

[58] S. G. Haslinger, S. Frecentese, and G. Carta, "Localized waves in elastic plates with perturbed honeycomb arrays of constraints," *Philosophical Transactions of the Royal Society A*, vol. 380, no. 2231, p. 20210404, 2022.

[59] J. Vila, R. K. Pal, and M. Ruzzene, "Observation of topological valley modes in an elastic hexagonal lattice," *Physical Review B*, vol. 96, no. 13, p. 134307, 2017.

[60] D. Qi, Z. Ren, and Z. Qu, "Valley-protected topological interface state of the elastic wave: from discrete model to multistable mechanical metamaterials," *Journal of Sound and Vibration*, vol. 529, p. 116908, 2022.

[61] H. Liu, "Multiband pure topological states in elastic structures," *Frontiers in Physics*, vol. 10, p. 909820, 2022.

[62] S. Han, M. J. Lee, and I. K. Oh, "Elastic valley hall edge wave in a hierarchical hexagonal lattice," *Journal of Sound and Vibration*, vol. 526, p. 116817, 2022.

[63] Z. Chen, Muhammad, X. Wang, and C. W. Lim, "Low frequency topologically protected wave transport in sinusoidal lightweight acoustic metamaterials," *Journal of Applied Physics*, vol. 130, no. 4, p. 045108, 2021.

[64] Z. Wen, Y. Jin, P. Gao, X. Zhuang, T. Rabczuk, and B. Djafari-Rouhani, "Topological cavities in phononic plates for robust energy harvesting," *Mechanical Systems and Signal Processing*, vol. 162, p. 108047, 2022.

[65] Y. Jin, D. Torrent, and B. Djafari-Rouhani, "Robustness of conventional and topologically protected edge states in phononic crystal plates," *Physical Review B*, vol. 98, no. 5, p. 054307, 2018.

[66] A. Ni and Z. Shi, "Robust elastic shear wave transport in membrane-type topological metamaterials induced by material difference," *Thin-Walled Structures*, vol. 197, p. 111609, 2024.

[67] F. Lemoult, M. Fink, and G. Lerosey, "Acoustic resonators for far-field control of sound on a subwavelength scale," *Physical Review Letters*, vol. 107, no. 6, p. 064301, 2011.

[68] Y. Achaoui, A. Khelif, S. Benchabane, L. Robert, and V. Laude, "Experimental observation of locally resonant and bragg band gaps in surface phononic crystal," *Physical Review B*, vol. 83, no. 10, p. 104201, 2011.

[69] M. R. Haberman and M. D. Guild, "Acoustic metamaterials," *Physics Today*, vol. 69, no. 6, pp. 42–48, 2016.

[70] X. Zhou, Y. Wang, Y. Wu, Y. Lai, and W. Wang, "Topological elastic metamaterials with robust pseudospin-dependent transport," *Nature Communications*, vol. 11, no. 1, p. 4768, 2020.

[71] D. Pham and R. Gault, "A comparison of rapid prototyping technologies," vol. 38, no. 10–11, pp. 1257–1287.

[72] E. Sachs, M. Cima, and J. Cornie, "Three-Dimensional Printing: Rapid Tooling and Prototypes Directly from a CAD Model," *CIRP Annals*, vol. 39, pp. 201–204, Jan. 1990.

[73] I. Gibson, D. Rosen, and B. Stucker, *Additive Manufacturing Technologies: 3D Printing, Rapid Prototyping, and Direct Digital Manufacturing*. New York, NY: Springer New York, 2015.

[74] Polytec GmbH, *Principles of Laser Doppler Vibrometry*, 2022. Application Note.

[75] D. Malacara, *Optical Shop Testing*. Wiley, 3rd ed., 2007.

[76] E. C. Xavier, "Comparison of homodyne and heterodyne interferometers," *Measurement Science and Technology*, vol. 22, no. 3, p. 035201, 2011.

[77] H. C. van de Hulst, *Light Scattering by Small Particles*. Dover Publications, 1981.

[78] P. Celli, B. Yousefzadeh, C. Daraio, and S. Gonella, "Bandgap widening by disorder in rainbow metamaterials," *Applied Physics Letters*, vol. 114, no. 9, p. 091903, 2019.

[79] A. S. Gliozzi, M. Miniaci, G. Cazzulani, F. Braghin, and M. Ruzzene, "Tunable photo-responsive elastic metamaterials," *Nature Communications*, vol. 11, p. 2576, 2020.

[80] M. Rahmati, J. J. Blaker, S. P. Lyngstadaas, J. F. Mano, and H. J. Haugen, "Designing multigradient biomaterials for skin regeneration," vol. 5, p. 100051.

[81] "Fused Deposition Modelling: The Advantages & Disadvantages," Oct. 2022.

[82] C. Koch, L. Van Hulle, and N. Rudolph, "Investigation of mechanical anisotropy of the fused filament fabrication process via customized tool path generation," *Additive Manufacturing*, vol. 16, pp. 138–145, Aug. 2017.

[83] "3D Printing Post Processing: Techniques, Tools and Types."

[84] G. Ma and P. Sheng, "Acoustic metamaterials: From local resonances to broad horizons," *Science Advances*, vol. 2, no. 2, p. e1501595, 2016.

[85] J. M. De Ponti, L. Iorio, G. J. Chaplain, A. Corigliano, R. V. Craster, and R. Ardito, "Tailored topological edge waves via chiral hierarchical metamaterials," *Physical Review Applied*, vol. 19, no. 3, p. 034079, 2023.

[86] Y. Wang, M. M. Sabaté, and B. Davies, "Edge modes in modulated metamaterials based on the three-gap theorem," *arXiv preprint*, 2025. Preprint, submitted January 10, 2025.

[87] R. Pal and M. Ruzzene, "Edge waves in plates with resonators: an elastic analogue of the quantum valley hall effect," *New Journal of Physics*, vol. 19, no. 2, p. 025001, 2017.

[88] T. J. Hughes, *The finite element method: linear static and dynamic finite element analysis*. Courier Corporation, 2012.

[89] COMSOL AB, *COMSOL Multiphysics Reference Manual*, version 6.1 ed., 2023.

[90] L. Brillouin, *Wave propagation in periodic structures: electric filters and crystal lattices*. New York: Dover Publications, 1953.

[91] O. Sigmund and J. S. Jensen, "Systematic design of phononic band-gap materials and structures by topology optimization," *Philosophical Transactions of the Royal Society of London. Series A: Mathematical, Physical and Engineering Sciences*, vol. 361, no. 1806, pp. 1001–1019, 2003.

[92] A. Khelif and A. Adibi, *Phononic Crystals: Fundamentals and Applications*. Berlin: Springer, 2015.

[93] Y. Shen and W. Lacarbonara, "Nonlinearity enhanced wave bandgaps in metamaterial honeycombs embedding spider web-like resonators," *Journal of Sound and Vibration*, vol. 562, p. 117821, Oct 2023.

[94] A. Palermo, J. Yang, J. J. Rimoli, and C. Daraio, "Rayleigh wave propagation in nonlinear metasurfaces," *Journal of Sound and Vibration*, vol. 526, p. 116772, 2022.

[95] T. Chen and L. Sun, "Wave propagation in elastic metamaterials with nonlinear local resonators," *Nonlinear Dynamics*, vol. 110, no. 4, pp. 3125–3142, 2022.

[96] Y. Shen and W. Lacarbonara, "Nonlinear plane-wave expansion method for analyzing dispersion properties of piezoelectric metamaterial lattices with encapsulated resonators," *Nonlinear Dynamics*, Oct 2024.

[97] L. Di Gregorio and W. Lacarbonara, "On bandgap sensitivity to three-to-one internal resonances between acoustic and optical waves in metamaterials," *Nonlinear Dynamics*, May 2025.

[98] X. Fan, X. Mao, Y. Dong, H. Liu, M. Shao, and L. Wang, "Tunable bandgaps of a metamaterial beam with nonlinear magnetic resonators," *Nonlinear Dynamics*, vol. 112, pp. 9743–9765, 2024.

[99] H. Bae, J. Kim, Y. Kim, and S. Lee, "Nonlinear elastic metamaterial for tunable bandgap at quasi-static frequency," *Mechanics of Materials*, vol. 165, p. 104155, 2022.

[100] B. Zhao, H. R. Thomsen, X. Pu, S. Fang, Z. Lai, B. Van Damme, A. Bergamini, E. Chatzi, and A. Colombi, "A nonlinear damped metamaterial: Wideband attenuation with nonlinear bandgap and modal dissipation," *Mechanical Systems and Signal Processing*, vol. 211, p. 111403, 2024. Originally available as arXiv preprint arXiv:2307.14165.

[101] X. Fang, J. Wen, and D. Yu, "Bridging coupling bandgaps in nonlinear acoustic metamaterials," *arXiv preprint*, 2018.

[102] A. H. Nayfeh and D. T. Mook, *Nonlinear Oscillations*. Weinheim: Wiley-VCH, 2008.

[103] B. Ungureanu, M. P. Makwana, R. V. Craster, and S. Guenneau, "Localizing elastic edge waves via the topological rainbow effect," *Physical Review Applied*, vol. 15, no. 1, p. 014057, 2021.

[104] W. Fang, Z. Chen, X. Zhang, and Y. Zhang, "Valley hall elastic edge states in locally resonant metamaterials," *Nature Communications*, vol. 13, no. 1, p. 1260, 2022.

[105] Y. Shen *et al.*, "Flexural edge waves and customizable local modes of circular plates," *Applied Mathematical Modelling*, vol. 136, pp. 50–62, 2025.

[106] T. Vasileiadis, J. Varghese, V. Babacic, J. Gomis-Bresco, D. Navarro-Urrios, and B. Graczykowski, "Progress and perspectives on phononic crystals," *Journal of Applied Physics*, vol. 129, no. 16, p. 160901, 2021.

[107] C. Shen, Y. Kong, T.-J. Lu, and S. Yang, "Localization of elastic waves in one-dimensional detuned phononic crystals with flexoelectric effect," *International Journal of Smart and Nano Materials*, vol. 13, no. 2, pp. 244–262, 2022.

[108] L. Cao, Z. Yang, Y. Xu, S.-W. Fan, Y. Zhu, Z. Chen, B. Vincent, and B. Assouar, "Disordered elastic metasurfaces," *Physical Review Applied*, vol. 13, no. 1, p. 014054, 2020.

[109] G. Gkantzounis, T. Amoah, and M. Florescu, "Hyperuniform disordered phononic structures," *Physical Review B*, vol. 95, no. 9, p. 094120, 2017.

[110] J. C. Ángel, J. C. Torres Guzmán, and A. Díaz de Anda, "Anderson localization of flexural waves in disordered elastic beams," *Scientific Reports*, vol. 9, no. 1, p. 3572, 2019.

[111] H. Hu, A. Strybulevych, J. H. Page, S. E. Skipetrov, and B. A. van Tiggelen, "Localization of ultrasound in a three-dimensional elastic network," *Nature Physics*, vol. 4, pp. 945–948, 2008.

[112] V. Babačić, M. Sledzińska, T. Vasileiadis, C. M. Sotomayor Torres, and B. Graczykowski, "Imperfect phononic crystals work too: The effect of translational and mid-plane symmetry breaking on hypersound propagation," *APL Materials*, vol. 12, no. 4, p. 041108, 2024.

[113] H. Ammari, B. Davies, and E. O. Hiltunen, "Anderson localization in the subwavelength regime," *Communications in Mathematical Physics*, 2024.

[114] F. Evers and A. D. Mirlin, "Anderson transitions," *Reviews of Modern Physics*, vol. 80, no. 4, pp. 1355–1417, 2008.

[115] S. E. Skipetrov and J. H. Page, "Anderson transition for elastic waves in three dimensions," *Physical Review B*, vol. 98, no. 6, p. 064206, 2018.

[116] J. Kepler, *Harmonices Mundi*. Linz: Johannes Planck, 1619.

[117] B. Grünbaum and G. C. Shephard, *Tilings and Patterns*. New York: W. H. Freeman, 1987.

[118] R. Penrose, "The role of aesthetics in pure and applied mathematical research," *Bulletin of the Institute of Mathematics and its Applications*, vol. 10, pp. 266–271, 1974.

[119] R. Penrose, "Pentaplexity: A class of non-periodic tilings of the plane," *The Mathematical Intelligencer*, vol. 2, no. 1, pp. 32–37, 1979.

[120] D. Levine and P. J. Steinhardt, "Quasicrystals: A new class of ordered structures," *Physical Review Letters*, vol. 53, no. 26, pp. 2477–2480, 1984.

[121] D. Shechtman, I. Blech, D. Gratias, and J. W. Cahn, "Metallic phase with long-range orientational order and no translational symmetry," *Physical Review Letters*, vol. 53, no. 20, pp. 1951–1953, 1984.

[122] The Nobel Prize Committee, "The nobel prize in chemistry 2011 – dan shechtman." `https://www.nobelprize.org/prizes/chemistry/2011/summary/`, 2011.

[123] R. Sainidou, N. Stefanou, and A. Modinos, "Phononic crystals: Aperiodic order and wave localization," *Physical Review B*, vol. 66, no. 21, p. 212301, 2002.

[124] Y. Chen, G. K. Hu, and G. Huang, "A design of active elastic metamaterials for control of flexural waves using the transformation method," *Journal of the Mechanics and Physics of Solids*, vol. 71, pp. 156–178, 2014.

[125] C. Sbordone and M. Guida, "Mathematical aspects of quasicrystals," *Rendiconti Lincei. Scienze Fisiche e Naturali*, 2023.

[126] D. J. Apigo, K. Qian, C. Prodan, and E. Prodan, "Topological edge modes by smart patterning," *Physical Review Materials*, vol. 2, no. 12, p. 124203, 2018.

[127] M. Florescu, S. Torquato, and P. J. Steinhardt, "Designer disordered materials with large, complete photonic band gaps," *Proceedings of the National Academy of Sciences*, vol. 106, no. 49, pp. 20658–20663, 2009.

[128] J. M. Luck and D. Petritis, "Phonon spectra in one-dimensional quasicrystals," *Journal of Statistical Physics*, vol. 42, no. 3/4, pp. 289–312, 1986. Received August 2, 1985.

[129] P. W. Anderson, "Absence of diffusion in certain random lattices," *Physical Review*, vol. 109, no. 5, pp. 1492–1505, 1958.

[130] M. Maldovan, "Sound and heat revolutions in phononics," *Nature*, vol. 503, pp. 209–217, 2013.

[131] H. H. Huang and C. T. Sun, "Band gaps in a multiresonator acoustic metamaterial," *Journal of Vibration and Acoustics*, vol. 132, no. 3, p. 031003, 2010.

[132] M. I. N. Rosa, Y. Guo, and M. Ruzzene, "Exploring topology of 1d quasiperiodic metastructures through modulated lego resonators," *arXiv preprint arXiv:2101.08810*, 2021.

[133] D. Beli, M. I. N. Rosa, C. De Marqui Jr., and M. Ruzzene, "Wave beaming and diffraction in quasicrystalline elastic metamaterial plates," *arXiv preprint arXiv:2201.12270*, 2022.

[134] X. Liu, D. Liu, J. H. Lee, *et al.*, "Spider-web-inspired stretchable graphene woven fabric for highly sensitive, transparent, wearable strain sensors," *ACS Applied Materials & Interfaces*, vol. 11, no. 2, pp. 2282–2294, 2019.

[135] E. K. Lee, R. K. Baruah, J. W. Leem, *et al.*, "Fractal web design of a hemispherical photodetector array with organic-dye-sensitized graphene hybrid composites," *Advanced Materials*, vol. 32, no. 46, p. 2004456, 2020.

[136] L. J. Gibson and M. F. Ashby, *Cellular Solids: Structure and Properties*. Cambridge Solid State Science Series, Cambridge, UK: Cambridge University Press, 2nd ed., 1997.

[137] S. Malek and L. Gibson, "Effective elastic properties of periodic hexagonal honeycombs," *Mechanics of Materials*, vol. 91, pp. 226–240, 2015.

[138] S. Sorohan, D. M. Constantinescu, M. Sandu, *et al.*, "On the homogenization of hexagonal honeycombs under axial and shear loading. part i: Analytical formulation for free skin effect," *Mechanics of Materials*, vol. 119, pp. 74–91, 2018.

[139] W. Lacarbonara, *Nonlinear Structural Mechanics: Theory, Dynamical Phenomena and Modeling*. Berlin, Germany: Springer, 1st ed., 2013.

[140] G. Formica, N. Vaiana, L. Rosati, *et al.*, "Pathfollowing of high-dimensional hysteretic systems under periodic forcing," *Nonlinear Dynamics*, vol. 103, no. 4, pp. 3515–3528, 2021.

[141] Y. Xiao, J. Wen, and X. Wen, "Flexural wave band gaps in locally resonant thin plates with periodically attached spring–mass resonators," *J. Phys. D: Appl. Phys.*, vol. 45, no. 19, p. 195401, 2012.

[142] Q. Li and M. Sheng, "An improved method for bandgap calculation of a locally resonant plate with multi-periodic multiple degree-of-freedom resonators," *Journal of Applied Physics*, vol. 129, no. 24, p. 245110, 2021.

[143] E. J. Miranda, E. Nobrega, A. Ferreira, *et al.*, "Flexural wave band gaps in a multi-resonator elastic metamaterial plate using kirchhoff–love theory," *Mechanical Systems and Signal Processing*, vol. 116, pp. 480–504, 2019.

[144] Polytec GmbH, *PolyWave*. Polytec GmbH, 2020. PolyWave software user documentation.